UNIVERSITÀ
DEGLI STUDI
FIRENZE

DOTTORATO DI RICERCA IN
FISICA E ASTRONOMIA

CICLO XXX

COORDINATORE Prof. Raffaello D'Alessandro

Organic nanocrystals and polymeric waveguides: a novel path towards integrated quantum nanophotonics

Settore scientifico disciplinare: FIS/03 Fisica della materia

Dottorando
Sofia Pazzagli

Tutori
Dr. Costanza Toninelli

Prof. Francesco S. Cataliotti

Coordinatore
Prof. Raffaello D'Alessandro

Anni 2014 / 2017

Contents

Introduction

Beyond fundamental science motivations for studying and controlling matter at the nanoscale [1, 2], there are also practical and socio-economical pushes. Among all, there is urgent quest for a new generation of multi-functional, low-loss and ultrahigh-density devices for information and communication with increased processing capacity and safer data transmission. Such technological advances are intimately linked with quantum physics, describing interactions among fundamental particles. Based on quantum effects, novel devices might be able to outperform classical ones. For instance, it is widely accepted that increasingly complex mathematical problems can be efficiently solved with quantum algorithms [3] and that new concepts of encryption based on quantum mechanics permit intrinsically secure data transfer [4].

Among quantum systems, photons, as quanta of the electromagnetic field, will play a prominent role to improve traditional devices' performances in terms of operation speed, energy efficiency, data storage and integrability [5]. Prompted by these potentialities and by the achievements of the last decades, nanophotonics, i.e. the ability to control and study light propagating at the nanoscale, has emerged as a driving future technology [6].

Open problems and current challenges in quantum nanophotonics require interdisciplinary approaches encompassing material science, quantum optics, atomic and molecular physics, as well as information science. In this context, an exciting frontier is the development of non-classical light sources producing streams of photons with controllable quantum correlations. These are fundamental resources for many quantum technologies, such as quantum secure communication schemes [7], random number generators [8], sensing, imaging and metrology applications [9, 10].

Nevertheless, quantum information and communication technology, concerned with using quantum effects and quantum states for information science, is perhaps the domain where single-photon sources find their most promising deployment [5, 11]. Indeed, single photons are very robust carriers of quantum information due their fast propagation speed and their weak interaction with transparent optical media and themselves, which minimizes decoherence.

Quantum information can be encoded in the photon polarization eigenstate (vertical and

horizontal in a given basis) or in the absence/presence of an excitation in a given mode (vacuum state and n = 1 state). Moreover, information can be manipulated and transferred among different degrees of freedom by means of conventional optical tools. Photons are therefore very well suited for carrying and distributing information across nodes in a hypothetical quantum network [12]. This architecture will be able to encode much more information than it is currently possible with the available computing technologies, and to exchange a secret key with theoretically no possibility of eavesdropping [13, 14].

However, processing single photons with all-optical gates ideally requires strong interaction among them, which is practically impossible with currently available non linear media. Alternative approaches relying on the reversible transfer of quantum information between light and matter have been conceived. For example, strong interactions can be achieved storing light in high-finesse optical cavities [15–17] or by coupling light to strongly interacting many-body systems [18]. Efficient light-matter interactions can also be accomplished by introducing a single atom or molecule in the strong evanescent field of optical nanofibers or on-chip waveguides [19, 20]. Indeed, a two-level system confined within an area comparable to its interaction cross-section has a non-linear response to the propagating field, associated to its saturable absorption.

In 2001 it was shown that quantum computing is also possible with all-optical means and without the need for a non-linear optical effect at the few photon level [21]. Linear optical quantum computing (LOQC) is only based on single-photon sources, single-photon detectors and optical circuits, consisting of beam splitters and phase shifters. Effective interaction is then provided by the exquisitely quantum phenomenon of photon coalescence, which stems from the bosonic nature of photons.

While building a general purpose linear optical quantum computer is not within reach in the near future, a special purpose subset of LOQC called *boson-sampling* has attracted a lot of attention in recent years. The boson-sampling problem, as argued by Aaronson and Arkhipov, states that, in general, the operation of a passive 'linear' optics interferometer with Fock state inputs cannot be simulated by a classical computer [22]. In particular, if one samples the output distribution utilizing photon-number discriminating detectors, one cannot predict the outcome with a classical computer without an exponential overhead in time or resources. Building a boson-sampler can therefore be considered as a step towards an optical quantum simulator or an optical quantum computer. Linear optical quantum computing and boson sampling rely on the scalable generation of indistinguishable single photons [23].

In the last years much effort has been devoted in the realization of optimal single-photon

sources and many physical systems have been investigated [24, 25]. Single quantum emitters under pulsed excitation have been proposed as deterministic sources of indistinguishable photons [26], hence representing an alternative route to the more used heralded photon generation by parametric down-conversion, which is inherently a probabilistic process [27]. Among them, atom-like emitters in the solid state - such as fluorescent atomic centers in diamond [28, 29], quantum dots [30] and single molecules [31] - are emerging due to the possibility of integrating them in photonic circuits [25].

Indeed, recent works have demonstrated tremendous progress in the fabrication and manipulation of these systems, allowing for their deterministic integration in (and hence strong interactions with) different nanophotonic devices [32–36]. In particular, coupling single emitters to a strongly confined guided mode - which can be realized with a simple dielectric waveguide - is a powerful strategy to collect a significant amount of single photons directly into on-chip guided modes [19] as no collection optics are necessary. This can help building a compact single-photon source, enabling as well logic operations and single-photon detection on the same chip [37].

In this thesis we focus on the investigation of different interfaces for the control of single-molecule emission, with the purpose of realizing an organic, integrated and efficient single-photon source, which could be readily scaled up.

Single molecules belonging to the family of Polycyclic Aromatic Hydrocarbons (PAH) in suitable host crystals have been demonstrated to be useful single-photon emitters both at liquid-helium temperatures and at room temperature [31]. These molecular systems show a high photostability under continuous and high-intensity irradiation, which makes them contenders for realistic implementations of single-photon sources. The system under investigation consists of single Dibenzoterrylene (DBT) molecules embedded in a crystalline matrix of anthracene (Ac). This solid-state emitter holds promise because of an almost unitary quantum yield [38] and negligible blinking, limited by the intersystem crossing yield (10^{-7}) to the short-lived triplet state [39]. It also shows photostable emission over days, with more than 10^{12} photons emitted before *photobleaching*, i.e. permanent loss of fluorescence [40]. At cryogenic temperatures, dephasing of the molecular dipole due to interactions with the phonons of the matrix vanishes, and as a result the purely electronic transition or 00-zero phonon line around 785 nm becomes extremely narrow, approaching the limit set by its natural linewidth [41]. Under pulsed excitation, the system can be operated as a source of indistinguishable, lifetime-limited single photons.
This thesis is structured in five chapter, which are briefly summarized as follows:

Chapter 1 provides the theoretical framework to motivate and understand the experiments described in this thesis. It introduces the relevant concepts concerning single-photon emission, wave-guiding in dielectric structures, as well as the coupling between a single quantum emitter to a guided optical mode. The chapter provides an overview of the available single-photon sources, with a greater emphasis on condensed matter systems. The finite-element method used to design the photonic structures for this thesis is here discussed, based on modal analysis performed with the commercial software COMSOL Multiphysics. This numerical approach was inspired by a one-month *Short Term Scientific Mission* in the group of Pr. Philippe Lalanne at the Institut d'Optique (Bordeaux, France), fully-founded by the COST Action Nanoscale Quantum Optics MP1403.

Chapter 2 introduces the DBT:Ac system and the experimental methods to efficiently collect fluorescence from single molecules. The experimental set-up used throughout this thesis is here presented. It consists of a custom-built epifluorescence scanning confocal microscope, fully equipped for single molecule microscopy at room temperature and single molecule spectroscopy at cryogenic temperature. This set-up has been developed in the group of Dr. Costanza Toninelli and during my PhD I learned how to use it independently and how to adapt it to different needs, associated e.g. with the investigation of integrated optics structures. A complete characterization of the DBT:Ac system measured with this set-up is provided at the end of the chapter. We here show that the intrinsic physical properties of single DBT molecules in bulk Ac crystals make this molecular system an excellent candidate as a reliable source of single photons.

Chapter 3 presents the design and realization of an integrated platform for the coupling of single photons from DBT molecules to dielectric single-mode waveguides (silicon nitride on glass). At room temperature, we observe that molecules in close proximity to the dielectric waveguides couple to the evanescent tail of the guided mode, with a measured coupling efficiency (β) up to $(42 \pm 2)\%$. This result is competitive with state-of-the-art single-photon emission into ridge waveguide modes from other solid state systems, demonstrating the potentiality of the molecule-based source of our choice. This research project is carried out in collaboration with the groups of Pr. Wolfram Pernice (Universität Münster, Germany) and Pr. Oliver Benson (Humboldt Universität zu Berlin, Germany) for what concern the fabrication of the photonic chip. Experimental investigation on the realized hybrid system is performed in our laboratories at LENS (European Laboratory for Non Linear Spectroscopy) and in the Department of Physics of the University of Florence. This work is published in ACS Photonics [42].

Chapter 4 describes the protocol developed during my PhD aiming to fabricate DBT:Ac

crystals with sub-micron size. In particular, two recipes has been optimized for the fabrication of individual nanocrystals suitable for single molecule experiments respectively at room and cryogenic temperatures. Besides a morphological analysis, optical measurements demonstrate the possible use of DBT:Ac nanocrystals as a highly pure and bright single-photon source at room temperature, able to deliver photostable lifetime-limited photons at cryogenic temperature. This work is the subject of a manuscript in preparation.

Chapter 5 reports on preliminary results about the integration of DBT:Ac nanocrystals in patternable polymers. On this subject we are currently performing a search for prior art and discussing a possible patent application. A first study focuses on two commercial photoresists processable with a 3D direct laser writing workstation (Photonic Professional, Nanoscribe GmbH), currently available in our laboratories. A complementary approach relying on the natural compatibility of organic nanocrystals with water-based polymers is also discussed. We show that hybrid organic nanocrystals-polymer platforms are promising for the development of single-photon sources integrated on-chip. We report on florescence coupled to a suspended polymeric waveguide and on the Stark tuning of molecules in a multilayer polymeric chip with a graphene electrode. In collaboration with the group of Frank Koppens, Institute of Photonic Sciences (ICFO) in Barcelona, we are currently working on the 2D materials-DBT:Ac-polymer hybrid devices and a manuscript on our recent results is in preparation.

1 Background and Theory

This chapter lays the theoretical framework for the experiments described in this thesis. The first part introduces the fundamental concepts related to the physics of single-photon emitters in the solid-state. The second part focuses on the essential principles of wave-guiding in dielectrics and on the coupling of quantum emitters to optical modes. We finally introduce the numerical methods employed in this thesis for the design of two different guiding structures which have been investigated within this work in relation to single molecule-based light emitters that will be discussed in the following chapters.

1.1 Single-Photon Sources

In Section 1.1.1 we introduce three classifications of light based on the photon statistics and on the photon distribution in time. In particular, the concepts of sub-Poissonian and antibunched light are discussed. In Section 1.1.2 we briefly recall the basic properties of light-matter interaction to show how single quantum emitters might be used as sources of single photons. We then introduce fundamental figures of merit to describe the performance of single-photon sources (Section 1.1.3), that will be used to give a meaningful overview on the available SPSs (Sections 1.1.4), with a greater emphasis on condensed matter systems.

1.1.1 About the quantum nature of light

Light emitted by a single-photon source (SPS) exhibits unique properties that can be used in a number of applications. Assuming the quantization of the electromagnetic field, a *Fock* or number state $|n\rangle$ is an eigenstate of the number operator $n = a^\dagger a$, where $a^\dagger$ and a are respectively the creation and annihilation operator of a photon of energy $\hbar\omega$ and correspond to a well-defined number of energy quanta n.

A single-photon state is hence $|1\rangle$, while coherent laser light is described by a coherent state $|\alpha\rangle$ defined by the (unique) eigenstate of the annihilation operator a associated to the eigenvalue α, i.e. $a|\alpha\rangle = \alpha|\alpha\rangle$. This is the closest approximation of a classical field as the

expectation value of the electric field operator on a coherent state represents the classical electric field, i.e. a stable oscillating wave.

In order to discrimate different flavours of light one can then imagine counting and recording the statistics of the number of clicks on a detector in a time window shorter than the source coherence time τ_c[1]. It can be shown that when detecting light from a laser, the probability of detecting n photons follows a Poissonian distribution, with mean value $\overline{n}$, given by [43]:

$$P(\overline{n}) = |\langle n|\alpha\rangle|^2 = \frac{\overline{n}}{n!}e^{-\overline{n}} \tag{1.1}$$

The Poissonian distribution describes processes that are intrinsically random, as e.g. the decay process of a radioactive elements or in our case the detection of coherent light, in which randomness is due to the discrete nature of photons. Poissonian statistics is fully characterized by its mean value, related to the standard deviation by the formula $\Delta n = \sqrt{\overline{n}}$. With respect to the reference case of coherent light, we can classify different "flavours" of light sources, according to their photon statistics (i.e. the statistics of the intensity fluctuations of an electromagnetic field), or the way the emitted photons are distributed in time. Three examples for different type of light are shown in **Figure 1.1a** in terms of the photon statistics and in **Figure 1.1b** in terms of photons streams, as described hereafter.

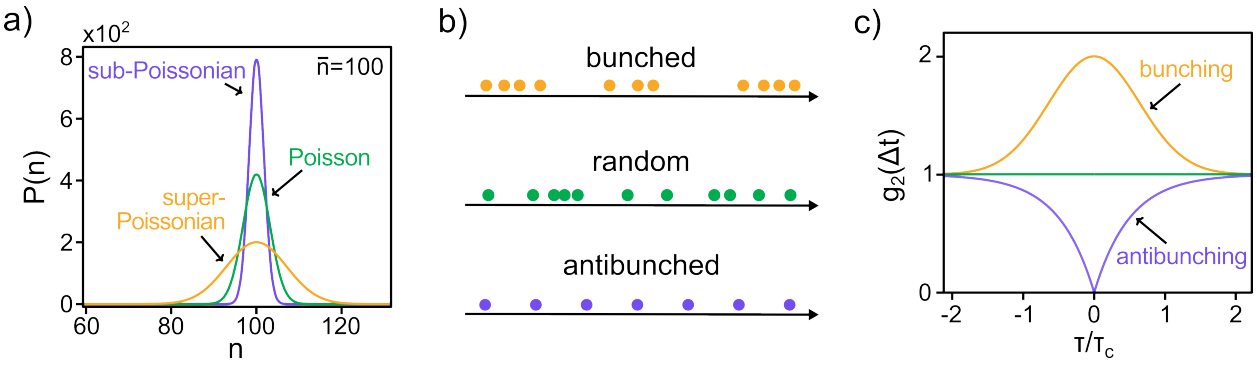

Figure 1.1 – **a)** Comparison of the photon statistics for Poissonian, super-Poissonian and sub-Poissonian light. All the distributions shown have an average photon number of $\overline{n} = 100$. **b)** Schematic of the distribution of photons as a function of time. **c)** Second-order correlation function $g^2(\tau)$ for the three ideal sources: a chaotic, thermal light source (solid orang curve) showing bunching, a coherent Poissonian source (dotted green curve) and a single-photon source (solid blue curve) showing antibunching. The time scale is given by the coherence time τ_c, i.e. the time over which a propagating beam may be considered coherent.

Classical forms of light, such as thermal light or black body radiation, are noisier than

[1]For an electromagnetic field, the coherence time is the time over which a propagating beam may be considered coherent.

the perfectly coherent one, in both classical sense (larger intensity variations) and quantum sense (larger photon number fluctuations), and are described by a super-Poissonian statistics, characterized by $\Delta n > \sqrt{\overline{n}}$. In this case, photons detected by a photon-counter distribute themselves preferentially in bunches rather than randomly, as for the case of coherent light (yellow and green dots in **Figure 1.1b**, respectively).

On the other hand, light emitted during a spontaneous emission process, as e.g. an atom upon continuous resonant excitation, is made of a stream of photons with a higher regularity in time, defined by the radiative lifetime of the considered transition. In this case, light follows a sub-Poissonian statistics with $\Delta n < \sqrt{\overline{n}}$, and is hence narrower than the Poissonian one (see **Figure 1.1a**). Unlike previous cases, the distribution cannot be described by classical theories and as such, is synonym of quantum light.

The statistics of the intensity fluctuations of an electromagnetic field are also efficiently described by the second-order correlation function $g^2(\Delta t)$, which is the joint probability of detecting two photons in a time interval Δt, classically written in terms of the intensities I of the detected fields as [44]:

$$g^2(\Delta t) = \frac{\langle I(t+\Delta t)I(t)\rangle}{\langle I(t)\rangle^2} \tag{1.2}$$

where average is taken over a stationary state of light [45].

Setting $\Delta t = 0$[2], with some calculations the second-order correlation function can be written, in terms of the number of detected photons, as [46]:

$$g^2(0) = 1 + \frac{(\Delta n)^2 - \overline{n}}{\overline{n}^2}. \tag{1.3}$$

This expression clearly underlines the connection between $g^2(\Delta t)$ and photon statistics, and the above classification of light can hence be re-phrased in terms of the second-order correlation function, as follows:

- for **coherent light** $g^2(0) = 1$. This means that, as a signature of the Poissonian photon statistics, photons are detected with equal probability within any given time interval. Coherent light is thus referred to as **random light**.

- for **thermal light** $g^2(0) > 1$. This means that if we detect a photon at time $t = 0$, there is a higher probability of detecting another photon at short times than at long times. In this case the photon stream is characterized by photons clumped together in bunches, and from here derived the name **bunched light**.

[2]The analysis done with $\Delta t \neq 0$ is rather complicated but would give the same result.

- for **quantum light** $g^2(0) < 1$. This means that after the detection of one photon, the probability of detecting another photon is small for small time interval and increases with Δt. Sub-Poissonian light is also referred to as **antibunched light**.

The different $g^2(\Delta t)$ functions are plotted in **Figure 1.1c** as a function of the time delay normalized to the coherence time τ_c. Note that in all cases, $g^2(\Delta t) \to 1$ for $\Delta t \to \infty$, since at long times there is no correlation.

Photon antibunching, like the related (but not equivalent [47]) sub-Poissonian photon statistics, represents a clear evidence of the quantum nature of light. Indeed, the correlation function of antibunched light violates the Cauchy-Schwarz inequality $\langle I(t')I(t)\rangle \geqslant \langle I(t)\rangle^2$ that any classical stationary function of time must satisfy.

In a perfect configuration, the correlation functions vanishes for zero time-delay. However, the observation of this effect is in practice very sensitive to optical losses and inefficient detection that tend to reinstate complete randomness. To overcome experimental limitations given by detector dead-times (typically around 50 ns) a scheme called Hanbury Brown-Twiss (HBT) [48] interferometer was developed, yielding to the first successful demonstration of photon antibunching from the atomic transition of sodium atoms [49].

The HBT set-up, described in details in the following chapter, is nowadays a well established technique to measure the second-order autocorrelation function, making the $g^2(0)$ a fundamental figure of merit for a quantum light source, as it quantifies its *purity* i.e. the probability of simultaneous multi-photon emission. Besides purity, a SPS should fulfill several non-trivial features that will be discussed in Section 1.1.3. But first, in order to understand the different criteria used to describe and compare the performance of a SPS, it is necessary to briefly recall the basic properties of light-matter interaction in atom-like emitters in the solid state, that are recently emerging as very promising SPS for on-chip implementations [25].

1.1.2 Physics of quantum emitters

A quantum emitter (QE) is generally defined as a quantum system that is capable of radiative electromagnetic transitions and whose optical properties are determined by its energy level diagram. In general, QEs in the solid state present complex energy level schemes, including also those deriving from interactions with the host material (involving vibrational states and dark states). However, for most experimental cases, a QE is probed by a monochromatic laser source resonant with only one of the optical transitions and, in first place, the coupling can be restricted to the two level system.

In this case, the quantum system is simply characterized by the ground state $|g\rangle$ and the excited $|e\rangle$ state with energy difference of $\hbar\omega$. All the other energy levels can instead be neglected since, being far from resonance, they only weakly interact with light.

In what follows we briefly recall the main aspects of light-matter interaction written in a fully quantum formalism, following the approach of [44, 50].

Light-matter interaction and spontaneous emission

The interaction of a two-level atom with a monochromatic light field is described by an interaction Hamiltonian H given by the sum of the Hamiltonians of the atom H_A, the light field H_L and their interaction H_I.

With the ground-state energy normalized to zero, the free atomic Hamiltonian is $H_A = \hbar\omega|e\rangle\langle e|$. The light field is expressed as the sum of normal modes (which can be either radiative or guided) with wavevector $\mathbf{k}$ and frequency ω_k, yielding an Hamiltonian formally analogous to that of an harmonic oscillator: $H_L = \sum_k \hbar\omega_k \left(a_k^\dagger a_k + \frac{1}{2}\right)$. For optical (i.e. in the visible range 400 nm to 700 nm) fields, the wavelength is large compared to the dimensions of the interacting quantum system (few nm) and the *dipole approximation* holds. In this case, the interaction Hamiltonian can be written as the scalar product between the quantized electric field operator $\mathbf{E}$ and the electric dipole operator $\mathbf{d} = e\mathbf{r}$ of the system, with $\mathbf{r}$ the position of the atomic electron[3].

Within the *rotating wave approximation*[4], the interaction can occur either via absorption of a photon and excitation of the atom, or via emission of one photon and atomic decay. This corresponds to $H_I = \hbar g \left(a|e\rangle\langle g| + a^\dagger|g\rangle\langle e|\right)$, where a single mode is considered and where g is the atom-field coupling strength given by [51]:

$$g = \sqrt{\frac{\omega_0}{2\varepsilon\hbar V}}|\mathbf{d}|(\hat{\mathbf{d}}\cdot\hat{\boldsymbol{\epsilon}}) \tag{1.4}$$

with $|\mathbf{d}|$ the scalar electric dipole element of the matrix corresponding to the atomic transition between the initial $|i\rangle$ and the final $|f\rangle$ states induced by the interaction with the

[3] The electric dipole moment for an atom is generally defined as $\mathbf{d} = \sum_i q_i\mathbf{r}_i$, where q_i and $\mathbf{r}_i$ are respectively the charge and the position vector for the i-th electron. Here we are assuming an hydrogen-like atom, i.e. the electromagnetic field interacts predominantly with one atomic electron.

[4] Starting in the dipole approximation, the interaction Hamiltonian H_I has terms oscillating with frequency $(\omega_k - \omega)$ and terms oscillating with $(\omega_k + \omega)$. When the electromagnetic radiation is nearly resonant with the atomic transition and its intensity is low, the dynamics of emission and absorption occur on a time scale much slower than $1/\omega$ or $1/\omega_k$ and the rapidly oscillating terms with frequency $(\omega + \omega_k)$ are assumed to average out on and are hence neglected in the Hamiltonian. This approximation is referred to as rotating wave approximation and correspond in dropping the terms in the total Hamiltonian which do not obey energy conservation.

electromagnetic field (i.e. $\langle f|\mathbf{d}|i\rangle$); the scalar product $(\hat{\mathbf{d}}\cdot\hat{\boldsymbol{\epsilon}})$ accounts for the angle between the polarization vector $\hat{\boldsymbol{\epsilon}}$ of the electric field and and the unit vector $\hat{\mathbf{d}}$ of the transition dipole; ε is the dielectric permittivity of the material surrounding the atom; and V is the quantization volume of the electromagnetic field.

The total Hamiltonian for the coupled radiation-atomic system is then given by:

$$H = \hbar\omega|e\rangle\langle e| + \hbar\omega\left(a^\dagger a + \frac{1}{2}\right) + \hbar g\left(a|e\rangle\langle g| + a^\dagger|g\rangle\langle e|\right) \tag{1.5}$$

considering a single mode with frequency ω_L near to the atomic transition (i.e. the atom-light detuning $\Delta = \omega_L - \omega \simeq 0$), as e.g. for the interaction between a QE and a resonant cavity. In many problems, H_I can be treated as a perturbation on the eigenstates of the unperturbed Hamiltonian $H_0 = H_A + H_L$, given by the tensor product of the electronic state and the eigenstate of the electromagnetic mode. In first order time-dependent perturbation theory, the transition rate between an initial and final state $\Gamma_{i\to f}$ is given by *Fermi´s golden rule*[5] [52]:

$$\Gamma_{i\to f} = 2\pi|g(\mathbf{r},\omega)|^2 D(\omega) = \frac{\pi\omega}{\varepsilon\hbar}(\hat{\mathbf{d}}\cdot\hat{\boldsymbol{\epsilon}})^2|\mathbf{d}|^2\frac{D(\omega)}{V} \tag{1.6}$$

where $D(\omega) = \frac{1}{\hbar}\frac{\mathrm{d}N}{\mathrm{d}\omega}$ is the photonic density of the final states and corresponds to the number of photonic states N with energy $\hbar\omega$ due to the specific nanoenvironment of the emitter, and is hence referred to as local density of states (LDOS).

Fermi's golden rule can be used to calculate the spontaneous emission rate $\Gamma_{2\to1} = \Gamma_{21}$ of an atom-like emitter when embedded both in an homogeneous medium with refractive index n and in the case of a non-uniform dielectric structure such as a waveguide, as it will be discussed in Section 1.2. Note that the decay rate Γ_{21} integrates all possible decay channels available for spontaneous emission, accounting for radiative (r) and non radiative (nr) transitions: $\Gamma_{21} = \Gamma_{\mathrm{r}} + \Gamma_{\mathrm{nr}}$. Radiative channels correspond to far-field emission of a photon, while non-radiative channels correspond to non radiative dissipative processes that can be due either to internal non-radiative channels and non-radiative processes induced by the environment. A measurement of the excited state lifetime τ of the QE provides a direct measurement of $\Gamma_{21} = 1/\tau$.

In the particular case of an atom-like emitter embedded in an homogeneous medium with

[5]This transition rate can also be regarded as a statement of energy conservation: transitions only occur when the energies of the initial and final states match. Note that equation (1.6) is derived via first order perturbation theory, thus it is always valid when light and matter weakly interact. In the case of strong laser fields, instead, Fermi's golden rule holds when the time of the measurement is much larger than the time needed for the transition [44].

refractive index n and dielectric permittivity $\varepsilon = n^2\varepsilon_0$, the LDOS is given by [53][6]:

$$D(\omega)^{\text{hom}} = \frac{2\omega}{3\pi(c/n)^3}V. \tag{1.7}$$

The equation (1.6) for the spontaneous emission hence becomes:

$$\Gamma_{21}^{\text{hom}} = \frac{n\omega^3}{3\pi\hbar\varepsilon_0 c^3}|\mathbf{d}|^2 \tag{1.8}$$

stating that, besides natural constants, the spontaneous emission rate in a homogeneous medium represents an intrinsic property of the QE, as it is determined only by the initial and final states (and the refractive index n). In this particular case, the emitter radiatively decays with an electric dipole-like electromagnetic field pattern.

If, instead, the emitter is surrounded by materials of different composition and shape, its radiative transition rate and angular distribution pattern can be strongly modified [54], as novel radiative and non-radiative channels become available.

The possibility to engineer the LDOS, and hence the optical properties of a QE, by placing it into a structured environment was first pointed out by Purcell [55], that computed the modification of the nuclear magnetic moment decay rate at radio frequency when coupled to a resonant circuit (Γ_{cav}) with respect to the decay rate in vacuum (Γ_0) as:

$$F_P = \frac{\Gamma_{\text{cav}}}{\Gamma_0} = \frac{3}{4\pi^2}\lambda^3\frac{Q}{V} \tag{1.9}$$

with $\lambda = 2\pi c/\omega$, Q and V the quality factor and the mode volume of the cavity, respectively. This result, usually referred to as the Purcell factor, led to the development of an increasing number of methods to either enhance or suppress the spontaneous emission by coupling atoms to single mirrors [56], waveguides [57] and planar or spherical cavities [58–60]. Advances in microfabrication techniques enabled the construction of high quality microcavities and triggered several experiments on solid state cavity quantum electrodynamics (CQED) [61–65]. Cavities are now widely used to improve characteristics, delivery rates and spectral ranges of SPSs [66].

[6] This can be derived as follows: wave vectors $\mathbf{k}$ with equal energy form spherical shells in the 3D reciprocal space. The integrated surface of such shells results in the number of modes N per energy interval $\Delta\hbar\omega$ from which the derivation $D(\omega) = \frac{1}{\hbar}\frac{\mathrm{d}N}{\mathrm{d}\omega}$ can be performed, yielding to equation (1.7).

Dynamics of a 2-level system driven by a resonant laser

To study the dynamics of a two-level atom driven by a single mode laser we recall the total Hamiltonian in equation (1.5) and introduce dissipation. Since the electromagnetic field remains roughly unaffected by the atom, it can be neglected from the dynamics of the coupled system and considered as a *reservoir*. Therefore the total Hamiltonian for the atom-field system reduces to:

$$H = \hbar\Delta\hat{s}_z + \frac{\hbar\Omega}{2}(\hat{s}_+ + \hat{s}_-) \tag{1.10}$$

where Ω is the Rabi frequency and is associated with the strength of the atom-field coupling g, $\hat{s}_z = |e\rangle\langle e| - |g\rangle\langle g|$ is the inversion operator, $\hat{s}_- = |e\rangle\langle g|$ and $\hat{s}_+ = |g\rangle\langle e|$ are the atomic lowering and raising operators, respectively.
The dynamics of the two-level atom in the rotating frame is now governed by the master equation [67]:

$$\frac{d\rho}{dt} = \frac{i}{\hbar}[H, \rho] + L(\rho) \tag{1.11}$$

with the Lindblad form $L(\rho) = -\frac{1}{2\tau}(\hat{s}_+\hat{s}_-\rho + \rho\hat{s}_+\hat{s}_- - 2\hat{s}_-\rho\hat{s}_+)$ and ρ the reduced density matrix operator of the atom[7] given by:

$$\rho = \begin{pmatrix} \rho_{gg} & \rho_{ge} \\ \rho_{eg} & \rho_{ee} \end{pmatrix} \tag{1.12}$$

where the diagonal elements, ρ_{gg} and ρ_{ee}, are referred to as populations and give the measurement probability for the system to be in the ground and in the excited states respectively ($\rho_{gg} + \rho_{ee} = 1$, assuming a closed system). The off-diagonal elements, ρ_{ge} and $\rho_{eg} = \rho_{ge}^\dagger$, account for the interference between the states and are thus referred to as coherences[8].

The equations of motion for the density matrix elements can now be derived from the master equation (1.11) and correspond to the well-known optical Bloch equations, in analogy to the motion of the nuclear magnetic moment in an electromagnetic field [68]:

$$\frac{d\rho_{ee}}{dt} = -\frac{d\rho_{gg}}{dt} = \frac{i\Omega}{2}(\rho_{eg} - \rho_{ge}) - \frac{1}{\tau}\rho_{ee} \tag{1.13}$$

$$\frac{d\rho_{ge}}{dt} = \frac{d\rho_{eg}^*}{dt} = \frac{i\Omega}{2}(\rho_{gg} - \rho_{ee}) - (\gamma_C + i\Delta)\rho_{ge} \tag{1.14}$$

where γ_C is the coherence damping rate and is related to two distinct mechanisms: population decay and population-conserving scattering processes[9], i.e. pure dephasing processes arising

[7] The density matrix is defined as $\rho = \sum_i p_i|\psi_i\rangle\langle\psi_i|$, stating that the only available information is that the system is in the state $|\psi_i\rangle$ with probability p_i ($p_i \geq 0$, $\sum_i p_i = 1$). The density matrix represents the state of a quantum system in a more general way than the state vector $|\psi\rangle$. In fact, only when we have complete information about a quantum system, it can be efficiently described by a state vector $|\psi\rangle$, called *pure state*. More in general, however, a quantum system interact with an external system whose evolution is unknown. In this case the quantum system is described by a *statistical mixture* of states, i.e. the density operator ρ. The density operator has the following properties:

- it is Hermitian: $\rho = \rho^\dagger$
- the sum of the diagonal elements of the density matrix is $Tr\rho = 1$ (probability conservation law)
- the mean value of an observable A is given by: $\langle A\rangle = Tr(\rho A)$
- its evolution is described by the *Schrödinger-von Neumann equation*: $\frac{d\rho}{dt} = -\frac{i}{\hbar}[H, \rho]$

. Consider now two distinct and independent systems A and B. The joint density matrix of the composite system is described by $\rho_{AB} = \rho_A \bigotimes \rho_B$. The subsystem A is then given by:

$$\rho_A = Tr_B\rho_{AB}$$

with Tr_B the partial trace over system B. Since the two-level atom and the radiation are now considered distinct and independent, the atom state is described by the reduced density matrix of the the two-level atom alone.

[8] In the rotating frame, populations don't change while coherences become $\tilde{\rho}_{eg} = \rho_{eg}e^{i\omega t} = \tilde{\rho}_{ge}^\dagger$.

[9] These two types of damping are sometimes called longitudinal relaxation and transverse relaxation, respectively, following Bloch's treatment of nuclear magnetic resonance.

from interactions with the environment and characterized by a dephasing time T_2'. The decoherence time $T_2 = 1/\gamma_C$ can then be written as:

$$\frac{1}{T_2} = \frac{1}{2\tau} + \frac{1}{T_2'} \tag{1.15}$$

and determines the broadening of the transition linewidth (full width at half maximum FWHM) as:

$$\Delta\omega_{\text{hom}} = 2\gamma_C = \frac{1}{\tau} + \frac{2}{T_2'} \tag{1.16}$$

In the absence of collisional damping, equation (1.16) reduces to the so-called natural or lifetime-limited linewidth $\Delta\omega_{\text{nat}} \equiv 1/\tau$ and the lineshape exhibit a "natural" homogeneous broadening with a Lorentzian profile.

For most quantum systems in condensed matter, as our experimental case of single molecules embedded in a solid matrix, the environment strongly affects the photophysics of the QE. At room temperature, solid state emitters are affected by dephasing (or decoherence), arising from perturbations of the oscillation frequency through the interaction with the environment. As a consequence, the electronic transition to the ground state is distributed over a broad rage of frequencies, involving vibrational levels and phonons. In this case, the dephasing time T_2' is by several order of magnitude shorter that the excited-state lifetime τ and a strong damping sets in ($\gamma_C \gg \Gamma_{21}, \Omega$). This means that coherences will be damped very quickly, whereas the populations will continue to evolve on much longer timescales. Coherences can thus be considered in equilibrium and the optical Bloch equation for the atomic populations reduces to the Einstein rate equations [69, 70]:

$$\frac{d\rho_{ee}}{dt} = -\frac{d\rho_{gg}}{dt} = -\Gamma_{21}\rho_{ee} - \Gamma_{12}(\rho_{ee} - \rho_{gg}) \tag{1.17}$$

where Γ_{12} is the absorption rate and is a linear function of the intensity I of the excitation laser.

Assume that at time $t = 0$ the two-level system is completely in the ground state and a continuous wave (CW) laser resonant with the atomic transition is switched on. The system is driven to a steady state ($\frac{d\rho_{ee}}{dt} = 0$) in which spontaneous emission exactly compensates excitation, as:

$$\rho_{ee}(t) = \rho_{ee}(t \to \infty)\left[1 - e^{-(\Gamma_{12}+\Gamma_{21})t}\right] \tag{1.18}$$

where $\rho_{ee}(t \to \infty) = \frac{\Gamma_{12}}{\Gamma_{12}+\Gamma_{21}}$ is the excited steady state occupation. For small excitation intensities, the population ρ_{ee} increases linearly with I. At increasing intensities, the slope decreases falling to zero in the limit of large intensities, where the largest possible excitation is reached ($\rho_{ee} = \rho_{gg} = 1/2$). Such a behaviour, namely the atomic saturation, is a clear signature of the quantum nature of the atom, since it is not expected in a classical model in which the emitter can be excited to arbitrarily high amplitude.

Consider now the dynamic behavior of the two-level system when the laser is suddenly turned off. The system decays exponentially from the excited state into the ground state through spontaneous emission:

$$\rho_{ee}(t) = \frac{\Gamma_{12}}{\Gamma_{12} + \Gamma_{21}} e^{-t/\tau}. \tag{1.19}$$

In a fluorescence experiment, the fluorescence intensity, i.e. the emitted photons rate R, rather than the population decay $\rho_{ee}(t)$ is measured. Since the emitted photon rate is proportional to the population decay $\rho_{ee}(t)$, referring to equation (1.19), the fluorescence intensity $I(t)$ decays exponentially as:

$$R(t) = R(0)e^{-t/\tau} \tag{1.20}$$

from which the excited state lifetime, and hence the spontaneous decay rate Γ_{21}, can be determined.
As fluorescence emission is a random process, only few emitters will emit their photons at precisely $t = \tau$ while the 63% of them decays at longer lifetime and the 37% decay at $t > \tau$ [71]. Experimentally, these curves can be obtained from measurements of the time resolved photon arrival probability, by means of time-correlated single-photon counting (TCSPC) technique, described in Chapter 2.3.1.

Let us note that the photon emission times under CW-excitation are not deterministic. A simple method of forcing single-photon emission on demand is based on off-resonant pulsed optical excitation, exploiting e.g. a vibrational level of the excited state to achieve population inversion. Once prepared in the excited state, the emitter decays generating a single photon on the time scale of the fluorescence lifetime which determine the optimal parameters for the laser source repetition rate and pulse duration [72, 73].

1.1.3 Key parameters of a SPS

The performance of a SPS can be quantified in terms of several parameters. The most important ones are here discussed focusing on solid state SPS and relying on the concepts presented in the previous section. The experimental method used to quantify them is also briefly introduced.

Purity

According to the definition given in Section 1.1.1, the first requirement for a SPS is that multiphoton emission probability is negligible, ideally zero. The parameter that quantifies the multiphoton emission probability is called purity and, as anticipated, is quantified by the dip of the second-order autocorrelation function $g^2(\Delta t)$ at zero delay time ($\Delta t = 0$), that is routinely measured with two highly efficient photodetector in a HBT configuration (see Chapter 2.3.2). For an ideal SPS we have seen that $g^2(0) = 0$, but typical experimental values lie in the range between $g^2(0) = 0.015$ and $g^2(0) = 0.3$ [74].

Several factors related to measurement imperfections can lower the single-photon purity of a source, increasing the probability to register two photons at the same time: an inefficient detection (collecting emission of two or more nearby emitters[10]) and background contributions due to dark counts of the detectors [76] and background (often broadband) photons [77].

Indeed, special care should be paid in properly filter, either spectrally and spatially, the photons collected from a SPS, and the use of low dark-count rate detectors is necessary. Moreover, in order to correctly interpret a measured $g^2(\Delta t)$-function, it is customary to correct the experimental purity with an independent measure of the background counts and of the time response of the HBT set-up. Given a signal-to-background ratio (S/B), one can estimate the actual value of $g^2(0)$ from the measured value $g^2_{\text{exp}}(0)$ as [78]:

$$g^2(0) = 1 + \frac{g^2_{\text{exp}}(0) - 1}{P}, \qquad P = \frac{S}{S+B}. \tag{1.21}$$

Quantum efficiency

A second requirement for efficient operations with a SPS is that the emitting species should have a high quantum efficiency, or quantum yield QY, defined as the probability that an

[10] Indeed, for N independent single emitters with equal emission intensities, the contrast of the g^2-function scales as $g^2(0) = 1 - 1/N$. Correspondingly, a minimum of $g^2(0) < 0.5$ corresponds to the presence of a single emitter [75].

optical photon is emitted per excitation cycle [79]:

$$\mathrm{QY} = \frac{\Gamma_r}{\Gamma_{21}} \tag{1.22}$$

where $\Gamma_{21} = \Gamma_\mathrm{r} + \Gamma_\mathrm{nr}$, i.e. is the sum of all the decay rates into the channels available for spontaneous emission, that can be either radiative and non-radiative, as discussed in the Section 1.1.2. Here we consider the intrinsic properties of the emitter and we are hence assuming that there is no contribution in the decay rate induced by the environment.

An ideal SPS should have QY = 1, but in practice it is reduced by internal (intrinsic) non-radiative processes or processes that do not lead to photon creation in the detected wavelength range. In particular, solid state emitters prepared in the excited state might undergo a transition to an intermediate state from which decay to the ground state can occur non-radiatively or via emission of a "non-usable" photon (phosphorescence).

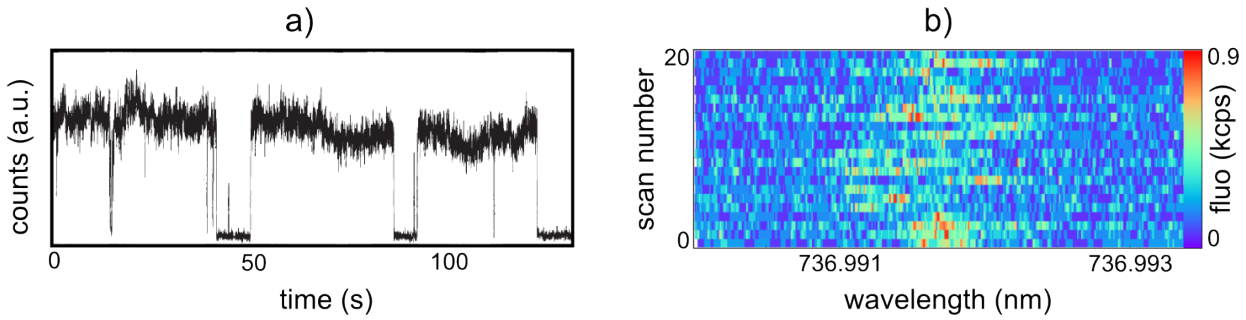

Figure 1.2 – **a)** The time dependence of the emission intensity of a single CdSe quantum dot coated with a seven-monolayer-thick ZnS shell under a continuous-wave excitation intensity, showing blinking behavior on time scales of seconds (Figure adapted from reference [80]). **b)** Resonant excitation to probe individual SiV-centres, showing spectral diffusion when repeating a frequency scan around the excitation line position (Figure adapted from reference [81]).

This transition translates into a temporary loss (intermittence) of fluorescence, known as blinking (see **Figure 1.2a**), that reduces the QY. Moreover, in the case of fluorescent molecules, as the one considered in this thesis, a permanent loss of fluorescence, called photobleaching, can occur due to quencher agents such as oxygen [82]. However, as it will be discussed in the next chapter, in certain matrices and at low temperature, photobleaching can be delayed almost indefinitely [83].

When a QE is hosted in a solid matrix, vibrational levels due to interaction with phonons makes emission broad in frequency, while for most applications the transition of interest is the purely electronic transition between the ground and excited states (the so-called zero-phonon line or ZPL). The ZPL at low temperatures can in fact reach its natural lifetime-limited value

but may still constitutes only a small % of the total emission, according to the Debye-Waller factor α_{DW} (see Chapter 2.1.2 for a more in-depth discussion). In particular, $\alpha_{\mathrm{DW}} < 1$ contributes in reducing the value of the QY.

Direct measurement of the QY is not straightforward, but can be estimated by measuring all possible decay rates. As anticipated, Γ_{21} can be derived measuring the fluorescence lifetime τ via time resolved photon arrival probability, by means of the TCSPC technique. Information about the shelving and de-shelving dynamics can be inferred by the study of the second-order correlation function $g^2(\Delta t)$ at long time delays [84].

Brightness

The brightness of a SPS represents the maximum rate R at which single photons can be emitted[11]. This rate depends on the excited state lifetime τ, on the probability of radiative decay QY and on the probability of the population of the excited state ρ_{ee} as:

$$R(I) = \frac{1}{\tau}\rho_{ee}(I)\mathrm{QY} \tag{1.23}$$

with I the intensity of the pump laser. Because of saturation, population of the excited state increases linearly with I until the system is driven to a steady state in which spontaneous emission exactly compensates excitation ($\rho_{ee} = \rho_{gg}$). At saturation the emitted photon rate reaches a maximum value R_∞, according to the formula [85]:

$$R(I) = R_\infty \left(\frac{1}{1 + I_s/I}\right) \tag{1.24}$$

where I_s, namely the saturation intensity, gives the intensity scale over which saturation sets in and is defined as $I_s := \frac{\hbar\omega}{2\sigma_0\tau}$ with σ_0 the absorption cross section. For resonant excitation, the maximum emitted rate is $R_\infty \simeq 1/2\tau$. In the case of off-resonant excitation, exploiting e.g. a vibrational level of the electronic excited state, a complete population inversion can be achieved and $R_\infty \simeq 1/\tau$. However, off-resonant excitation typically affects indistinguishability, that is defined further on.

Experimentally, the brightness of a SPS is quantified by studying the saturation behavior of the system, detecting the fluorescence intensity of emitted photon rate at different excitation intensities. However, for a correct analysis, collection and detection efficiencies should be consider. As discussed for the quantum efficiency, the emitted photon rate might also vary in time due to blinking and bleaching.

[11] Brightness and purity are not independent. Indeed, alternative definitions of brightness refer to pulsed excitation and amounts to the number of pulses containing one and only one photon per pulse.

Indistinguishability

In most proposals of quantum computing schemes, a SPS should provide subsequent indistinguishable photons, i.e. Fourier-limited photons with identical spectral and spatial modes. Experimentally, photon indistinguishability can be tested via two-photon interference (or coalescence) experiments [86, 87]: when two indistinguishable photons simultaneously impinge on different input ports of a 50:50 beam splitter, quantum mechanics predicts that both photons always exit the beam splitter at the same output port, as first discovered by Hong, Ou and Mandel [23]. Indeed, for symmetry reasons, there is destructive interference between the probability amplitude of the two processes describing one photon reflected and the other transmitted.

For solid-state emitters, in contrast with atomic systems, the creation of indistinguishable photons is challenging owing to the pure optical dephasing originating from scattering with the phonon bath (see Chapter 2.1.2 for a more in-depth discussion). This leads to a considerable broadening of the transition which limits the spectral overlap of subsequent photons, as expressed in equation (1.16). However, tuning the emitter resonance, by e.g. placing it in a resonant cavity, and working at low temperatures to control the spectral bandwidth, proved to be an efficient route towards the creation of single indistinguishable photons (NVs: [88, 89], molecules: [90, 91], QDs [86, 92]). In fact, at cryogenic temperature dephasing vanishes and the ZPL can reach its natural lifetime-limited linewidth. Moreover, if a cavity mode is tuned to the ZPL, emission to higher phonon modes is suppressed, with a consequent enhancement of the Debye-Waller factor α_{DW}. For indistinguishability, stability of the ZPL in time is also crucial. Spectral diffusion, i.e. sudden jumps in the emission wavelength of the narrow emission line (see **Figure 1.2b**), can in fact occur due to change of the local electrostatic environment of the emitter [93].

Hence, a stable lifetime-limited emission is a pre-requisite for the generation of indistinguishable photons. This can be measured comparing the excitation spectrum of the emitter at cryogenic temperature with the lifetime of the excited state, measured independently, and recording the time traces of the excitation spectra of the ZPL.

Overall, the ideal single-photon emitter should be bright and photostable, and able to deliver highly pure and indistinguishable photons on demand. In vision of realistic implementation in integrated quantum networks, other relevant optical properties are a narrow emission bandwidth (to enable e.g. narrow-band, efficient filtering against background photons and coupling with quantum memories [94]), a well-defined and preferably linear polarization state (to be used to encode information) and a high repetition rate (limited by the excited state

lifetime).

Up to date, achieving all these properties simultaneously remains a challenge and thus the SPS has to be chosen according to the application in view. Moreover, due to the relative recent interest in studying and comparing SPS, there is currently a lack of consistency in the available values of their properties, as e.g. they are measured under incomparable experimental conditions.

Let us remark here that the intrinsic properties of a QE as a source of single photons can be significantly improved by e.g. coupling the emitter to a resonant cavity mode. As previously discussed, a cavity can strongly modify the LDOS accessible to the emitter, enhancing its spontaneous emission rate. In particular, it can increase the rate of photon production, it can channel the emitted photons into a well-defined spatial and polarization mode to improve collection efficiency and to match further utilization, or it can restrict the spectral range of the emission.

An alternative approach to tailoring single-photon emission into specific modes includes integrate the single emitter into metallic structures supporting surface plasmon polaritons (SPP), such as plasmonic antennas and plasmonic waveguides [95]. Finally, also dielectric structures with high refractive index, such as micropillars, nanofibers and dielectric waveguides can strongly affect the emission properties of a QE, as it will be discussed in Section 1.2.

1.1.4 Zoology of single-photon sources

Since the first demonstration of a SPS from the atomic transition of sodium atoms [49], various systems and processes have been studied to generate single photons. We here briefly summarize the most studied available SPS, indicating for each class advantages and weaknesses. For a more in-depth discussion the reader is referred to the reviews [24, 25].

An immediate and relatively easy way to produce single photons is to use a strongly attenuated coherent light source. The output signal-to-noise of these non-deterministic SPS is fundamentally limited by the Poisson shot noise of the source and hence multiple photon emission increases with the emission rate. Therefore, one must inevitably accept either a low photon rate or a significant fraction of multiple photons. While for some practical applications this approach of a faint light source is sufficient [96], it is important to note that attenuation does not change the photon statistics, which means that faint laser light will still follow Poissonian statistics, while a real SPS is fundamentally different.

Cold atoms and ions in the gas phase efficiently produce single photons on demand [97]

and have been successfully employed in the development of large entangled systems [98] as well as in fundamental physics experiments [63, 64, 99, 100]. Gas phase systems offer single photons with long coherence length and, because of the absence of non-radiative channels, they are characterized by QY = 1 and a single narrow and lifetime-limited transitions, ranging from VIS to near-IR frequencies. Typical radiative lifetimes are about 15 ns corresponding to a spectral linewidths of about 10 MHz. These sources are very stable under laser illumination, as they do not present long-lived dark states [24]. Nevertheless, due to the required complicated trapping and cooling mechanisms, it is questionable whether the gas-phase experiments can drive the advancement for future quantum technologies.

Alternatively, single photons can be generated via well-established nonlinear processes, such as spontaneous parametric down-conversion [27] (SPDC) and spontaneous four-wave mixing [101], in which pairs of correlated photons are produced. The detection of one photon "heralds" the existence and timing of its twin whose trajectory, polarization and wavelength are determined by constraints of phase matching and energy conservation. Since the pair production is a probabilistic process, there is no control or prior knowledge on when the heralding event will occur. In addition, to avoid multi-pair generation, one must operate at low one-photon probabilities, limiting the SPS brightness. Nevertheless, these processes are currently considered as the premier photon sources and are widely exploited in many quantum information applications, thanks to multiplexing schemes[12] developed to rearrange the generated heralded photons into regular interval [102–104] and hence achieving a truer approximation of single photons on demand.

Recently, a number of 2D materials have been shown to host SPSs, including transition metal dichalcogenides, in which the quantum defects are ascribed to localized weakly bound excitons [106], and hexagonal boron nitride, in which single-photon emission is associated with defects deep within the bandgap [107].

The last class of SPS is that of atom-like emitters in the solid state - such as semiconductor quantum dots, color centers in wide band gap material and single molecules (some literature examples are reported in **Figure 1.3**) - in which the emission process is that of spontaneous emission. The probability of emitting two ore more photons can be completely neglected for appropriate pumping schemes, as the processes involved intrinsically lead to the emission of photons one at a time. These emitters are hence well suited to be operated on demand, e.g.

[12]The basic idea of multiplexing, which can be implemented with both spatial and temporal schemes, is to use an array of down-converters pumped simultaneously by the same laser source, so that there is a high probability of producing only one photon pair somewhere in the array. Each down-converter is associated with a single-photon detector that allows to determine which of the down-converters has fired. This information is then used to control an optical switching circuit directing the heralded photon onto a single-output channel.

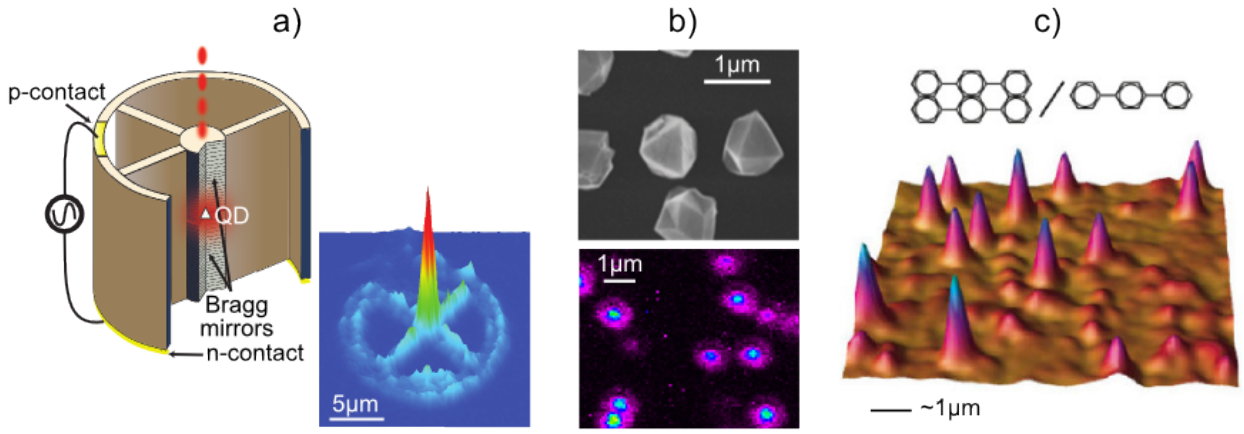

Figure 1.3 – **a)** Scheme of an electrically controlled single-photon source made of a micropillar coupled to a InGaAs QD (top) and photoluminscence map (bottom). Figure adapted from reference [92]. **b)** As-grown nanodiamond particles on a silicon substrate (top) and confocal photoluminescence map (bottom) recorded at room temperature, showing silicon-vacancy centers in nanodiamonds. Figure adapted from reference [105]. **c)** Fluorescence from single terrylene molecules in a p-terphenyl crystal at room temperature. Figure adapted from reference [26].

upon pulsed excitation and subsequent emission of a photon (see Section 1.1.2) and their main features are briefly summarized hereafter.

Quantum Dots

A quantum dot (QD) consists of nanoscale islands of a lower band gap semiconductor, such as gallium arsenide (GaAs), embedded in higher band gap semiconductor, such as aluminium gallium arsenide (AlGaAs). The band offset gives rise to a 3D-confinement of electrons and holes. In the initial state, electrons are present in the valence band and holes in the conduction band. By optical or electrical excitation, electron-hole pairs are formed which quickly non-radiatively decay into the QD excited state, forming an exciton bound state. A photon is emitted following the radiative recombination of the exciton state. QDs are grown epitaxially on single-crystalline substrates by chemical vapour deposition. This fabrication process is standard in the semiconductor industry which hence facilitate the integration of QDs in embedding structures. The high index of refraction of the embedding semiconductor, however, strongly limits the photon extraction efficiency and a variety of methods have been developed to overcome this issue.

One disadvantage of QDs is that they suffer from spectral diffusion and blinking [108–110]. Furthermore, in self-assembled QDs multiple excitations are possible, leading to multi-exciton lines. For a SPS these must be eliminated to ensure that only photons from the single-exciton transition are selected. Non-classical emission of light form QDs has been

demonstrated [111], even at room temperature [112]. At cryogenic temperatures, the emission line is close to the natural width. Up to date, self-assembled InAs/GaAs QDs in pillar cavities exhibits the highest performance as SPSs, in terms of purity and indistinguishability [92, 113]. For more information on QDs as SPSs refer to the review by Buckley and colleagues [30].

Colour Centres

Point defects and vacancies in inorganic crystals often give rise to color centres with very strong absorption and fluorescence bands. Since these are inorganic materials, a great advantage is that of a high photostability and mechanical rigidity, especially in the case of diamond. Nitrogen-vacancy (NV) centres in diamonds were the first single colour centre ever detected [114] whose single-photon emission was demonstrated by means of antibunching measurements [77, 115]. The ZPL around 637 nm is visible even at room temperature thanks to the stiffness of the diamond lattice, however the lifetime-limited emission is strongly affected by spectral diffusion because of the influence of the matrix [116]. Furthermore, the branching ratio into the ZPL is poor even at low temperatures (Debye-Waller factor 0.04). Since diamond has a high refractive index, extraction of fluorescence light is rather difficult, however resorting to nanocrystals [117, 118] improves collection efficiency. Additionally, the presence of a spin triplet ground state is extremely appealing for solid-state quantum communication and computing schemes [119]. Experimental spin-photon entanglement demonstrations over the recent years have strengthen the potential of NV centres as one of the key candidates for quantum registers in a future quantum network realization [120].

Recently, other diamond defects have emerged as promising SPS. Among them, Silicon-vacancy (SiV) centres in diamonds are probably the more attractive alternative. Their ZPL is narrow and very intense (Debye-Waller factor 0.8) and, being at 738 nm, it falls in a region where background fluorescence from diamond is low. Single-photon emission and Hong-Ou-Mandel interference from SiV centres has been demonstrated [121, 122], and as such they are good SPS candidates [29]. Other defects with similar optical properties, for example germanium-vacancy centres, are currently being investigated as promising alternatives [123].

Single Molecules

Single fluorescent molecules radically differ from previous platforms as e.g. all molecules are identical and any difference from one to the other is due to local environment effects. Additionally, molecular-based SPSs are relatively easy to fabricate, relying on well-developed chemical synthesis. Moreover, with their typical sizes around few nm, molecules are truly

nanoscopic emitters.

The main limit in using single molecules for quantum optics applications is their lack of stability when embedded in polymers, aqueous environments or simply dispersed on surfaces, where blinking and photobleaching phenomena strongly limits their emission brightness [124, 125]. Conversely, when embedded in crystalline matrix, the fluorescent molecules are protected by the host from exposure to diffusing quenchers (such as oxygen) and profit from the ability to emit host phonons to prevent thermally induced damage. Moreover, the interactions with the lattice hinders or prevents molecular rotation, trapping single molecule such that extended measurements on the same single molecule are achieved. This corresponds to an extremely high photostability at both room and cryogenic temperature, where single molecules can provide more than 10^9 photons before irreversible termination of emission [126–128].

Photon antibunching in single-molecule emission was first observed in 1992 for the pentacene in p-terphenyl [129] and recent experiments have demonstrated that single terrylene molecules in a p-terphenyl crystal can be operated to generate single photons on demand at room-temperature [26]. When cooled down to cryogenic temperatures, dephasing of the transition due to interactions with the phonons of the matrix vanishes. As a consequence, the ZPL between the first excited state and the ground state becomes extremely narrow and can approach lifetime-limited values of the order of 10 MHz [130].

In order to obtain the best performance in terms of single-photon emission, a careful choice of both the guest emitter and the host matrix must be made. The most stable guest impurity molecules have been selected exclusively from the class of rigid conjugated polycyclic aromatic hydrocarbons (PAHs). Common hosts are organic crystals - such as naphtalene and anthracene - in which the guest molecules tend to embed at well-defined insertion sites. Here, the molecular emission becomes particularly stable with narrow 00-ZPLs, limited only by the excited state lifetime. A comprehensive review of the most used dyes, hosts and their properties can be found in reference [128]. Since single fluorescent molecules are the main focus of this work, their photophysics will be described in more details in the following chapter, focusing on the specific host-guest combination of our choice.

1.2 Theory of Waveguide-Dipole Coupling

In this section we introduce the principle behind the coupling of a QE to a confined light-field supported by a dielectric waveguide, which is of particular interest in the field of integrated quantum photonics. A hybrid system made of a single QE efficiently coupled to a waveguide

is in fact the primary step towards the implementation of a compact integrated SPS, whose single-photon emission can route directly on-chip, paving the way toward a fully integrated photon-processing platform.

The basic concepts of waveguides are first discussed in Section 1.2.1, considering a 1D-confined waveguide structure which forms the basis for the analysis of guided modes in rectangular waveguides, that are the one employed in this thesis.

The coupling of a single QE to a waveguide can be quantified by two figures of merit: the coupling efficiency β and the emission enhancement α, that will be introduced in Section 1.2.2. The numerical tools employed in this thesis to estimate α and β are then introduced (Section 1.2.3). Later on, these concepts will be used to discuss two different waveguiding structures featuring a rectangular cross-section for implementing evanescent (Chapter 3) and integrated (Chapter 5) coupling with a molecule-based SPS.

1.2.1 Survey on optical waveguide modes

Optical waveguides are fundamental for the implementation of any integrated photonic platform, as they route light across the photonic chip and connect the various optical devices, either on or off-chip. Moreover, the presence of a waveguide modifies the local density of state (LDOS) available for a nearby emitter and a significant amount of its emission can be directly couple into guided modes. An efficient collection of the emission implies mutual coupling between the emitter and the guided optical mode, which can help building a compact SPS and is beneficial for the optical read-out of the QE's internal degree of freedom.

In general, dielectric optical waveguides consists of cladding materials of lower refractive indices surrounding a high refractive index core, in which the electromagnetic radiation can be confined in two dimensions and guided along the third dimension (there are exceptions, like the so-called *slot* waveguides and the photonic crystal waveguides, but they will not be considered in this study).

In a classical ray-optics picture, waveguiding can be understood in term of total internal reflection, prohibiting the transmission of light from the waveguide into the cladding for all angles above the critical angle $\theta_c = \arcsin(n_{\text{clad}}/n_{\text{core}})$. In a more complete electromagnetic wave-picture, optical waves travel in the waveguide in distinct optical modes, that are spatial distribution of optical energy (in one or two dimensions) that remains constant in time.

The fundamental properties of waveguiding in dielectric structures are here discussed following the approach of [131]. Key results are presented with minimal proof, to give a general understanding of the nature of light propagation in an optical waveguides.

We consider the simple case of an asymmetric planar geometry, as the one sketched in

Figure 1.4a, composed of three semi-infinite layers with refractive indexes such that $n_2 > n_1 > n_3$, to ensure guiding in the intermediate layer by total internal reflection. The structure considered is not meant to be a practical waveguide for optical integrated circuits, but serves as a basis for the analysis of rectangular waveguides as the one sketched in **Figure 1.4b**, studied throughout this thesis. In fact, for rectangular waveguides, guided modes cannot be resolved analytically[13] and a computational methods allowing for precise numerical solution will be used (Section 1.2.3).

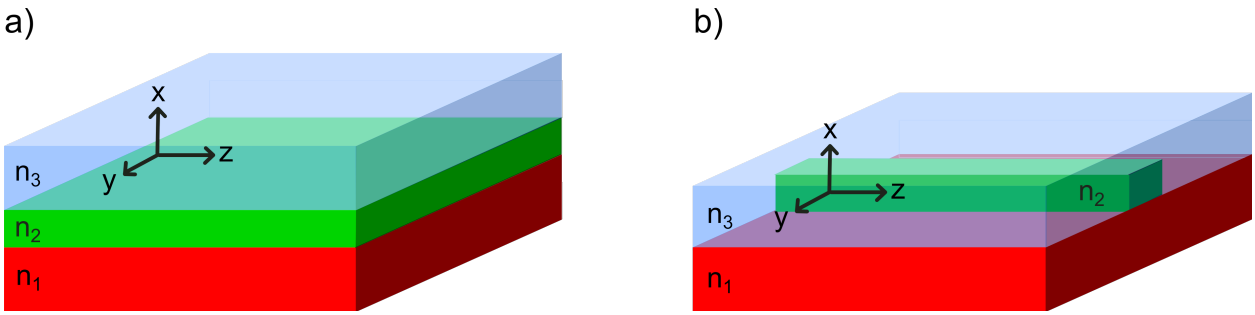

Figure 1.4 – Asymmetric z-invariant dielectric waveguides. In the planar geometry **(a)** light is confined in the x direction, while in the rectangular geometry **(b)** light is confined in both x and y directions.

The general problem of finding light waves with a frequency ω propagating in the z-direction amounts to solving Maxwell's equations in the absence of any source, subject to the continuity conditions on the tangential components of the electric and magnetic fields at the dielectric interfaces, and the outgoing wave conditions at infinity. Assuming homogeneous materials, the solutions for the electric field $\mathbf{E}(\mathbf{r}, t)$ and the magnetic field $\mathbf{H}(\mathbf{r}, t)$ are called optical modes:

$$\mathbf{E}(\mathbf{r}, t) = \mathbf{E}(x) \exp\{i(\beta z - \omega t)\} \tag{1.25}$$

$$\mathbf{H}(\mathbf{r}, t) = \mathbf{H}(x) \exp\{i(\beta z - \omega t)\} \tag{1.26}$$

where β is a propagation constant to be determined, that is a complex number to account for possible losses (absorption and scattering).

For a given refractive index profile there is, in general, an infinite number of eigenvalues β, corresponding to the infinite number of modes that are eigenvectors of the differential Maxwell's equation. Among them, only a discrete number of modes are guided, i.e. confined near the middle layer (core), and propagate freely (absorption or roughness are neglected)

[13] There exist in literature methods to approximate mode profiles and propagation constants, such as the Marcatili's method [132]. However, in order to evaluate the coupling parameters later on, knowledge of the precise local electric field strength is essential.

along z. These modes can be enumerated using the integer mode index m ($= 0, 1, 2, ...$) and are limited in the range $k_0 n_3 \leq \beta_m \leq k_0 n_2$. Each guided mode m is then characterized by an effective refractive index $n_{\text{eff}} = \beta_m / k_0$ that represents the effective phase velocity of the guided light $v_f = c/n_{\text{eff}}$.

$\mathbf{E}_m(x)$ and $\mathbf{H}_m(x)$ are vector fields of mode m which denote the distributions of the electric and magnetic fields in the transverse x-direction: they are sinusoidal inside the waveguide and decay exponentially in the cladding layers (white region in **Figure 1.5a**). As it is customary, the modal number m is used to indicate the number of nodes in the core. Note that the transverse fields $\mathbf{E}_m(x)$ and $\mathbf{H}_m(x)$ have no y or z dependence because the planar layers are assumed to be infinite in these directions and reflections occur only at the interfaces between different layers. Referring to **Figure 1.5a**, guided modes present evanescent exponential tails extending into the cladding layers. These are necessary to evanescently couple light emitted from a QE placed nearby the waveguide structure. As we will discuss later on, a careful choice of the waveguide geometrical parameters should be consider for this purpose.

Guided modes can show different directions of polarization and can be separated into two general groups: TE (Transverse Electric) and TM (Transverse Magnetic). TE modes present the electric field entirely transverse (i.e. perpendicular to the direction of propagation z), with a component of magnetic field in the direction of propagation. Analogously, TM modes have the magnetic field entirely transverse to the direction of propagation, but have a component of the electric field in the direction of propagation.

A convenient (operative) description of the optical modes in a guiding structure is given by the dispersion diagram, directly inspired from the band diagram of electrons in solid state, in which the energy (proportional to $\omega/c = 2\pi/\lambda$) is plotted as a function of the $Re(\beta)$[14]. Assuming non-dispersive materials, light curves $\omega/c = Re(\beta)/n_i$ ($i = 1, 2, 3$) are straight lines, plotted as dashed line in **Figure 1.5a**, and are the dispersion curves of plane waves propagating in each bulk (uniform) material n_i. Bounded, i.e. guided, modes can only be found in the region $n_3\omega/c < Re(\beta) < n_2\omega/c$. In fact, when $Re(\beta) > n_2\omega/c$ (grey region in **Figure 1.5a** and **b**), the mode profiles must be exponential in all three regions, corresponding to not-physical solutions as the field increase unboundedly, implying infinite energy. For $Re(\beta) < n_1\omega/c$, the fields are oscillatory in all three regions of the structure

[14]By construction, z-invariant waveguides possess a mirror-symmetry for transverse planes perpendicular to the z-axis. If the materials are reciprocal, this guaranties the existence of pair of counter-propagating modes with opposite propagation constants, β_m and $-\beta_m$. It is hence sufficient to know the mode profile of one element of the pair to know the other. Correspondingly, the dispersion diagram in **Figure 1.5b** is symmetric with respect to the y-axis, where the quadrant for negative x (not shown here) conventionally represents modes propagating towards the negative z-direction.

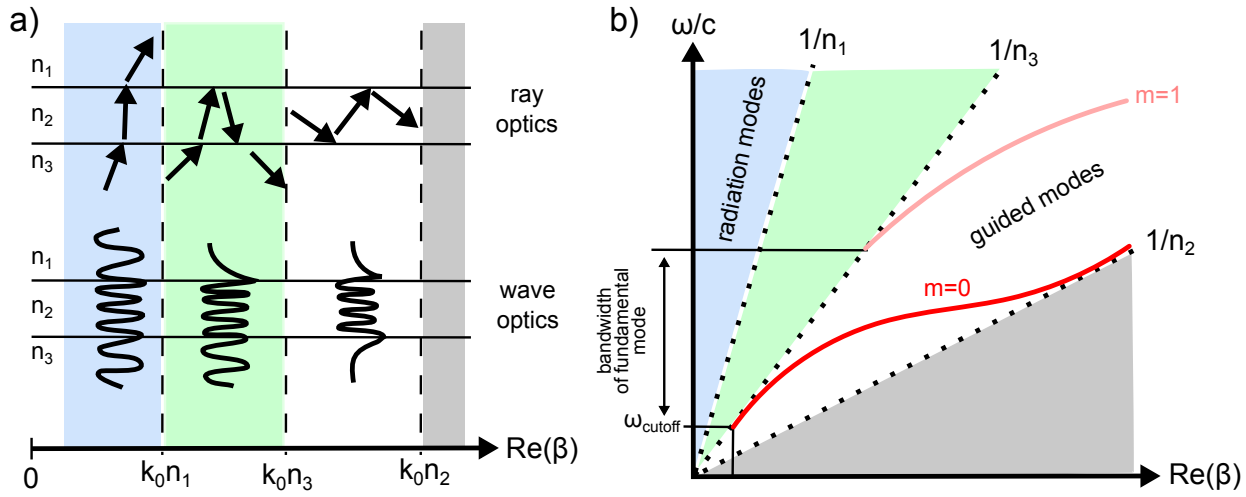

Figure 1.5 – **a)** Illustration of optical waves propagating in an asymmetric slab dielectric waveguide for various values of the propagation constant β, in both ray-optics (top) and electromagnetic (bottom) pictures. Guiding occurs when $n_3\omega/c < Re(\beta) < n_2\omega/c$ (white region). **b)** Sketch of the waveguide's dispersion diagram. The dashed lines are the dispersion curves of plane waves propagating in bulk (uniform) materials with refractive indices n_i $(i = 1, 2, 3)$. The red curve is the fundamental guided mode $(m = 0)$ which is bounded between the two light lines. The bandwidth of the fundamental mode is defined by the range of frequency between its cut-off and the cut-off of the first order mode (light red curve). The same behavior is obtained either for TE or TM modes.

and the energy is free to spread out of the waveguiding region 2, corresponding to radiation modes (light blue region in **Figure 1.5a** and **b**). When $n_1\omega/c < Re(\beta) < n_3\omega/c$, the modes are confined at the upper layer interface but sinusoidally varying in the other layers, and are not guided since energy is continuously lost from the waveguiding region to the substrate region as it propagates (light green region in **Figure 1.5a** and **b**).

The red curve in **Figure 1.5b** is the fundamental guided TE mode $(m = 0)$. The large dispersion of this mode can be qualitatively explained observing that, for small ω, the wavelength is much larger than the core size and the mode essentially spreads into the cladding material. Note that there exists a cut-off frequency[15] corresponding to $Re(n_{\text{eff}}) = n_3$: here the fields become oscillatory and hence waveguiding cannot occur. The bandwidth of the fundamental mode is defined by the range of frequency between its cut-off and the cut-off of the first order mode (light red curve in **Figure 1.5a**).

At a fixed frequency ω, the number of modes supported by the structure is related to the thickness t of the waveguiding layer and on the refractive indices of the materials, according

[15] A fundamental mode possesses no cut-off only in a symmetric dielectric structure, where $n_1 = n_3$.

to [133]:

$$\Delta n = n_2 - n_3 = \frac{(2m+1)^2\lambda^2}{32 n_2 t^2}. \tag{1.27}$$

While this condition is valid only for the special case of a planar asymmetric waveguide, it offers a convenient means to estimate how many modes can be supported by a particular waveguide, with a given Δn and/or a ratio of λ_0/t. Alternatively, equation (1.27) provides what change in index of refraction is needed to permit waveguiding of a particular mode at a given wavelength in a chosen material, for a range of thickness t achievable with a specific fabrication method.

For the experimental case we are going to discuss in Chapter 3, a silicon nitride waveguide is chosen ($n_2 = 2$). With t on the order of λ_0, equation (1.27) predicts that a Δn on the order of 0.02 is sufficient to support waveguiding of the TE_0 mode. A simple glass substrate ($n_3 = 1.5$) is hence effective, on top of which a Si_3N_4 waveguide are fabricated relying on well-established electron-beam lithographic methods.

A similar change in index is required for a polymer based waveguide, as the one we are going to present in Chapter 5 ($n_2 = 1.54$). In this case, owing to the small refractive index of the polymer, air is chosen as a cladding material and the waveguide is fabricated by direct laser writing, allowing for a three-dimensional structure.

As a final remark on guiding structures, we observe that light which propagates along real waveguides is attenuated due to material absorption and scattering due to imperfections in the fabrication. When absorbing or scattering centers are distributed along the waveguide, propagation losses can be described in statistical terms, as a mean loss per length. The loss per absorbing or scattering center is proportional to the local power in the mode, given by flux of the Poynting vector through a surface containing the waveguide section. The guided power per propagation length z, can then be written according to Beer's law as:

$$P(z) = P_0 e^{-z/B} \tag{1.28}$$

where B is the decay rate representing the propagation loss per length. This attenuation of optical power along waveguides is referred to as transmission, which is an essential parameter to quantify the performances of waveguides. A standard method to measure propagation losses of a waveguide rely on measuring the transmission of identically fabricated waveguides with different lengths, as it will be discussed in Chapter 3 and Chapter 5.

1.2.2 Figures of merit of waveguide-dipole coupling

We here recall some concepts discussed in Section 1.1.2 and in particular the Fermi's golden rule, stating that the optical properties of a QE - namely the rate and the spatial distribution of its spontaneous emission - are determined by its surrounding environment. In an environment structured by dielectrics, Maxwell's equations define certain allowed optical modes, resulting in a modified LDOS available for the QE with respect to the case of a homogeneous isotropic environment. Specifically, the presence of a dielectric waveguide can boost the QE properties in a way that a significant amount of its fluorescence photons are directly coupled into the guided modes supported by the structure.

The coupling of a single QE to a waveguide can be quantified, in analogy with the Purcell factor (equation (1.9)), by the emission enhancement α, defined as:

$$\alpha = \frac{\Gamma_{\mathrm{WG}}}{\Gamma_{\mathrm{hom}}} \tag{1.29}$$

with Γ_{WG} the emission rate into a waveguide mode[16] and $\Gamma_{\mathrm{hom}} = \Gamma_{21}^{\mathrm{hom}}$ the emission rate of the emitter when embedded in a homogeneous medium (equation (1.8)).
This parameter accounts for the modification of the emitter decay rate (or equivalently its excited state lifetime) with respect to the case of an homogenous dielectric environment but it doesn't directly determine the ratio of photons coupled into the waveguide.

This ratio is instead quantified by the waveguide-to-dipole efficiency β. The β-factor represents the probability of a photon being emitted into a guided mode[17] and is given by:

$$\beta = \frac{\Gamma_{\mathrm{WG}}}{\Gamma_{\mathrm{tot}}} \tag{1.30}$$

where Γ_{tot} is the total decay rate in free space of the QE that, in the presence of the waveguide, becomes $\Gamma_{\mathrm{tot}} = \Gamma_{\mathrm{r}} + \Gamma_{\mathrm{nr}} + \Gamma_{\mathrm{WG}}$, where Γ_{nr} accounts for intrinsic non-radiative decay channels available for the QE.

We consider a rectangular waveguide structure invariant in the propagation direction z as the one sketched in **Figure 1.4b**, defined by a refractive index distribution $n(x, y)$ which confines light in two dimensions (x and y). For sake of simplicity, the waveguide is assumed to be single-mode, meaning that only one guided field distribution $\mathbf{E}(x, y)$ exists. The rate of photon emission into the waveguide Γ_{WG} can be calculated from the Fermi's golden rule (equation (1.6)). The quantization volume V for the considered guided mode is given by the

[16] We here consider both propagation directions.
[17] Alternatively, β can be interpreted as the probability of the two-level system absorbing a photon accounting from both sides of the guided mode.

product of a quantization length L and the effective mode area, defined as [134]:

$$A_{\text{eff}}(\mathbf{r}_0) = \frac{\iint n^2(x,y)|\mathbf{E}(x,y)|^2 \mathrm{d}x\mathrm{d}y}{n^2(\mathbf{r}_0)|E_{\parallel}(\mathbf{r}_0)|^2} \tag{1.31}$$

where $E_{\parallel}(\mathbf{r}_0)$ is the electric field component parallel to the dipole at the position of the emitter $\mathbf{r}_0$. The effective mode area hence represents a measure of the mode field concentration at the dipole position.

The local density of photonic states $D(\omega)$ for the waveguide we are considering is given by [19]:

$$D(\omega) = L/(2\pi v_g(\omega)) \tag{1.32}$$

with $v_g(\omega) = c(n_{\text{eff}} + \omega \frac{\mathrm{d}n_{\text{eff}}}{\mathrm{d}\omega})^{-1}$ the group velocity of the guided mode[18]. With these definitions, equation (1.6) becomes:

$$\Gamma_{\text{WG}} = \frac{\omega}{2\hbar n^2 \varepsilon_0 A_{\text{eff}} v_g} |\mathbf{d}|^2 \langle \hat{\boldsymbol{\epsilon}} \cdot \hat{\mathbf{d}} \rangle^2 \tag{1.33}$$

where both directions of propagation are considered. This equation suggests three possible strategies to maximize the emission rate into the guided mode: shrinking the effective mode area A_{eff}, shaping the electric field distribution to maximize the electric field component parallel to the dipole at the position of the emitter $\mathbf{r}_0$ (and hence the intensity $|E_{\parallel}(\mathbf{r}_0)|^2$) and reducing the group velocity (i.e. increasing the interaction time between the emitter and photon).

From equation (1.33) and equation (1.8) we can now derive an analytical expression for the enhancement factor α:

$$\alpha = \frac{\Gamma_{\text{WG}}}{\Gamma_{\text{hom}}} = \frac{1}{2} \frac{c}{n(\mathbf{r}_0) v_g} \frac{\sigma}{A_{\text{eff}}(\mathbf{r}_0, \hat{\mathbf{d}})} \langle \hat{\boldsymbol{\epsilon}} \cdot \hat{\mathbf{d}} \rangle^2 \tag{1.34}$$

with $\sigma = 3\lambda_0^2/(2\pi n^2)$ the scattering cross-section of a dipole embedded in a homogeneous medium of refractive index n.
Using dielectric waveguides, an effective mode are A_{eff} of the same order of magnitude as the photonic scattering cross-section can be reached, resulting in an α around 1. This means that the excited state lifetime of the quantum emitter is not relevantly affected by the presence

[18] It is noteworthy that the group velocity depends not only on the material dispersion (n_{eff} changes with the wavelength because the refractive index n changes), but also on the geometrical dispersion (even if n is constant, n_{eff} generally varies with ω, as previously discussed).

of the waveguide. If from one side achieving high α is desirable as the overall emission rate is enhanced, the first step towards an integrated SPS is to achieve a high β. Referring to equation (1.30), let us note that maximizing α does not necessarily coincide with the maximization of the coupling efficiency β.

The calculation of the emission rates into free space in presence of the waveguide (Γ_{tot}) and into the waveguide (Γ_{WG}) is rather difficult and an analytical expression has been found only for the case of an atom coupled to a silica optical nanofiber [135]. These calculations can however be performed by means of 3D numerical simulation, from which the β-factor can be extracted, according to the equivalence [51, 134]:

$$\frac{\Gamma_{\text{WG}}}{\Gamma_{\text{tot}}} = \frac{P_{\text{WG}}}{P_{\text{tot}}} \tag{1.35}$$

stating that the ratio of the spontaneous emission rates into the waveguide to that in free space is equal to the ratio of the total classical dipole radiated power into the waveguide to that in free space. Similarly, an estimation of α can be derived. It has to be noted that simulations are not able to determine the absolute value of the decay rats but only their mutual relative values [136]. A numerical approach as the one used in this thesis and discussed in the following section, has the advantage of being very flexible in the design of the hybrid structure. For instance, an emitter inserted in a solid matrix, as our experimental case of a single molecule embedded in an organic crystal, can easily be included in the simulations.

1.2.3 Computational modelings

In the last years, several numerical approaches have been developed to solve electromagnetic problems [137]. In this thesis, to model light propagation in optical waveguides, we employ the commercial software COMSOL Multiphysics (Radio Frequency and Wave Optics modules, [138]), which implements the finite-element method (FEM).

The validity and versatility of the FEM in describing dielectric waveguides is in fact well known and has been demonstrated by comparing the numerical results with the exact solutions on different geometries, finding an almost perfect[19] agreement in the determination of both propagation constants and field distributions [139]. The basic principle of FEM is to convert the resolution of the continuous partial differential Maxwell's equations in a dielectric environment with arbitrary geometry into a discretized problem applying the *Galerkin's*

[19] Limitation of FEM can be approached when operating at frequencies close to the cut-off of the considered mode. In this case, in fact, the field is expected to extend infinitely, which cannot be described with a simulation volume that is by definition truncated.

approximation method. We here recall the general steps of the FEM: details can be found in reference [137].

The first step is to define a simulation domain, whose size should be chosen carefully in order to correctly simulate the electromagnetic problem under study, without introducing significant artifacts into the computation due to the space truncation. Usually, the simulation space size is of the order of several free-space wavelengths and is terminated with proper boundary conditions that avoid unphysical reflection. For this purpose, it is convenient to add an artificial bulk material at the boundary of the simulation domain, called *perfectly matched layer* (PML), that totally absorbs any incident electromagnetic mode [140]. The basic idea behind this artificial material is that any plane wave propagating in the simulation domain and impinging on the inner boundaries of the PML has its reflection coefficients equal to zero, for any wavelength and any angle of incidence. Propagating waves in the simulation domain are hence converted into evanescent waves in the PMLs. The size of the PML should be large enough to contain these evanescent tails and the total simulation space can now be correctly truncated imposing the *perfect electric conductor* boundary conditions, i.e. $\mathbf{n} \times \mathbf{E} = 0$, where $\mathbf{n}$ is the vector normal to the interface.

The simulation space is then divided into subdomains describing the geometry of the problem, each of them is characterized with the dielectric constant of the materials involved. At the dielectric interface between any medium 1 and 2, the continuity condition on the tangential components of the fields

$$\mathbf{n} \times (\mathbf{E_1} - \mathbf{E_2}) = 0, \quad \mathbf{n} \times (\mathbf{H_1} - \mathbf{H_2}) = 0 \tag{1.36}$$

are fulfilled.
Finally, the total simulation domain is discretized into a grid of elements (also called *mesh*) of various shape, such as triangular or quadrilateral finite elements in a 2D domain, and tetrahedral or hexahedral finite elements in 3D.

Since the solver finds an approximate solution of the Maxwell's equation at each discretization point, the choice of the grid size is crucial. A finer mesh would reduce numerical errors arising from the discretization step, but longer calculation time and bigger memory space are required. A compromise between accuracy and memory/solving-time requirements can be found using a non-uniform mesh, which allows to capture nonlinearities and gradients in the spatial locations where the fields are expected to rapidly change, for instance at the interface between different materials or in the close proximity of a dipole source. To avoid numerical errors, a very fine mesh (size $<< \lambda$) is recommended mostly in these regions, and can be reduced to a coarser mesh (size $\simeq \lambda/2$) in the regions where the fields are expected

to be only slowly varying.

In this work, FEM simulations with Comsol are employed to model two dielectric guiding structures designed to efficiently collect and guide the emission from the SPS of our choice. In particular, numerical models are used to calculate the optical modes supported by two guiding structures and to estimate the coupling efficiency β and the emission enhancement α of the coupling between the SPS and the guided modes. The methodology to construct these models follows the steps of space truncation, material domains definition and non-uniform discretization described above and is presented hereafter to give a general overview. The analysis of the resulting physics will be presented in Chapter 3 and Chapter 5.

Rectangular translational-invariant waveguide mode calculations

In this thesis we employ dielectric waveguides that are z-translational invariant. The complete analysis of their modes can hence be done with the Mode Solver from Comsol, in a 2D domain that includes the cross-section of the waveguide. The solver finds numerical solution of the Maxwell equation in the absence of sources and determines the field distributions of the modes supported by the guiding structure and their effective refractive indices $n_{\text{eff},m}$ for a certain wavelength.

The so-obtained parameters can then be extracted and displayed as plots or contour plots for immediate and meaningful interpretation. To show an example, we consider the waveguide design we are going to discuss in Chapter 3. In this case, the waveguide has an asymmetric cladding configuration and is made of silicon nitride Si_3N_4 ($n_{Si_3N_4} = 2$) on a glass substrate ($n_{\text{glass}} = 1.51$) and with air on top ($n_{\text{air}} = 1$). The cross-section is rectangular, with height $a_x = 175$ nm and width $a_y = 500$ nm (inset in **Figure 1.6a**).

Figure 1.6a shows the dispersion diagram of the first three modes supported by this waveguide, within a range of wavelength between 300 nm and 1 µm: in this frequency range the materials are not dispersive. From this study we observe that the fundamental mode (red curve in **Figure 1.6a**) has a cut-off at 860 nm and a bandwidth of about 160 nm, since the first-order mode appears at about 700 nm (orange curve). A second-order mode is supported starting from 530 nm (yellow curve) and from 480 nm a third-order mode starts contributing (not shown in the figure).

Figure 1.6b shows the 2D color-coded plots of the normalized electric field intensity of the first three modes just above the cut-off of the second-order mode, at 530 nm. For each mode the effective refractive index is reported in the figure. For all modes, most of the electric field is located within the waveguide core, but it is also non-zero outside the waveguide boundary.

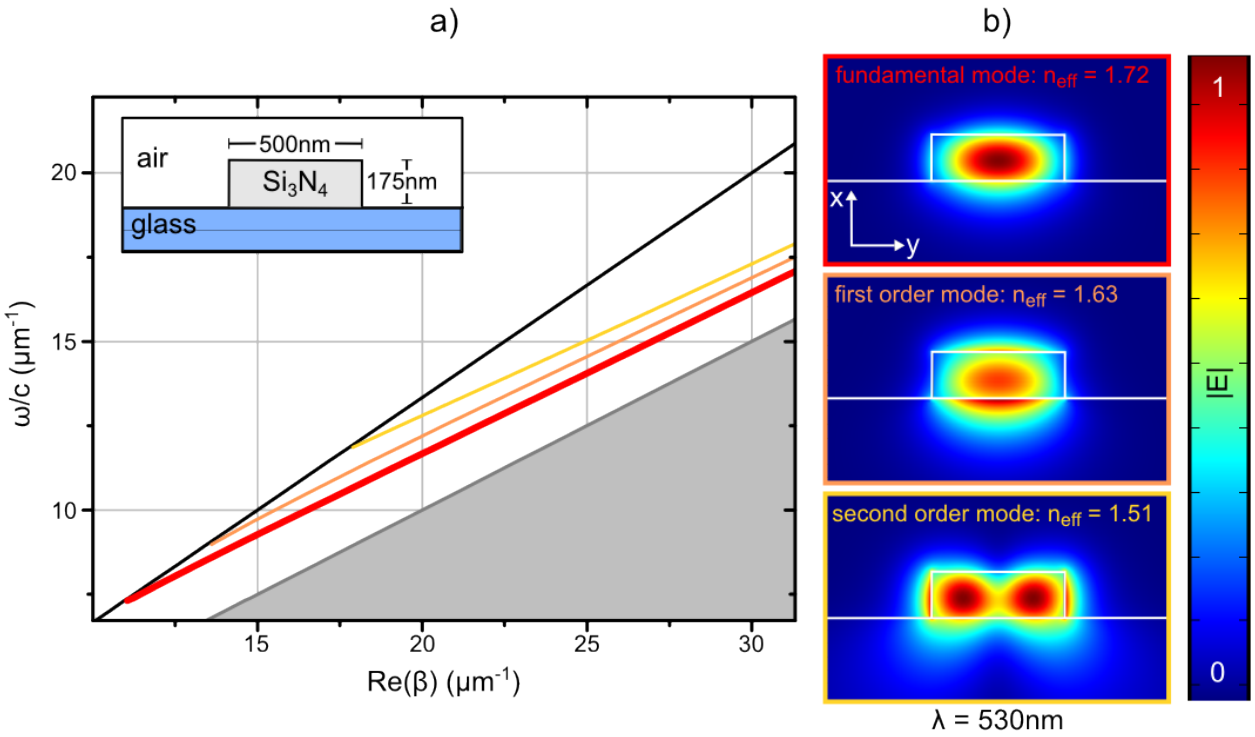

Figure 1.6 – **a)** Dispersion diagram within a range of wavelength between 300 nm and 1 µm for the rectangular waveguide we are going to discuss in Chapter 3 and illustrated in the inset. The guiding structure is made of Si_3N_4 ($n_{Si_3N_4} = 2$) on a glass dice ($n_{glass} = 1.51$), with height $a_x = 175$ nm and width $a_y = 500$ nm. The diagram plots the light lines for Si_3N_4 and glass and the first three guided modes. The fundamental mode has a cut-off at 860 nm and a bandwidth of about 160 nm before the first mode appears (at about 700 nm). **b)** 2D color-coded plots of the normalized electric field intensity of the first three modes at 530 nm.

The electric field amplitude decreases exponentially with distance from the waveguide and, as we will discuss in Chapter 3, this evanescent field enables the waveguide to interact with a single SPS in a way that a fraction of the emitter's radiative emission is directly coupled to the guided mode of the waveguide.

In general, the modes supported by a rectangular waveguide are hybrids of TE- and TM-modes. For a waveguide as the one illustrated in the inset of **Figure 1.6a**, due to the high aspect ratio ($a_x/a_y << 1$), these two polarization are often referred to as quasi-TE and quasi-TM modes, since they are closely related to those of the slab waveguide discussed in Section 1.2.1. This is shown e.g. analyzing the field components of the fundamental mode - which is the only supported at 785 nm (our operating wavelength) - with $n_{eff} = 1.55$. In **Figure 1.7**, the electric field and the magnetic field components are shown in the upper and lower rows respectively. At the central mirror plane (including the x and z axis), E_x and E_z are zero due to the symmetry of the mode. This means that, for an emitter placed along

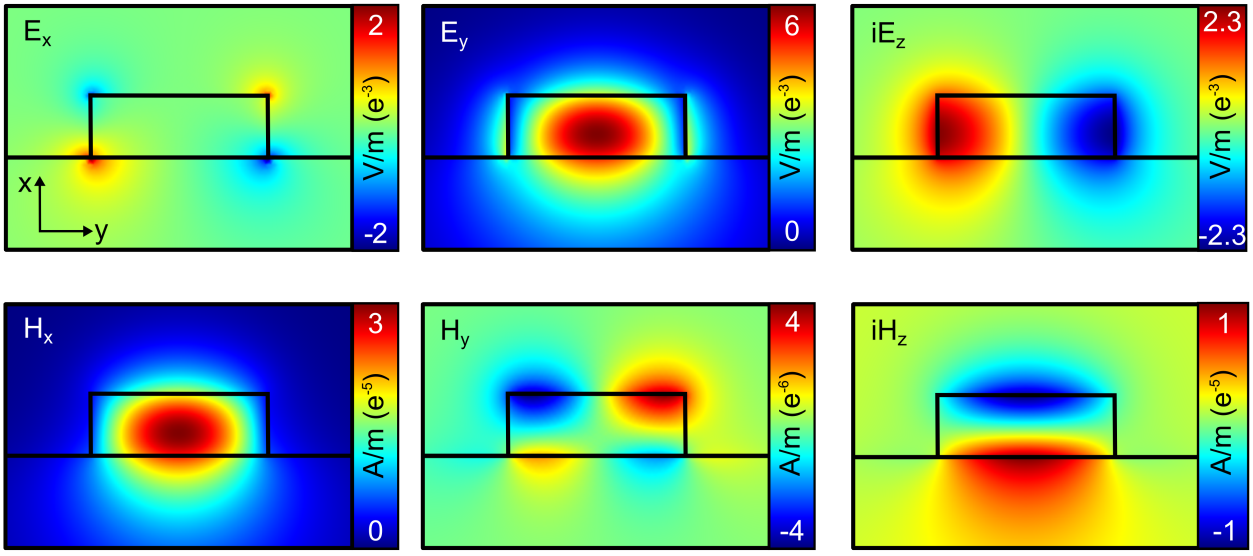

Figure 1.7 – Electric (top) and magnetic (bottom) field components of the horizontally polarized fundamental mode supported by the waveguide in **Figure 3.1a**. at 785 nm, with $n_{\text{eff}} = 1.55$.

this plane, coupling can only be expected when the dipole is oriented along the y-direction.

Electric dipole emission in 3D domains

FEM simulation with Comsol allows to compute the emission of a dipole coupled to a waveguide, from which both the coupling efficiency β and emission enhancement α can be determined. In this case, a 3D domain is needed to render the guiding structure and the dipolar source, and the software computes the electromagnetic field excited by the dipole. The emitter is modeled as a linear harmonic electric current of length l oriented along $\hat{\mathbf{d}}$ with an associated dipole moment $\mathbf{d} = (i\mathbf{I_0}l/\omega)\hat{\mathbf{d}}$, where I_0 is the linear distribution of current and $\omega = 2\pi c/\lambda$ [141]. In order to satisfy the dipole approximation, the length l is kept very short in comparison with the emission wavelength. To model an infinitely long waveguide with negligible reflection due to the space truncation, the waveguide enters the PML where the guided electromagnetic waves are properly absorbed.

According to equation (1.35) the β factor can now be calculated as the ratio between the guided power and the total radiated power. The power in the waveguide mode is well described by the summation of the Poynting vector flux through the two end faces of the waveguide before the PML, while the total radiated power is given by the power flow through the surface of a volume containing the emitter. In order to estimate the enhancement factor α, the same simulation domain is converted into a homogeneous medium by simply setting the refractive indices of all subdomains equal to that of vacuum or to the dielectric medium

embedding the source. The parameter α is then given by the ratio between the total radiated power calculated in the presence and in the absence of the waveguide.

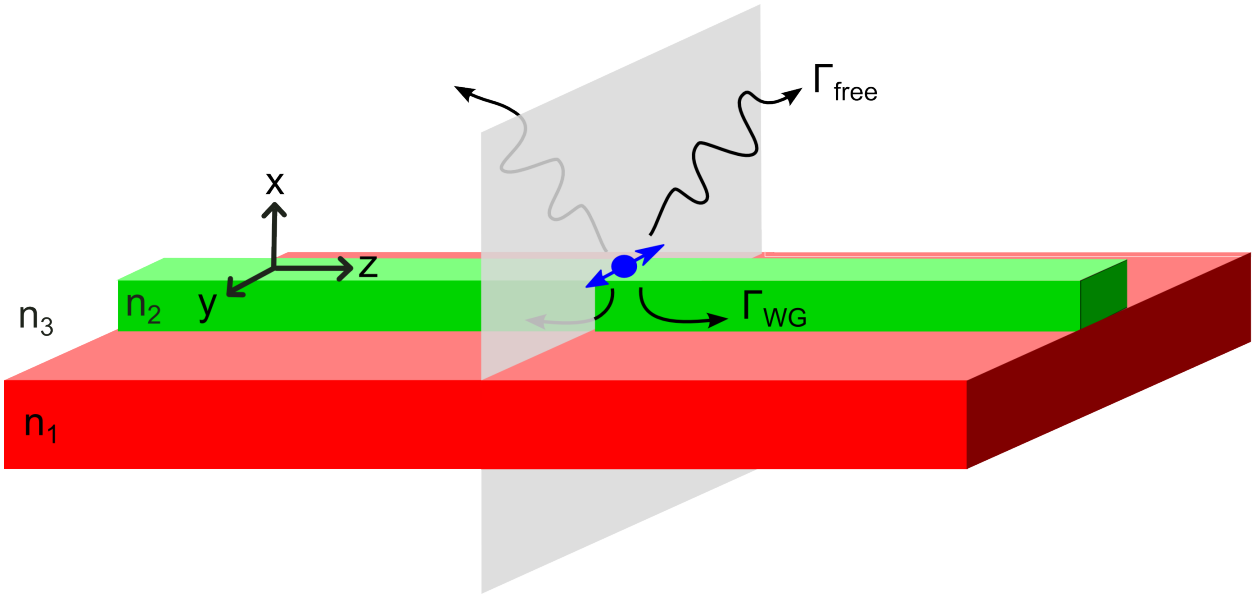

Figure 1.8 – Illustration of the 3D numerical model used to to compute the emission of a dipole coupled to a waveguide. If the dipole is oriented in-plane along the y-axes and orthogonal to the propagation direction z, the simulation domain can be divide in half with a vertical plane containing the emitter and orthogonal to the direction of the guided electromagnetic field z applying the boundary conditions corresponding to a perfect magnetic conductor.

For a dipole with a well defined orientation, as the case of the molecule-based source we consider in this work, the symmetry of the system can be exploited to reduce the size of the simulation domain. In **Figure 1.8** we illustrate the model we are going to discuss in Chapter 3, made of a quantum emitter placed in the near-field of the rectangular dielectric waveguide introduced above. The dipole is oriented in-plane along the y-axes and orthogonal to the propagation direction z. In this case, the simulation domain can be divide in half as shown in the figure, with respect to a vertical plane containing the emitter and orthogonal to the direction of propagation z. We then apply to this cutting plane the boundary condition corresponding to a perfect magnetic conductor (PMC):

$$\mathbf{n} \times \mathbf{H} = 0 \tag{1.37}$$

which imposes a null value of the magnetic field tangential component on the plane, i.e. a non null tangential electric field, thus ensuring the dipole emission. Let us note that the PMC plane acts as a mirror for the dipole, doubling its dipole moment. Consequently, the computed electromagnetic field in the truncated simulation domain must be divided by two

to obtain the result for the full system.

2 Single Fluorescent Molecules

Optical and spectral properties of fluorescent molecules are here discussed for the specific host-guest combination that we propose and study in this work, made of single dibenzoterrylene molecules embedded in anthracene crystals. This system holds promise because of a very bright and stable single-photon emission at both room and cryogenic temperature, where the purely electronic emission in the ZPL around 785 nm approaches its lifetime-limited value, showing a natural width of about 40MHz (Section 2.1).

In this work, experiments on single molecules are done through fluorescence excitation spectroscopy, which is briefly described in Section 2.2, after an overview on the fundamentals of single molecule detection. The experimental set-up employed in this work is then presented in details in Section 2.3.

In section 2.4 we present a complete optical characterization of the DBT:Ac system: this allows to test the performance of our experimental set-up. This characterization also represents a bench mark for the research on nanocrystals discussed in the following chapters.

2.1 DBT in Ac: an Optimal Dye-Matrix Match

A system made of single Dibenzoterrylene (DBT) molecules embedded in anthracene (Ac) crystals ($n = 1.8$) is particularly attractive as a single-photon source for applications in quantum optics at both room and cryogenic temperatures, due to the remarkable optical and spectral properties originating from the specific structure of its energy levels. These are discussed in details in Sections 2.1.1 and 2.1.2.

As a host matrix, anthracene has several advantages. First, it is cheap and can be easily purified and handled. Moreover, it is stable at room temperature and doesn't undergo any phase transition during the cool down process. Noteworthy is the availability of extremely easy fabrication processes, allowing to obtain high quality Ac crystals with thickness of few tens of nm, as detailed in Section 2.1.3.

Finally, in Section 2.1.4, we present an overview on the relatively recent literature results employing the DBT:Ac system.

2.1.1 Energy levels and transitions

DBT and Ac are both aromatic compounds consisting of 8 and 3 benzene rings, respectively (**Figure 2.1a**). Due to their similar chemical structure, DBT nicely finds its place within the crystalline structure of anthracene, mostly in the main insertion site centered at 785 nm [41]. This near-IR emission makes DBT:Ac system particularly interesting for the proximity to the atomic lines of rubidium and potassium; indeed, interfacing molecular photons to atomic alkali vapours has already been proposed as a fundamental step towards the realization of quantum memories [142]. Furthermore, the spectral region covered by this system conveniently lies in the operating range of silicon-based photodetectors, whose detection efficiency peaks around 750 nm.

Figure 2.1b shows the Jablonski diagram [71] that describes the complex multilevel system of DBT in the main insertion site, where energy increases along the vertical axis. In a molecule at its electronic ground state, electrons are usually paired with their spin antiparallel inside the bonding molecular orbital; the fundamental electronic level is therefore a singlet state, which we denote with $|S_0\rangle$. Electronic excited states can be both singlet $|S_i\rangle$ or triplet states $|T_i\rangle$[1]. The diagram depicts the singlet and triplet electronic states with the respective vibrational bands, together with all radiative (solid arrows) and non-radiative processes (dashed arrows) that occur between the absorption and emission of light, limited to the excitation and detection schemes employed in this thesis.

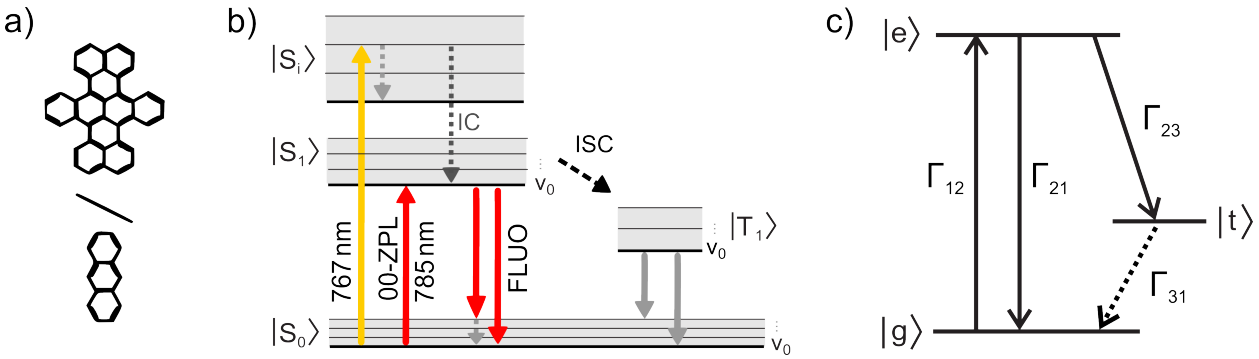

Figure 2.1 – **a)** Chemical structures of DBT and Ac. **b)** Jablonski diagram of the DBT:Ac system. S and T label the singlet and triplet electronic states respectively, above which vibrational levels (v_i) are present. Radiative transitions are represented by solid arrows while dashed arrows indicate non-radiative transitions. **c)** Simplified energy-level diagram of the DBT:Ac system.

Single-molecule experiments start by pumping with a laser the DBT molecule from the

[1] In the organic molecule jargon, the ground state is often called Highest Occupied Molecular Orbital (HOMO), whereas the first excited state is the Lowest Unoccupied Molecular Orbital (LUMO).

vibrational ground state of $|S_0\rangle$[2]. Resonant excitation (or coherent pumping) is achieved with a 785 nm laser, yielding to a purely electronic transition that brings an electron from the ground to the first excited state $|S_1\rangle$[3]. As we will discuss in Section 2.4, this scheme is employed in cryogenic temperature experiments to probe and collect the emission from 00-ZPL. For room temperature experiments an alternative non-resonant (or incoherent) excitation scheme is used, where the molecule is pumped with a 767 nm laser. The electron now is promoted to a vibrational level of a higher excited electronic state $|S_{i,\nu=n}\rangle$. In this case, the excited state can be completely occupied and population inversion can be reached, yielding a higher emitted photon count rate at saturation.

For both excitation schemes, absorption takes place on the femtosecond time scale. From a general excited state $|S_{i,\nu=n}\rangle$ the molecule decays to the $|S_{1,\nu=0}\rangle$ state mainly through one of these non-radiative processes:

vibrational relaxation: non-radiative relaxation process in which the molecule decays to a lower vibrational state within the same electronic level on the scale of picoseconds. Dissipation is mostly in the form of transfer of thermal energy through collisions with the surrounding environment.

internal conversion (IC): non-radiative relaxation process similar to vibrational relaxation but involving transition between vibrational levels of different electronic states. This process is more likely to dominate at high electronic states, where it is facilitated by the strong energy overlap between electronic states and the manifold of vibrational levels.

The molecule is now prepared in the $|S_{1,\nu=0}\rangle$ state where two mechanisms compete to determine the lifetime τ of this state and the final relaxation to the ground state:

fluorescence (FLUO): radiative transition corresponding to the relaxation to the electronic ground state through the emission of a photon. Fluorescence results red-shifted (*Stokes*-shifted) in the energy spectrum compared to the excitation wavelength and can be easily separated from the excitation laser by means of proper optical filters, thus enabling single molecule experiments.

intersystem crossing (ISC): radiation-less process due to spin-orbit coupling and involving the transition between the two almost iso-energetic vibrational levels of $|S_1\rangle$ and $|T_1\rangle$.

[2]This is true at both cryogenic and room temperature. In the latter case, in fact, the thermal energy is small compared to a quantum of vibrational energy.

[3]Since the photon cannot flip spins, the state $|S_1\rangle$ is reached after absorption, even if the triplet state $|T_i\rangle$ is at lower energy.

According to electronic selection rules, this transition is spin-forbidden and is hence weakly allowed. For the same reason, the radiative de-excitation from $|T_1\rangle$ to $|S_0\rangle$ - termed phosphorescence - is very slow, with a lifetime typically in the ms-to-s-range.

According to the fast time-scale in which the vibronic transitions take place, we can consider a simplified energy-level scheme, mapping a single DBT molecule embedded in anthracene as a three-level system (Figure 2.1c). Labelling with $|g\rangle$ and $|e\rangle$ the singlet states $|S_0\rangle$ and $|S_1\rangle$, and with $|t\rangle$ the triplet state $|T_1\rangle$, the dynamics of the three-level system can be easily derived with argumentations similar to the case of the two-level system discussed in Chapter 1. Accounting for all the possible non-radiative decays and radiative transitions depicted in **Figure 2.1c**, the transition rates are given by:

$$\frac{d}{dt}\rho_{ee}(t) = \Gamma_{12}\rho_{gg}(t) - (\Gamma_{21} + \Gamma_{23})\rho_{ee}(t) \tag{2.1}$$

$$\frac{d}{dt}\rho_{gg}(t) = \Gamma_{21}\rho_{ee}(t) - \Gamma_{12}\rho_{gg}(t) + \Gamma_{31}\rho_{tt}(t) \tag{2.2}$$

$$\frac{d}{dt}\rho_{tt}(t) = \Gamma_{23}\rho_{ee}(t) - \Gamma_{31}\rho_{tt}(t) \tag{2.3}$$

with Γ_{ij} the rate of the transition $i \to j$.
The triplet state T_1 plays a central role on the emission properties of the DBT:Ac system. All the time the molecule gets trapped in the long-lived triplet state, fluorescence intermittency (blinking) occurs, limiting the overall QY of the system. Indeed, if the ISC transition is strongly facilitated, the resulting weakened fluorescence signal can make single molecule detection impossible [39]. Hence, a good host-guest system for single-photon source, exploitable in single molecule studies, should have a short triplet lifetime and a low ISC rate (Γ_{23}), to allow photon-efficient fluorescence cycles. The triplet state parameters (Γ_{31} and Γ_{23}) depend on the dye but also on the matrix into which the molecules are embedded and, specifically, the host lowest's triplet state should lie at a lower energy than the guest's fluorescent singlet state.

Among different organic crystals, anthracene, with its triplet state at 680 nm, is hence a good host candidate for DBT molecules. The ISC yield is indeed very low at 10^{-7} [83] and the triplet state is short-lived, with a lifetime ($1/\Gamma_{31}$) of 1.5 µs [40]. The effect of the triplet state is therefore negligible and the whole description of DBT:Ac system reduces to that of a two-level atom. When no external loss channels are available, the excited DBT molecule relaxes mainly through radiative emission with a QY close to 1.

Since the anthracene matrix does not contribute to the depopulation of the excited state, fluorescence intensity decays in time as a single exponential, with a typical excited state

lifetime of 4.2 ns [143]. Another important property is the brightness of this system, with a photon count rates from a single molecule around 10^6 per second at pump intensities close to saturation. As a matrix, anthracene efficiently shields the molecule from quencher agents such as oxygen, ensuring a high photostability at room temperature: bleaching of DBT in anthracene was measured to exceed 10 hours of strong illumination (to compare with the typical few-second timescale during which a dye molecule emits in solution) [40]. DBT molecules emit more than 10^{12} photons before photobleaching, while other molecular emitters typically bleach after $10^4 - 10^7$ photon emissions [144].

Another important feature is that DBT molecules are hosted in Ac with a well-defined orientation, parallel to the crystal plane, so as to minimize Gibbs free energy [40]. This property allows to achieve efficient evanescent coupling of the emitted photons to a nearby photonic structure, as we will discuss in Chapter 3.

2.1.2 Spectral properties

Lineshape and homogeneous broadening

As for all molecules embedded in a solid matrix, the host material strongly affects the spectral features of the molecule emission. Specifically, all optical transitions from the excited state $|S_{i,\nu=0}\rangle$ to one of the vibrational levels of the ground state result in a ZPL and in a phonon side band (PSB). These features, completely hidden at room temperature, starts to appear below 40 K, as schematically shown in **Figure 2.2a**.

As the name suggests, the ZPL is a transition without net creation of phonons, i.e. quanta of vibrational excitations in the host lattice. The normalized line shape for purely electronic transitions has usually a Lorentzian shape, reflecting the Fourier transform of the exponential decay of the population [51]:

$$I(\nu - \nu_0) = \frac{1}{4\pi^2} \frac{\Delta\nu_{\text{hom}}}{(\nu - \nu_0)^2 + (\Delta\nu_{\text{hom}}/2)^2} \tag{2.4}$$

where ν_0 is the peak's center and $\Delta\nu_{\text{hom}}$ is the homogeneous linewidth, related to the pure dephasing time T_2^* and the finite lifetime τ of the excited electronic state, according to equation (1.16). In a crystalline host matrix at cryogenic temperatures, T_2^* tends to infinity. Therefore the ZPL is only limited by its natural broadening which depends on the lifetime of the electronic excited state ($\Delta\nu_{\text{nat}} \simeq 1/(2\pi\tau)$). For the DBT:Ac system it has been demonstrated that below 4 K, dephasing due to phonons vanishes and the line becomes almost lifetime-limited, showing a natural width of about 40 MHz corresponding to a lifetime of 4.2 ns. Let us note, however, that any measured linewidth of the 00-ZPL will suffer from

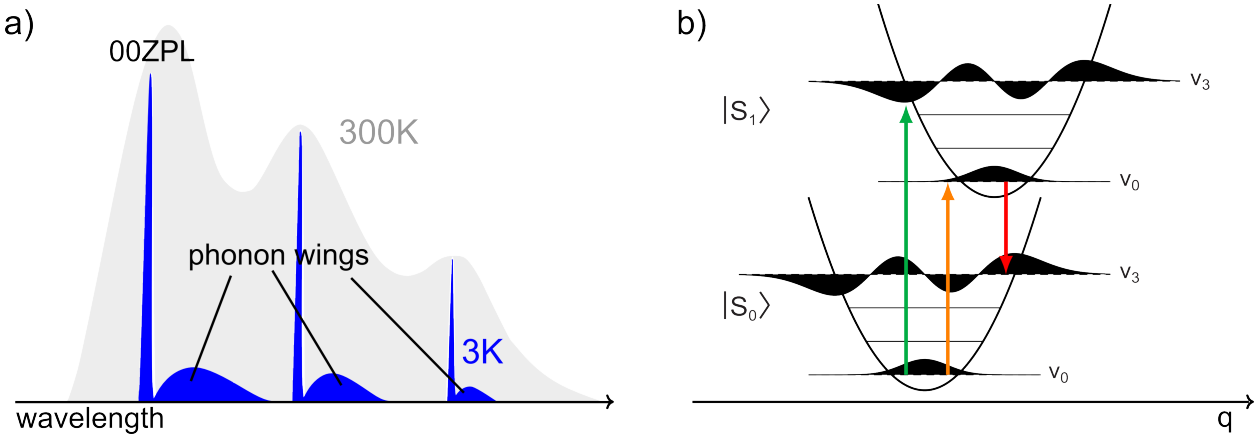

Figure 2.2 – **a)** Illustration of the emission spectrum of a single molecule embedded in solid matrix at room temperature (light grey). When the temperature is lowered, the spectrum becomes narrower (blue) and the ZPLs and the phonon wings are resolved. Specifically, the ZPL shape at cryogenic temperature becomes Lorentzian, with a width determined by the solely excited-state lifetime τ. The relative intensity of the two components depends on the temperature and is determined by the Debye-Waller factor α_{DW}. **b)** Configuration diagram showing the vibronic levels of a single molecule as a function of the nuclear displacement q. Transitions are drawn as vertical arrows since, according to the Frank-Condon principle, they occur on a time scale much shorter than the nuclear motion, so that the atomic coordinate remains unchanged.

some power broadening, even under conditions far below saturation [130]. This effect on the spectral broadening is described as:

$$\Delta\nu(I) = \Delta\nu_{\mathrm{hom}}\sqrt{1 + I/I_s} \tag{2.5}$$

showing that the true lifetime-limited 00-ZPL could only be measured at an excitation intensity $I = 0$.

The PSB, also known as phonon wing, originates from linear electron-phonon coupling which allows transfer of molecular excitations into lattice vibrations. In principle, the emission spectrum for a particular vibrational mode should consist of a series of discrete lines, each corresponding to a specific number of phonons. In practice, the electronic states can couple to many different phonon modes with a large range of frequencies and thus the spectra usually form a continuous band. The PSB is hence the envelope of all phonon excitations and can be modeled with a Gaussian profile [145]. This band is quite broad (about a few ps) as is limited by the lifetime of the vibrations. Therefore, in order to have a strong narrowband emission of indistinguishable photons, emission into these broad sidebands should be as low as possible.

Whether the intensity of a given line goes into the ZPL (I_{ZPL}) or into the PSB (I_{PSB}) is

accounted for the Debye-Waller factor

$$\alpha_{\mathrm{DW}} = \frac{I_{\mathrm{ZPL}}}{I_{\mathrm{ZPL}} + I_{\mathrm{PSB}}}, \tag{2.6}$$

which strongly depends on temperature [146].
The strength of the 00-ZPL is also related to the branching ratio between the decay rate into the ground state $|S_{0,\nu=0}\rangle$ and the rate of decay into all other vibrational sublevels. This branching ratio can be understood in terms of the Frank-Condon principle, which states that electronic transitions occur without altering the molecular configuration, i.e. they don't change the interatomic distance in the molecule[4]. As a consequence of the Frank-Condon principle, in a configuration diagram as the one shown in Figure 2.2b, transitions are drawn as vertical arrows since they are so fast that the atomic coordinates (on the horizontal axis) remain unchanged. The intensity of the purely electronic line is measured in terms of the Frank-Condon factor α_{FC} which expresses the overlap integral of the ground vibrational wavefunction between the electronic states. If the wavefunction overlap is poor, then the purely electronic line has a lower fluorescence probability, in favor of other vibronic red-shifted lines.

Typical value for α_{FC} is 0.4 [147], and for the DBT:Ac system $\alpha_{\mathrm{DW}} > 0.3$ has been measured [73]. This value is much higher than the 0.03 measured for NV-centers in diamonds [148] but still below the 0.9 measured for the silicon-vacancy centers [149]. However, it can be enhanced via coupling the DBT:Ac system to an optical cavity tuned to be resonant with the 00-ZPL, so that emission to higher phonon modes is suppressed [150].

Noteworthy, thanks to the good structural match between anthracene and DBT, the 00-ZPL is very stable against spectral diffusion and no spectral jumps are observed on timescales of hours [39]. As discussed in Chapter 1.1.3, the stability of the transition frequency is a very desirable property for a single-photon source. Additionally, it allows to the use of DBT:Ac as a probe for electrical or other dynamical processes taking place at the nanoscale, resulting in a shift in the spectral line. Indeed, the spectral characteristics of molecules in solid matrices is strongly affected by the host matrix, as discussed below.

[4]This follows from the *Born-Oppenheimer approximation*, according to which electronic and nuclear motion are treated separately. The approximation holds because electrons have a much smaller mass than nuclei and therefore move on shorter time scales, which allows to factor the total wavefunction into an electronic and a nuclear component.

Inhomogeneous broadening

Any solid state matrix presents local defects, random internal strain fields, crystal edges, impurities and dislocations in the host matrix, and all contribute to create slightly different electrostatic environments. Correspondingly, within the same matrix, different molecules - even if chemically identical - present transition frequencies centered on different values, as schematically shown in **Figure 2.3**. This distribution of frequencies is called inhomogeneous broadening and is likely to have a Gaussian distribution, according to the randomness of the environmental fluctuations as felt by each molecule.

The amount of the inhomogeneous broadening is determined by the particular choice of the dye-matrix pair and, for a given pair, can change for different sample preparation techniques. As for the order of magnitudes, the inhomogeneous broadening of the 00-ZPL transition can be smaller than 1 GHz in unstressed sublimated crystals, and as high as 10 THz in polymers or other amorphous materials [151, 152].

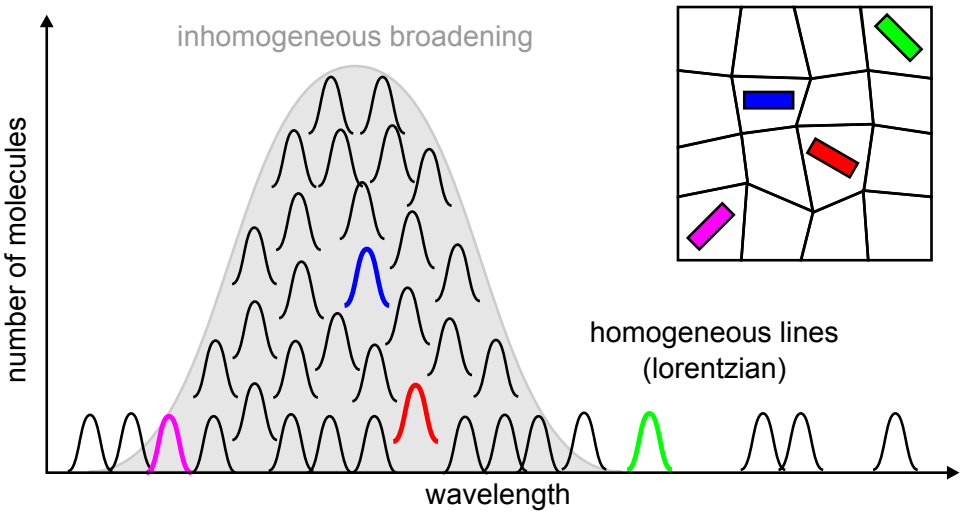

Figure 2.3 – In a real crystal, imperfections exist like strain fields or defects. Due to the different nano-environments for each single emitter, their homogeneous lorentzian shape transition are inhomogeneously distributed in frequency.

The existence of the inhomogeneous broadening indicates that a single molecule could be used as an extremely sensitive probe for the nanoscopic environment. Given that a lifetime-limited transition can be as narrow as a few MHz and considering that the optical transition frequency is of the order of 500 THz (visible light), the quality factor Q of the 00-ZPL can be as high as 10^8. It is therefore clear that very small changes in the nanoenvironment, such as weak perturbations produced by local electric, magnetic or strain fields, do cause a detectable shift in the resonance.

Moreover, as we will see in Section 2.3, at cryogenic temperatures the inhomogeneous broadening of the lifetime-limited 00-ZPLs can be exploited to spectrally address individual molecules, even in a highly doped matrix, by tuning a narrowband laser.

2.1.3 Fabrication Methods

Anthracene crystals embedding DBT molecules are relatively easy to fabricate. Depending on the application and type of measurement, two different fabrication techniques are currently available: co-sublimation and spin-coating.

Co-sublimation

Co-sublimated crystals can be obtained with a simple set-up consisting of a glass pipe kept in a 150 mbar nitrogen atmosphere [153] (**Figure 2.4a**). At the bottom of the pipe, a mixture of DBT and anthracene in powder is heated up so that the vapour pressure rises and small (about 50 µm average lateral size) crystals start to form in the convective nitrogen flow. These flying crystals can then be captured on a substrate, as shown in **Figure 2.4b**, from

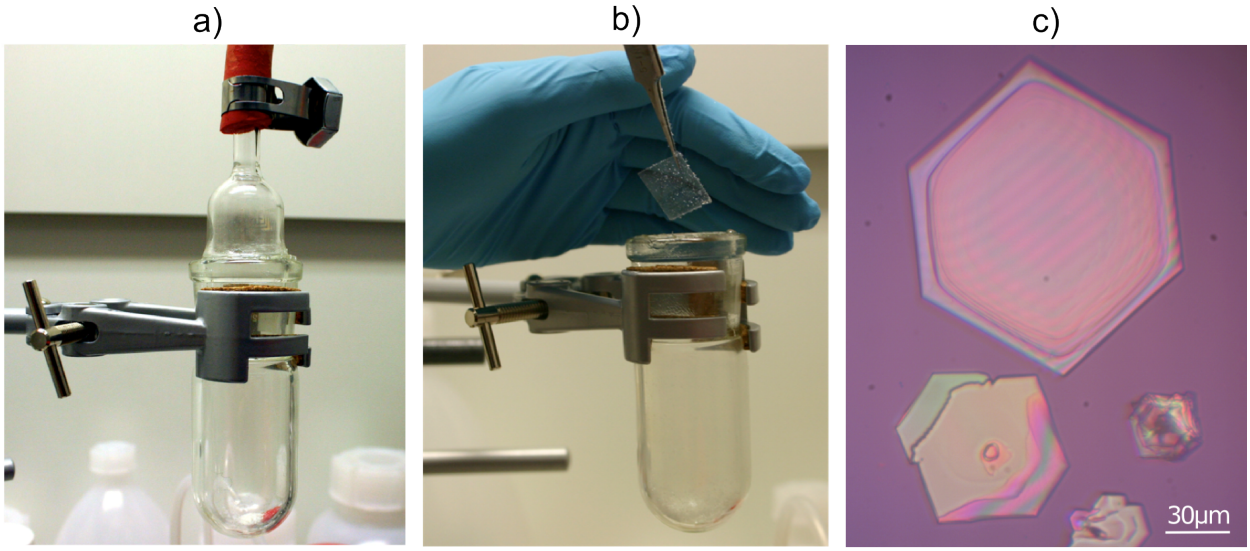

Figure 2.4 – Co-sublimation takes place inside a glass pipe kept in a 150 mbar nitrogen atmosphere, where a mixture of DBT and Ac in powder is heated up **(a)**. When the vapour pressure rises, small crystals start to form in the convective nitrogen flow and can be captured on a coverslide **(b)**. Crystals obtained with this protocol have a much more pure crystalline structure as is also hinted by the macroscopic almost perfect hexagonal shapes **(c)**.

which they can be eventually picked up by means of a tapered fiber mounted on a 3D-stage positioner.

Crystals obtained with this protocol have a pure crystalline structure, as hinted by their macroscopic almost perfect hexagonal shapes (see **Figure 2.4c**). Co-sublimated DBT:Ac crystals have an average thickness around 100 nm, according to AFM measurements. Being smaller than the radiation wavelength, they can in principle enable near-field interaction between single DBT molecules and a nearby photonic structure.

With this procedure, DBT concentration is hard to control. However, owing the their high crystallinity, co-sublimated crystals are usually employed for cryogenic measurements, where single molecules can be addressed spectrally, exploiting the inhomogeneous broadening of the narrow 00-ZPL.

For completeness, we report on a recent up-graded protocol developed by Hinds's group in Imperial College (London), which relies on a crystal growth oven. The set-up is more complex than the one presented here, but allows for the fabrication of bigger (several mm across and a few µm thick) Ac crystals doped with a controlled concentration of DBT molecules [154].

Spin-coating

Spin-coating is a well-known procedure to form uniform thin crystalline films into flat substrates [155]. For this protocol, a solution of Ac in diethyl ether (2.5 mg ml^{-1} concentration, both pursued from Sigma Aldrich) is first prepared. This solution is used to stepwise dilute a 10 µM solution of DBT and toluene, to finally obtain a 1 nM DBT in 2.5 mg ml^{-1} Ac in diethyl ether. This recipe provides a sufficiently low concentration of DBT molecules such that they result well spatially separated within the crystalline film, hence allowing for room temperature experiment on single molecules [40].

The crystals are obtained by drop-casting a 20 µL of this solution on the desired substrate, placed in the rotating plate of the spin-coater. The drop is then spun at high speed with a pre-programmed two-steps recipe (3000rpm/30sec and 1500rpm/15sec). The viscous flow created by rotation and the evaporation of the solvent results in a gradual thinning of the anthracene film due to the centrifugal force. The thinning process - schematically shown in (**Figure 2.5a**) - is driven by the viscous flow at the beginning and then by evaporation of the solvent [156], producing DBT:Ac crystalline islands with different shape and size all over the substrate surface (**Figure 2.5b**).

Among the few clusters (islands with orange-pink colors), we can distinguish crystals up to several hundreds of µm^2 size (blueish islands), showing clear-cut facets and thickness ranging from 20 nm to 80 nm with a typical surface roughness on the order of 1 nm, according to atomic force microscopy (AFM) measurements.

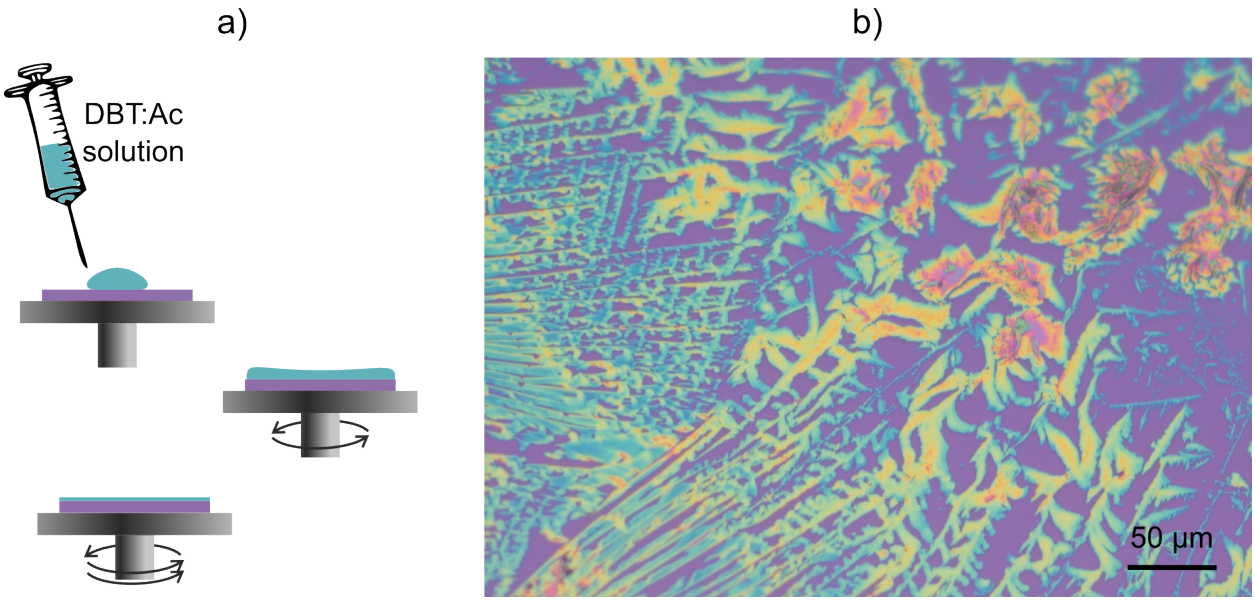

Figure 2.5 – **a)** A 20 µL drop of a mixture of DBT:Ac in solution is casted on a substrate, placed in the rotating plate of the spin-coater. The substrate is then rotated at high speed in order to achieve a gradually thinning of the anthracene film. **b)** A microscope image of DBT:Ac crystalline islands resulting from the spin-coating procedure. The blueish regions show clear-cut facets and a uniform thickness ranging from 20 nm to 80 nm.

2.1.4 Overview on Recent Results

All the properties described so far demonstrates that the DBT:Ac system is an ideal candidate for experiment with single molecules and, to date, it has been proposed and successfully operated in several experiments.

It was first proved to be a sensitive nanodetector [153] and detection of Stark shifts in single DBT molecules has been used to investigate transport of electrical charge in anthracene in a field-effect transistor configuration [157]. More recently, it has been used as a sort of nanomicrophone to probe acoustic strain, i.e. to detect localized low-frequency acoustic vibrations, which is a first step towards detection and control of nanomechanical oscillators by optical means [158, 159]. As for sensing applications, DBT:Ac system has also been employed for a graphene-based fundamental ruler at the nanoscale, relying on the efficient energy-transfer mechanism between single molecules and low-doped graphene monolayers [143].

As a source of single photons, DBT molecules trapped in an anthracene crystal have been proven to be a source of nearly indistinguishable photons, allowing for the generation of polarization-entangled photon pairs [91]. The DBT:Ac system was successfully integrated in a robust design of a planar optical antenna, able to beam the single-photon emission at

small angles without stringent requirements on the emitter position [160], and more recently it was employed in the first demonstration of coherent interaction between a single organic molecule and a microcavity [161].

For scalable quantum optical platforms, two schemes have been proposed to achieve reliable light matter interfaces employing DBT molecules and dielectric nanoguides. One scheme relies on fabricating the nanoguide with the same organic matrix embedding the molecules: this has been demonstrated using naphtalene as the host matrix [162]. In an alternative scheme proposed by Hwang and colleagues [19], a single molecule deposited nearby a high-refractive index waveguide may provide an efficient collection of the emitted photons into the guided mode via evanescent coupling, and large localized optical nonlinearities. Relying on the simple spin-coating procedure, we demonstrate at room temperature that the emission of single photons from DBT molecules into a ridge waveguides can reach a coupling efficiency up to $40 \pm 3\%$. This result, that will be discussed in details in Chapter 3, is competitive with state-of-the-art single-photon emission into propagating guided modes from solid state systems [32], while offering a novel platform with unprecedented versatility.

However, to fully exploit molecules in solid state as nanoscale single-photon sources for mature integrated quantum technologies, reducing the size of the system on a sub-micrometric scale is desirable as precise positioning method can be conceived. We hence explore a novel fabrication method of DBT:Ac allowing to grow sub-micrometric crystals. This will be discussed in Chapter 4. Quite surprisingly, we demonstrate that the remarkable features of DBT in Ac are preserved even for matrix sizes below the micron.

2.2 Principles of Single Molecule Detection

The fundamental parameter for single-molecule experiments is the absorption cross-section $\sigma(\omega)$, i.e. the effective photon-capture area of a single molecule under coherent excitation. The interaction between a single molecule and an external light field is indeed proportional to the ratio between the absorption cross-section of the molecule and the area on which the incident light field is focussed. Therefore, for single-molecule detection, the absorption cross-section should preferably be as large as possible [145] while simultaneously confining light into a small area.

The maximal achievable absorption cross-section for a single two-level system in vacuum under a plane wave illumination is given by [43]:

$$\sigma(\omega) = \frac{3}{2\pi}\lambda^2 \tag{2.7}$$

assuming a transition dipole moment perfectly oriented along the incident polarization of the incoming resonant light with wavelength λ. Interestingly, the scattering cross-section on resonance is only dependent on the transition frequency and independent on all other atomic or molecular properties.

For a molecule doped into a solid matrix with a multi-level energy diagram as the one show in **Figure 2.1**, several factors contribute to a reduction of $\sigma(\omega)$. As discussed in Section 2.1.2, under ambient conditions the transitions are broadened and not lifetime-limited. Moreover, for a resonantly driven molecule only a part of the light is emitted on the 00-ZPL, according to the amount of the Franck-Condon factor α_{FC} and the Debye-Waller factor α_{DW}. A further reduction is due to the angle θ between the transition dipole moment of the molecule and the electric field vector of the excitation light, that gives rise to an additional geometrical factor of $3\cos^2(\theta)$.

Taking into account all these factors, the absorption cross-section in equation (2.7), is re-written for a single molecule in a solid matrix as:

$$\sigma(\omega) = \alpha_{\mathrm{FC}}\alpha_{\mathrm{DW}}\frac{3\lambda^2}{2\pi}\frac{\Gamma_{nat}}{\Gamma_{hom}}\cos^2(\theta). \tag{2.8}$$

At low temperature, the absorption cross-section in equation (2.8) results larger (typically by 7 order of magnitude) than the absorption cross-section of the same molecule at room temperature and 10^4 times bigger than the physical size of the molecule itself [163]. This explains why, compared to the first observations on quantum systems such as attenuated atomic beams or single ions in traps, experiments on single molecules developed at a slower rate and are a relatively recent technological achievement.

The first observation of a single molecules was done in 1989 by Moerner and Kador [164], who performed a sensitive measurement of a molecular optical absorption at cryogenic temperatures by confining the laser light to a small spot of 3 µm. One year later, Orrit and Bernard observed single pentacene molecules embedded in a p-terphenyl crystal by detecting their fluorescence after excitation [165], with a higher signal-to-noise ratio compared to absorption-based methods. The first observation of single molecules at room temperature followed later, using aperture scanning near-field optical microscopy [166].

Since then, over almost 30 years, the field has expanded considerably and detection of single molecules is now a well-established technique used in many different areas, ranging from quantum optics to biophysics, where it is employed for both fundamental research towards application oriented engineering[5] [167, 168].

[5]From a more fundamental point of view, the experimental access to single molecules completely remove the normal ensemble averaging that occurs when a large number of molecules are probed simultaneously,

Among the currently available experimental methods to detect single molecules (for a comprehensive review see e.g. reference [85]), the simplest and today most common technique is to measure their Stokes-shifted fluorescence[6] with a confocal epifluorescence microscope, whose working principle is described hereafter.

2.2.1 Epifluorescence confocal microscopy

There are several challenges one has to overcome in order to successfully detect single fluorescent molecules. One has to first isolate a single molecule among billions to trillions of host molecules and properly excite it with a laser source. The resulting weak fluorescence signal should then be efficiently collected and detected against background and dark counts from the detectors, while ensuring the stability of the system against photobleaching for extended periods of time.

The first requirement, i.e. the optical isolation of a single molecule, is accomplished using microscope objectives to excite small volumes of the sample. A high resolution is obtained with high numerical aperture (NA) objectives, as they stretch the Abbe resolution limit [169]:

$$D = 0.5\frac{\lambda_{\text{exc}}}{\text{NA}} \tag{2.9}$$

where D is the smallest resolvable distance between two points on the sample, λ_{exc} is the excitation wavelength and NA is defined as:

$$\text{NA} = n\sin(\theta) \tag{2.10}$$

n here is the refractive index of the medium between the objective and the sample and θ is the half planar angle of the maximum cone observed by the objective.
For a fixed lens size, a shorter focal length corresponds to a higher NA. Then, given certain focal length, the NA can be maximized using a liquid immersion objective[7], in which a high

allowing to gain detailed informations on the basic optical properties of the molecule itself and its interactions with the surrounding local environment (the *nanoenvironment*). This is particularly powerful for biological applications, where a molecule/protein/area of interest in a cell can be covalently linked to a fluorescent molecule, and the measurement of its optical properties measurement allows to study position, local environment and even activity in real time.

[6] Depending on the molecule-matrix system and the filters in use, part of the Stokes-shifted fluorescence is depleted together with the resonance fluorescence of the molecule. Nevertheless, fluorescence excitation measurements are easier to perform than absorption experiments, in which the coherently scattered light, which has exactly the same wavelength of the excitation light, is detected.

[7] The liquid immersion technique can be exploited to enhance a microscope optical resolution for room temperature experiments but is technologically complicated for cryogenic applications where solid immersion lenses are used.

refractive index material, like water ($n = 1.33$) or oil (n up to 1.56), is placed between the objective and the sample. In order to prevent total internal reflection[8], and thus enhance the fluorescence intensity of the emitting molecule, the immersion medium must index-match the dielectric material in which the molecules are embedded or the substrate material[9]. Liquid immersion objectives also guarantee a high collection efficiency, i.e. the fraction of light collected by the objective for an isotropic light source, as it fast increases with NA [156].

Indeed, most common fluorescence microscopes in use are epifluorescence microscopes, where excitation of the molecule and detection of the fluorescence are done through the same microscope objective. In this configuration the most effective way to separate fluorescence is spectral filtering with a dichroic mirror which splits an incoming light into two beams of different wavelength. A non-polarizing beamsplitter that exploits the different propagation directions can also be used to separate the fluorescence light from the excitation laser beam.

Epifluorescence configuration is the basis for more advanced microscope designs, such as the confocal microscope and wide-field configuration that will be introduced in the following. The peculiarity of epifluorescence microscope is that, once the excitation beam is collimated, also the beam of collected light results collimated. Therefore, it is possible to easily introduce filters and other optical elements anywhere into the beam path, in order to enhance the signal-to-background ratio and hence optimize the fluorescence detection. In fact, in any real system there is a background signal including residual laser emission in the spectral range of the detected fluorescence, residual transmission of backscattered laser light through the filters and dark counts from the detector. Additionally, impurities on the sample can also give rise to unwanted fluorescence, therefore special care has to be taken while preparing and handling the samples.

Indeed, provided a diffraction limited excitation volume, isolation of single molecules should also be ensured either spatially or spectrally (or by a combination of the two). In the first case, a very diluted sample where the molecule is embedded as an impurity within a transparent matrix is prepared, so as to ensure that a single molecule lies within the confocal spot of the excitation beam ($\simeq$ µm). At cryogenic temperatures, as previously discussed, inhomogeneous broadening due to interactions with the environment causes random shifts in the lifetime-limited lines. A narrow-band laser (linewidth $\simeq 1$ MHz) tuned into the wings of the inhomogeneous line - where fewer molecules are found - can therefore be used to

[8] When a propagating electromagnetic wave crosses a boundary between materials with different refractive indices, it will be partially refracted and partially reflected. If the angle of incidence is greater than the critical angle, the wave will not cross the boundary and is instead totally back reflected.

[9] In this work, since the objective-oil chemically interacts with the DBT:Ac system, Zeiss coverglasses with refractive index of $n = 1.52$ are used as a substrate, as they index-match the refractive index of the objective-oil.

successfully excite single molecules by spectral selection.

Even though the use of a microscope objective already reduces the probe volume, all the molecules within the excited volume contribute to the fluorescence signal, as shown in the inset in **Figure 2.6**. By properly inserting a pinhole in the detection line it is possible to further decrease the volume of observation, isolating light coming from the focal plane. Light not originating from the focal area will not be able to pass through the detection pinhole and hence cannot reach the detector. Beams originating from points displaced along the optical axis will not be focused in the detection plane and are therefore strongly attenuated.

The size of the detection pinhole must be correctly matched to the diameter of the focal spot (given by the Abbe criterion), provided that the excitation beam overfill the objective back-aperture. Only in this case, in fact, the focussed spot is diffraction limited. This

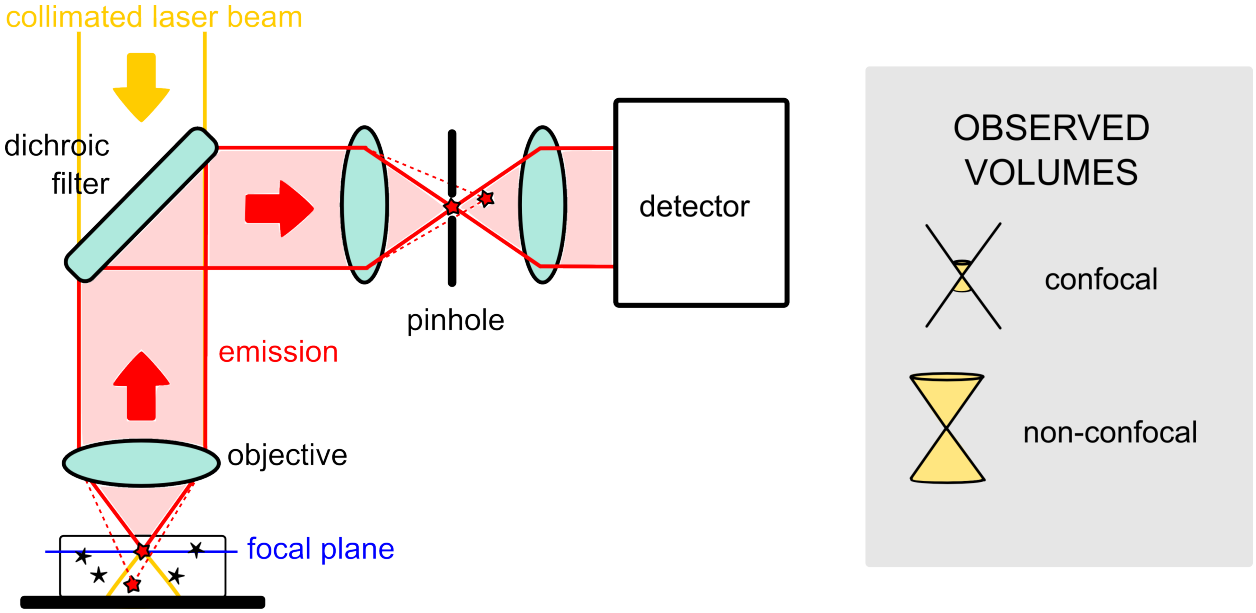

Figure 2.6 – The confocal principle: the pinhole is placed at a focal point in the detection light path. By ray tracing of the light path one can see that light from above or below the focal plane is not focused onto the pinhole and hence does not reach the detector.

detection method strongly reduces the background signal and optimizes single molecule fluorescence detection [170]. When only a point-like volume of the sample is imaged onto the photodetector, the microscope is termed confocal. Conversely, in wide-field illumination a greater portion of the sample is illuminated, as in a traditional microscope.

The confocal microscope is usually upgraded to scan an area of the sample to be imaged point-by-point. There are mainly two possibilities for scanning: one can move either the sample itself with piezo-electric transducers (sample scanning), or the laser beam focus by means of tilting mirrors (beam scanning).

The technical solutions that enable single molecules detection pointed out so far can be summarized as follows:

- **highly efficient detectors** such as avalanche photodiodes, photomultipliers tubes or electron-amplifying CCDs, which exhibit low dark-counts.
- **efficient collection and high spatial resolution** by using high-NA optics.
- **low BG signal** via spatial isolation (low molecule concentration sample, and small excitation volume) and via spectral isolation (efficient optical filters with an optical density[10] OD ~ 6).

2.3 Optical Set-Up and Experimental Techniques

The experimental set-up used in this thesis to perform single molecule microscopy and spectroscopy is a home-built, versatile epifluorescence scanning confocal microscope. **Figure 2.7** shows a simplified version of the set-up which is briefly described in the following, considering separately the excitation and the detection paths.

Excitation arm

For the excitation, depending on the molecular transition to excite and hence the measurement to be performed, several lasers can be coupled to the fluorescence microscope by means of flippable mirror or polarizing beam splitter cubes and half-wave plates. A white light (WL) lamp is instead used for simple imaging of the sample.

For non-resonant excitation at 767 nm we employ a continuous-wave (CW) single mode laser (Toptica DL110-DFB) and a pulsed Ti:sapphire laser (Tsunami by Spectra-Physics), optimized to emit pulses with 200 fs width and repetition rate of 81.2 MHz. Resonant pumping is performed with a narrowband DFB (Toptica, LD-0785-0080-DFB-1) laser emitting at 784.6 nm, whose frequency can be scanned continuously over a range of about 800 GHz. Optical isolators are used to prevent scattered light to be reflected back into the laser head and, where needed, additional elements such as anamorphic prism pairs and cylindrical lenses are used to optimize the laser spot into a collimated circular shape.

In order to be properly focused onto the sample, the laser beam should remain collimated over the entire excitation path length and impinge on the objective with a Gaussian

[10] Optical Density (OD) is a convenient way to describe the blocking ability of an optical filter. Higher OD values indicate a higher level of filtering.

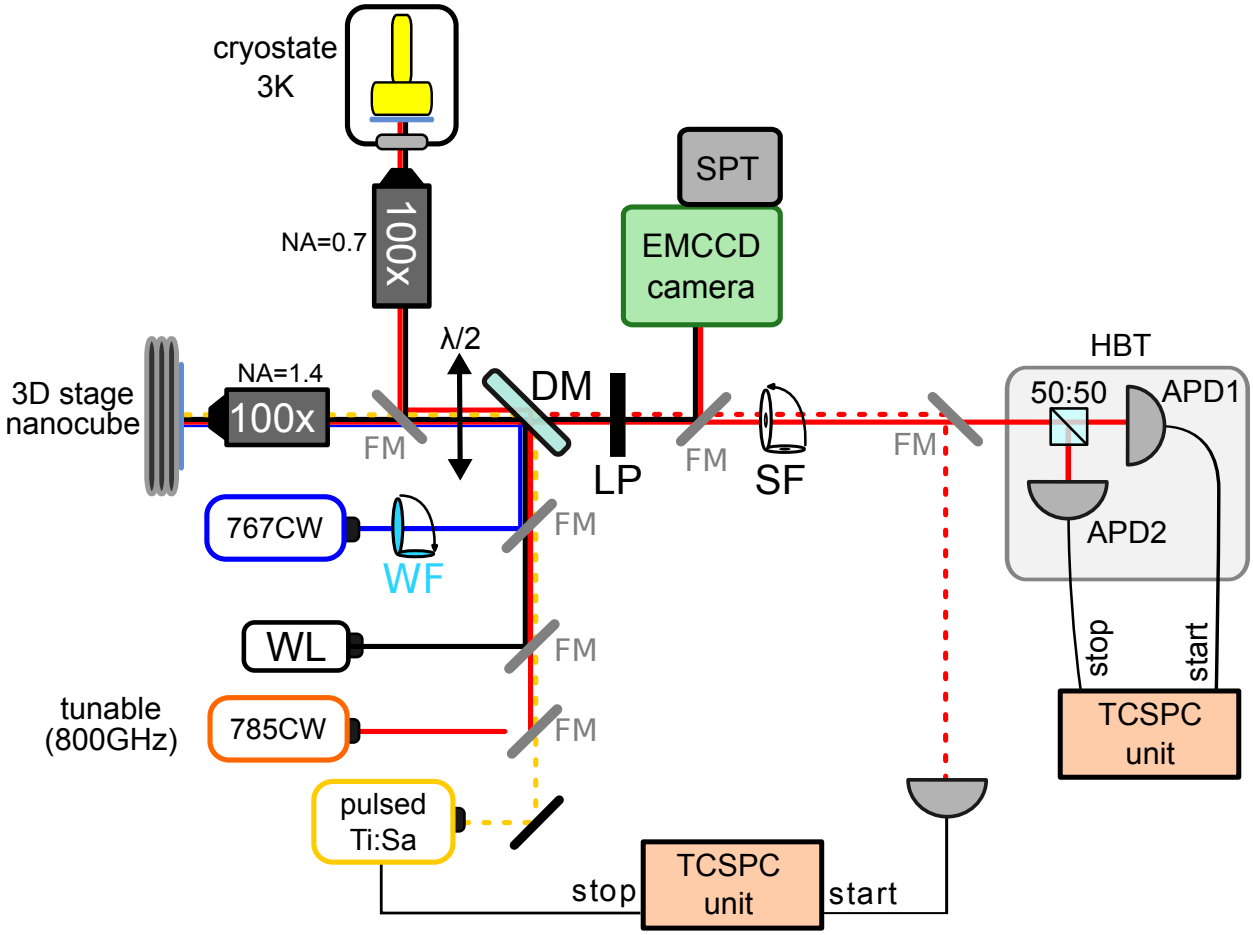

Figure 2.7 – Simplified diagram of the experimental set-up. Flippable Mirrors (FM) allow to switch between several fiber-coupled laser light sources. A white light lamp (WL) can also be used to image the sample, whereas a wide-field lens (WF) can be inserted to perform fluorescence imaging. High NA objectives are used to efficiently collect fluorescence light. Samples can be mounted either on a piezo stage for room temperature measurements or inside a cryostat for measurements down to 3 K. In the latter case, the laser spot is scanned on the sample by using a galvo mirror and a telecentric system (not shown in the scheme). Fluorescence is separated by excitation light through a dichroic mirror (DM) and is collected through a longpass filter (LP) in both confocal and wide-field configurations. A telescope and a pinhole act as a spatial filter (SF), increasing resolution and contrast and allowing for confocal detection. Two avalanche photodiodes (APDs) - arranged in Hanbury Brown-Twiss configuration (HBT) - and an EM-gain CCD camera equipped with a grating spectrograph are placed inside a box to efficiently shield residual light.

profile. For this reason, each laser light is spatially filtered by coupling it to a polarization-maintaining single-mode optical fiber with a core diameter of 4 µm, allowing for confocal excitation. At the entrance of the fiber we place a half-wave plate to rotate the linear polarization to match that of the fiber. At the fiber output, narrow band-pass (BP) interference filters or short pass (SP) filters are used to remove unwanted spectral components

and residual fluorescence from the laser beam.

The stability of the laser sources is monitored by directing a small portion (8%) of the beam through a pellicle beamsplitter into a scanning Fabry-Perot cavity (FP) (FSR = 5 GHz). The transmission frequency of the cavity is tuned by adjusting the length of the cavity using piezo- electric transducers. The controller generates a voltage ramp that repetitively scans the length of the FP cavity in order to sweep through one FSR of the interferometer. The transmitted light intensity is measured using a photodiode (Thorlabs PDA10A) and then displayed by an oscilloscope (Tektronix DPO2024B, 200 MHz) where eventual multimode emission corresponds to the observation of more than one isolated peak.

Laser intensity is adjusted without wavelength discrimination by means of neutral density filters and monitored measuring the excitation power at the back aperture of the objective with a wide-area detector (Ophir Nova with PD300-1W sensor head).

A system made of a diverging and a converging achromatic lenses can be inserted in the excitation path switching between confocal to wide-field (WF) excitation. In this case, the laser beam is focused onto the objective back-aperture, causing a wider area to be illuminated on the sample than in confocal excitation.

Finally, a non-polarizing dichroic mirror (DM, Semrock FF776-Di01) sends the collimated excitation light to the microscope objective which focuses the light on the sample, while letting the collected fluorescence light into the detection box. Following the light path, a half-wave plate is used to rotate the polarization of the linearly polarized laser light until optimal alignment with the transition dipole moment of the target molecule is reached, ensuring maximization of both excitation and detection processes.

Sample accomodation

The final part of the excitation path is divided into two independent lines, one for cryogenic cooling and one for room temperature measurements. For low temperature (LT) measurements, the sample is placed inside a closed cycle helium cryostat (Cryostation by Montana Instruments) and mounted inside the cryostat's vacuum chamber at the top of a cold finger capable of cooling samples down to 2.9 K. A low working distance window ensures optical access and allows regular room temperature optical components to be placed as close as 1 mm from the cooled sample. In this configuration, an air objective with NA = 0.7 and a working distance of 6 mm (Mitutoyo 100X Plan Apochromat) is used. The excitation light enters the objective through a telecentric system which, together with a dual-axis galvo mirror, allows the laser spot to be scanned over different points on the sample. This is necessary since at the moment we don't have a system of nanopositioners inside the cryostat chamber.

For room temperature (RT) measurements, the sample is mounted on a piezoelectric nanopositioner (NanoCube by Physik Instrumente) fixed on a dual-axis goniometer and a manual translation stage for coarse positioning. In this case we commonly use a high NA oil-immersion objective (Zeiss Plan Apochromat, 100X, NA=1.4).

Detection arm

The emitted red-shifted fluorescence signal is collected by the objective and travels back in the excitation path, where it is separated from the laser signal by the DM and then enters a box in which all detectors are placed to shield them from non-signal light. Standard DMs do not present high OD and thus cannot completely separate excitation and fluorescence photons. This means that, besides the fluorescence signal, scattered laser light collected into the objective is present in the detection path. In order to filter out this residual excitation light from the fluorescence signal and to increase the signal-to-background ratio, a longpass[11] (LP) filter (Semrock RazorRedge-785RS-25) with OD > 6 is inserted after the DM.

A (flippable) spatial filter (SP) made of a 1:1-telescopic system (f = 100 mm) including a 50 µm pinhole is inserted after the LP. This allows for confocal detection of the fluorescence signal in confocal mode, i.e cutting light originating from out-of-focus planes on the sample and from nearby emitters, thus greatly increasing resolution and contrast.

To detect the weak fluorescence signal, highly efficient detectors with reduced electronic background are used. Light can be focused on a multi-elements electron multiplying CCD (EM-CCD) camera (Andor iXon 885, 1004×1002 pixels, pixel size 8 µm×8 µm) for fluorescence or white-light imaging. When enabled, EM gain ensures high performance in low light scenarios, thanks to the generation of secondary electrons via impact-ionization processes. Alternatively, single-element (pixel) APDs (Tau-Spad-50 Single Photon Counting Modules by PicoQuant) with low dark count rates (< 50cps), short dead time (<70 ns) and detection efficiency up to 50% at 785 nm is used for single molecule measurements performed in confocal configuration. Finally, light can be spectrally analyzed using a grating Czerny-Turner spectrometer with 0.1 nm resolution that is directly connected to the EM-CCD camera.

A standalone time-correlated single photon counting (TCSPC) system (PicoHarp300 by PicoQuant) is used to study the dynamics of the sample, according to the principle of operation discussed below. When the trigger from the pulsed laser is used as a stop signal and the fluorescence intensity detected by a single APD as a start signal, the TCSPC system allows to measure the molecule decay trace (from which the molecule excited-state lifetime

[11] A LP is a dielectric multilayer optical device that transmits wavelengths above a cut-on wavelength which can be blue-shifted tilting the filter around an axis orthogonal to the optical one.

can be extracted). When start and stop signals derive both from two APDs arranged in Hanbury Brown-Twiss (HBT) configuration[12], the entire g^2-function is reconstructed.

Data acquisition and control software

All electronic devices of our set-up are interfaced and operated together with a dedicated acquisition software, developed by Giacomo Mazzamuto during his PhD thesis in our group [171] and featured on the National Instrument's catalogue of case studies [172].

A typical measurement session on single molecules starts with the acquisition of a fluorescence map, where single molecules are easily identified as diffraction-limited spots. This map is built up acquiring the fluorescence count rates with a single APD while physically scanning the sample under the objective (for RT measurements) or by moving the galvo head placed at the pivot point of a telecentric system (for LT measurements). Once candidates of single molecules are identified, the software allows to move the excitation spot to specific coordinates on the map where we can then perform time-resolved measurements, such as antibunching and lifetime curves.

The software makes also possible to measure fluorescence count rates while varying the frequency of the resonant laser, by sending a digital ramp to the DFB laser driver. This allows to measure the molecular excitation line corresponding to the 00-ZPL. Repeating this procedure several times permits to build up a map to study the spectral stability of the emission in time. Finally, our custom software controls flippable mounts on the optical table, such as the mirror in front of the EM-CCD camera and the pinhole acting as a spatial filter, which guarantees similar detection conditions on measurements acquired over several measurements sessions.

2.3.1 Time-correlated single photon counting

TCSPC is a well established and common statistical method to record low level light signals with picosecond time resolution [173]. The principle of TCSPC is based on the detection of single photons and the accurate registration of their arrival times relative to a reference signal. Depending on the optical system and on which timescale the photon are correlated, the TCSPC method allows to probe single-molecule relaxation dynamics and to build up the waveform of the fluorescence signal (from which the emitter lifetime can be calculated) or to address the autocorrelation functions [174, 175].

[12] To split signal towards the two APDs a 50:50 NIR broadband non-polarizing beamsplitter cube, Thorlabs BS017, has been used.

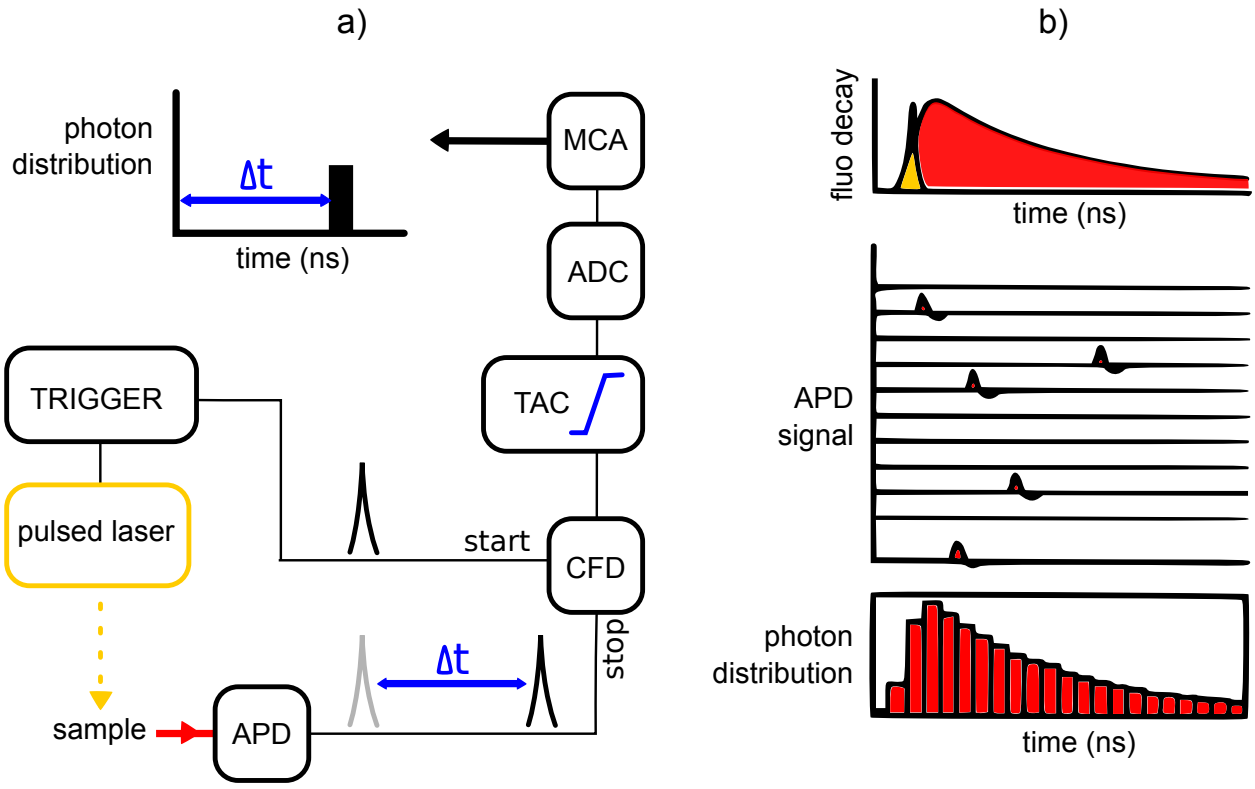

Figure 2.8 – Electronic scheme **(a)** and working principle **(b)** of the TCSPC. The sample is excited with a pulsed laser and the emitted fluorescent photons are detected, fed into the TCSPC module and processed to measure their arrival time with respect to the excitation pulse. Repeating this process over multiple excitation-emission cycles yields to a histogram representing the distribution of the photons arrival time, from which the excited state lifetime can be extracted.

For excited-state lifetime measurements, the emitter is excited with a pulsed laser, used as the reference signal. As discussed in Chapter 1, the lifetime of a quantum emitter is a statistical average and the intensity decay given in equation (1.20) represents the time distribution of the emitted photons. A high repetitive laser source is employed, in order to accumulate a sufficient number of photon events and hence to collect significative statistics. The limit of the laser repetition rate is set by the expected lifetime, as the pulsed source should ensure the observation of a complete fluorescence decay.

The excitation source should also be sufficiently intense in order to significantly populate the excited state and thus working near saturation guarantees a favorable signal-to-background ratio. Moreover, the fall-time of the excitation pulse should be short enough not to affect the fluorescence decay signal. In principle, such fall time sets the limit of the resolution. Though, a posteriori analysis by deconvolution algorithms allows to go beyond the instrumental value.

To detect the low fluorescence signal, the TCSPC makes use of a high quantum effi-

ciency detector, typically an avalanche photodiode (APD), which generates a pulse per each detected photon with very accurate timing of the photon arrival (typical timing jitter = 100 ps). The pulse is then fed into the TCSPC electronics whose block diagram is sketched in **Figure 2.8a**. The time difference between excitation and emission is measured by means of fast electronics: production of a light pulse starts the timing that will be stopped by a signal from the detector, triggered when a fluorescence photon hits the APD. The emitted light signal and the excitation pulses are processed through a constant fraction discriminator (CFD), which accurately measures their arrival time. After passing through the CFD, the laser pulse activates a time-to-amplitude converter (TAC) circuit, which is basically a highly linear integrator and generates a voltage ramp. The TAC charges a capacitor which holds the signal until the pulse from the detected photon stops the voltage ramp. The TAC now contains a voltage proportional to the time delay between the excitation and emission signals. This data is digitalized by an analog-to-digital converter (ADC) and a multi-channel analyzer (MCA) to get a data output.

Provided a low fluorescence photon detected rate - ensured in the case of single molecule detection - the probability to detect one photon in one signal period is much less than one. Therefore, the *pile-up effect*[13] is avoided and the fluorescence intensity decay can be reconstructed by repeating this process over multiple excitation-emission cycle, with the principle shown in **Figure 2.8b**. The registered decay histogram hence represents the time distribution of the photons by a single quantum emitter which can be fitted with a single exponential decay[14] yielding the statistical average of its fluorescence lifetime.

A configuration in which the periodic excitation source provides the sync signal and the detected fluorescence photon provides the stop signal is named *forward mode*. In our case, however, the repetition rate of the excitation laser is much higher than the rate of detected photons, since not all the excitation pulses cause a photon event. Having such a low probability of detecting more than one photon per cycle, the TAC overflows and has to be reset every time, i.e. the electronics is uselessly kept busy. To use the electronics at its full capability without decreasing the count rates, it is therefore more convenient to use TCSPC electronics operating in *reverse mode*, with the photon arrival signal as the starting event and the following laser pulse as the stop. The consequence of using this approach is that the measured times are those between a fluorescence photon and the following laser pulse, instead of those between a laser pulse and a corresponding photon event. This can be how-

[13] When the number of photons per excitation cycle are more than one, the system registers the first photon and thus misses the following one. This lead to an over-representation of early photons in the histogram, an effect called pile-up.

[14] Excited molecules embedded in inhomogeneous environment and suffering of quenching processes and other environmental influences can exhibit multi- or even non-exponential decay behavior.

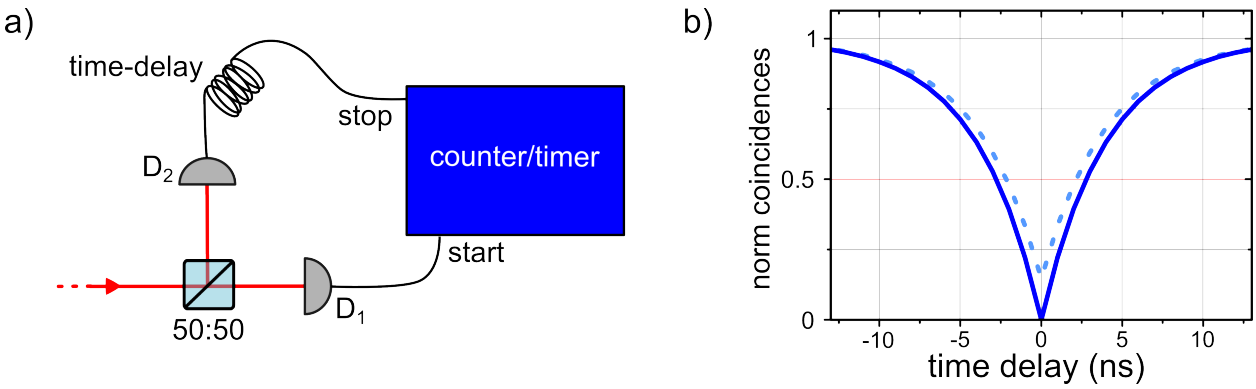

Figure 2.9 – **a)** Schematic diagram of the HBT set-up. Coincidences between counts on the two detectors, D1 and D2, give access to the $g^2(\Delta t)$ correlation function. **b)** Expected g^2-function for and ideal quantum emitter (dark blue line) as processed from the TCSPC. It presents a dip for zero time delay which tends exponentially to its long-time value $g^2(\Delta t \to \infty) = 1$. Experimentally, background photons are responsible for false start-stop measurements, that result in an g^2-function that does not cancel out for zero time-delay (light blue dashed line).

ever circumvented by inserting a long delay cable so that the reference signal arrives at the TAC later than the start pulse from the detector.

With the same operational principle, a TCSPC card coupled to the HBT set-up allows to perform photon correlation experiments and build up the antibunching curve, as discussed hereafter.

2.3.2 Hanbury Brown-Twiss set-up

The HBT set-up consists of two highly efficient photodetectors (two APDs in our case) monitoring the outputs of a 50:50 beamsplitter (**Figure 2.9a**). At the beamsplitter, the incoming photon stream is equally splitted, giving equal detection probability at each detector. Photons impinge on the detectors and the resulting output pulses are fed into the start and stop inputs of the TCSCP module described above, that here records the time delay Δt between the pulses from the two detectors (D1 and D2 in the figure), while simultaneously counting the number of pulses at each input. The result is a histogram that displays the number of events registered at each value of Δt between the start and stop pulses, which approximates the g^2-function at short times. In our experimental configuration, the stop pulses are delayed by 20 ns in order to place the coincidence point in the centre of the recorded time interval, as shown in **Figure 2.9b**.

When the incoming light originates from millions of atoms (as e.g. in a discharge lamp), there is a high probability that the two detectors click simultaneously and photon bunching is observed. In the case of a single quantum emitter, instead, the incoming stream consist

mainly in single photons arriving one at the time. Therefore, a simultaneous click of the two APDs is unlikely and, correspondingly, a strong antibunching dip in the $g^2(\Delta t)$-function is expected.

The obtained distribution of coincidences normalized by the average photon count rate gives the normalized autocorrelation:

$$g^2(\Delta t) = 1 - b\exp\{-|\Delta t|/\gamma\} \tag{2.11}$$

where γ accounts for the excitation and spontaneous emission rates [73] and b is the dip depth, related to the purity as $b = 1 - g^2(0)$.
Ideally, for $\Delta t = 0$ the second-order autocorrelation function is zero, since a single photon Fock-state is generated and hence the probability to detect two photons at the same time vanishes (dark blue line in **Figure 2.9b**). For long time delay Δt, the $g^2(\Delta t)$ function reaches one, indicating that photons are uncorrelated.

If instead light is coming from more than one molecule, coincident emission of photons is likely and will result in an g^2-function that does not cancel out for zero time-delay (light blue dashed line in **Figure 2.9b**). Experimentally, background photons are also responsible for false start-stop measurements, leading to coincidence counts higher than 0 at zero delay and giving rise to a less pronounced antibunching dip. As long as the second-order degree of coherence $g^2(0)$ is less than 0.5 (which ideally corresponds to the detection of two molecules), the fluorescence can be considered as expressed by single emitter [72].

2.4 Optical Characterization of the DBT:Ac System

In this section we present a complete optical characterization of single DBT molecules embedded in anthracene crystals. The measurements here discussed allows to test the experimental set-up and assess the performance of DBT:Ac as a single-photon source. This characterization will build a knowledge of the typical expected values for the experimental observables, representing the reference for what will be discussed in the following chapters.

RT characterization is performed exciting the molecule to a vibrational level of an excited electronic state i.e. with the off-resonant lasers at 767 nm. This pumping configuration requires for spatially well isolated molecules and we hence employ a sample made of DBT molecules in anthracene crystals spin-coated on a coverglass recommended for applications with our oil-objective.

Spectroscopic analysis is instead performed at LT, exciting the resonant 00-ZPL at 785 nm and exploiting the inhomogeneous broadening to spectrally select single DBT molecules. The

sample is made of co-sublimated crystals collected on a sapphire substrate.

Single molecule microscopy

The DBT:Ac spin-coated sample is first imaged on the EM-CCD camera with the white lamp. A big, flat and with well-defined edges Ac crystal is selected on the sample by means of the micrometric manual stage (**Figure 2.10a**). DBT molecules can now be localized with respect to the Ac crystals by means of wide-field fluorescence detection (**Figure 2.10b**).

A high resolution fluorescence scan of the chosen area is shown in **Figure 2.10c**. It is acquired in confocal configuration (typically of 10×10 µm^2, with 0.2 µm-step size and 0.1 s integration time), after precise positioning of the detection pinhole. The bright features in

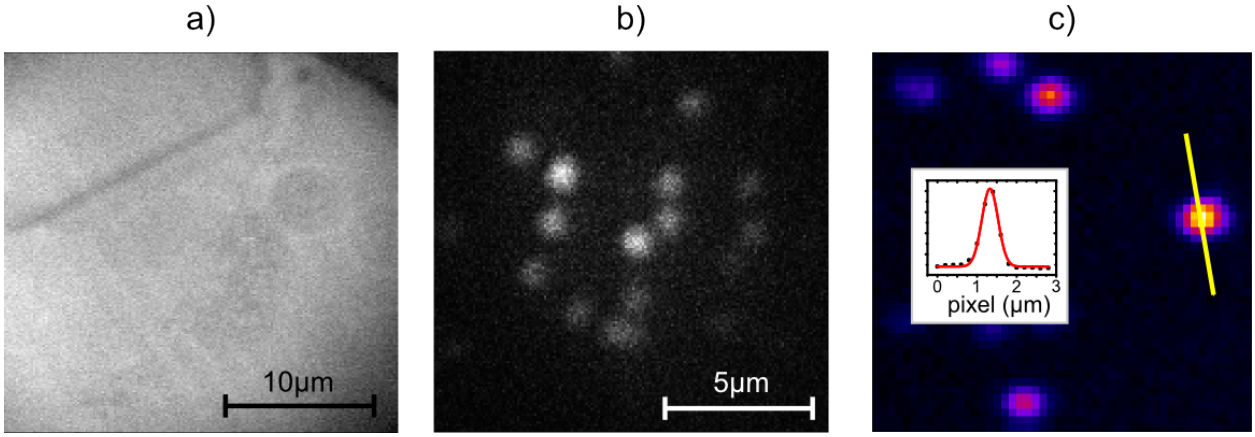

Figure 2.10 – White light **(a)** and wide-field **(b)** EM-CCD images of the same region, allow to check the quality of the fabricated anthracene crystal and to therein localize DBT molecules. **c)**: confocal fluorescence scan on a region of 10×10 µm^2, with 0.2 µm-step size and 0.1 s integration time. The intensity profile along the yellow line drawn across one molecule has a Gaussian shape (inset), with a width of about 0.4 µm, as expected for a 767 nm-confocal spot.

this image are candidate locations for single DBT molecules. Being $\simeq 1$ nm in size, a DBT molecule acts as a point source, and its image reveals the diffraction-limited spot of the excitation beam at the focal plane. The intensity profile along the yellow line drawn across one of the features is plotted in the inset of **Figure 2.10c**. A Gaussian function fitted to this profile has a width of about 0.4 µm, in agreement with the expected confocal spot of a 767 nm-laser (around 0.3 µm). The variation in intensity observed from different spots is attributed to the different depths of single DBT molecules in the anthracene crystal and to their slightly different orientations within the host matrix (and hence to a not efficient alignment of the excitation polarization).

In order to verify that the observed fluorescence stems from individual emitters, molecules are singled out in confocal mode and an antibunching measurement is performed with the

HBT set-up. The polarization of the excitation laser is aligned with the emitter dipole maximizing the photon count rate detected with the APDs by means of the half-wave plate in the excitation line. Figure shows the histogram of the observed coincidences featuring a strong antibunching dip (black line). The experimental data is fitted with equation (2.11), yielding a dip depth $b = 1 - g^2(0) = 93\%$, and hence a purity $g^2(0) = 0.07$.

As discussed in Chapter 1.1.3, photon statistics is critically affected by optical losses and noise, therefore a high signal-to-noise ratio is required to observe a pronounced anti-bunching dip. Indeed, in our case background photons are responsible for false start-stop measurements, leading to coincidence counts higher than 0 at zero delay. For the reported measurement, we have a typical count rate of 300 kcps for the fluorescence signal and 15 kcps for the background noise. Recalling equation (1.21), we find a corrected purity as low as $g^2(0) = 0.02$.

To characterize the brightness of the DBT:Ac system at RT, fluorescence saturation curves from single molecule are recorded, changing the CW 767 nm laser power impinging on the sample by means of neutral density filters. The change in intensity of the background signal due to laser scattering is also measured, revealing the expected linear behavior, as shown in **Figure 2.11c** (blue squares). Here, a typical background-subtracted fluorescence signal (red squares) is plotted as a function of the excitation intensity and fitted with the saturation model given by equation (1.24). The fit-procedure (red line) yields a saturation intensity $I_s = (108 \pm 15)\ \mathrm{kW\,cm^{-2}}$ and a maximum detected rate $R_\infty = (660 \pm 20)$ kcsp, which were typical values considering other DBT molecules analyzed. Since the APD quantum efficiency η_{det} is about 50%, the maximum value of the emitted photon rate is $R_\infty \sim 1.3\,\mathrm{MHz}$. Comparing this value with the theoretical $1/\tau \sim 240\,\mathrm{MHz}$, the detection efficiency of the RT optical set-up described in Section 2.3 is found to be around 0.5%. This low value is ascribed to the limited NA of the optics and their transmission, combined with the expected molecule emission profile. Indeed, the detection efficiency η of the optical set-up can be written as: $\eta = \eta_{\mathrm{det}}\eta_{\mathrm{opt}}\eta_{\mathrm{geom}}$, where $\eta_{\mathrm{opt}} \simeq 10\%$ accounts for the collection efficiency of the optical set-up given by the measured transmissions at 785 nm, and $\eta_{\mathrm{geom}} \simeq 30\%$ is due to the dipole emission pattern and the response function of our objective, whose transmission at 785 nm drops down to 50% at a polar angle of 55° and is around 10% at 67°[15], where is directed most of the radiated power of our on-plane molecule [160].

A single DBT molecule is then excited with the pulsed source in confocal configuration, with an impinging power of 250 µW (about $108\,\mathrm{kW\,cm^{-2}}$ for a 767 nm-diffraction limited spot) and its relaxation dynamics is then recorded by a single APD, coupled to the TCSPC

[15] As discussed in the Supplementary Informations of [160], this result is consistent with the fact that 785 nm is at the edge of the wavelenght working range of our oil-objective.

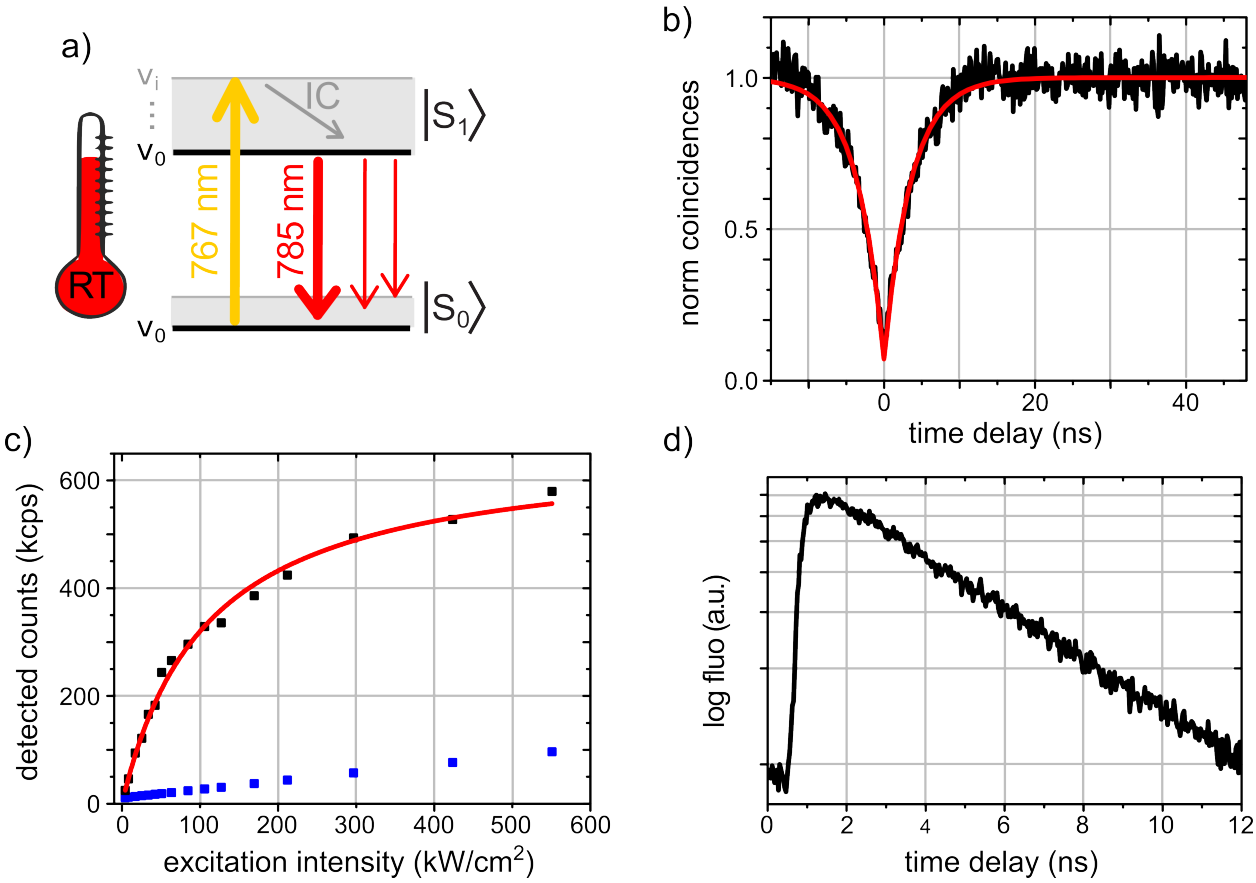

Figure 2.11 – **a)** At room temperature, single molecule microscopy is performed pumping a single DBT molecule into a vibrational state of an electronic excited state (off-resonant pumping at 767nm) and detecting the red-shifted fluorescence originating from the decay to the vibrational modes of the ground state. **b)** Measured photon anti-bunching from a single DBT molecule without any background correction (black curve).The experimental coincidence reduction obtained at zero-time delay yields a background-corrected purity $g^2(0) = 0.02$. **c)** Detected rates for the fluorescence of a single DBT molecule (black squares) and for the background (blue squares), plotted as a function of the excitation intensity. The fitted curve yields a saturation intensity $I_s = (108 \pm 1)5$ kW cm^{-2} and a maximum deteced rate $R_\infty = (660 \pm 20)$ kcsp. **d)** Time-resolved measurement of the fluoresce decay of a single DBT molecule. A single exponential fit yields an excited state lifetime of (4.4 ± 0.1) ns.

unit (20 s acquisition time). A typical recorded fluorescence signal is shown in **Figure 2.11d** and fitted with a single exponential decay, yielding an excited state lifetime of (4.4 ± 0.1) ns, in agreement with literature results.

Single molecule spectroscopy

As discussed in Section 2.1.2, the spectral properties of the DBT:Ac system are strongly dependent on temperature. The non-resonant emission spectrum of DBT molecules in an

Ac co-sublimated crystals detected with the spectrometer is shown in **Figure 2.12a**. The

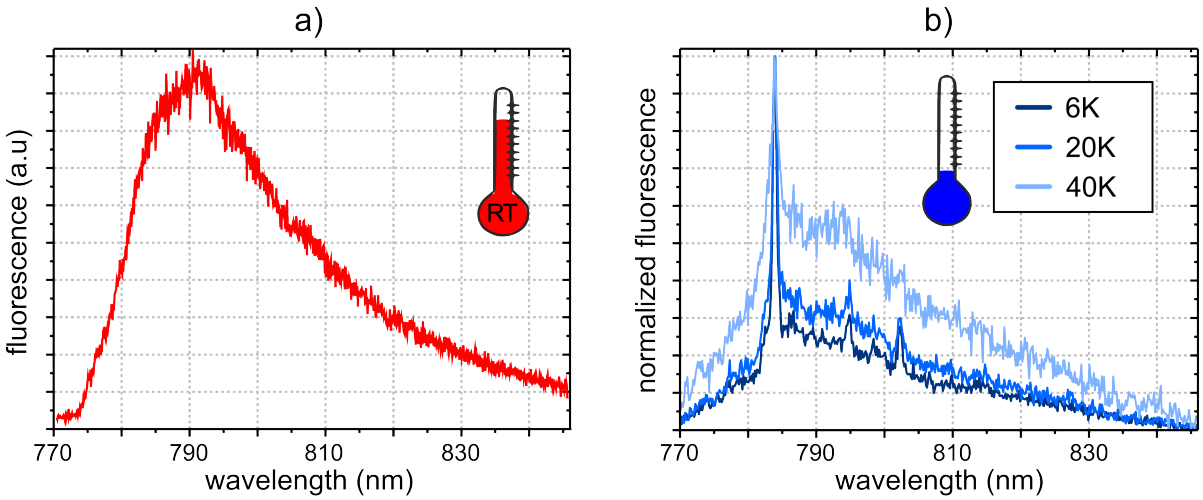

Figure 2.12 – **a)** Non-resonant emission spectrum of DBT molecules in Ac recorded at room temperature, with a width of about 50 nm around 785 nm, owing to the dephasing originating from scattering with the phonon bath of the crystallin matrix. **b)** Non-resonant emission spectra at cryogenic temperatures. Below 40 K, the ZPL and the PSB start to be resolved.

pure optical dephasing originating from scattering with the phonon bath of the crystalline matrix leads to a considerable broadening of the transition, with a width of about 50 nm. At temperatures below 40 K, the ZPL and the PSB start to appear, as demonstrated in **Figure 2.12b**. The resolution of the spectrometer, however, hinders the effective linewidth of the 00-ZPL, expected to reach a lifetime-limited value of about 40 MHz. Indeed, to measure the linewidth of the 00-ZPL, excitation spectroscopy measurements are needed, as discussed later on in this section.

Figure 2.13a shows the wide-field fluorescence image of a DBT:Ac co-sublimated crystals, pumped off-resonance at a temperature of 3 K. The hexagonal shape of the crystal is clearly visible thanks to a guiding effect of light along the crystal perimeter. At cryogenic temperature, photophysical properties of single DBT molecules are studied under resonant excitation, pumping the 00-ZPL at 785 nm and detecting the red-shifted fluorescence. In this scheme (**Figure 2.13b**), single DBT molecules can be addressed spectrally one at a time by tuning a narrow-band laser centered at 785 nm and exploiting the inhomogeneous distribution of their resonances.

During the preliminary step of looking at the sample in wide-field illumination to identify single molecules, we immediately notice a first hint of a strong reduction of the linewidth. Indeed, as the laser excitation frequency is varied over just a few GHz around the central wavelength of 785 nm, we can clearly observe diffraction-limited spots being turned on and

off (**Figure 2.13c**). These spots correspond to single DBT molecules that fluoresce only when the excitation frequency is at resonance with their ZPLs.

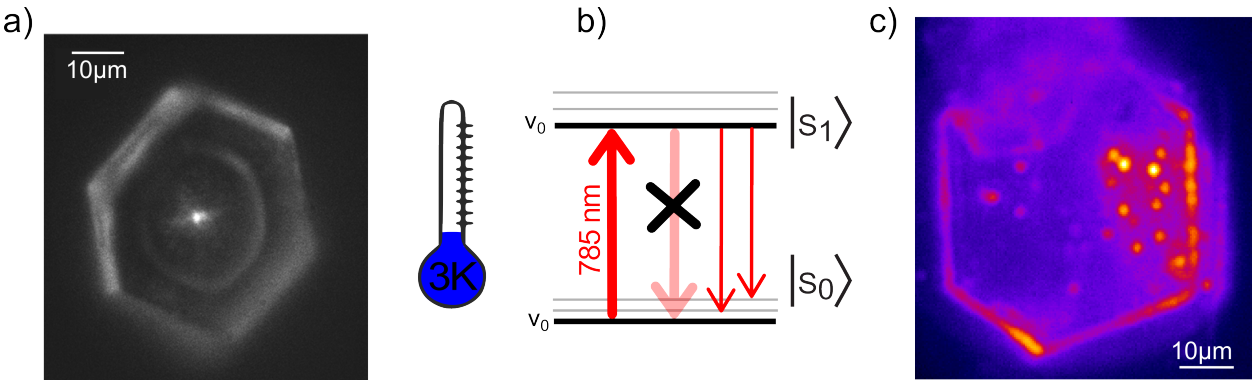

Figure 2.13 – **a)** Fluorescence image in off-resonant wide-field illumination from DBT molecules embedded in a co-sublimated anthracene crystal at 3 K. **b)** At cryogenic temperture we employ a resonant pump scheme, exciting single DBT molecules with the 785 nm-laser. **c)** Fluorescence image in on-resonant wide-field illumination from DBT molecules. This image is obtained from the superposition of 350 frames taken while varying the laser excitation frequency in a 3 GHz range. As the laser frequency is scanned, different single molecules are turned on/off thanks to the inhomogeneous broadening of the narrow 00-ZPL. Animated version available online [176].

In **Figure 2.14a** a total detuning of 1.5 GHz is shown, in which only a single molecule is excited with an intensity below saturation to limit power broadening effects. The line shape of this transition is correctly fitted with a Lorentzian with a linewidth of (50 ± 3) MHz. Repeating this procedure on 22 molecules leads to the distribution displayed in **Figure 2.14b**, showing a low-width cut-off consistent with the lifetime-limited value of 40 MHz. The presence of molecules with broader linewidth is mostly due to saturation effects since, when studying the temporal stability of single DBT fluorescence, we do not observe spectral jumps that are know to contribute to the broadening of the detected 00-ZPL [177].

To verify the absence of spectral diffusion, we study the stability of the 00-ZPL for several molecules, by continuously scanning the excitation frequency of the pump laser around the resonance in a range of 1.2 GHz and recording for about 1 hour their excitation spectra with a single APD. These time traces are plotted as 2D color maps, with time on the vertical axis, the laser frequency on the horizontal axis and the fluorescence intensity coded in the color scale, as first introduced by Moerner and colleagues [147]. In most cases we observe a behavior as the one shown in **Figure 2.14c**, where no spectral jumps and blinking are observed.

Finally, we study the influence of the temperature T on single-molecule lines. Indeed, a line broadening for increasing temperatures is expected due to an increase in the phonon

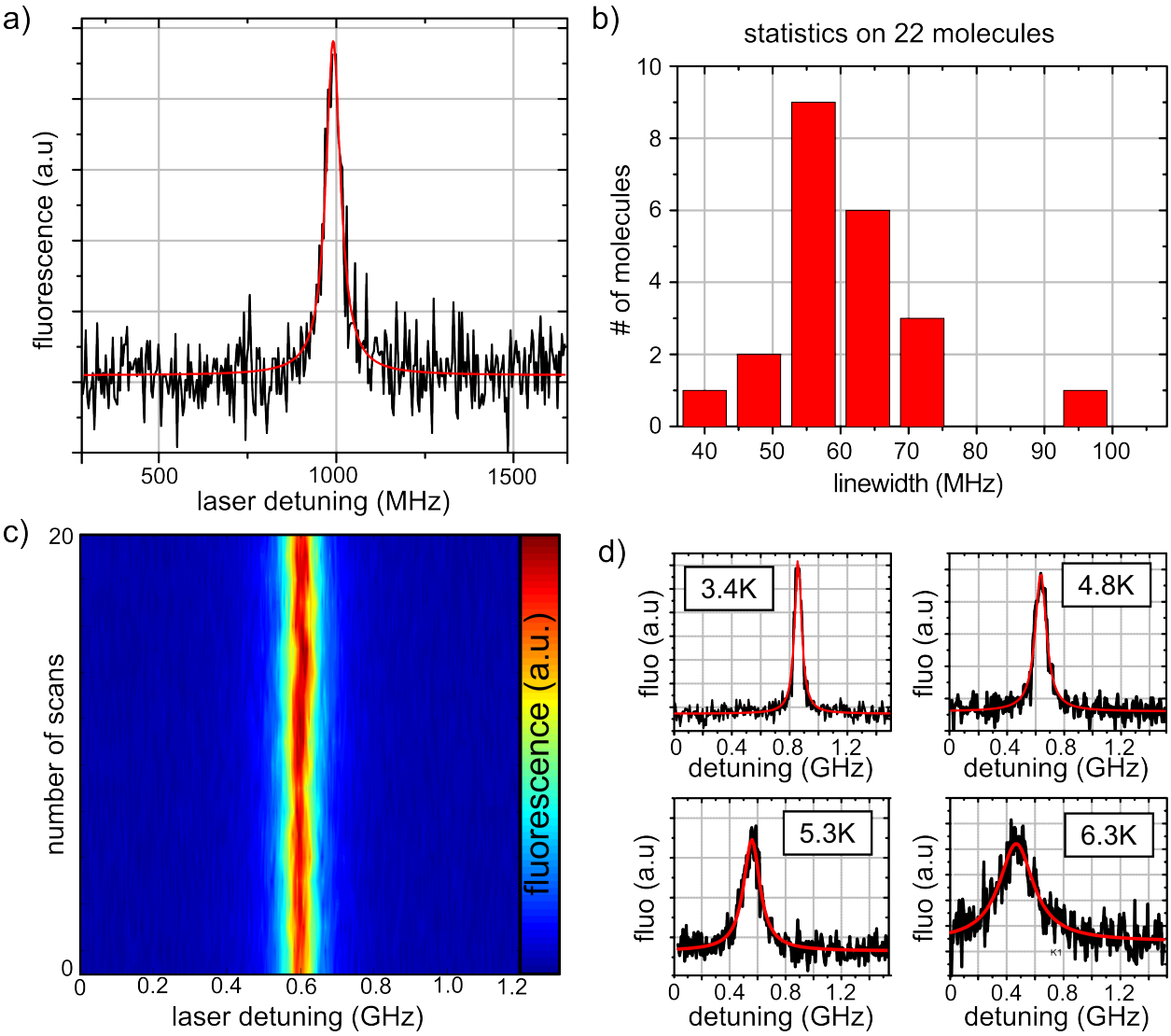

Figure 2.14 – **a)** Resonant excitation spectrum of a single DBT molecule. Fitting a Lorentzian yields a natural linewidth of (50 ± 3) MHz. Repeating this procedure on 21 molecules leads to the distribution displayed in **b)**. **c)** Typical spectral time trace of a single molecule recorded for approximately 1 hour, where no spectral jump are observed. **d)** Linewidth dependence on temperature for DBT molecules in Ac crystal.

population, as stated by the Arrhenius law [178]:

$$\Delta\nu(T) = \Delta\nu_0 + A \exp\left\{-\frac{E_a}{k_B T}\right\} \tag{2.12}$$

where $\Delta\nu_0$ is the line width at zero temperature, k_B is the Boltzmann constant, E_a is the activation energy (equal to the energy of the local phonon) [179] and A is a constant depending on the electron-phonon coupling.

For applications in quantum photonics it is hence important to identify a temperature range of reasonably narrowband emission of the DBT:Ac system. The result of this analysis is shown in **Figure 2.14d** for $T = 3.4, 4.8, 5.3, 6.3$ K for the same molecule resonantly excited with a constant power of 250 nW, which is well below saturation for this specific molecule. The fitting procedure with a Lorentzian line yields the following respective values for the linewidths: (56 ± 2) MHz, (94 ± 4) MHz, (142 ± 7) MHz, (293 ± 9) MHz.

3 Single Molecules Evanescently Coupled to a Nearby Dielectric Waveguide

In this chapter we design, fabricate and experimentally characterize the evanescent coupling between the DBT:Ac system and a rectangular waveguide made of silicon nitride. Room temperature measurements on this hybrid device demonstrate a molecule-to-waveguide coupling efficiency β up to $(42 \pm 2)\%$ for molecules in close proximity of the guiding structure. Moreover, measurements of the second-order autocorrelation function show a low multi-photon probability inside the waveguide. The content of this chapter results from a fruitful collaborative project with the groups of Pr. Wolfram Pernice (Universität Münster, Germany) and Pr. Oliver Benson (Humboldt Universität zu Berlin, Germany) and was published in 2017 in ACS Photonics [42].

3.1 Background and Motivations

The theoretical analysis presented in Chapter 1.2 shows that enhancement and control of light-matter interaction can be achieved placing a quantum emitter in the strong evanescent field of optical dielectric waveguides on-chip. More in general, by decreasing the mode area of the interacting light field, a significant overlap between the absorption cross-section of the emitter and the guided light field is realized, which guarantees efficient collection and routing of the emitted photons. Versatile platforms to achieve such a small mode area of the light field are e.g. optical nanofibers [180] or integrated photonic platforms [181]. To this date, coupling efficiencies β up to 98% have been measured in hybrid systems made of QDs coupled to photonic crystals waveguides [182], but it remains a challenge to efficiently out-couple the guided photons into e.g. an optical fiber. This, in fact, limits the overall source efficiency to values around 10-15% [183].

In this context, the building block is made of a single-photon source and a detector con-

nected by an optical mode of a light guiding structure. Once verified that this integrated platform can be efficiently implemented, it is possible to add different stages of interaction with other system to achieve different functionalities, exploiting quantum optical effects on-chip. The realization of such device can be separated into three main steps.
Firstly, a quantum emitter with intrinsic bright and stable single-photon emission is chosen, accounting for the probability with which efficient coupling to a waveguide can be practically realized. We have shown in Chapter 2 that DBT molecules in Ac crystals, with their long-term photostability and almost unitary QY, are bright sources of single photons at room temperature and can be easily fabricated in few tens-of nanometer thin film, making them particularly promising for the coupling to evanescent fields in the proximity of surfaces.

Second, a guiding structure is designed to simultaneously achieve a strong mode confinement and low loss along the propagation. These features are achievable in high refractive index dielectric waveguides (WGs), with geometrical parameters optimized to be single mode for a specific working wavelength and to have a strong evanescent field in the range of positions the emitter can achieve once placed on the WG surface.

Finally, a structure that efficiently couple the guided photons to another quantum system or an external photo-detector has to be implemented. Such interfaces should exhibit high coupling efficiencies and, fabrication-wise, it is also advantageous to integrate them along with the waveguiding structures.

In this chapter, we demonstrate the potential of a hybrid technology made of single DBT molecules in Ac thin crystals and dielectric chips, consisting of rectangular WGs and grating far-field couplers made of silicon nitride. In Section 3.2 we present the design of a single-mode rectangular WG operating at 785 nm with grating optimized to support a Gaussian-like mode in free space, both fabricated in a single lithographic process. The single-photon source is placed onto the WG-structured photonic chip by spin-coating the DBT:Ac solution with the procedure described in Chapter 2.1.3, that provides crystals of optimal thickness for efficient evanescent coupling to the WG, as demonstrated by numerical simulations. In Section 3.3, we first briefly present the fabrication of the photonic chip, carried on at the laboratory of Pr. Wolfram Pernice. Experimental investigation at room temperature performed in our laboratories in LENS (European Laboratory for Non Linear Spectroscopy) and in the Department of Physics of the University of Florence, are then discussed (Section 3.4).

3.2 Design of the Photonic Chip

3.2.1 Mode profile of the rectangular cross-section waveguide

The WGs are fabricated on top of a glass dice ($n_{\text{glass}} = 1.51$) for optical access and are made of silicon nitride (Si_3N_4), a well characterized dielectric material with a relatively high refractive index ($n_{Si_3N_4} = 2$) and a wide optical bandgap, providing broadband optical transparency in the entire visible range and up to the near infrared. Moreover, Si_3N_4 is compatible with CMOS-based processes for low-cost mass fabrication and we observe no autofluorescence and no Raman peaks around 785 nm, which is crucial for sensitive experiments on the single-photon level.

The WG is left uncovered in order to couple light from the DBT:Ac system placed on the WG surface. The cross-section has a rectangular shape, which is the natural result of a top-down lithographic processes, allowing to fabricate WGs with almost arbitrary size parameters a_x and a_y, the hight and the width respectively. The geometric parameters of the WG are optimized for single-mode operation at 785 nm and in order to maximize the electric field of this fundamental mode at the position of the emitter, i.e. to enable efficient coupling of the emitter's emission into the WG. This optimization procedure is performed with the Mode Solver from Comsol, which allows to calculate the modes (i.e. their field distributions and the effective refractive index $n_{\text{eff},m}$) supported by a WG with specific geometric parameters for a certain wavelength (see Chapter 1.2.3).

The evanescent electric field at the core-air interface is first maximized by reducing the height a_x of the WG. The width a_y is then chosen to feature the first-order mode cut-off far from the spectral range of the emitter's emission of about 50 nm around at 785 nm at room temperature (see Chapter 2.4). This procedure yields the optimal values $a_x = 175$ nm and $a_y = 500$ nm.

Figure 3.1a illustrates the geometry of the design and **Figure 3.1b** shows the normalized intensity distribution of the fundamental quasi-TE mode. Because of the asymmetric cladding configuration, the quasi-TE mode is shifted into the substrate.

This predominantly horizontally polarized mode features an electric field which is strongest inside the core, with evanescent tails in the claddings as well as at the sides. Referring to the mode profile along y at $x = 0$, plotted below the color map in **Figure 3.1b**, we can observe a jump in the intensity of the electric field (specifically of the y-component of the field), due to the continuity relations occurring at the dielectric interfaces on the left and right sides of the WG. This means that the mode is dominantly on the y-direction.

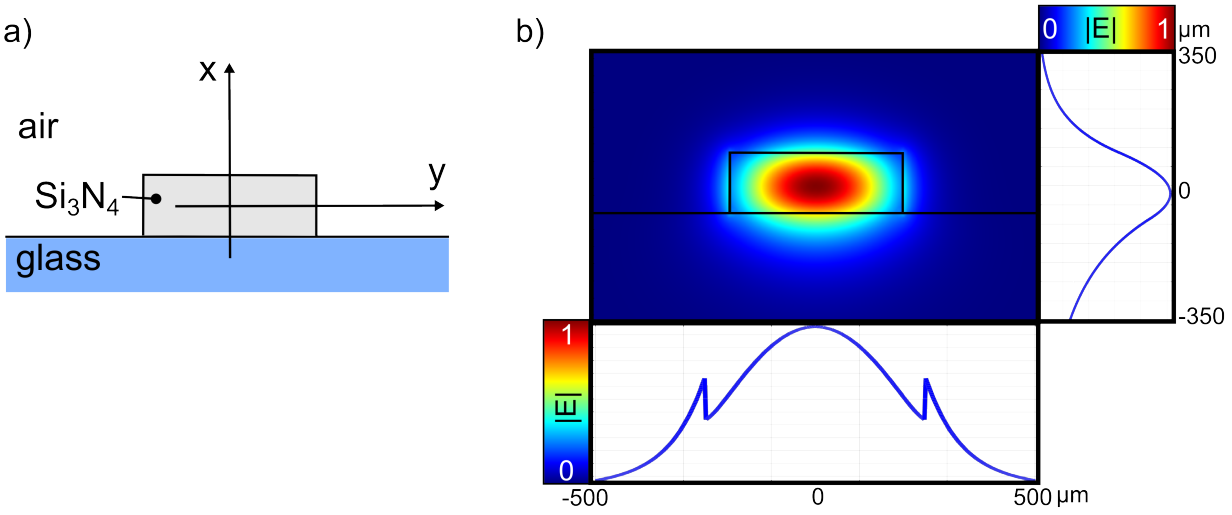

Figure 3.1 – **a)** Geometry of the silicon nitride Si_3N_4 ($n_{Si_3N_4} = 2$) waveguide on a glass substrate ($n_{glass} = 1.51$) resulting from the optimization procedure that yields a height $a_x = 175$ nm and a width $a_y = 500$ nm. **b)** 2D color-coded plot of the normalized electric field intensity of the quasi-TE fundamental mode, which is the only one supported by the waveguide at 785 nm. Central cuts through the mode profile at $y = 0$ and $x = 0$ are plotted on the right and below the color map, respectively.

3.2.2 Dipole coupling efficiency estimation

As introduced in Chapter 1.2.2, the key figures of merit for an integrated single-photon source is the emitter-WG coupling efficiency β and the emission enhancement α. In order to estimate the molecule-to-WG coupling efficiency (β_{sim}), we perform 3D numerical simulation using the commercial software Comsol Multiphysics to compute the electromagnetic field excited by a dipolar source embedded in an anthracene matrix into the nearby dielectric WG.

The simulated device is sketched in **Figure 3.2a**, assuming a free space wavelength $\lambda = 785$ nm. We consider the simplest geometry for the DBT:Ac spin-coated crystal, modeled as a parallelepiped placed on top of the WG, with height h and width equal to that of the WG (500 nm). The emitter is placed inside the anthracene crystal at a distance d_x from the WG top surface, and is modeled as a linear harmonic current of length $l = 1$ nm oriented along the y-axes (white arrow in **Figure 3.2a**), with an associated dipole moment of $D = (iI_0l/\omega)\hat{y}$. This orientation is parallel to the most prominent field component of the only guided mode. To model an infinitely long WG, the spatial domain of interest is properly terminated with PMLs that absorb the outgoing electromagnetic waves with negligible reflection (see Chapter 1.2.3).

The symmetry of the system allows to divide the simulation domain in half, using a

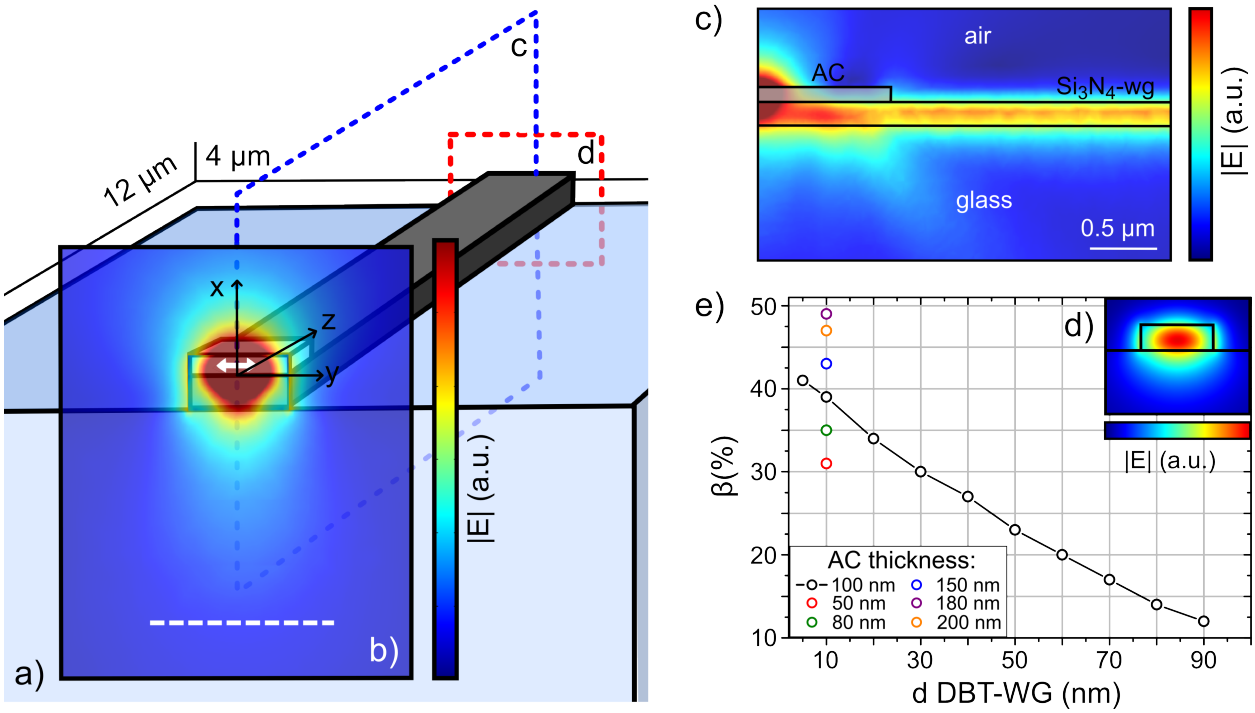

Figure 3.2 – **a)** Layout of the 3D numerical simulations displaying half of the waveguide total length (24 µm). A dipolar emitter (white arrow) mimicking a single molecule is placed in a 100-nm-thick Ac crystal ($n_{\mathrm{Ac}} = 1.8$). **b)** Plot of the normalized electric field on the plane containing the dipole. The dashed white line represents the objective acceptance angle. Panels **c)** and **d)** display the normalized electric field in the two respective waveguide sections. **e)** Coupling efficiency into the waeguide mode reported as a function of the dipole distance to the waveguide top surface (black dots) and for different crystal thicknesses (colored dots).

perfect magnetic conductor (PMC) as a boundary condition on the vertical plane containing the emitter and orthogonal to the direction of propagation z. The size of the obtained simulation domain is of the order of $300\lambda^3$ and is meshed non-uniformly with smaller element sizes of approximately $\lambda/300$ in the dipole neighborhood.

The β-factor is calculated as the Poynting vector flux through a section containing 98% of the guided mode (the detected area being the one depicted in **Figure 3.2d**) and placed at the end of the WG in the simulation domain. This value is then normalized with the total radiated power given by the power flow through a volume containing the emitter.

Experimentally, molecules' position and orientation within the Ac crystal is unknown a priori, and spin-coating on the structured chip can give rise to a wider distribution of Ac thickness than for the case of a flat substrate. To account for this variability and understand the experimental results, we perform numerical simulations to estimate the range of values of the molecule-to-WG coupling efficiency β_{sim} achievable on our device, as a function of the anthracene thickness (h) and the dipole position, in terms of its distance to the WG surface

(d_x) and its horizontal displacement with respect to the center of the WG (d_y).

We start analyzing β_{sim} as a function of the dipole distance to the WG top surface d_x for a fixed value of the Ac thickness $h = 100$ nm and emitter lateral displacement $d_y = 0$, i.e. at the center of the WG. This is plotted in **Figure 3.2e** as black dots. As expected, the coupling efficiency β_{sim} increases for decreasing d_y, reaching a maximum value around 40% for $d_x = 10$ nm. In panels **b**, **c** and **d** of **Figure 3.2** we report the normalized electric field in three sections of the simulation domain, as marked in the cartoon, for $d_x = 10$ nm.

In the same graph in **Figure 3.2e**, we plot in color dots the variation of β_{sim} with the Ac thickness h, varied within the experimentally estimated range, for a dipole at $(d_x, d_y) = (10, 0)$nm. This result is also shown in **Figure 3.3a** for convenience. Here we can observe that β_{sim} shows its maximum for a thickness of 180 nm. For larger h it starts diminishing due to interference effects, as observed also in [184].

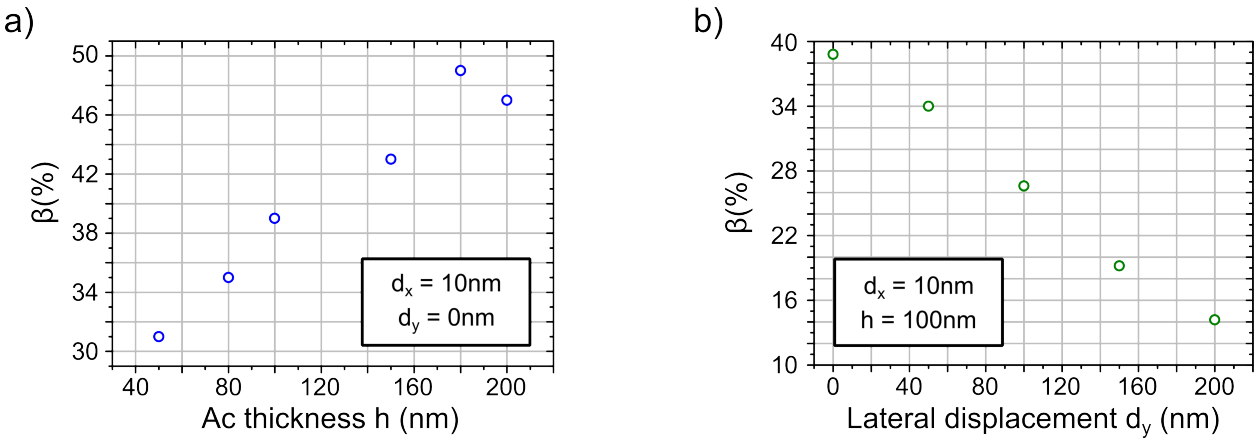

Figure 3.3 – Simulation results for the coupling efficiency β_{sim} for several thicknesses (h) of the Ac spin-coated crystal within the experimentally estimated range **(a)** and lateral displacement (d_y) of the molecule **(b)**. The emitter position is here fixed at $d_x = 10$ nm from the waveguide top surface.

Finally, we study the dependence of β_{sim} with the dipole horizontal position, for $h = 100$ nm and $d_x = 10$ nm. As expected β_{sim} decreases as the dipole gets farther from the maximum of the guided mode.

In order to estimate the enhancement factor α, the same simulation domain is converted into a homogeneous medium by simply setting the refractive indices of all subdomains equal to that of Ac. We note that the total radiated power calculated from simulations when the molecule is in close proximity to the WG with respect to the power emitted by the DBT molecules in a homogeneous volume of Ac has a variation of only 10% towards higher values. This suggests that the attained β-factor should be interpreted as a redistribution of the emission into the guided mode of the field otherwise radiated at high polar angles in

the glass substrate. Hence, we expect to measure no relevant variation in the fluorescence lifetime with respect to the reference value of 4.2 ns.

3.2.3 Mode conversion with Bragg mirrors out-couplers

To efficiently couple light in and out from the chip is crucial for single-photon processing, which requires high signal-to-noise ratio to be implemented. This task is in general non trivial since it requires coupling structures capable to overcome differences in effective index and asymmetry of two modes with intensity profiles different in shape and size. For this purpose, various techniques have been developed to achieve a high coupling efficiency, large band-width and large tolerances to alignment errors [133].

In our experiment, we employ focusing grating couplers as described in references [185, 186] and illustrated in **Figure 3.4a.** The gratings are fully etched, buried in a 760 nm-thick hydrogen silsequioxane (HSQ, $n_{\mathrm{HSQ}} = 1.4$) with a 120 nm-thick gold mirror on top to enhance directionality. These coupling devices are alignement-free and have the advantage to be manufactured in the same lithographic steps of the device. The HSQ cladding reduces the scattering strength of the single grating element and prevents the formation of Ac crystals in the coupler areas.

For our device, the grating couplers are designed so as to obtain maximum out-coupling efficiency, fulfill mode-matching with a gaussian-like mode (affordable with the resonant laser) and allow imaging of the whole device in the same field of view (around 100 µm diameter). Starting from the latter requirement, we minimized both WG tapering length and grating coupler size. In particular, shortening the tapered section down to few µm requires the introduction of bent grooves so as to match the rapidly expanding phase front from the guided mode with the one (almost flat) of the free-space gaussian mode.

The geometrical parameters are then optimized maximizing the output coupling from the guided mode to free space by means of 2D[1] finite-element simulations with Comsol, with a model sketched in **Figure 3.4b** that corresponds to the lateral view of the grating coupler along the propagation axis.

A line source (1) is placed inside the Si_3N_4 WG (2), which is set long enough to select the guided part of the radiation; artificial absorbers are also placed to dump uncoupled light (3). The coupler structure is then composed by a gold layer (4) on top of the buffer HSQ layer (5) that represents a cladding for the grating. Regions (6) and (7) correspond to air

[1] A 2D representation for the couplers is indeed effective since, after tapering, the WG is more than 3 µm wide, and the effects of the lateral confinement with respect to the bulk medium are negligible (change in the effective refractive index $< 0.5\%$)

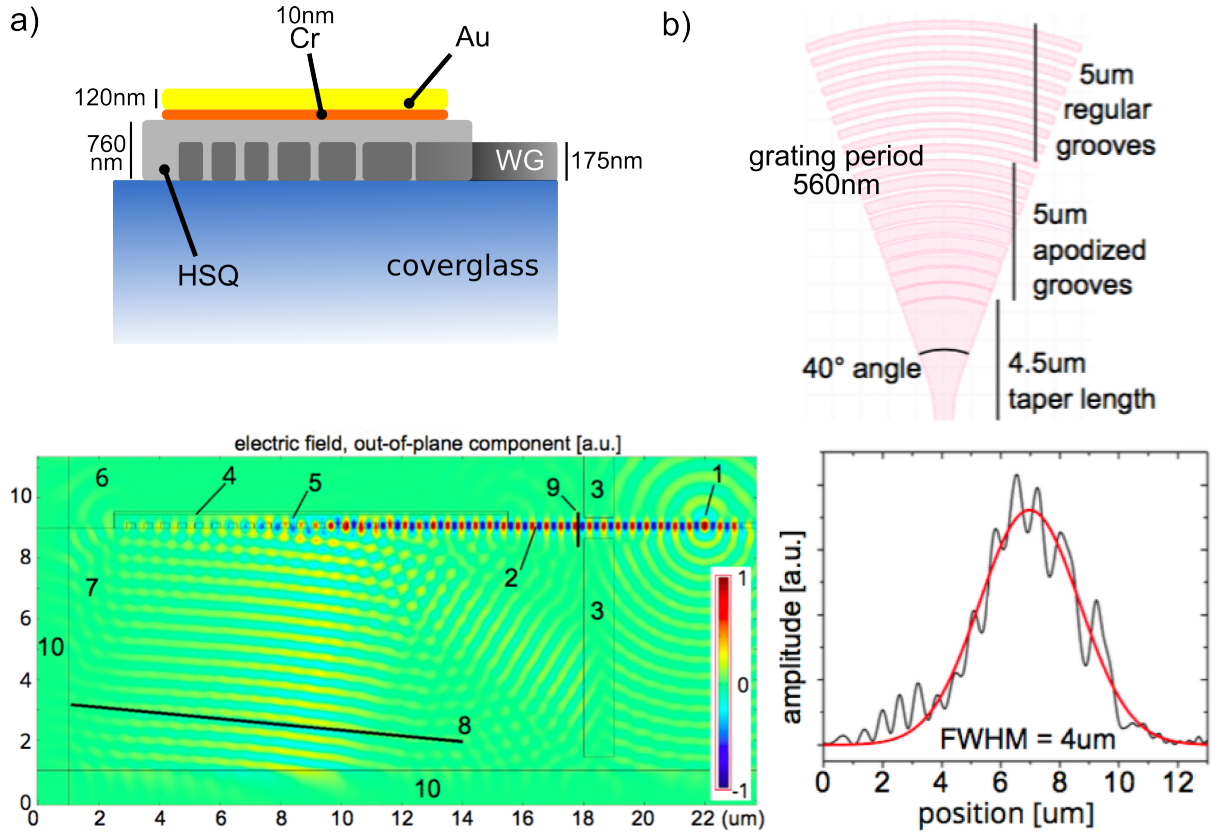

Figure 3.4 – **a)** Sketch of the lateral view of the focusing grating couplers: they are fully etched in the same lithographic step of the Si_3N_4 waveguide, buried in a 760 nm-thick hydrogen silsequioxane (HSQ, $n_{HSQ} = 1.4$) with a 120 nm-thick gold mirror on top to enhance directionality, with 10 nm-thick chromium layer to guarantee adhesion of gold. **b)** Geometry of the couplers resulting from the optimization procedure: grooves width 280 nm (regular series) and 50-50-65-80-95-120-150-180-180 nm (apodized series). **c)** 2D simulation model used for the grating's geometrical parameters optimization. The color plot corresponds to the out-of-plane component of the electric field distribution in the case of 89% coupling efficiency. The guided mode is pumped by a line source (1), and the amount of light directed toward the output direction after scattering on the grating region (5) is evaluated as the energy flux through the detector line (8). **d)** Simulated intensity profile of the output beam (flux through the output detector (8)) for the fabricated gratings (black solid line) and gaussian fit to it (red solid line).

and glass substrate, respectively. The domain of simulation is terminated with PMLs(10) to avoid un-physical reflections. The coupling efficiency η_c is finally calculated as the ratio between the power flow through the output detector (8) and the reference detector (9).

The output of our optimization procedure is a grating coupler composed of 18 grooves, with the 9 closer to the guide following an apodization recipe and the others keeping a constant filling factor (Si_3N_4 portion of a period) between 50% and 65% (see caption of Figure 3.4a for all geometrical parameters). The grating period is optimized to match the

central emission wavelength of DBT around 785 nm under an angle θ of about 8° through the glass substrate. This angle is enough to suppress reflections into the WG due to second order Bragg scattering, and at the same time keeps the beam well within the NA of the objective.

Constructive interference from the 120 nm-thick gold mirror towards the glass is achieved with a layer of HSQ of 710 nm. The maximal coupling obtained in simulations reaches 90%. However, the parameters of the fabricated structures slightly deviate from the optimal ones. In fact, in order to obtain more robust performances, 10 nm layer of chromium are added on top of the buffer HSQ layer to guarantee adhesion of the gold mirror. Accounting for this additional layer, the expected coupling efficiency η_c is reduced to 60%. Moreover, the fabricated HSQ layer is 760 nm thick, representing the most limiting factor on the performances of our coupling devices.

In order to match the free space output mode with the laser quasi-Gaussian profile (with a measured FWHM $\simeq 4\,\mu$m), we set a tapering length of 4.5 µm (to match the longitudinal profile of the input beam in free space) and act on the apodization recipe to maximize the symmetry of the transverse profile. The results of this procedure is shown in Figure 3.4d, where the simulated intensity profile (power flow) through the output detector (8) is well described by a gaussian fit with FWHM = 4 µm.

Experimentally, the matching between the electric field distributions of the mode diffracted by the grating out-coupler (E_1) and the Gaussian laser beam (E_2) can be calculated with the integral overlap:

$$\eta_{\text{ov}} = \frac{|\int (E_1^* \cdot E_2)\mathrm{d}A|^2}{\int |E_1|^2 \mathrm{d}A \int |E_2|^2 \mathrm{d}A} \tag{3.1}$$

where A is the surface at which modes are calculated.

3.3 Fabrication of the Silicon Nitride-on-Glass Photonic Device

The Si_3N_4-nanophotonic devices are fabricated in the lab of Prof. Pernice, from 175 nm stoichiometric Si_3N_4 grown via LPCVD on top of 500 µm glass substrate. These films contain high tensile stress, yielding a measured refractive index of $n_{Si_3N_4} = 2.00 \pm 0.02$. The fabrication of the device is performed by three steps of electron-beam lithography (EBL) followed by reactive ion etching. In the first lithography step the nanophotonic circuits are defined using *ma-N 2403* negative tone electron-beam resist. The unexposed *ma-N 2403* is washed

away by the developer *MF-319* and the WGs are then fully dry-etched into the Si_3N_4 layer using a CHF_3/O_2 plasma.

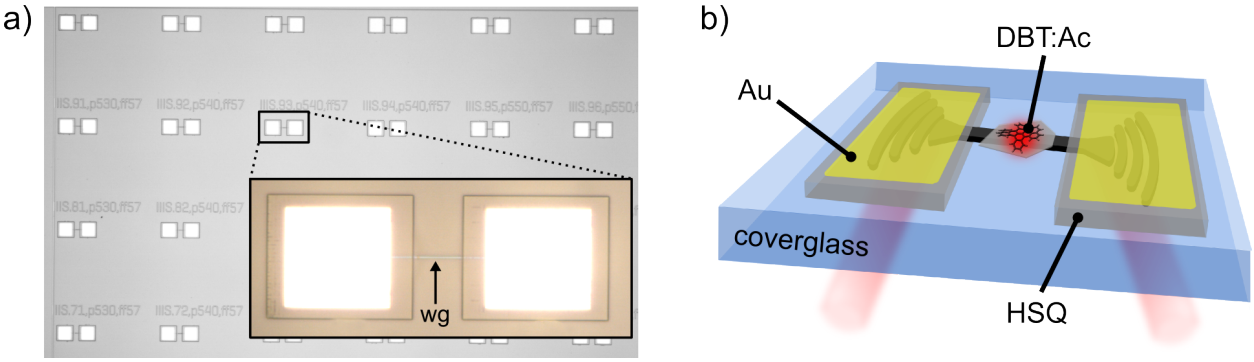

Figure 3.5 – **a)** Optical micrograph of the fabricated nanophotonic device containing several guiding structures, where the gold mirrors highlight the coupler regions. **b)** Cartoon of the device showing the Si_3N_4 waveguide with two focusing grating outcouplers, coated with HSQ and gold. A single molecule embedded in a thin anthracene crystal lying on top of the bare waveguide region emits a train of guided single photons that are sent in the far-field through the grating, optimized to redirect the guided single-photon emission through the glass in a quasi-Gaussian mode.

The gratings, with the geometry discussed in the previous section, are fully-etched as described above together with the WGs. The buffer layer of HSQ is then spin-coated on the chip and reshaped by a second EBL step. The last lithographic step defines the areas of the gold mirrors on top of the couplers, using PMMA resist with a thickness of 850 nm. Gold mirrors are realized by e-beam deposition of a 10 nm Cr adhesion layer and 120 nm of Au, followed by lift-off in acetone.

Figure 3.5a shows a typical fabricated chip containing several devices, each with a size of about 50 nm. A zoom on a single structure allows to identify the 500 nm-wide WG between the bright gold mirrors that highlight the coupler regions. The hybrid device is completed by drop-casting the DBT:Ac solution onto the WG-structured photonic chip, mounted on the rapidly spinning plate of the spin-coater according to the protocol described in Chapter 2.1.3. The concept of the obtained device is skecthed in **Figure 3.5b**.

3.4 Experimental Results

3.4.1 Set-up modification

The experimental set-up described in Chapter 2.3, is here equipped with a 50x air objective (N.A.=0.55) to achieve a field of view of about 100 µm diameter and thus allowing imaging of the whole device onto the EM-CCD camera. In order to couple light into the grating

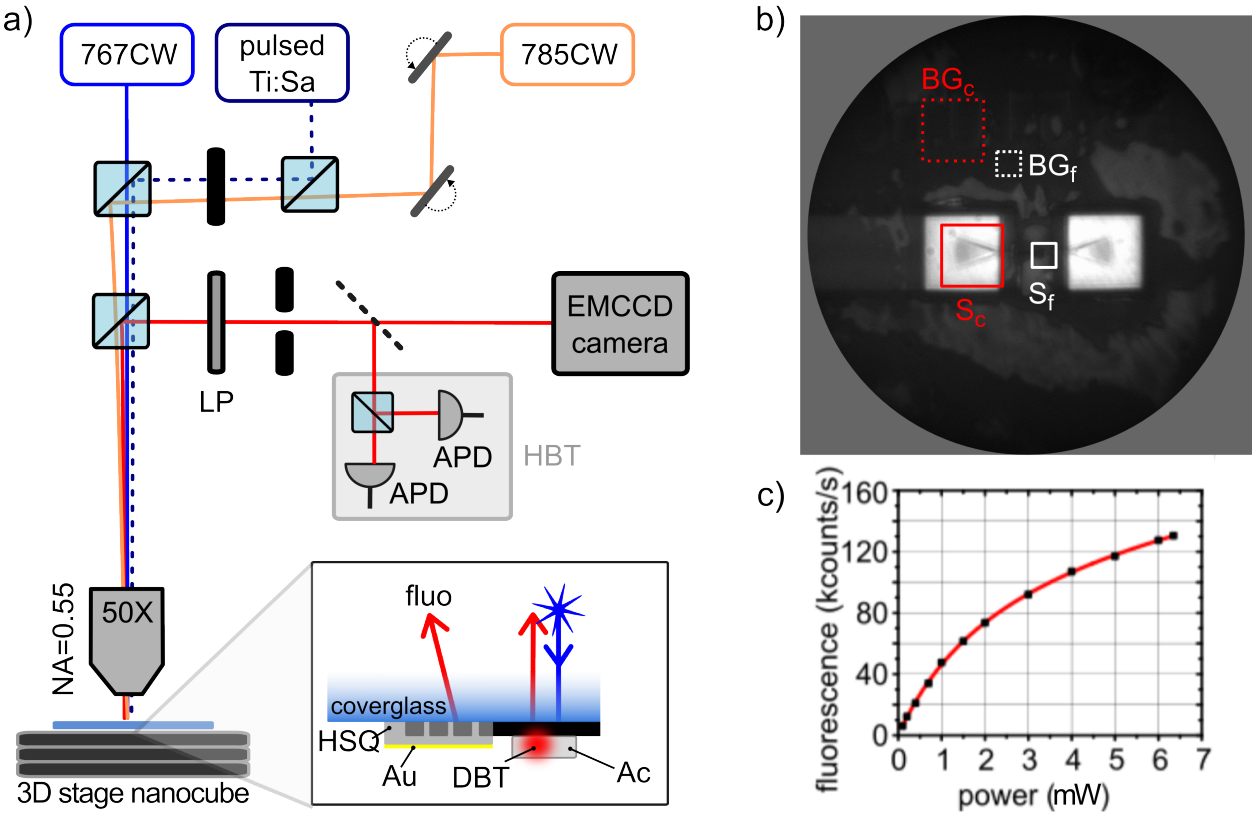

Figure 3.6 – **a)** The experimental set-up presented in Chapter 2.3 is here equipped with a 50X air objective and is used as a two-channel confocal-microscope implemented to focus at the same time both the off-resonant excitation beam (767 nm) through the substrate onto the waveguide area and the resonant reference laser (785 nm) onto one of the grating couplers under the optimal angle. **b)** The 100 µm-diameter area imaged on the camera, showing the white light image of one fabricated device. DBT:Ac spin-coated crystals (light grey islands) are randomly distributed in the waveguide region: note that no crystals are formed on the couplers area (thanks to the presence of the HSQ buffer layer), while a small portion of it covers part of the waveguide. White and red squares approximately indicate the areas from which light is collected in the experiments, upon background correction (corresponding to the counts collected from the corresponding dashed squares far from the device). **c)** Typical saturation curve of molecules far from the device, from which we extract a saturation power of (2.5 ± 0.3) mW and a maximum detected rate of $R_\infty = 160$ kcps.

couplers with the proper angle, we insert in the excitation path two additional adjustable mirrors to "walk the beam", i.e. to focus the laser spot with a specific angle on the sample as schematically shown in **Figure 3.6a**. This configuration is know as two-channel confocal-microscope and allows to focus at the same time both the off-resonant excitation beam (767 nm) through the substrate onto the WG area and the resonant reference laser (785 nm) onto one of the grating couplers under the optimal angle, and is used for APDs alignment

and throughput measurements (see Sections 3.4.3 and 3.4.4).

A typical white light image of the sample under investigation (spin-coated DBT:Ac crystals on a WG-coupler device, addressed from air through the glass substrate) is shown in **Figure 3.6b**. The red square around the coupler represents an approximation of the area considered to detect the guided light (labeled in the text as S_c and given by the sum of counts from all the considered pixels) in all measurements performed with the EM-CCD camera, corrected for background counts (BG_c) collected from an area of the same size far from the device (dashed red area). In a similar way, the white square area indicates the area considered for the fluorescence signal emitted by the molecule in free space S_f (with corresponding BG_f integrated from the white dashed square). For measurements performed with the APDs, instead, spatial selection of the areas of interest and their respective backgrounds is done by inserting pinholes with proper size in detection, while properly shifting the sample with the three-axis piezo-positioner: signal and background counts are labeled hereafter in the text with a tilde ($\tilde{S}_c$, etc...).

In order to determine the saturation parameter and the collection efficiency of the set-up, we perform saturation measurements on DBT molecules located far from any photonic structure. A typical example of the collected count rate as a function of the excitation power is shown in **Figure 3.6c** (black dots) together with the fitting function (1.24), from which we extract a saturation power of (2.5±0.3) mW. All measurements on single molecules presented hereafter are performed well below saturation at about (0.5 ± 0.1) mW, as it represents a good compromise between working with a reasonable S/N and minimazing probability of photobleaching.

The maximum detected rate is found to be $R_\infty = 160$ kcps. Lifetime measurement yields the typical average value of 4.4 ns, which allows to estimate the overall collection efficiency as $R_\infty/\tau \simeq 0.4$ ‰.

3.4.2 Waveguide transmission

Before spincoating the DBT:Ac system, the bare WG-coupler devices (whose typical white light image is shown on top of **Figure 3.7a**) are pre-characterized measuring the off-chip coupling and the transmission of the grating couplers.

The out-coupling efficiency of each WG on the chip is estimated with transmission measurements, focusing the resonant laser at 785 nm into one of the couplers and collecting the out-coupled light with the EM-CCD camera (without longpass filter), upon optimization of the incident angle (as sketched in the bottom of **Figure 3.7a**). Counts integrated over the out-coupler area (i.e. S_c referring to **Figure 3.6b**) are normalized with those integrated in

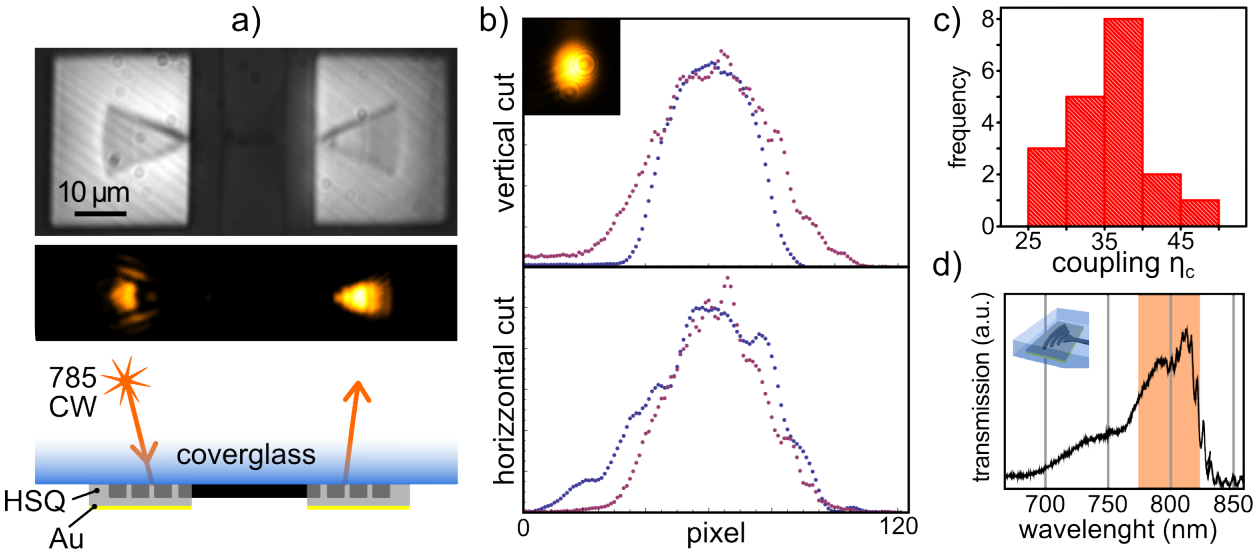

Figure 3.7 – **a)** From top, typical white light image of an empty device and the corresponding signal detected from the EM-CCD camera upon excitation according to the scheme sketched below. **b)** The out-coupler spot profile in a) is compared with the EM-CCD image of reflection of the laser beam on the silver mirror (shown in the inset). Vertical and horizontal line-cuts from the two images suggests a good mode matching between light diffracted by the grating and the Gaussian laser mode, as confirmed by numerical evaluation of the overlap integral, yielding values close to 0.9. **c)** Distribution of the out-coupling efficiencies with an average value $\eta_c = (35 \pm 5)\%$. **d)** Transmission spectrum of the couplers showing a 50 nm-broadband operation around the DBT:Ac fluorescence window (orange-shaded area).

an area with the same size and containing the laser spot reflected from a silver mirror. Both values are corrected for the background, corresponding to the average counts collected from an area with the same size but far from the out-coupler and the laser spot respectively.

The square root of this value corresponds to the single coupler efficiency, which is found to have an average value of $\eta_c = (35 \pm 5)\%$ (see histogram in **Figure 3.7c**). The discrepancy between this value and the 60% derived from simulations is attributed to a non-optimal HSQ thickness in the fabricated chips.

To verify that our grating design is effectively optimized to support a Gaussian mode in free space with a FWHM $\simeq$ 4 µm, we compare the out-coupler spot profile with the reflection of the laser beam on the silver mirror, as imaged in transmission measurements (inset in **Figure 3.7b**). Vertical and horizontal line-cuts from EM-CCD images are plot in **Figure 3.7b**. The numerical evaluation of the overlap integral in equation 3.1 between the two spots yields values close to 0.9.

Finally we measure the couplers' transmission spectrum, focusing the white light on one coupler and analyzing with the spectrometer the signal collected from the other one. The result, displayed in **Figure 3.7d**, demonstrates that our WG-coupler device has a broadband

operation (bandwidth of about 50 nm) around the DBT:Ac fluorescence window (orange-shaded area).

The propagation loss of the WG is determined by measuring the transmission through devices with WGs of different lengths fabricated on the same chip. This measurement, performed in the laboratory of Prof. Pernice, yields a propagation loss of 0.49 dB/mm.

3.4.3 Qualitative investigation of the coupling

A 20 µL amount of the DBT:Ac solution is now spin-coated onto the pre-characterized photonic chip as described in Chapter 2.1.3, forming DBT:Ac crystals with expected thickness below 100 nm. The result of this procedure is then examined by white light images demonstrating that about 40% of the devices are successfully covered with Ac. An example is shown in **Figure 3.8a** and **b** and labeled for convenience as device 1: we can see from its white light image that just a tiny portion of the crystal covers the WG central region. Switching to 767 nm-wide field illumination, we observe that 1/3 of the covered devices show fluorescing molecules close to the WG.

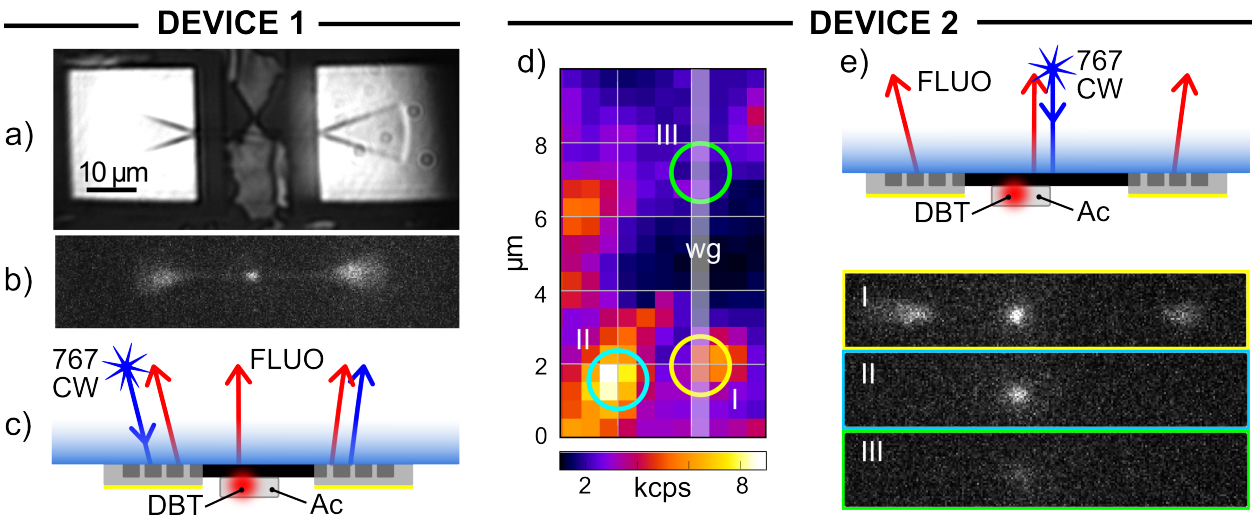

Figure 3.8 – DEVICE 1: white light image and corresponding fluorescence signal detected from the EM-CCD camera upon excitation with the scheme sketched below, in which pump light is sent through one coupler into the WG. DEVICE 2: **a)** The fluorescence map allows to determine the spatial distribution of DBT molecules within the Ac crystal in the region of the WG. **b)** Cartoon of the experimental configuration: Excitation is performed at three different positions, indicated with colored circles in **a)**, while fluorescence from the whole device surface is imaged with the EM-CCD camera. Fluorescence from the output couplers is observed only when the molecule close to the WG is excited (yellow circle - panel I), while no light is guided coming either from a molecule far from the WG (light blue circle - panel II) or from a region of Ac without DBT molecules (green circle - panel III).

As a first experiment, we send the off-resonant laser light into the WG through one coupler, optimizing the angle and matching the polarization by means of a half-wave plate (see the cartoon in **Figure 3.8c**), while imaging the entire system with the EM-CCD camera, after filtering out the pump light. Molecules placed in close proximity to the WG are excited by the evanescent tail of the guided pump light. The emitted fluorescence partially goes in free space (bright spot at molecule position) and partially couples back into the WG, propagating in two opposite directions toward the grating couplers. This is verified for device 1, that exhibit the expected fluorescence from the grating couplers.

However, to better isolate the fluorescence emission from the pump, it is necessary to excite the molecule directly, so to reject most of the pump light. We hence acquire a fluorescence map of about $50\,\mu m^2$ by scanning the sample under the diffraction-limited laser spot while detecting fluorescence from the same position with a single APD. The polarization of the laser is here adjusted with the half-wave plate to match the field in the guided mode, in order to highlight the emission from molecules oriented correctly for an efficient evanescent coupling to the guided mode.

An example of such a fluorescence map for another device, labeled 2, is displayed in **Figure 3.8d** (the gray-shaded rectangle indicating the WG), where we can identify several molecules within the scanned region, on of which is in close proximity of the WG structure. We then focus the laser in different spots of the sample, acquiring the fluorescence image with the EM-CCD (see cartoon in **Figure 3.8e**).

When the laser pump is focused on the molecule placed of the WG (yellow circle), fluorescence from the output couplers is detected, evidence of the evanescent coupling (panel I). Conversely, when exciting a molecule far from the WG (light blue circle), only the bright spot corresponding to the fluorescence of the molecule is observed, with negligible contribution of direct scattering between the confocal fluorescence spot and the gratings (panel II). We observe that the fluorescence signal in the panels is more intense for molecule I than for molecule II, in contrast with what displayed in the fluorescence map (**Figure 3.8b**). This is due to the different polarization used for the pump light, adjusted in these measurements for maximum signal in the EM-CCD at the coupler position, i.e. matching the molecule orientation. We note that, the difference in polarization angle is usually smaller than 20 degree, as expected.

Finally, when the pump is focused on the Ac crystal on top of the WG but in an area without DBT molecules (green circle), we observe some light on the illumination point that however vanishes at the couplers (panel III). This signal can be associated with some residual fluorescence from the anthracene matrix and is about a factor 5 smaller than the typical signal

from a single DBT molecule.

In the same way we identify all devices showing guided fluorescence. On these devices we estimate the emitter-WG coupling efficiency from the intensity distribution around the illumination point and the coupler areas, as explained hereafter.

3.4.4 Measurement of the molecule-waveguide coupling efficiency

We measure the value of the molecule-WG coupling efficiency, β, in two independent ways, comparing the obtained results at the end of this section.

First, the β-factor is estimated by comparing the measured count rate from both out-couplers ($S_{\mathfrak{fl}}$) with the estimated emission rate from the molecule, i.e.

$$\beta_{\text{est}} = \frac{S_{\mathfrak{fl}}}{\eta_c}\left(\frac{\text{QY}}{\tau}\frac{s}{s+1}\right)^{-1} \tag{3.2}$$

where τ, QY and s are respectively the lifetime, the quantum yield and the saturation parameter of the molecule, $S_{\mathfrak{fl}}$ is the photon flux at the first lens and η_c the measured coupling efficiency for the device under investigation.

Here $S_{\mathfrak{fl}}$ is obtained from the counts, background corrected, collected from the two couplers with the APD ($\tilde{S}_{ci}$) and corrected for the collection and detection efficiency. Referring to device 3 in **Figure 3.10a**, we underline that signals from the couplers are collected by shifting the position of the device and by inserting a suitable spatial filter (pinhole with size of 200 µm) in detection, as approximately indicated with the dashed light blue circle around the coupler area. As for the background counts, they correspond to light detected with the APD from the same area, but focusing the laser pump in a spot far from any WG and molecule. For this device we find $S_{\mathfrak{fl}} = (2.3 \pm 0.3)$MHz.

From saturation curve measurements (Section 3.4.1) we find a saturation parameter $s \simeq 1/5$, since the power used in all experiments is always around 5 times lower than the estimated saturation power. As for the fluorescence lifetime τ, we perform measurements on the coupled molecule (collecting with the APD from the excitation point) with the TCSPC system, finding an average value of $\tau_f = (4.4 \pm 0.4)$ ns. This is comparable with the average value measured for uncoupled molecules, within the experimental uncertainty, as suggested by the numerical model and also observed in reference [19].

Assuming finally a QY $\simeq 95$ % and considering the pre-measured $\eta_c = (25 \pm 2)\%$ for device 3, we obtain $\beta_{\text{est}} \simeq 24\%$.

As an alternative way to estimate the β-factor we compare the fluorescence intensity on

the EM-CCD camera in the coupler areas, S_c, with the molecule residual emission into the free space, S_f, after respective background subtraction. Accounting for the corresponding collection efficiencies, the coupling probability to the WG can be calculated as:

$$\beta_{\text{meas}} = \frac{S_c/\eta_c}{S_c/\eta_c + S_f/\eta_f} \tag{3.3}$$

with η_c the pre-measured efficiency of the coupler and η_f the collection efficiency for the residual light emitted into free space. For light coming from the WG-guided mode, the collection efficiency is determined solely by the efficiency of the grating coupler η_c, since the scattered mode entirely fits within the objective NA. In contrast, the collection efficiency η_f for the residual light emitted into free space depends on the radiation pattern of the emitter, which is strongly modified by the presence of the WG.

For the estimation of this geometrical parameter we rely on 3D numerical simulations, with the same model described in Section 3.2.2. In particular, to determine η_f we calculate the Poynting vector flux through the base of a cone of 21°-semiaperture around the dipole polar axis in the collection half space (white dashed line in **Figure 3.2a**), which corresponds to NA=0.55 after the glass-air interface. The value is then normalized with the overall power flow subtracting the total guided power.

Since the emission pattern is expected to change as a function of the dipole position and Ac thickness (d_x, d_y, h), we have repeated simulations varying independently the three parameters. The results are shown in **Figure 3.9**. Although for a given measurement we do not know the exact values for (d_x, d_y, h), the phase space available can be restricted by imposing the condition $\beta_{\text{meas}}(\eta_f(dx, dy, h)) \leq \beta_{\text{sim}}(dx, dy, h)$, which corresponds to allowing for a misalignment of the dipole orientation with respect to the WG TE mode. We then choose the average value for η_f in this sub-space and estimate the uncertainty as the maximum deviation.

For device 2 in **Figure 3.8**, this procedure yields $\eta_f = (5.1 \pm 1.5)\%$, where the error bar is estimated by varying the dipole position and orientation within the anthracene layer. Using this value for η_f, we then determine β_{meas} solely from EM-CCD images, integrating signals from both couplers and obtaining a maximum value of $(42 \pm 2)\%$. Referring to the measurement reported in panel III of **Figure 3.8**, we observe that signal levels is comparable for both couplers and also to the signal collected from the area of the point source, considering the non-unitary grating out-coupling efficiency (around 27% in this case) and the different areas over which light is spread.

In the same way we characterized several devices, obtaining a range of different coupling

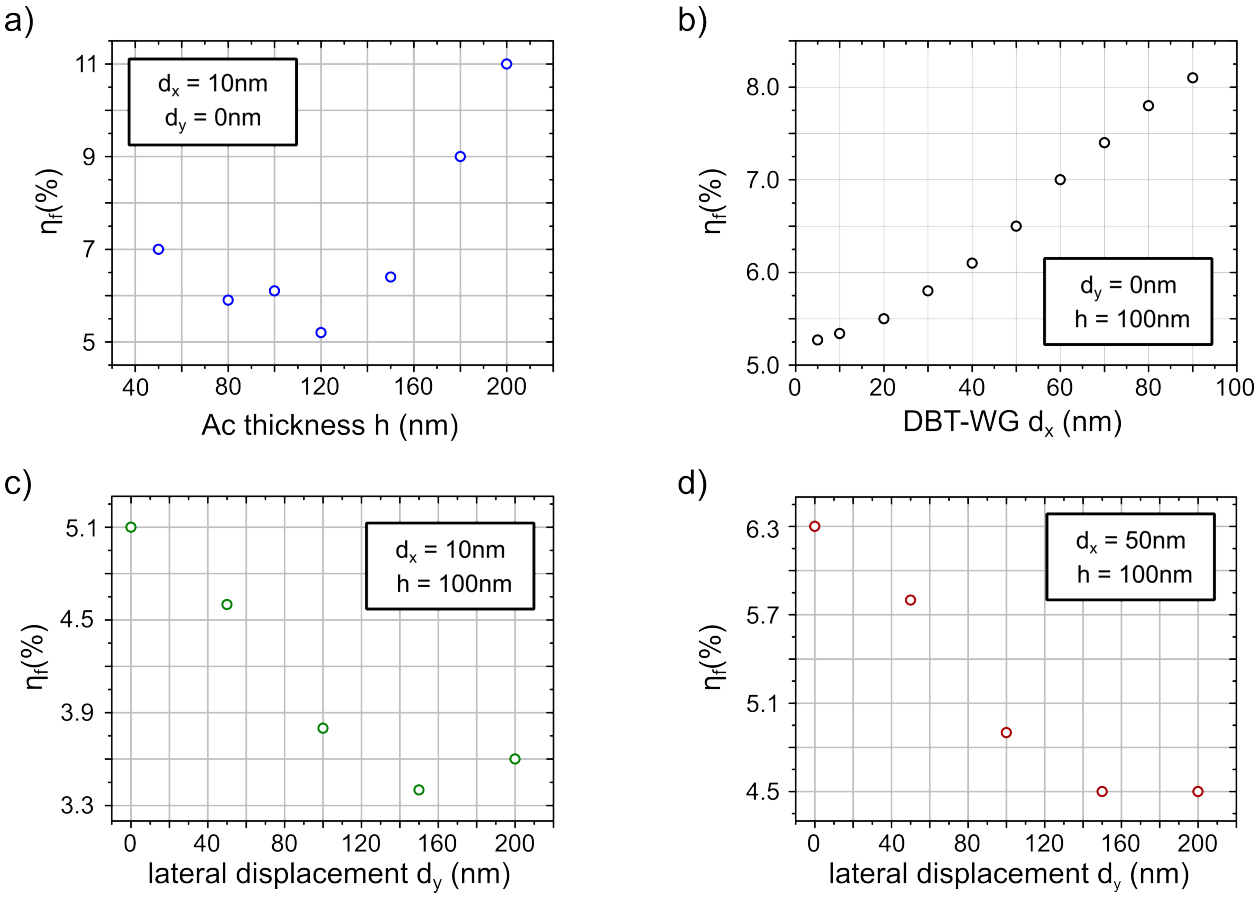

Figure 3.9 – Simulation results for the collection efficiency for the residual light emitted by the molecule into free space η_f as a function of the Ac thickness in **a)** and the dipole position in **b)**, **c)** and **d)**.

efficiencies and finding an average value for β_{meas} around 20%, with the peak value of $\beta_{\text{meas}} = (42 \pm 2)\%$ measured for device 2. We observe that the experimental results are correctly described by the numerical model, when the variation in the coupling efficiency β is accounted for by different possible values of d_y and h.

With this method we find for device 3 $\beta_{\text{meas}} = (20 \pm 51)\%$ (with collection efficiency $\eta_f = (5.0 \pm 1.5)\%$), that is consistent with the value of the β-factor derived with the procedure described above. Let us note, however, that this second method is more trustworthy, being independent from the set-up response function and from the molecule QY.

3.4.5 Quantum nature of the waveguide-coupled light

To conclude, we analyze the quantum nature of the WG-coupled light by measuring the second-order correlation function $g^2(\Delta t)$, with the HBT set-up, comparing the counts col-

lected off-chip from one coupler, $g^2_{\text{off}}(0)$, with that collected from the illumination point, $g^2(0)$. Those signals are detected from a selected area by shifting the position of the device

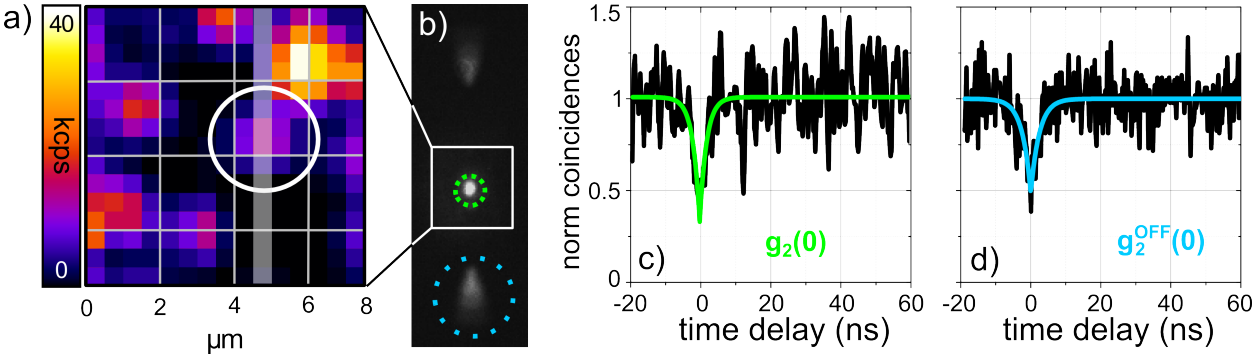

Figure 3.10 – DEVICE 3. In panel **(a)** a fluorescence confocal scan allows identifying possibly coupled molecules. The fluorescence from the highlighted molecule is then imaged onto the EM-CCD camera in **(b)**, showing signal from the illumination point as well as in correspondence with the grating out-couplers (see the dashed circles marked). The coupling of nonclassical light into the WG finds evidence in the antibunching dip relative to the confocal spot **(c)** and to the coupler area **(d)**, respectively. The excitation laser power is 1/5 in units of saturation power.

and by inserting a suitable spatial filter (pinholes with size of 100 µm for the source and of 200 µm for the coupler) in detection, as approximately indicated with dashed circles in **Figure 3.10b**. Evidence of single-photon emission is obtained from the illumination point (**Figure 3.10c**), where the fit yields a $g^2(0) = 0.33 \pm 0.09$.

For light scattered by a single coupler (**Figure 3.10d**) we find $g^2_{\text{off}}(0) = 0.50 \pm 0.05$, ascribed to a lower signal to background ratio (S/N) with respect to that from the source. Indeed, in this case, the measured signal is about a factor 1.6 smaller than the one collected from the molecule position for a comparable background.

Operations with an integrated single-photon source are ideally performed before off-chip read-out, and hence the relevant parameter is the on-chip source purity $g^2_{\text{on}}(0)$ rather than $g^2_{\text{off}}(0)$, for which click of the detector are affected by light directly scattered by the illumination point, corresponding also to non-guided background photons. To determine $g^2_{\text{on}}(0)$ we therefore need to eliminate the background contribution (measured as described above) to the signal.

We can now calculate the probability of obtaining a click in the detector from the guided light (either fluorescence or pump) as $p = \tilde{S}_{\text{c}}/(\tilde{S}_{\text{c}} + \widetilde{BG}_{\text{c}}) \simeq 71\%$. The on-chip source purity is then given by [78]:

$$g^2_{\text{on}}(0) = 1 + \frac{g^2_{\text{off}}(0) - 1}{p^2} = 0.01 \pm 0.10, \tag{3.4}$$

indicating a low multi-photon probability inside the WG.

3.5 Conclusions

In this chapter we discuss the design and the realization of a hybrid molecules-nanophotonic system made of spincoated DBT:Ac crystals on Si_3N_4 WGs, terminated with grating out-couplers optimized to support a Gaussian mode in free space, useful for potential coupling to an optical fiber. Due to the intrinsic variability imposed by the spin-coating procedure of DBT:Ac system on the chip, molecule-to-WG coupling efficiency is estimated as a function of the molecule position and the Ac thickness by means of 3D numerical simulation, providing a range of values to interpret the experimental measurements of the β-factor, performed at room temperature.

The best measured performance are:

- for the out-copling efficiency of the focusing grating: $\eta_c = (40 \pm 2)\%$.
- for the evanescent molecule-to-WG coupling: $\beta = (42 \pm 2)\%$
- for the integrated photon source: an on-chip purity $g^2_{\mathrm{on}}(0) = (0.01 \pm 0.10)$ and a photon-flux on chip at saturation $S^{\mathrm{on}}_{sat} = \frac{1}{2\tau}\mathrm{QY}\beta_{\mathrm{meas}} \simeq 48\,\mathrm{MHz}$.

These results are competitive with state-of-the-art single-photon emission into ridge WG modes from other solid state systems [32, 183, 187] while offering a novel platform with high versatility and advantages such as a small foot-print, simple fabrication methods and scalability towards arrays of integrated single-photon sources for on-chip quantum computation. We observe that for protocol relying on indistinguishable photons, DBT:Ac should be operated at liquid helium temperatures, where it exhibits lifetime-limited emission into the ZPL (around 40 MHz linewidth) with a Debye-Waller factor larger than 0.3. This is though compatible with all the procedure discussed so far, upon reduction of the background signal achievable with an optimized fabrication of the hybrid device.

A straightforward extension to many quantum emitters in a single 1D channel could allow instead the study of many-body effects and quantum correlations [188]. In order to enhance the coupling efficiency to the WG mode while keeping on-chip losses small, more complex photonic designs can be envisioned. For example, replacing one output coupler with a Bragg mirror at the appropriate distance would readily provide a factor 2 improvement, whereas inscribing a slot into the ridge WG would yield a higher field concentration.

4 DBT-doped Anthracene Nanocrystals Showing Photostable Single-Photon Emission

In this chapter we propose and report on anthracene (Ac) crystals with average size of few hundreds nanometer, doped with controllable concentration of dibenzoterrylene molecules (DBT), preserving the remarkable features of the bulk system described in Chapter 2. In particular, they exhibit photostable single-photon emission at room temperature, that is almost lifetime-limited (50MHz) and spectrally stable at low temperatures. The combination of such properties in a nanocrystalline environment is unique and opens the way to the use of organic nanocrystals for quantum technologies and for single-photon applications in general.

4.1 Background and Motivations

In the last 40 years, nanoparticles and nanocrystals - ranging in size from tens to several hundred nm - have been extensively investigated, triggered not only by the advantage of their small size but also by the impressive tunability of their physical and chemical properties, resulting from the confinement of the material to the nanoscale. This feature was first observed at the end of the 18th century by Faraday, that discovered the dependence of gold particles' colors on their size [189]. Much later, in 1980, it was discovered that the electronic characteristics of semiconductor nanocrystals, i.e. colloidal QDs, depend on their size and shape [190, 191], resulting in an absorption (and emission) maximum shift to higher energy with decreasing size [192]. Nowadays, relying on well-established fabrication methods - including epitaxial techniques, ion implantation and chemical synthesis - metallic and semiconductor nanoparticles are employed in a variety of research fields, spanning from biomedicine (e.g. targeted drug delivery [193]) to high resolution imaging (e.g. surface-enhanced Raman spectroscopy[194]).

In photonics, we witness today an ubiquitous deployment of single quantum emitters in

sub-micrometric size crystals, stemming for their nano-positioning opportunities and from the possibility of mass-production at low costs [195]. However, today-available nanocrystals (NCs) present important shortcomings for their implementation in quantum technologies. Photoinduced charge rearrangements in the passivation layer and in the environment of inorganic semiconductors QD NCs[196] leads to spectral instability of the exciton line [197], hindering basic quantum optics operations with the emitted photons. Moreover, intermittence in the photoluminescence [198] seriously affects the average fluorescence QY and hence the photon state purity for quantum optics applications. Although important results have been obtained by improving synthesis protocols [199] or introducing perovskite materials [200, 201], the emitter photostability in time or frequency is still below expectations. Notably, similar issues characterize the emission of color centres in nanodiamonds, including those which possess superb optical properties in bulk such as the widely studied negatively charged silicon vacancy [81, 202], or chromium-related defects [203]. Hence, despite the wealth of different materials and processing technologies, there still are fundamental limitations for the use of such inorganic NCs in single-photon/quantum applications.

In this chapter we propose a novel fabrication method to grow sub-micrometric Ac crystals doped with controlled and tunable concentration of DBT molecules. In fact, despite the DBT:Ac system has been successfully integrated in nanophotonics layered structures thanks to the 50nm-thickness of Ac crystals grown via spin-coating [42, 143, 160], the available fabrication methods - discussed in Chapter 2.1.3 - inherently limit the control on the emitter position. Kewes and colleagues [204] have recently proposed a manipulation technique based on atomic force microscopy (AFM). By operating the AFM in contact mode, they demonstrate the possibility to cut a DBT:Ac spin-coated crystal into two sub-µm-sized pieces. The cantilever tip is also used to push the fragments several hundreds of nm across the sample. This method assure sub-µm precision positioning, but it is cost- and time-demanding.

To fully exploit molecule-based solid state systems as nanoscale single-photon sources, a reduced size of the emitter is desirable. Indeed, in the last years, deterministic positioning methods have been developed to integrate QDs and nanodiamonds in complex photonic structures owing to their reduced size. Deterministic integration of such sub-micrometric quantum emitters relies mainly on two different approaches: structuring the material that is embedding the emitters [205–207] or nano-manipulating a pre-selected emitter, usually in a pick-and-place procedure [208–210]. For molecule-based systems, only the first approach has been investigated [162]. In sharp contrast to random methods, with these deterministic approaches contamination of the whole sample with unwanted nanoparticles is avoided.

Moreover, pick-and-place methods are scalable, since positioning of a second nanoparticles takes the same time needed to position the first one.

The developed growth protocol and the morphological characterization of the fabricated DBT-doped Ac NCs is presented in Section 4.2.1 and Section 4.2.2, respectively. A detailed analysis of the optical properties is then discussed in Section 4.3. Here we demonstrate that the thermal instability of the organic matrix, which is totally suppressed at cryogenic temperature, is not affecting the optical properties of the single-photon emission from individual DBT molecules within one-day time scale at room temperature. Moreover, the integration of DBT-doped Ac NCs in suitable polymeric matrix can suppress Ac sublimation at room temperature, as it will be discussed in the following chapter.

4.2 Growth method and morphological characterization

Organic NCs exhibit controllable properties such as electroluminescence [211] and high nonlinear optical efficiency [212], making them appealing for several applications, such as organic light emitting diodes (OLED), organic field effect transistors (OFET) and photovoltaic cells [213]. However, with respect to their inorganic counterpart, relatively small progress has been achieved for the preparation of free-standing organic nanoparticles due to their thermal instability, i.e. morphological modifications in time due to thermal decomposition. The available techniques developed for the preparation of organic nanoparticles range from a simple "crush technique" to molecular beam deposition or laser ablation (for a review, see [214]). A simple, reproducible and cost-efficient procedure, named *reprecipitation method*, was developed by Nakanishi and co-workers [215] and allowed the production of a series of nanoparticles - including perylene [216], polydiacetylene [217], pyrazolines [218] and anthracene [219] - which were found to possess size-dependent properties below a threshold size of 100 nm. This fabrication method relies on the insolubility of organic materials in water. It consists in dissolving the organic compound in a water-soluble solvent and disperse this solution drop-wise into vigorously stirred water at room temperature. After few minutes of stirring, the compound is reprecipitated in the form of NCs dispersed in water, with size and shape determined by several conditions such as water temperature, droplet size, injected solution concentration or presence of surfactants [219].

In order to fabricate DBT-doped Ac crystals with sub-µm size we first develop a simple mechanical procedure to crush sublimated crystals grown with the protocol described in Chapter 2.1.3. The method consists in sandwiching the crystals between two coverglasses and then pressing and gently moving the top glass. The resulting NCs, however, show

a broad range of sizes and crystal modification due to mechano-thermal effect cannot be excluded. We therefore develop a more reproducible procedure based on reprecipitation, as detailed hereafter.

4.2.1 Fabrication of DBT-doped Ac nanocrystals

Our protocol to grow DBT-doped Ac NCs is adapted from the procedure developed by Kang and colleagues [220], who demonstrate that sonication allows to fabricate NCs better dispersed than with magnetic stirring and with average size on the order of few hundreds nm. The procedure starts with preparing a 1mM solution of DBT in toluene and a 5mM solution

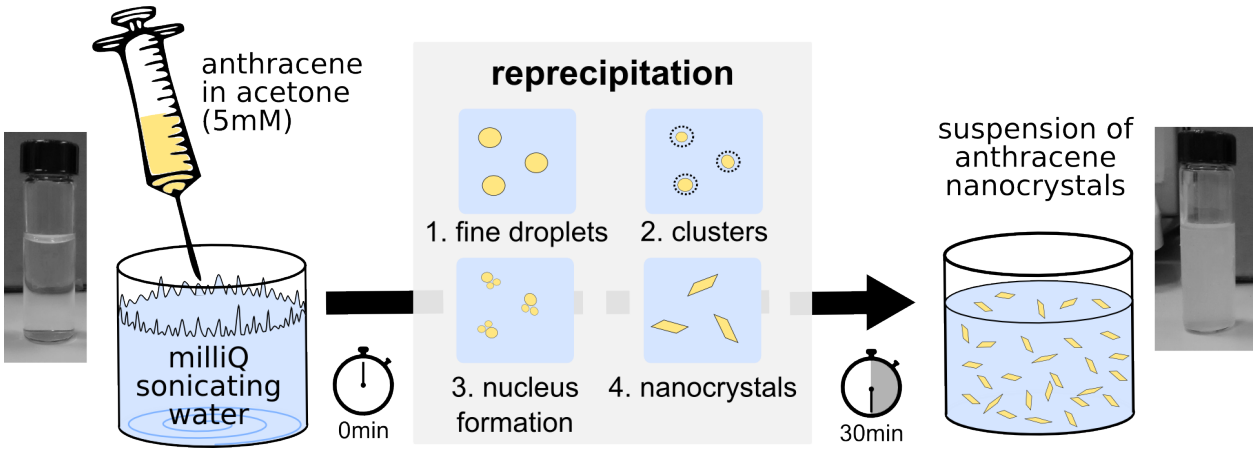

Figure 4.1 – Scheme of the reprecipitation protocol and of the DBT-doped Ac NCs formation process.

of anthracene in acetone, that are then mixed together in different proportion. From the optical characterization, that will be discussed in Section 4.3, we find two optimal recipes:

1. individual Ac NCs with single molecule concentration are obtained when diluting by a factor of 10^8 the DBT:toluene solution with the Ac:acetone mixture. The so-obtained NCs are meant to exhibit single-photon emission at room temperature;

2. with a dilution ratio of 10^2, DBT concentration within single Ac NCs is still sufficiently low to allow spectral selection of single molecules with our set-up for cryogenic temperature experiments.

As sketched in **Figure 4.1**, 250 µL of the mixture are injected into 5 mL sonicating water (deionized by a Milli-Q Advantage A10 System, 18.2 mΩ cm at 25 °C) at room temperature, where it divides into small droplets. Acetone gradually dissolves in water and, correspondingly, the concentration in the micro-droplets becomes super-saturated until the compound

is reprecipitated in the form of NCs. The exact mechanism of crystal formation is still under debate, but it is believed that the growth process starts with the formation of clusters and amorphous nanoparticles, which aggregate to form NCs within 30 min to 1 h after reprecipitation [221]. We thus continuously sonicate the system for 30 min, obtaining an off-white turbid suspension indicating the successful formation of DBT:Ac NCs.

As for most crystallization processes, the so-called heterogeneous nucleation - i.e. nucleation induced by impurities or by container walls where water it is likely to have a different molecular structure - can occur. This can influence how the reprecipitated clusters assemble and grow [222] and hence may affect the size dispersion of the grown NCs, the reproducibility of the fabrication procedure and the suspension stability in time.

All these aspects can be experimentally monitored with dynamic light scattering (DLS), a method that provides ensemble averaged estimation of nanoparticles size in suspensions [223]. DLS measurements are performed at the CSGI - Center for colloid and surface science in Florence (Italy), with a set-up as the one sketched in **Figure 4.2a**. Light from a

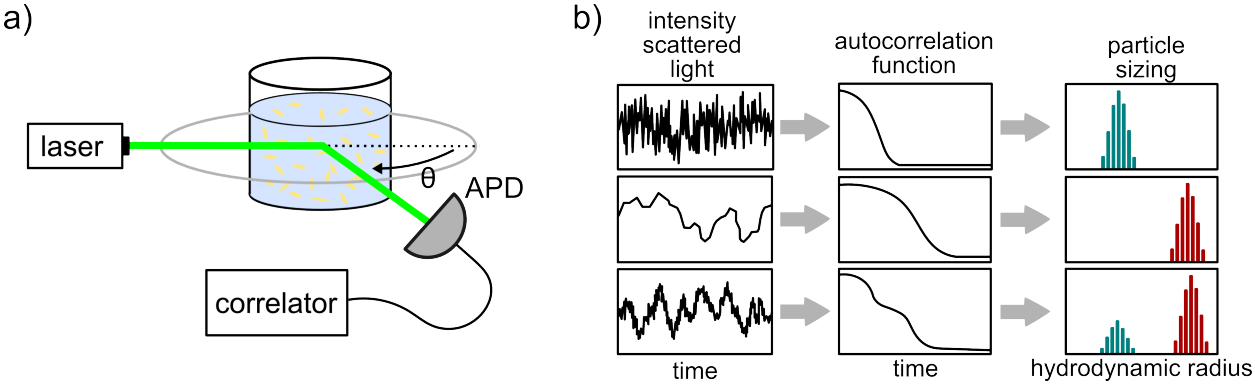

Figure 4.2 – **a)** Sketch of the set-up used for dynamic light scattering (DLS) measurements: light from a single mode laser is sent to the water suspension of DBT:Ac NCs. Light undergoes multiple scattering, owing to the Brownian motion of NCs at ambient conditions. The intensity fluctuations of the scattered light at an angle θ is detected and processed to build up the second-order correlation function. The analysis of the autocorrelation function provides the diffusion coefficient of the particles from which the particle size distribution can be calculated, according to the Stokes-Einstein equation. **b)** The intensity of the light scattered from the particles shows fluctuation in time corresponding to the size distribution of the particles. Small particles diffuse fast, resulting in a rapidly fluctuating intensity signal and hence a faster decay time of the autocorrelation function as compared to large particles, which diffuse more slowly. A more complex behavior is observed for polydisperse particles.

single mode laser (λ = 532 nm, Torus Photonic Solutions) is sent to the suspension that is conveniently transferred into a glass cuvette. Light undergoes multiple scattering from the NCs suspension. The net intensity $I(t)$ of the scattered light fluctuates in time, owing to the Brownian motion of NCs at ambient conditions. Scattered light at an angle θ is

detected with an avalanche photodiode (APD, PerkinElmer) and processed with an autocorrelator (BI-9000AT, Brookhaven Instruments) to build up the second-order correlation function $g^2(\Delta t) = \frac{\langle I(t)I(t+\Delta t)\rangle}{\langle I(t)\rangle^2}$. Let us note that this function is here referred to the Brownian motion of the suspended NCs and should not be confused with that introduced in Chapter 1.1.1 to describe the internal dynamics of a quantum emitter.

Photon counts here obey a Gaussian statistics and the $g^2(\Delta t)$ is related to the first-order correlation function of the electric field $g^1(\Delta t)$ with equation $g^1(\Delta t) = \sqrt{g^2(\Delta t) - 1}$, which decays in time as:

$$g^1(\Delta t) = A \cdot e^{-Dq^2\Delta t} + B \tag{4.1}$$

where A is the amplitude of the correlation function (and is related to the suspension concentration), B is the baseline, D is the translational diffusion coefficient of the particles and $q = (4\pi n/\lambda)\sin(\theta/2)$ is the magnitude of the scattering vector, that depends on the refractive index n of the medium.
From the diffusion coefficient D the NCs' size distribution can now be derived from the Stokes-Einstein equation:

$$D = k_{\mathrm{B}}T/(6\pi\eta r_{\mathrm{h}}) \tag{4.2}$$

with T and η the temperature and the viscosity of the medium, and r_{h} the hydrodynamic radius, i.e. the radius of a sphere that moves in the same manner as the scatterer.
Small particles diffuse fast, resulting in a rapidly fluctuating intensity signal and hence a faster decay time of the $g^1(\Delta t)$ as compared to large particles, which diffuse more slowly (see **Figure 4.2b**). This result, that holds for a monodisperse (i.e. single population) suspension of spherical particles, remains valid also for polydisperse suspensions, for which the autocorrelation function is a sum of the exponential decays corresponding to each species in the population. It is important to note that the size determined by DLS will include any other molecules or solvent molecules that move in the medium together with the particles.

Figure 4.3 displays the DLS results obtained from three suspensions of DBT:Ac NCs in water, prepared independently and measured approximately 1 h after sonication ended. These measurements are performed at ambient temperature (water viscosity = 0.7978 mPa s) and detecting the scattered light at an angle $\theta = 90\,^{\circ}$. **Figure 4.3a** shows the autocorrelation functions obtained from the three suspensions (black lines) and analyzed with the *cumulant method* [224] (colored lines). The cumulant analysis yields to the particle size distributions shown in **Figure 4.3b**, demonstrating that the DBT:Ac NCs grown under our experimental

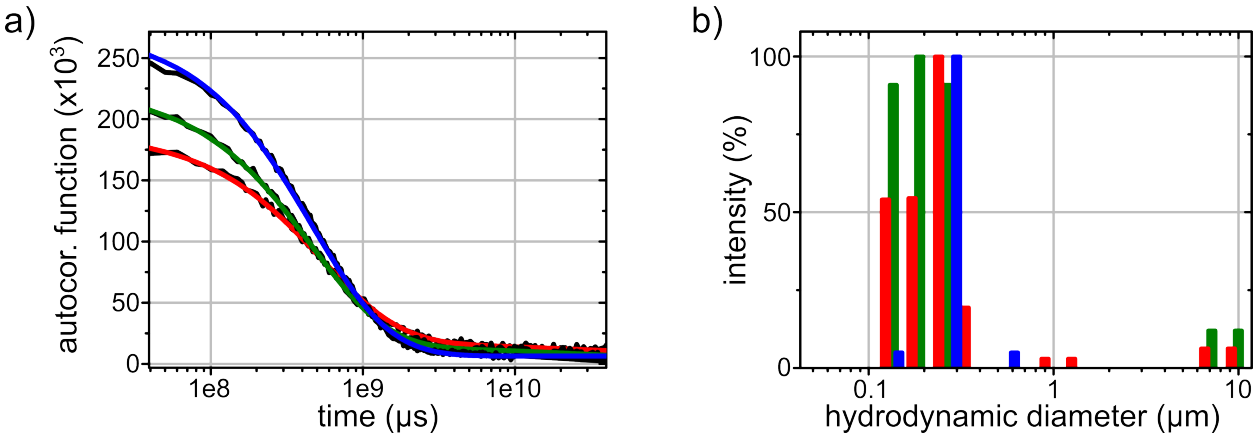

Figure 4.3 – **a)** Autocorrelation functions measured with DLS from three aqueous suspensions of DBT:Ac NCs prepared independently. The three curves are analyzed with the cumulant method, yielding a particle size distribution shown in **b)**.

conditions are mostly monodisperse, with an average hydrodynamic diameter around 200 nm and can reach sizes as large as few µm (particle with size larger than 5 µm are more likely to be due to dust contamination).

The average size larger than 100 nm suggests that no relevant modification of the optical properties of Ac due to its reduced size are expected. Indeed, our goal is to fabricate sub-micrometric Ac crystals in which DBT molecules exhibit the same features of the bulk system. The presence of µm-particles can be attributed to aggregation between the dispersed NCs already right after reprecipitation, as pointed out by Chung and colleagues [219]. This clusterization process can be relevantly slowed down with the addition of surfactants, which can additionally be effective in reducing the size of the nanoparticles [220].

As a final remark, we observe that after weeks the suspensions present some precipitated particles. Ideally periodical DLS measurements of the samples would show an increasingly broader distribution of particles toward larger hydrodynamic radius in correspondence to particles aggregation, hence providing a detailed analysis of the suspension stability in time.

After these preliminary investigations on the NCs in suspensions, we drop them on a coverglass substrate (or on a different substrate when needed, as specified in the text) and let water dry in a desiccator. The morphological characterization presented hereafter and the subsequent optical investigations are performed on this sample.

4.2.2 Nanocrystals morphology and cristallinity

The size of the free-standing NCs is evaluated by scanning electron microscopy (SEM, Phenom Pro, PhenomWorld) and atomic force microscopy (AFM, Pico SPM from Molecular

Imaging in AC mode equipped with a silicon probe NSG01 (NT-MDT) with 210 kHz resonant frequency) whose typical results are displayed respectively in **Figure 4.4a** and **Figure 4.4b**. For some NCs we can identify some peculiar features of crystalline Ac - such as the

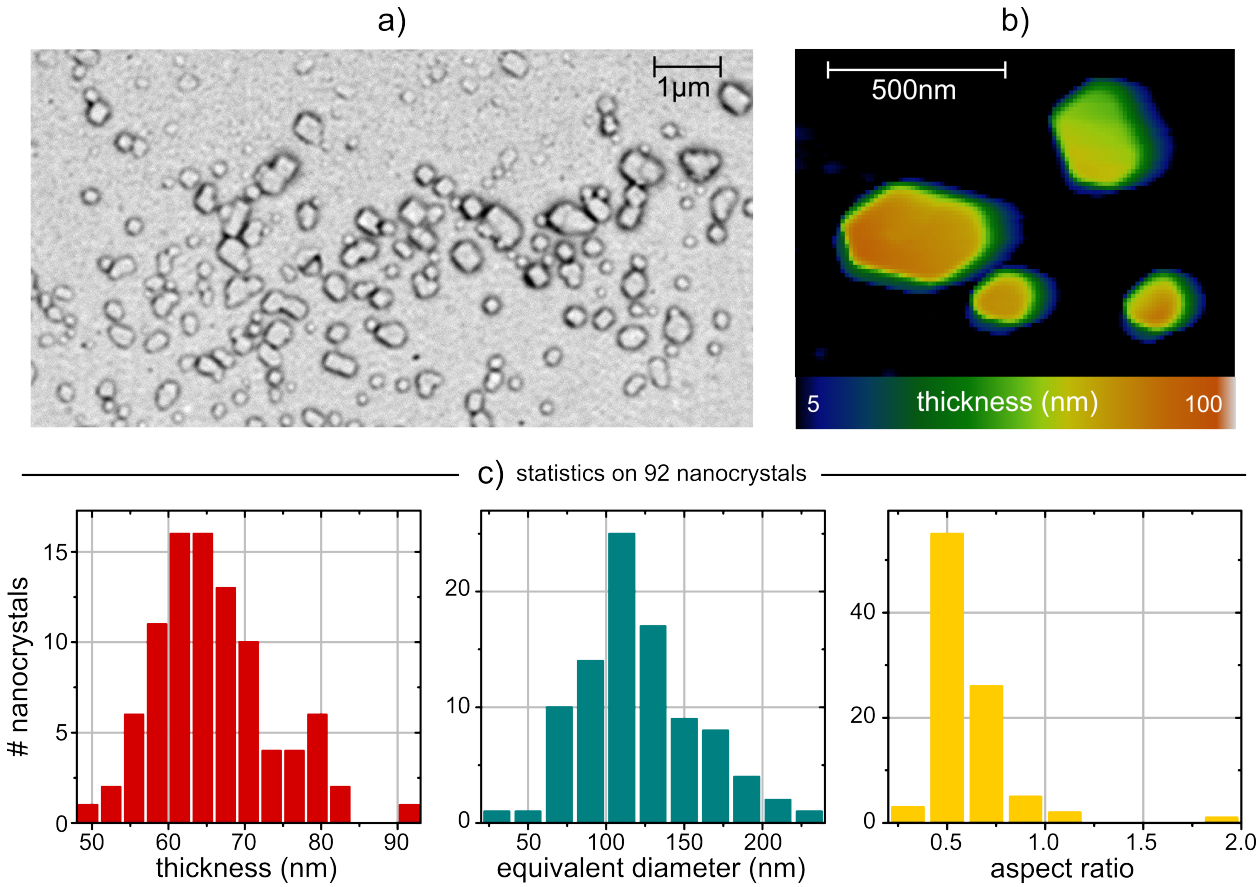

Figure 4.4 – Typical SEM **(a)** and AFM **(b)** images of DBT:Ac NCs, once drop-casted and desiccated on a bare coverglass. **c)** Statistical analysis on AFM images yields the following average values: NC thickness (65±13) nm, NC equivalent diameter (113±64) nm and aspect ratio (0.6±0.2).

hexagonal-like morphology - while others exhibit a round-like shape, possibly due to a few nm acetone-rich solvent cage.

From AFM measurement analysis performed with the open-source software Gwyddion [225], we collect statistics on 92 NCs (**Figure 4.4c**), finding an average thickness t of (65±13) nm and an equivalent diameter d_{eq} of about (113 ± 64) nm, which we consider a good estimation of the crystals' lateral size. The aspect ratio, defined as t/d_{eq}, is (0.6 ± 0.2).

These values are compatible with what estimated from DLS measurements. Indeed, DBT:Ac NCs present a complex geometry which cannot be inferred from the measurement of the solely hydrodynamic radius determined at a fixed angle of 90°. On the other hand, DLS measurements, averaging over a macroscopic volume of the suspension, provide

a more reliable information on the average size of the NCs and more elaborated multi-angle measurements can determine the full particle size distribution.

The crystalline nature suggested by the clear-cut edges in **Figure 4.4b**, is verified by X-ray diffraction (XRD), that is an analytical technique allowing to study the crystal structures and atomic spacing among planes in a crystal lattice [226]. XRD measurements are performed at CRIST, the Crystallographic Centre of the University of Florence (Italy), by means of a XRD Bruker New D8, whose set-up is sketched in **Figure 4.5a**. An X-ray tube with a copper (Cu) anode beam source mounted on a goniometer generates X-rays, that are then collimated and directed onto a silicon-low background sample holder (Bruker AXS) mounted on the goniometer axis, where a few µL of suspension have been previously desiccated.

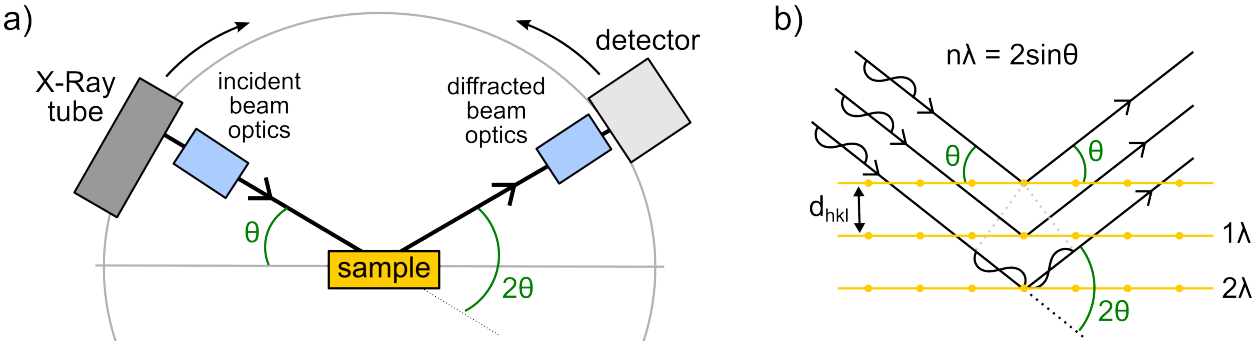

Figure 4.5 – **a)** Schematic arrangement of the XRD diffractometer, whose main component are a source of X-ray and a detector mounted on the two arms of a goniometer. The sample-holder is placed on the goniometer axis. **b)** The incoming beam (coming from upper left) causes each scatterer to re-radiate a small portion of its intensity as a spherical wave. If scatterers are arranged symmetrically with a separation d, these spherical waves will interfere constructively only in directions where their path-length difference $2dsin\theta$ equals an integer multiple of the wavelength $n\lambda$. In that case, part of the incoming beam is deflected by an angle 2θ, producing a reflection spot in the diffraction pattern.

The interaction of the incident rays with the sample produces constructive interference (and a diffracted ray) according to Bragg's Law ($n\lambda = 2d\sin\theta$, with integer n), which relates the wavelength λ of the electromagnetic radiation to the diffraction angle θ and the lattice spacing d in a crystalline sample (see **Figure 4.5b**). The diffracted X-rays are detected by a sodium iodide scintillation detector mounted on the other arm of the goniometer at an angle of 2θ. When the geometry of the incident X-rays impinging the sample satisfies the Bragg Equation, peaks appear in the diffraction pattern that, converted into d-spacings, allows identification of the crystalline material by comparison of standard reference patterns (by means of the software TOPAS, Bruker). Ideally, by scanning the sample through a suitable range of 2θ, all possible diffraction directions of the lattice are resolved. In the case of Ac, the more intense peaks are displaced between 5 degree and 40 degree [219, 227].

Figure 4.6a compares the normalized XRD patterns measured for DBT:Ac NCs, spin-coated DBT:Ac and sublimated DBT:Ac crystals. In all cases, we observe a strong diffracted peak at 9.17°, that corresponds to the (001) plane, and other equivalent periodic peaks corresponding to (002), (003), and (004) planes, matching the crystallographic data of an anthracene monoclinic system [228].

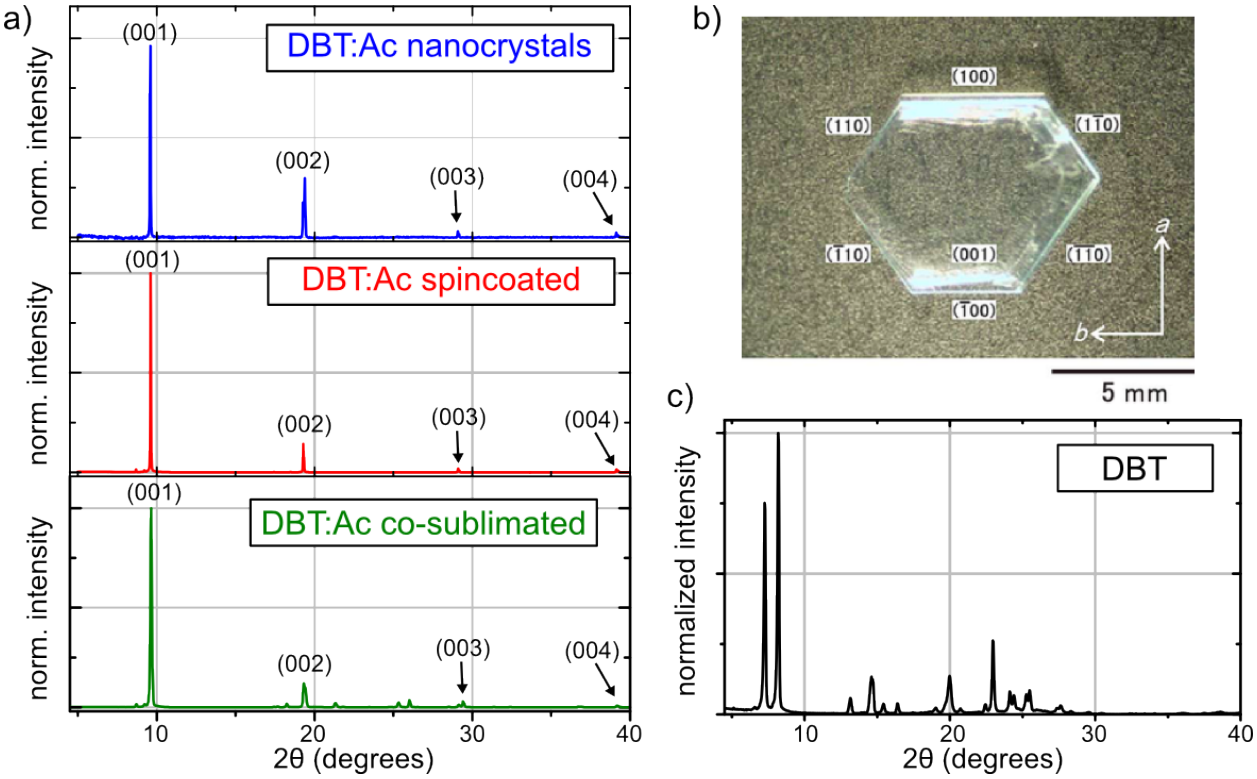

Figure 4.6 – **a)** Comparison of the normalized XRD patterns measured for DBT:Ac NCs, spin-coated DBT:Ac and co-sublimated DBT:Ac crystals, in which only the (001) and its higher order reflection are well resolved. This means that, once deposited on the substrate, Ac crystals and NCs tends to be iso-oriented with c-axis perpendicular to the substrate, due to their natural platelet-like morphology. **b)** Figure adapted from [229], showing a 10 mm-sized Ac single crystal obtained by physical vapor growth, reported here for convenience to illustrate how the crystal's edges reflect its fundamental structure. **c)** XRD pattern measured for the solely DBT powder.

Since crystals morphologies are identical irrespective of their sizes, a picture of a 10 mm-sized Ac single crystal, fabricated via physical vapor growth by Jo and colleagues [229], is reported in **Figure 4.6b** for convenience to illustrate how the crystal's edges reflect its fundamental structure. The large size mismatch between the hexagonal (001) plane and the other lateral planes imposes Ac crystals to be oriented with c-axis perpendicular to the substrate and, due to their platelet-like morphology, peaks corresponding to the lateral planes cannot be resolved. **Figure 4.6c** reports the XRD pattern measured from the solely DBT

powder, not yet reported in literature. We observe that DBT peaks are not resolved in any of the XRD patterns in **Figure 4.6a**, as DBT molecules are just impurities within the Ac matrix.

We can therefore conclude that with a simple reprecipitation method we can fabricate high quality Ac crystals with average size around 200 nm that, once deposited on a flat surface, are mainly iso-oriented with c-axis perpendicular to the substrate. Let us recall that the transition dipole moment of a DBT molecule in the main insertion site of an Ac crystal is mainly oriented along the b-axis [41] and thus should be mainly parallel to the substrate even for the case of Ac NCs. This will be confirmed by measurements of single DBT molecule's emission pattern, discussed in the following section.

4.3 Optical Characterization

The sub-micrometric size of the Ac crystalline matrix may affect the optical properties of DBT molecules with respect to the case of the bulk Ac matrix presented in Chapter 2.4, due to e.g. strain within the crystal and imperfection at the interfaces that may cause fluorescence instability and linewidth broadening, as reported for other nanocrystalline guest-host systems [81, 230].

We thus perform a complete optical characterization of DBT molecules in Ac NCs by means of the home-built confocal microscope described in Chapter 2.3. NCs grown with recipe 1 are doped with a single-molecule concentration, i.e. each of them is meant to host a single DBT molecule and hence to provide single-photon emission at room temperature. This is investigated in Section 4.3.1, pumping the system off-resonance at 767 nm and relying on the spatial dispersion of the NCs on the substrate.

Single DBT spectroscopy is studied at cryogenic temperature in Section 4.3.2, pumping on-resonance (785 nm) single NCs grown with recipe 2 and desiccated on a sapphire substrate. These NCs are meant to be doped with a concentration of DBT molecules that allows for spectral selection of single molecules within the frequency range probed by our tunable resonant laser.

4.3.1 Microscopy at room temperature

Typical white light and wide-field fluorescence images are compared in **Figure 4.7a**, demonstrating that more than 90% of the Ac NCs are successfully doped with DBT. The varying intensity of the molecules can be attributed to slightly different orientations of DBT

molecules within the host nanocrystalline matrix (and hence to a not efficient excitation polarization alignment).

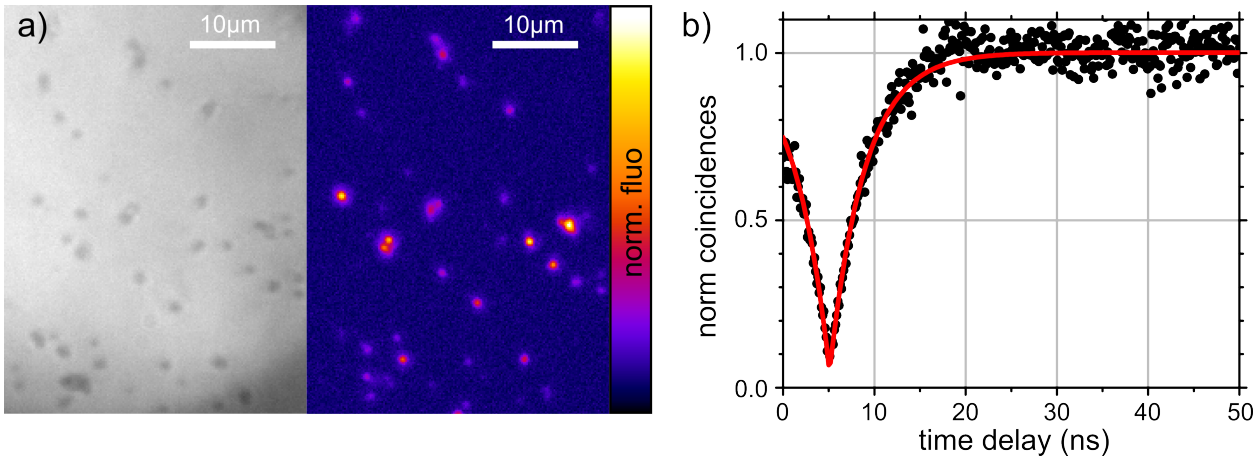

Figure 4.7 – **a)** White light and fluorescence wide-field EM-CCD images of the same region of a sample made of DBT-doped Ac NCs (recipe 1) drop-casted on a cover-glass. More than 90% of the Ac NCs are successfully doped with DBT. **b)** Measured photon anti-bunching from the emission of a single DBT:Ac NC without any background correction (black dots).The experimental coincidence reduction obtained at zero-time delay yields a background-corrected purity $g^2(0) = 0.0025$.

To prove that the detected fluorescence stems from individual DBT molecules, single isolated crystals are illuminated in confocal mode with an excitation intensity of $15\,\mathrm{kW\,cm^{-2}}$, which is well below saturation. The polarization of the excitation source is aligned with the emitter dipole by means of the half-wave plate in the excitation line so to maximize the photon count rate detected with the APDs. The correlation between photon arrival times is measured with the HBT interferometer. The analysis performed on 40 NCs shows that 73% of them displays an antibunching dip larger than 50%. This result demonstrates that recipe 1 is a reliable protocol to grow individual Ac NCs doped with single DBT molecules.

Figure 4.7b shows the histogram of the observed coincidences from a single NC, featuring a strong antibunching dip. The experimental data are fitted at short time delays Δt with the equation (2.11) for the second-order autocorrelation function $g^2(\Delta t)$, yielding a dip depth of 95%, and hence a purity $g^2(0) = 0.05$. As discussed in Chapter 1.1.3, background photons are responsible for false start-stop measurements and hence to coincidence counts higher than 0 at zero time delay. For the reported measurement we have a typical count rate of 400 kcps for the fluorescence signal and 20 kcps for the background noise. Recalling equation (1.21), we find a background-corrected purity as low as $g^2(0) = 0.0025$.

To gain further information on the molecule's property within the sub-micrometric crystalline matrix, we study the relaxation dynamics by means of TCSPC measurements, collecting photons generated by 767 nm-pulsed excitation at $20\,\mathrm{kW\,cm^{-2}}$ with a single APD.

Figure 4.8a shows a typical measured fluorescence decay curve from which the lifetime τ of the excited state can be derived via a single exponential fit in the presence of a constant background: the fit (red curve) yields an excited state lifetime of (4.2±0.1) ns. Repeating the measurement on 40 NCs we obtaine the distribution for the excited-state lifetime displayed in the inset of **Figure 4.8a**. The distribution can be fitted with a Gaussian centered at 4.2 ns with FWHM = 0.4 ns, in agreement with what measured for the bulk system (Section 2.4).

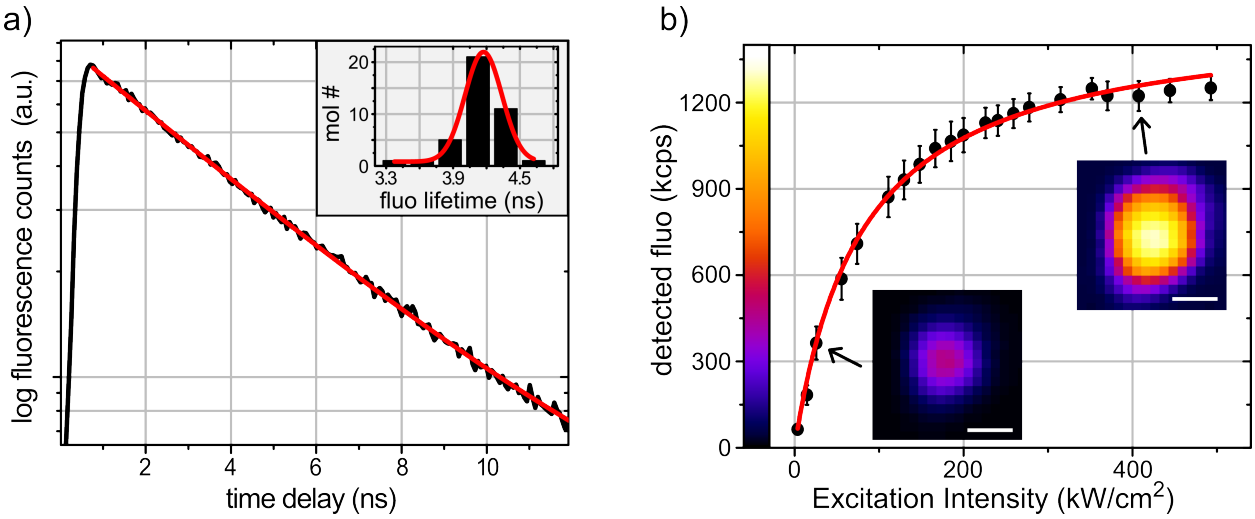

Figure 4.8 – **a)** Time-resolved measurement of the fluoresce decay from a single DBT:Ac NC. A single exponential fit yields an excited state lifetime of (4.2 ± 0.1) ns. The inset shows the distribution of the excited-state lifetime collected from 40 NCs. The red-curve is a Gaussian fit centered at 4.2 ns with FWHM = 0.4 ns. **b)** Saturation measurement performed on a DBT:Ac NC (black dots). Several fluorescence scans of the laser spot corresponding to a single molecule are acquired at different excitation powers by scanning the sample under the confocal laser spot in the small region where the molecule is located (two of them are shown as insets in the figure). The fitted red curve yields a saturation intensity of $I_s = (80 \pm 6)$ kW cm^{-2} and a maximum detected rate $R_\infty = (1.50 \pm 0.02)$ Mcps.

The brightness of the fluorescence emission is quantified by studying the saturation behavior of the system, detecting the red-shifted fluorescence with a single APD at different excitation intensities while scanning the sample under the confocal laser spot in the small region where the NC is located. From the obtained fluorescence maps (two of them are displayed as insets in **Figure 4.8b**), the mean value within an area around the brightest pixel is extracted and corrected for the background counts, given by the mean value in an area out of the NC and that show the expected linear behavior with laser power. Data are plotted as a function of the laser intensity I (black dots in **Figure 4.8b**) and fitted with the function describing the saturation of the photon detection rate $R(I)$ (equation 1.24). The

fit-procedure yields $I_s = (80 \pm 6)$ kW cm^{-2} and a maximum detected rate $R_\infty = (1.50 \pm 0.02)$ Mcps, which can be considered as a typical value.

Accounting for the quantum efficiency of the APD ($\eta_{det} = 50\%$), the measured R_∞ corresponds to a collected photon rate of 3 MHz at the detector, consistent with what reported for the bulk system (Section 2.4). Moreover, comparing this value with the theoretical one of 240 MHz related to the measured lifetime through the relation $R_\infty \simeq (1/\tau)$, we estimate a total collection efficiency of our set-up at room temperature to be around 1%, ascribed to the limited NA of the optics and their transmission combined with the expected molecule emission profile.

Knowledge of the molecular emission pattern is crucial for assessing and enhancing the excitation and collection efficiencies of the DBT-doped NCs. While in free space the radiation pattern of a molecule is given by the well-known $\sin^2(\theta)$ distribution [231] - with θ being the angle between dipole axis and observation direction - when a molecule is close to dielectric interfaces the emission pattern is altered. This is because light is scattered, refracted or reflected at the interfaces, resulting in interference effects that significantly modify the observed angular distribution.

Dipole orientation and measurement of its emission pattern

The emission pattern can be accessed by performing back-focal-plane (BFP) imaging. Indeed, the spatial distribution of the emitted light is directly encoded in the intensity profile collected on the back-focal plane of the objective (i.e the back-aperture plane) [232]. **Figure 4.9a** gives a simple illustration of how this happens by considering the simple laws of geometrical optics: photons emerging from the source dipole with different orientations of the wave vector k - i.e. forming different angles q with the optical axis - are taken to different points on the objective BFP, whereas parallel wave vectors end up on the same point on the BFP. The intensity profile observed on the BFP can be therefore directly mapped to the angular distribution of the emitted light. In terms of Fourier optics, what happens is that the objective projects the Fourier transform of the field at the entrance pupil onto the BFP.

As shown in **Figure 4.9a**, an image of the BFP can be obtained by placing the camera lens off focus, so that the BFP - rather than the sources - is imaged onto the CCD. This is achieved with a dedicated lens mounted on a flippable holder in front of the camera. The distance between the BFP lens and the camera can be obtained from the well-known lens

equation $\frac{1}{f} = \frac{1}{p} + \frac{1}{q}$:

$$q = \frac{l \pm \sqrt{l^2 - 4lf_{\mathrm{BFP}}}}{2} \tag{4.3}$$

where $l = p + q$ is the total distance between the objective BFP and the camera, f_{BFP} is the focal length of the BFP lens and $p = p_1 + p_2$ as shown in the figure.

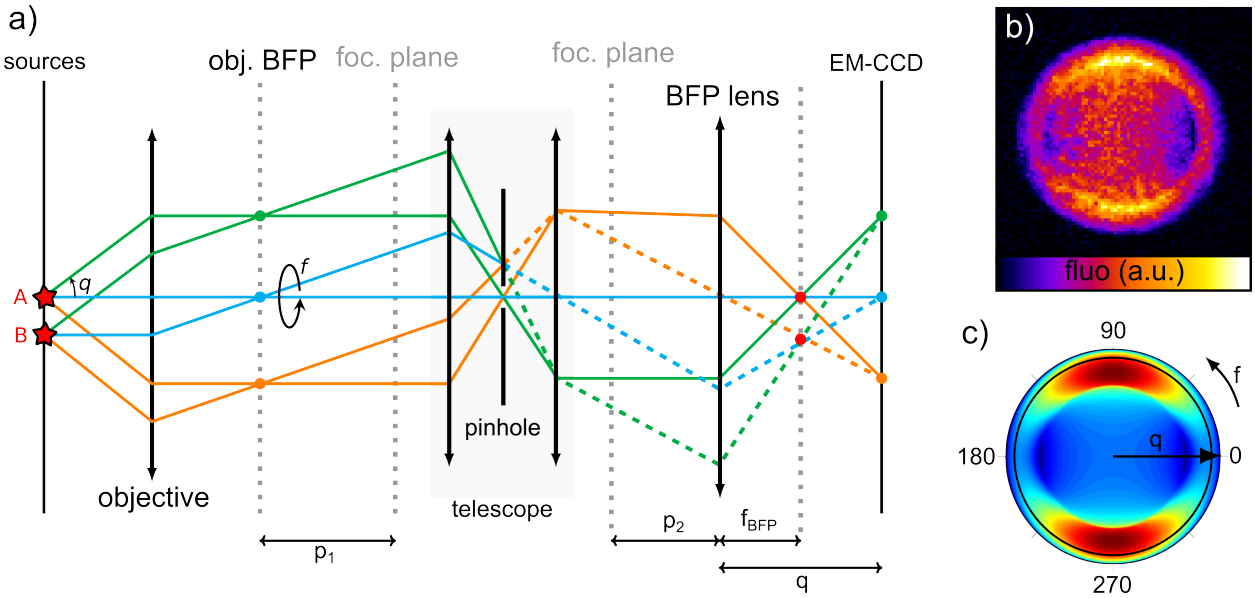

Figure 4.9 – **a)** Schematic representation of the optical configuration used to acquire BFP images. Light emerging from the source dipoles with different orientations of the wave vector k is taken to different points on the objective BFP, which is imaged onto the EM-CCD with the BFP lens. A spatial filter made of a telescope and a pinhole increases resolution and contrast. **b)** BFP image of a single DBT molecule in confocal illumination after background subtraction. **c)** Theoretical prediction for the normalized intensity, collected on a plane in the far field from an in-plane oriented dipole embedded in a 60 nm-thick anthracene layer emitting at 785 nm. The black circle at $q = 67°$ shows the maximum angle that our objective can collect (NA = 1.4) and f is the azimuthal angle on the BFP.

Figure 4.9b shows a typical BFP image of a single NC in confocal illumination, where the emission pattern features two side lobes facing each other, beyond the critical angle ($q_c = \arcsin(n_{\mathrm{air}}/n_{\mathrm{Ac}}) \simeq 34°$) corresponding to the coupling between the evanescent wave in air with the propagative wave in the coverglass [233].

Different single molecules exhibit very similar emission patterns, the geometry of which allows us to conclude that DBT molecules are embedded inside anthracene with their dipole preferentially parallel to the crystal plane [232, 234], or at most out of plane by just a few degrees, in agreement with previous studies on the bulk system [40, 41]. This result is also compatible with the XRD observations previously discussed.

Figure 4.9c shows the theoretical prediction as computed by S. Checcucci [235] for the far field intensity from a single DBT molecule embedded in a 60 nm-thick anthracene layer, oriented with the molecular dipole parallel to the anthracene layer. The inner black ring at $q = 67°$ highlights the maximum angle that we can collect with our oil-immersion objective ($\theta_{\max} = \arcsin(\mathrm{NA}/n_{\mathrm{oil}})$). Comparison of the two figures shows a good agreement between the theoretical model and the observed profile.

To conclude on the observed photophysical properties of the DBT-doped Ac NCs (recipe 1) at room temperature, let us note that the repeated excitation of the same molecule to study its saturation behavior is a qualitative proof of the stability of its fluorescence. After several hours of measurements at room temperature, though, some molecules start exhibiting fluorescence blinking behavior, typically before they stop to fluoresce completely. Photobleaching is most probably due to chemical reactions of the dye molecule with ambient oxygen [236], a process that is more likely to occur in conjunction with the sublimation of Ac at room temperature. For our sub-micrometric crystals we observe that sublimation takes place on a time-scale of about one day but it is completely suppressed when covering the sample with a thin layer of of polyvinyl alcohol (PVA).

4.3.2 Spectroscopy at cryogenic temperature

At cryogenic temperature, single DBT molecules can be addressed spectrally one at a time by tuning the frequency of the narrowband resonant laser and exploiting the inhomogeneous distribution of the molecular resonances, as discussed in Chapter 2.1.2. Let us recall that, depending on the host matrix, single molecules ZPL's can be distributed over a frequency range as wide as few nm [236].

We found that DBT-doped Ac NCs prepared with recipe 2 are suitable for single molecule spectroscopy within our experimental full range of 800 GHz around 784.6 nm, as demonstrated in **Figure 4.10a**. Here excitation spectra collected at 2.9 K from two single NCs are displayed, where we can distinguish more than 80 peaks, each corresponding to a single molecule. Since this measurement is done with a linearly polarized pump, the difference in the peaks' intensity stems from a pumping that is not optimal for all molecules.

The same measurement performed simultaneously on 20 NCs illuminated in wide-field for two orthogonal polarizations of the laser pump allows to estimate the inhomogeneous distribution of the ZPLs of DBT molecules in Ac NCs. The result of this analysis is plotted in the histogram in **Figure 4.10b** from which we deduce a mean value of the transition frequency equal to 785.1 nm with a standard deviation of 0.4 nm (or equivalently 180 GHz), which is

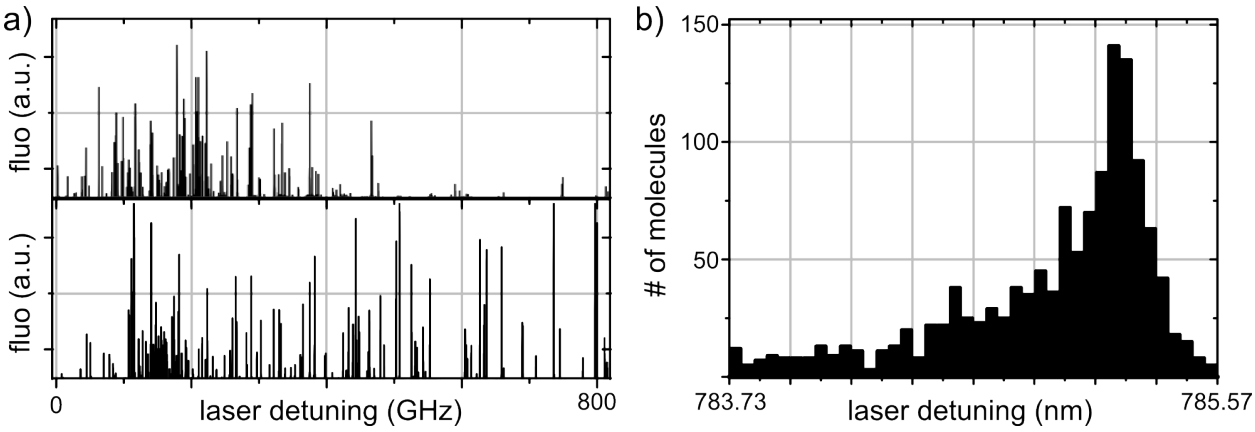

Figure 4.10 – **a)** Excitation spectra collected from two NCs at 2.9 K, within a frequency range of 800 GHz around 784.6 nm. Each peak corresponds to a single molecule. **b)** Estimation of the inhomogeneous distribution of the ZPLs, obtained from the simultaneous detection of the excitation spectra from 20 NCs illuminated in wide-field for two orthogonal polarizations of the laser pump. The distribution yields a standard deviation of of 0.4 nm around a mean value of 785.1 nm.

in agreement with the inhomogeneous broadening measured for other dyes in crystalline systems [85].

Figure 4.11a shows the excitation spectrum of a single DBT molecule illuminated in confocal mode at intensities below saturation (0.3 W cm^{-2}), recording the red-shifted fluorescence with a single APD (black circles). The homogeneously broadened spectral line is fitted with a Lorentzian profile (red curve) yielding a FWHM of 51 MHz, with an uncertainty of 10 MHz given by the standard deviation of four consecutive measurements of the same spectrum.

Repeating this procedure on 35 molecules in different NCs leads to the distribution displayed in the inset of **Figure 4.11a**, with a low-width cut-off consistent with the lifetime-limited value of 40 MHz. The presence of molecules with broader linewidth can be explained in terms of the reduced size of the NCs, which provide an environment for DBT molecules less homogeneous than of the bulk Ac and where interface effects on fluorescence stability and hence linewidth broadening are more likely to occur. However, let us note that the observed linewidth distribution is narrower than what measured by Gmeiner and colleagues [237] for dibenzanthanthrene (DBATT) molecules in annealed naphtalane nanochannels, confirming the high crystallinity of the Ac NC grown via reprecipitation.

Figure 4.11b shows a typical saturation profile of a single molecule in logarithmic scale and its line broadening at low temperatures, obtained by measuring its excitation spectrum for several pump powers and plotting the detected maximum fluorescence count rate at resonance (blue circles) and the FWHM (red circles) as a function of the excitation intensity.

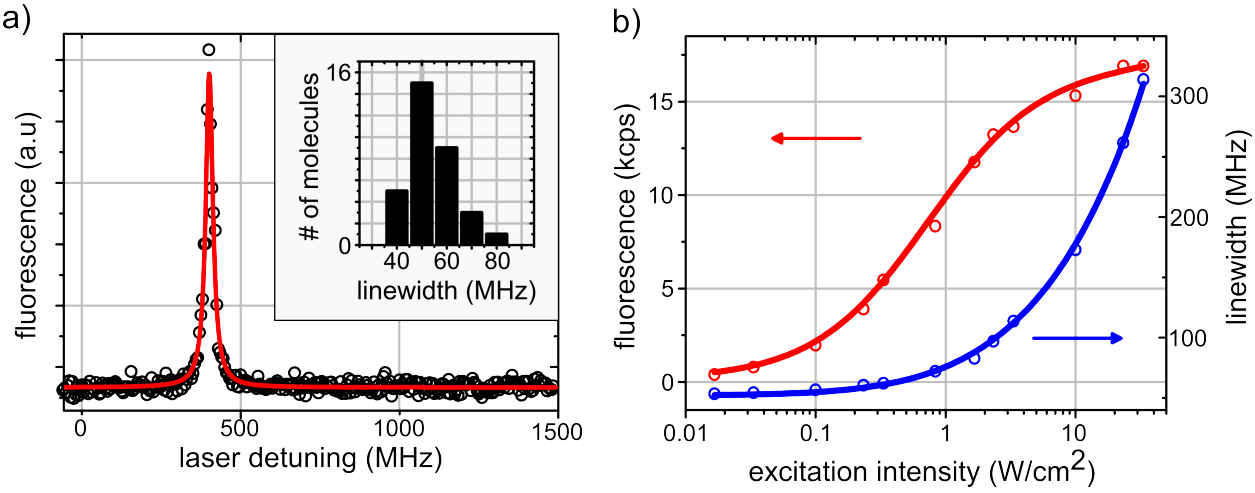

Figure 4.11 – **a)** Resonant excitation spectrum of a single DBT molecule in Ac NCs measured at 2.9 K. The homogeneously broadened spectral line is fitted with a Lorentzian profile (red curve) with a FWHM of (51±10) MHz, averaged over four consecutive measurements. Repeating this procedure on 35 molecules in different NCs leads to the distribution displayed in the inset. **b)** Saturation curve (red) and power broadening (blue) of the homogeneous 00-ZPL collected as a function of the resonant excitation intensity. Both behaviors fit perfectly with the expected saturation laws: saturation yields a maximum number of detected photons $R_\infty = (16.8 \pm 0.04)$ kcps.

Detected counts are fitted with equation (1.24), providing a saturation intensity $I_s = (0.73 \pm 0.03)$ W cm^{-2} - of the same order of magnitude measured for the bulk system - and a maximum number of detected photons $R_\infty = (16.8 \pm 0.04)$ kcps (or equivalently $R_\infty = 34$ kcps accounting for the detection efficiency). This count rate is compatible with the collection efficiency of our experimental set-up for low temperature measurements of about 0.3^{-3}, mainly limited by the orientation of the emissive dipole and the low NA of the collecting optics. The power broadening of the homogeneous spectral line $\Delta\nu(I)$ fits perfectly with the expected saturation law (blue line in **Figure 4.11b**) given by the equation (2.5), which assumes negligible spectral diffusion.

An important property of a single molecule system, in particular in view of quantum optics experiments, is indeed the stability of the absorption frequency of single molecules over time. In polymers and glasses the stability of the absorption frequency is deteriorated by local degrees of freedom, which at cryogenic temperature can be modeled by two-level tunneling systems that interact with the molecule via electric or strain fields [238].

We therefore carefully analyze the spectral stability of the molecule transition frequency, which hence turns out to be a key result of this study. In **Figure 4.12a**, the NC fluorescence counts from an APD are displayed in a 2D color map, obtained repeatedly scanning for about 1 h the excitation frequency of the pump laser over 10 GHz. The excitation of two different

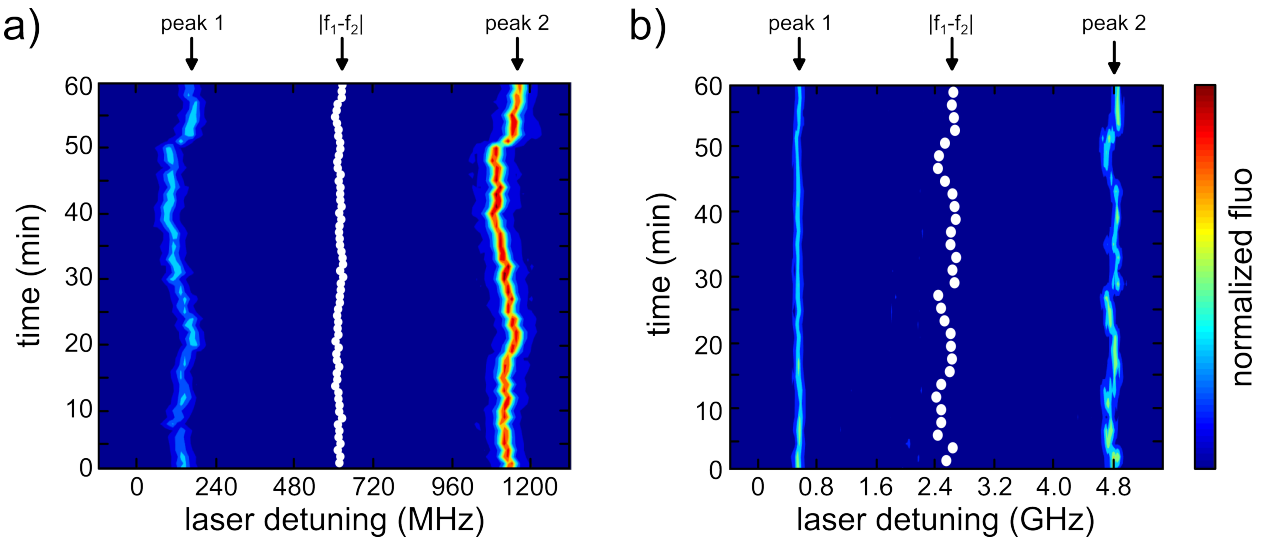

Figure 4.12 – 2D plots representing the time traces of the spectral lines of single molecules. Since our resonant laser is not referred to any absolute frequency standard, investigation on spectral diffusion is done collecting spectral time traces in a frequency range where two molecules within the same NC are excited. To get rid of the laser instability contribution, the analysis of spectral diffusion is done on the difference of the two peak central frequencies, plot as white circles in the map. In the time traces mapped in **a)**, the maximum variation of such differential value is 17 MHz, which is well within the molecule linewidth and suggests the absence of spectral diffusion. The time traces in map **b)** is the only observed case of a molecule undergoing spectral diffusion, yielding a maximum variation in the difference between the two peak centers of 54 MHz.

molecules can be recognized. The mean value and standard deviation for the two FWHM of the spectral lines over all measurements is (65 ± 6) MHz for peak 1 and (59 ± 4) MHz for peak 2. The common-mode fluctuation of the peak central frequencies is a clear indication of the pump laser residual instability (the laser diode is thermally stabilized but not referred to any absolute frequency standard).

To get rid of this contribution and highlight possible spectral diffusion, we analyze the difference of the two peak central frequencies, plot as white circles in the map. The maximum variation of such differential value is 17 MHz, which is well within the molecule linewidth and suggests the absence of spectral diffusion for DBT:Ac NCs at 2.9 K. Indeed, performing the same analysis on couple of molecules in 8 different NCs we observe only one molecule undergoing spectral diffusion, shown in **Figure 4.12b**. Here, from the time trace of the excitation spectra of the 2 molecules, we calculate a FWHM $= (64 \pm 7)$ MHz for peak 1 and a FWHM $= (86 \pm 30)$ MHz for peak 2. The difference of the two peak centers shows a maximum variation of 54 MHz, which thus represents an estimation of the spectral diffusion observable in DBT:Ac NCs.

The spectral analysis discussed above should be compared with the behavior of aromatic

molecules in polymers or other amorphous hosts, where linewidths as large as few GHz are accompanied by large spectral jumps (of the order of tens of GHz) [236, 238, 239]. Moreover, when molecules are embedded in a poor crystalline environment, a broadening of both linewidth distribution and inhomogeneous distribution is observed and spectral jumps, even if in a narrow frequency range of tens of MHz, are more likely to occur [237].

4.4 Conclusions

In this chapter we propose a novel protocol to fabricate high quality DBT-doped Ac crystals with average size of few-hundreds nanometer. The growth procedure is based on reprecipitation, an easy and inexpensive method that allows for a precise tuning of DBT concentration within single Ac NCs. X-ray diffraction confirms the crystallinity of the NCs, and AFM analysis shows their average thickness of 65 nm, which is particularly promising for the coupling to evanescent fields in the proximity of surfaces [20].

The photophysics of DBT molecules within the Ac nanocrystalline environment is characterized at room temperature by measuring the second order autocorrelation function, the emission radiation pattern, the excited state lifetime and the saturation behavior, demonstrating 1.5 MHz count rate from single molecule in a NC, with a purity as high as 0.0025 and a well defined dipole orientation.

Further investigations at 2.9 K demonstrate that the vast majority of molecules show linewidths close to the lifetime-limited value over a relative narrow inhomogeneous distribution of 0.4 nm (or equivalently 180 GHz) around a mean value of 785.1 nm. Remarkably, due to the crystallinity of the host, most of the single molecules observed show stable absorption lines allowing long time measurements with no spectral jumps. Accurate study on their photostability shows in fact that each NC embeds several molecules exhibiting stable fluorescence lines, with no signs of blinking or spectral diffusion on time scales of hours. Spectral jumping over a frequency range of about 50 MHz is observed on one molecule, probably located close to the NC interface.

Being easier to handle and manipulate than the bulk system, DBT-doped Ac NCs can in principle be pre-characterized and deterministically integrated into complex nanophotonic devices, such as cavity or waveguides, as demonstrated for other sub-micrometric quantum emitters. We believe that the enabling of site-specific emitter engineering will open new perspectives for the use of molecules in the development of realistic quantum technologies. Indeed, this feature, together with the possibility to match molecule transition frequencies by applying a Stark voltage [159], paves the way towards the deterministic implementation

of several single-photon sources in parallel to realize complex photonic networks for on-chip quantum operations.

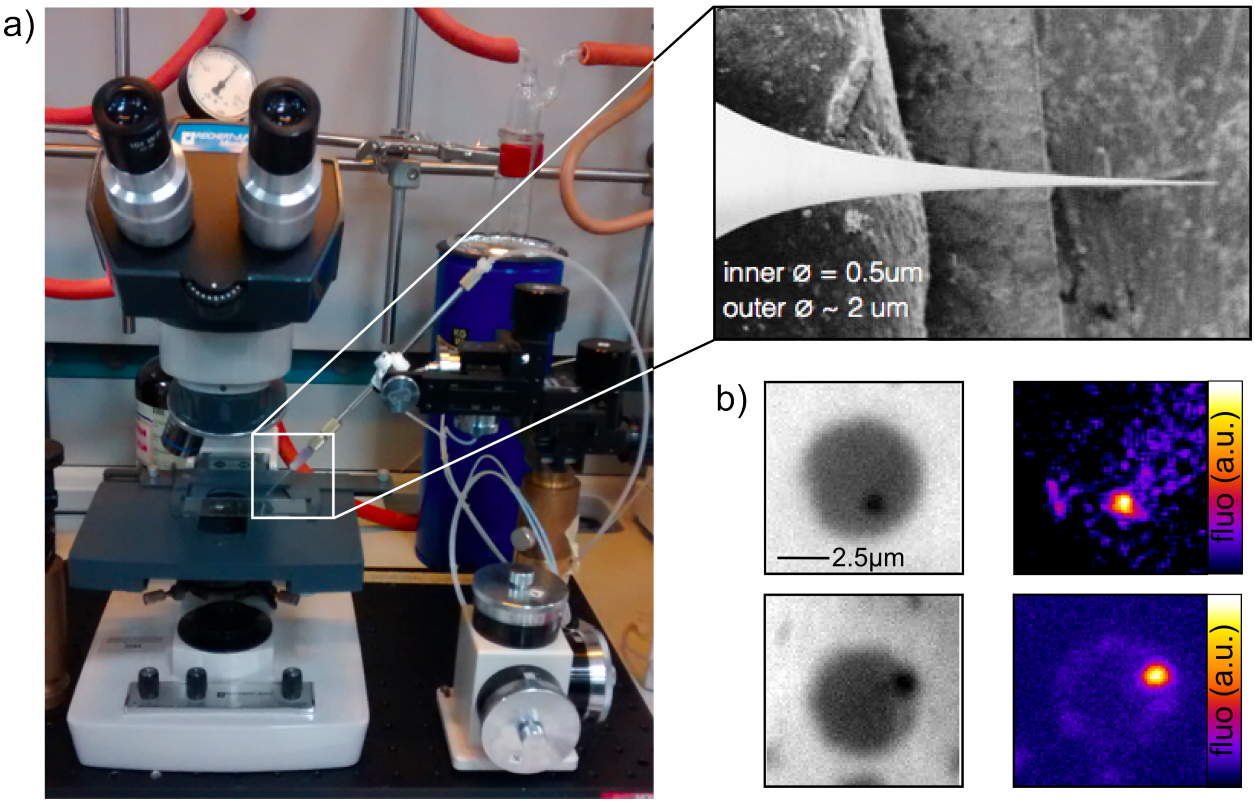

Figure 4.13 – **a)** Microinfiltration system mounted on a commercial standard microscope equipped with10X and 50X objectives used to monitor the pipette µm-movement on a substrate. The pipette has an outer diameter of 2 µm and inner diameter and 0.5 µm. **b)** Comparison of white-light and fluorescence wide-field images of two infiltrated holes.

As a proof of principle, we demonstrate that, dispersed in water, NCs can be easily handled and manipulated at room temperature with the micro-infiltration set-up shown in **Figure 4.13a**. This system, developed for molecular applications, has been used to infiltrate individual pore in photonic crystal structures with liquids of different refractive index, suggesting a procedure to write either permanent or rewritable photonic circuits [240]. The micro-infiltration set-up (Eppendorf Femtojet) consists of a micropipette (Eppendorf Femtotips) - with external diameter of about 2 µm and inner diameter of 0.5 µm - held on a 3D micrometric stage. NCs-water suspension is injected in the micropipette, upon filtering with a 450 µm pore size-filter (Sartorius Minisart) to get rid off eventual clusters of NCs or other impurities with size larger than the pipette's inner diameter.

An optical microscope, equipped with a 10X and 50X objectives (respectively Officine Galileo NA=0.22, and Olympus SLM Plan NA=0.45), is used to monitor the approach of

the pipette to the sample surface, where it can be positioned with sub-micrometric precision by means of hydraulic transmissions. **Figure 4.13b** shows white light and fluorescence wide-field images of two infiltrated holes etched on a silicon chip with 5 µm diameter, acquired after water evaporation. Their comparison demonstrates that DBT:Ac NCs in suspension can be handled and deterministically integrated at room temperature, remaining stable for a time scale of hours (accounting for the suspension preparation, infiltration of multiple holes and their optical observation).

The micro-infiltration set-up may represent a reliable manipulation technique for applications requiring micrometric precision in the emitter displacement. For nanostructures working in the visible range, however, other pick-and-place methods can be used to enable positioning of support-free DBT:Ac NCs with sub-micrometric precision. For example, one may pick up a pre-characterized NC with tapered fibers mounted on a nanomanipulator or with the tip of an AFM, mounted on top of the inverted confocal microscope for optical access and hence allowing positioning in a controlled manner. Alternatively, NCs can be embedded in polymeric patternable materials. This approach appears a natural and promising pathway for integrated quantum photonics, and we will discuss it in the following chapter.

5 Organic Nanocrystals Integrated in Polymeric Structures

In this chapter we report on preliminary results concerning the compatibility of DBT-doped Ac nanocrystals with polymers and their patternable processes. In particular, we investigate 3D-direct laser writing and electron-beam lithography. Our results find immediate applications for the development of single-photon sources integrated on-chip and for the study of the interaction between single quantum emitters and 2D materials.

5.1 Background and Motivations

The quest for miniaturized photonic integrated circuits is triggering research on novel materials which can be processed with easy and cost-effective fabrication processes enabling high integration density of reduced size components. Semiconductor and dielectric materials are in fact relatively expensive and the processes used to fabricate photonic devices in those materials are usually very complex. Realistically, the development of increasingly complex photonic circuits will rely on materials that enable novel functionalities and processable with fabrication techniques that are compatible with the existing silicon electronics.

Particularly promising for this purpose are polymeric materials. The term polymer refers to a large molecule, or macromolecule, whose structure is that of a covalently bonded chain composed of many repeated subunits, known as monomers. One of the advantages of polymers over other materials is that their synthesis (namely polymerization[1]) is relatively inexpensive and allows broad tunability of the material electro-optical and mechanical properties. Indeed, the physical and optical properties of polymers can be tailored to a large extent by controlling their chemical structure with different processes, including oxidation, cross-linking[2] and end-capping [241]. Moreover, polymers can be processed using a variety

[1]Specifically, polimerization is the chemical process in which monomers assemble together to form a polymeric chains or three-dimensional networks of polymers.

[2]A cross-link is a bond that links one polymer chain to another. For example, a liquid polymer where the chains are freely flowing can be turned into a "solid" or a "gel" by cross-linking the chains together.

of methods - as e.g. solution and gas-phase deposition - and can be made compatible with arbitrary substrates by suitable surface functionalization.

Polymers can be patterned with well-established technologies, such as e-beam lithography [242, 243], reactive ion etching [244], nano-imprinting [245] and photolithography followed by wet etching [246]. Interestingly, advanced lithographic techniques that provide access to truly 3D polymeric geometries are also available. Among them, direct laser writing (DLW) is rapidly emerging and holds promise for photonic applications. Indeed, this fabrication process inherently enable scalability and interconnection for 2D and 3D networks and its compatibility with planar semiconductor-based optical circuits made by standard electron-beam lithography has been recently demonstrated [247].

All the mentioned features are currently promoting polymers in the field of nanophotonics, where they can be employed for several purposes. First, they can be used as sacrificial layers or templates for producing photonic structures with complex design. Alternatively, they can possess useful optical properties themselves, such as photoluminescence or nonlinear optical properties [248]. Additionally, passive photonic components such as resonators [249], waveguides [250, 251], photonic crystals [252] and wirebonds for interchip communication [253] can be fabricated. Finally, they can readily produce hybrid nanocomposites in which they act as matrices for optically active species such as dyes [254], quantum dots [255, 256], and metal nanoparticles [257, 258].

Recently, integration of single sub-micrometric quantum emitters in 3D polymeric structures has been proposed [36], yielding to the first demonstration of guided single-photon emission from NV-centers in nanodiamonds embedded in a suspended waveguide fabricated with DLW [259].

These first experiments highlight the great potentialities of patternable polymers for quantum photonic applications. Indeed, the embedding of NCs in polymeric photonic structures represents an improvement in terms of coupling efficiencies with respect to the performances achievable in conventional schemes, where the emitters are positioned on the structures' surface and evanescently coupled to it. In a waveguide geometry, a sub-micrometric quantum emitter can now be located at the maximum of the guided mode field, with a corresponding increase of the emission rate into the guided mode. Moreover, provided a small refractive index mismatch between the emitter matrix and the waveguide material, losses due to scattering - unavoidable in the case of evanescent coupling - can be strongly reduced. To date, only inorganic NCs have been employed, due to their natural compatibility to most of the solvents used in the fabrication steps and to the high energy irradiation employed in the most common lithographic processes. However, as discussed in Chapter 4, their opti-

cal properties are sub-optimal for basic quantum optics operations with the emitted photons.

In this chapter we report on preliminary studies on the compatibility of DBT-doped Ac NCs with different polymeric materials and with their patternable processes. In particular, we focus on two possible applications:

1. integration of organic NCs into photoresists developed for DLW. The goal is to verify that the remarkable optical properties of the NCs are not strongly affected by this lithographic process. This is discussed in Section 5.2 choosing, as a first photonic platform, a 3D suspended waveguide fabricated around a single NC. The experimental realization of such device and preliminary results are presented in Section 5.3.

2. integration of organic NCs into water-soluble polymer as they are naturally prone to embed the NCs and prevent their sublimation at room T. This is discussed in Section 5.4, choosing a material that combines good membrane-forming properties and patternability opportunities. These features are promising to study e.g. the nanoscale interaction between single quantum emitters and exfoliated 2D materials, which can be safely deposited on top of the polymeric flat (and eventually patterned) layer with the well-know scotch-tape method [260] (Section 5.4.1).

5.2 Direct Laser Writing of Polymeric Waveguide

In DLW a femtosecond pulsed laser is tightly focused inside a photosensitive material (or photoresist). Patterning occurs by two-photon absorption that induces polymerization. This process, briefly described in in Section 5.2.1, causes a permanent chemical and physical modification of the photoresist within a small volume determined by the laser intensity distribution. Hence, by moving the sample, the material can be polymerized along arbitrary 3D trajectories.

In this work, we employ a commercial DLW workstation that is presented in Section 5.2.2. In order to fabricate a polymeric suspended waveguide embedding in its center a single DBT-doped Ac NC, we employ two commercially available negative-tone[3] photoresists (Section 5.2.3), in which the NCs can be sandwiched. A simple design of a suspended guiding structure able to fully envelope a single NC is discussed in Section 5.2.4. The proposed geometry

[3]Photosensitive materials suitable for DLW belongs to two classes: the negative-tone photoresists, in which two photon absorption is associated to cross-linking of polymer chains, allowing the unexposed resist to be washed out; and positive-tone resists, where two photon absorption leads to chain scission, creating shorter units that can be dissolved and washed away in the development process.

promises coupling efficiencies up to $\beta = 52\%$ between the fully integrated emitter and the guided modes supported by the suspended waveguide.

5.2.1 Two-photon polymerization

The possibility to use UV light to induce polymerization was first pointed out by Kodama and colleagues [261]. In this process, one UV photon is absorbed through a linear absorption mechanism, either directly by the reactant monomer or mediated by a photoinitiator, which absorbs light and transfers energy to the material, inducing its polimerization or cross-linking.

Single-photon polymerization lends itself for 3D patterning [262] but, due to the poor penetrating ability, the UV light is absorbed within the first few micrometer in the photoresist and hence does not satisfy the modern requirements for device miniaturization. However, the same reaction induced by the linear absorption of UV light can be activated exploiting a two-photon absorption process induced by a near-IR femtosecond laser [263]. Materials with one-photon energy well below the two-photon absorption edge are perfectly transparent in the near-IR, allowing light to deeply penetrate into the photosensitive material.

In this nonlinear process, transition of a molecule from the ground to the excited state is mediated by a virtual state with an extremely short lifetime (order of fs), and can occur only if the second photon is absorbed before the decay of this virtual state.

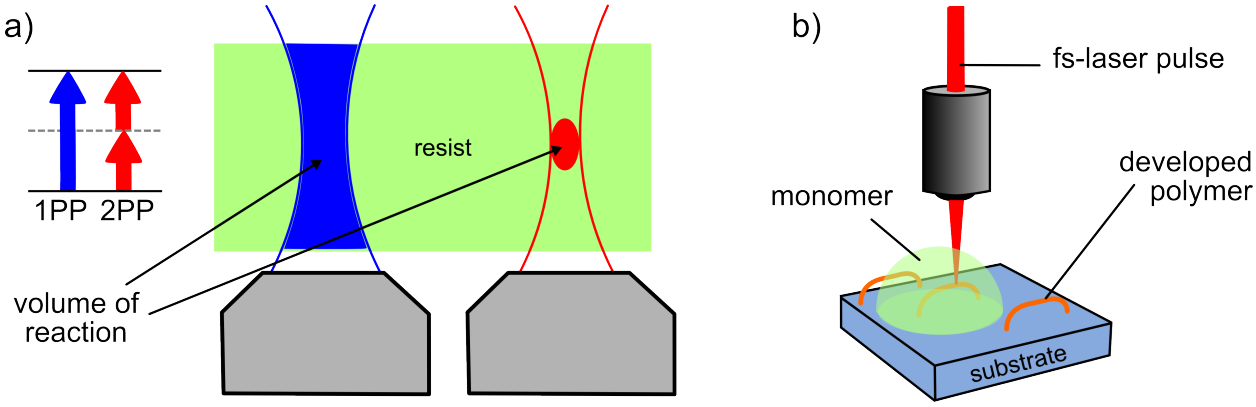

Figure 5.1 – **a)** Comparison between one-photon and two-photon absorption processes and the volumes they respectively activate in a photoresist. Since the non-linear two-photon absorption process scales with intensity, the polymerization occurs where the intensity is the highest, i.e. in the focal volume (voxel) of the laser. **b)** Illustration of the DLW process of a negative-tone photoresist, designed such that single photons from the writing laser cannot be absorbed, but a two-photon absorption can induce polymerization. By moving the sample (or the laser focus), arbitrary 3D trajectories can be polymerized, with the resolution being limited by the voxel size.

Being a third-order process, two-photon absorption depends on the square of the light

intensity and can hence dominate over linear absorption only at high intensities. **Figure 5.1a** compares the volumes activated by one-photon and two-photon absorption, when a microscope objective is employed to focalize a UV- and IR-laser, respectively. The volume of two-photon absorption is much smaller than the one activated by the linear process, since polymerization occurs where the intensity is the highest, i.e. in a confined 3D volume around the laser focus, named voxel. Hence, by moving the laser spot (or the photoresist drop-casted on a substrate), arbitrary 3D trajectories can be polymerized, with a resolution limited by the voxel size. At the end of the writing process, the unexposed parts of the photoresist are washed away in organic solvents, leaving a free-standing 3D structure on the substrate (**Figure 5.1b**).

In the last 30 years, several photosensitive materials have been chemically synthesized with the desired two-photon polymerization (2PP) cross-section and are now commercially available for the fabrication of ultraprecise 3D-microstructures with high resolution [264]. To date, lateral voxel sizes down to 120 nm for illumination at a wavelength of 780 nm have been reported [265], well below the diffraction limited resolution that is about 280 nm for this wavelength. Such fabricated structures are proposed for many applications, ranging from microfluidics [266] and biomedical implants [267] to micro/nanophotonics devices [268].

5.2.2 The set-up

The instrument used in this research is a commercial DLW workstation (Photonic Professional GT, Nanoscribe GmbH), currently available in our laboratories. The main components of the set-up and its working principle are sketched in **Figure 5.2**. The system includes a pulsed erbium-doped fiber laser source that delivers 120 fs-pulses with a 100 MHz repetition rate[4] at a center wavelength of 780 nm. The laser power is calibrated by the use of an acousto-optic modulator (AOM) to compensate for intensity fluctuations and drifts. The laser and the optics are hosted in a protective housing equipped with an electrical interlock switch, and are assembled on an optical table to ensure a passive vibration isolation.

The laser beam is tightly focused through a high NA oil objective (100X, Zeiss Plan Apocromat, NA = 1.4) into the photoresist deposited on a substrate mounted in an inverted microscope configuration. Depending on the resist, the objective can be dipped directly into it (dip-in lithography) or into the immersion oil matching the refractive index of a transparent substrate supporting the photoresist (immersion lithography). When the light

[4]It has been demonstrated that operating with this high repetition rates and short pulses lead to high-resolution structures [269].

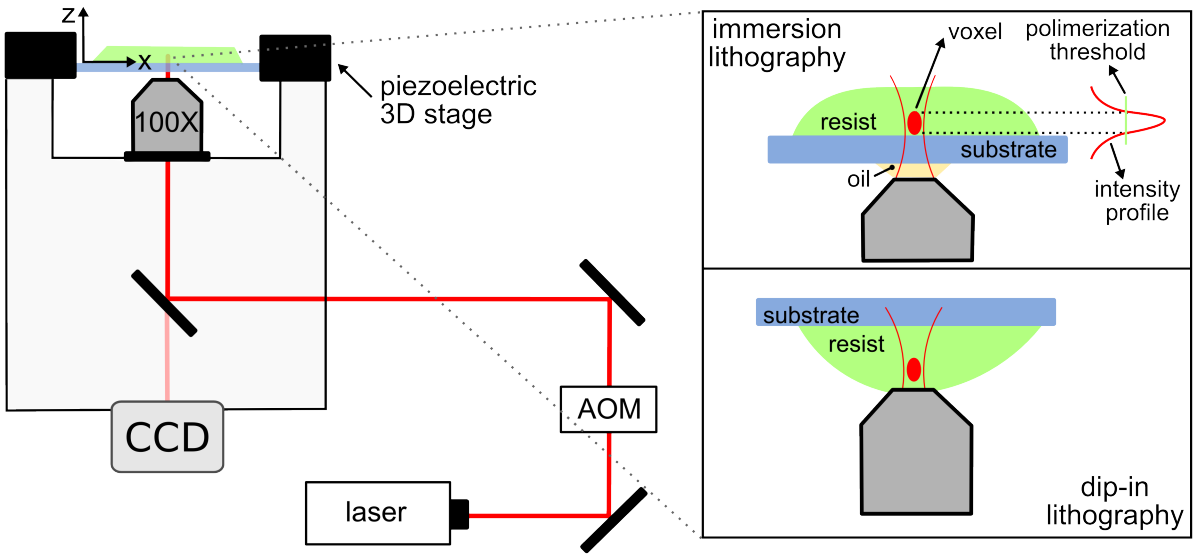

Figure 5.2 – Illustration of the commercial DLW workstation used in this work, consisting of a piezo-stage mounted on top of an inverted microscope and a pulsed laser with 120 fs pulse-width, 780 nm wavelength and 100 MHz repetition rate. The laser power is calibrated by the use of an acousto-optic modulator (AOM) to compensate for intensity fluctuations and drifts. A high numerical aperture (N.A. = 1.4) objective tightly focuses the light into a tiny volume (i.e. voxel). The objective can be dipped into an immersion oil when the photoresist is above the substrate (immersion lithography) or can be dipped directly into the resist when the resist is eligible (dip-in lithography).

intensity inside the voxel exceeds the threshold[5] for initiating the 2PP process, the writing process starts.

The sample holder is mounted on a three-axis piezo stage that scans the sample relative to the fixed focal spot (piezo-scan mode[6]) on a range of about 300 µm^3, allowing for 3D-shaping of the photoresist. Additionally, the piezo stage can be moved as a whole by a manual 3D-stage that offers the opportunity to write at different positions on the same substrate.

The writing process is monitored real-time with a CCD camera and is operated remotely by means of software components included in the Photonic Professional system. In particular, the software NanoWrite is employed to calibrate the system and control the sample stage,

[5]The polymerization threshold is defined as the lowest power able to create a well-defined polymeric line at the glass-resist interface after the development process. This parameter depends on several effects, and can be experimentally determined by performing writing tests at the glass-resist interface while varying the writing speed and the laser power.

[6]The system provides an alternative mode, consisting in scanning the focal spot by means of galvo mirrors, while maintaining the sample on a fixed position along the xy-plane (galvo-scan mode). The piezo-stage is here only used for z-displacements, allowing to write 3D structures layer by layer. The minimum scan speed is higher than that provided by the piezo-scan, as this mode is meant for printing millimeter-scale structures.

according to an input .gwl (General Writing Language) edited with the provided text editor Describe. The .gwl file specifies all the parameters of the process (such as the laser power and the writing speed) and describes the trajectories to be followed during the writing process.

As discussed in Section 5.2.1, the resolution of the 3D writing process is determined by the voxel. It has typically an ellipsoidal shape whose dimensions depends on several parameters, such as the laser power, the exposure time (i.e. the writing speed) and the NA of the objective lens. Moreover, due to the linear dependence of the intensity on the refractive index value, the voxel dimensions depend also on the employed photosensitive material. Therefore, before starting the fabrication of a 3D structure, it is necessary to establish the best suited parameters for the specific photoresist in use and for the geometry of the final structure, in order to find the best compromise between a reduced fabrication time and high quality of the fabricated device.

5.2.3 Materials and methods

In order to write a suspended waveguide embedding a single NC, we follow the concept proposed by Shi and colleagues [259] in which a nanodiamond is deposited in between two layers of negative-tone photoresist with very similar refractive index, high enough to ensure tight confinement of the supported guided mode. Since it is important that the particle does not move during the writing process, Shi et al. underline that the lower layer should be preferably solid.

In our case, the choice of the photoresist is done accordingly to the following requirements:

1. the chemical composition of the photoresist should be compatible with Ac so to minimize deterioration of DBT optical properties;

2. owing to the platelet-like shape of the NCs, a highly viscous material would prevent penetration of the NCs in the lower photoresist and can be considered in alternative to a solid photosensitive material, usually requiring a high temperature backing step;

3. to ensure a low S/N and hence detectability of the single-photon signal, the resist should not fluorescence in the near-IR;

4. the main risk in our case is the exposure to the high field intensity femto-laser and the developing step with organic solvents and hence a photoresist requiring relatively low exposure and developing time is preferable;

5. finally, with the long-term vision of employing a similar structure as an integrated SPS of lifetime-limited photons, the photoresist should be compatible with cryogenic temperatures.

FEATURES	IP-L (780)	IP-G (780)	IP-Dip
refractive index at 780 nm **unexposed**	1.48	$\simeq 1.5$	1.52
prebake	no	yes	no
cast process	drop-casting	drop-casting and spin-coating	drop-casting
exposure	2PP at 780 nm	2PP at 780 nm	2PP at 780 nm

Table 5.1 – General features of the IP-series.

Among the commercially available photosensitive materials for DLW we employ the series of negative-tone IP-photoresists provided by Nanoscribe, as they satisfy the requirements outlined above. The main features of these photoresist are summarized in **Table 5.1**. Note that the refractive index values are that of the unexposed material: upon polimerization, an increase in effective index of about 0.02 is expected [270].

The IP-photoresists can provide high resolution and high mechanical stability for structures in the micro- and sub-micron range. In fact, these resists have typically low stress, little shrinkage, low proximity effect and a high adherence to a glass substrate. Moreover, they are easy to manipulate as they don't require sophisticated safety tools. Finally, their glass transition occurs at temperature higher than room temperature and they are hence employable for cryogenic cooling.

The concept of the fabrication procedure of our hybrid device is sketched in **Figure 5.3a**, where DBT-doped Ac NCs suspended in water are drop-casted and desiccated on a spin-coated layer of IP-G. The viscosity of this photoresist increases during the baking step (30 min at 100 °C), preventing the vast majority of the crystals to dip into it. As for the substrate, we use fused silica ($n = 1.45$) in order to ensure a sufficient refractive index contrast with the IP-G layer. This is convenient to find the relative interface during the writing process and hence correctly bind the suspended structure to the substrate.

Spin-coating a reasonably thin and uniform IP-G layer is not trivial as the resist viscosity change every time its bottle is opened, owing to the high volatility of the employed solvent

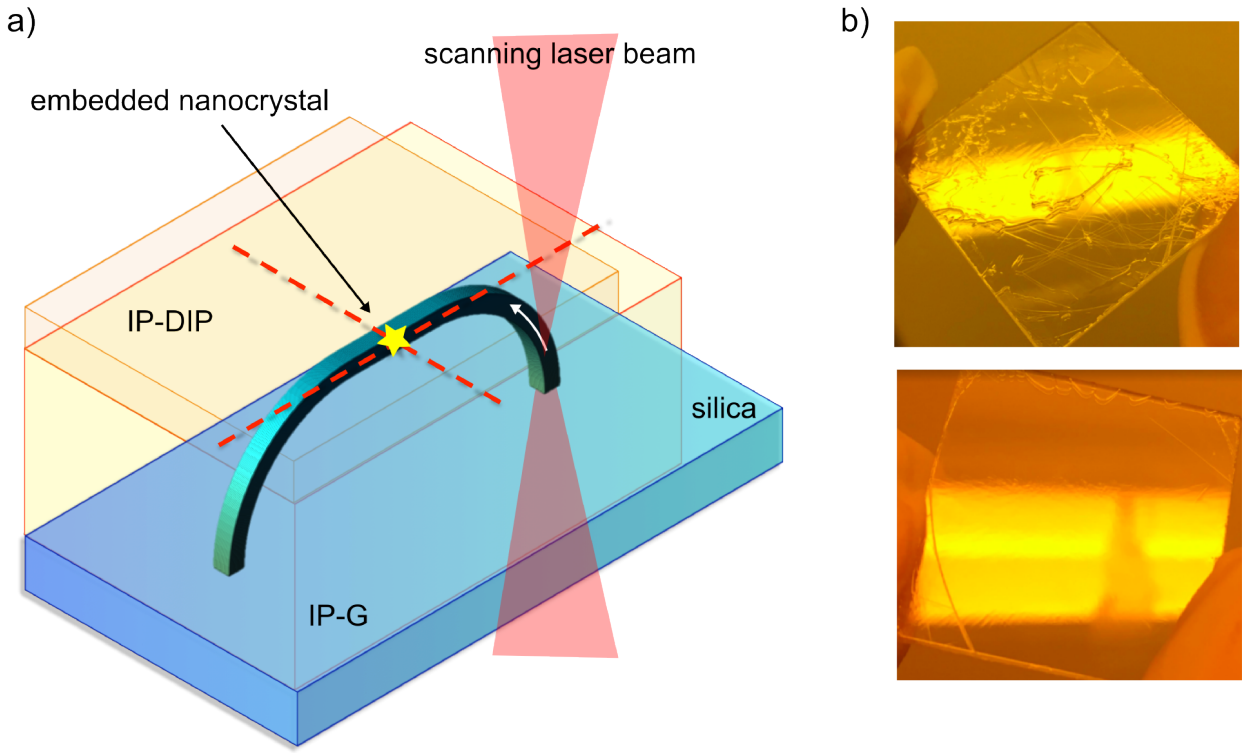

Figure 5.3 – **a)** Concept of the proposed hybrid device, consisting in a single DBT:Ac NC sandwiched between two photoresist (IP-G and IP-Dip) with almost identical direct laser writing parameters, hence allowing to wire up the NC in a suspended waveguide fabricated via DLW in one step. **b)** The high viscosity of IP-G makes spin-coating of this photoresist not trivial and spaghetti-like features on top of the spin-coated layer are likely to occur.

(butanone) [271]. By means of profilometric measurements, we find that spin-coating 40 µL at 300 rpm for 2 s with a subsequent step at a high speed of 9999 rpm (the highest achievable with our instrument) for 45 s, yields rather uniform layers (roughness less than 0.1 µm) with a thickness variation between 3 and 20 µm from sample to sample. Despite this great variability, this recipe turns out to be the most reproducible in terms of layer uniformity, with a low probability to obtain spaghetti-like features on top of the spin-coated layer (see **Figure 5.3b**). For stability reason, that will be discussed in Section 5.3.2, IP-G layers with thickness up to 13 µm are acceptable for our purpose.

The layered structure is then covered with a drop of IP-Dip (no baking steps, that would promote Ac sublimation, are required), allowing for in-dip lithographic processing of the guiding structure, written around a single NC.

After the writing step, the unexposed photoresists are removed with a development bath of

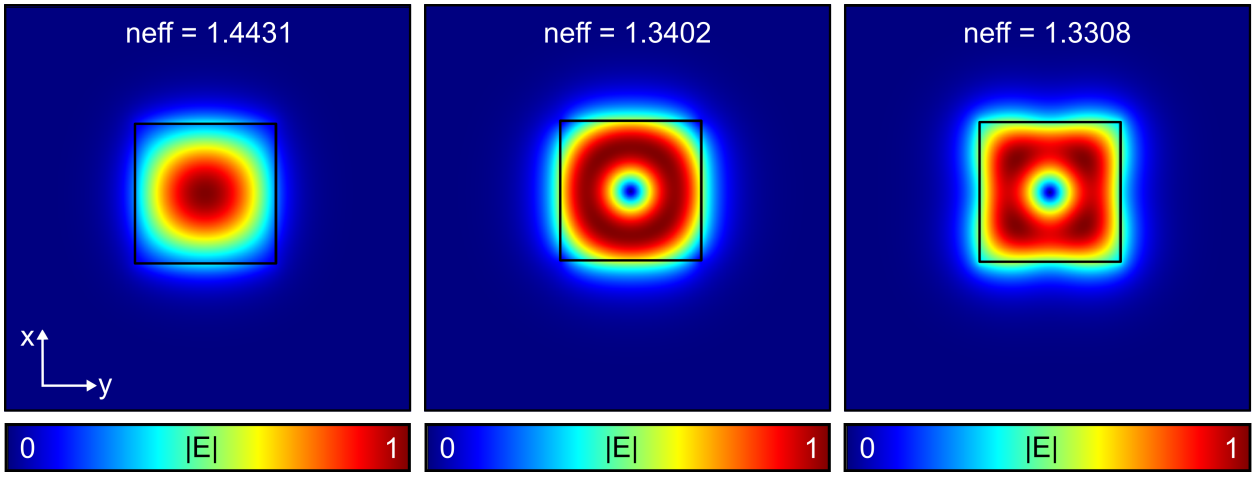

Figure 5.4 – 2D color-coded plots of the normalized electric field intensity of the first three modes supported by the polymeric waveguide with square-cross section (lateral size of 1 µm) at 780 nm and respective effective refractive indices.

15 min in propylene glycol methyl ether acetate (PGMEA, Sigma Aldrich) and subsequently immersed in hot 2-propanol[7] (50 °C for 15 min), to completely dissolve the unpolymerized material without any degradation of the polymerized structures. Finally, the substrate with the written structure is gently blow-dried with nitrogen.

5.2.4 Design Considerations

Since our goal is to fabricate waveguides capable of integrating individual DBT:Ac NCs and test the degree of survival of the fluorescent system to the writing process, the design of the guiding structure is kept very simple, fulfilling basic fundamental requirements.

First, we aim at guiding structures with a tight mode confinement inside the waveguide, where the NC is located. Furthermore, the waveguide should be written with relatively easy trajectories. A squared cross-section is hence chosen for convenience, with a lateral size of 1 µm to ensure that the NC is completely enveloped inside the structure.

Using the Mode Solver from Comsol, we calculate the modes (i.e. their field distributions and the effective refractive index $n_{\mathrm{eff},m}$) supported by the waveguide at 785 nm. The results of this analysis demonstrate that the waveguide supports several modes at our operating wavelength (the three first modes are shown in **Figure 5.4**). Due to the refractive index contrast between waveguide and air, the fundamental mode field is tightly confined inside the structure; higher order modes present instead an evanescent component in the cladding. Since in our case the dipole is placed close the center of the waveguide and mainly orientated

[7]Since the IP-photoresists are low soluble in 2-propanol, heating up to 50 °C is recommended.

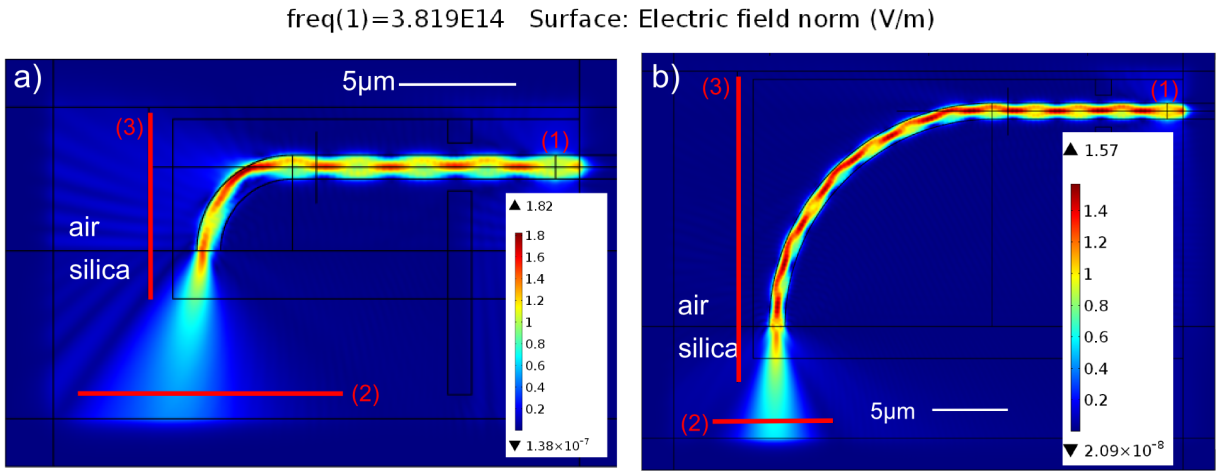

Figure 5.5 – 2D simulation model used to study the bend losses of the quarter rings coupling structures. The color plots correspond to the norm of the electric field distribution for the lower and the higher fabricated waveguide, respectively 3 µm **(a)** and 13 µm **(b)**. The guided mode is pumped by a line source (1), and the amount of the bent losses, accounting for both radiation and transition contributions, is evaluated as the energy flux through the detector line (2) normalized with the sum of the energy fluxes through detectors (2) and (3).

along the y-axes, low excitation probability of the higher order modes is expected.

Perpendicular coupling structures are employed for collection of light through the glass substrate. These are obtained by gently bending the guiding structure itself so that the light propagation is rotated to be perpendicular to the substrate surface. In this way, the couplers' end facets do not need any preparation as they naturally stand at the interface between the resist and the glass substrate, holding the entire structure.

For simplicity, we consider coupling structures made of quarter rings connecting the waveguide to the substrate, with a radius r (to be chosen accordingly to the specific thickness of the IP-G layer) and with same cross-section of the waveguide. While along the straight part of the structure the guided field propagates parallel to the waveguide axis with the same phase velocity, in the bent part the field and the phase front rotate about the center of curvature with constant angular velocity. Correspondingly, the guided mode is deformed and shifted from the waveguide center toward the radial direction and two loss contributions appear. One contribution is related to the increase of the phase velocity from the center of curvature to the external boundary of the bend. Since the phase velocity cannot exceed the speed of light value, this effect give rise to a radiation loss. The second contribution, named transition loss, is rselated to the change of the effective refractive index in the bent part with respect to the value of the straight part of the waveguide [131].

Both contributions are accounted for in the estimation of the power in the radiation field,

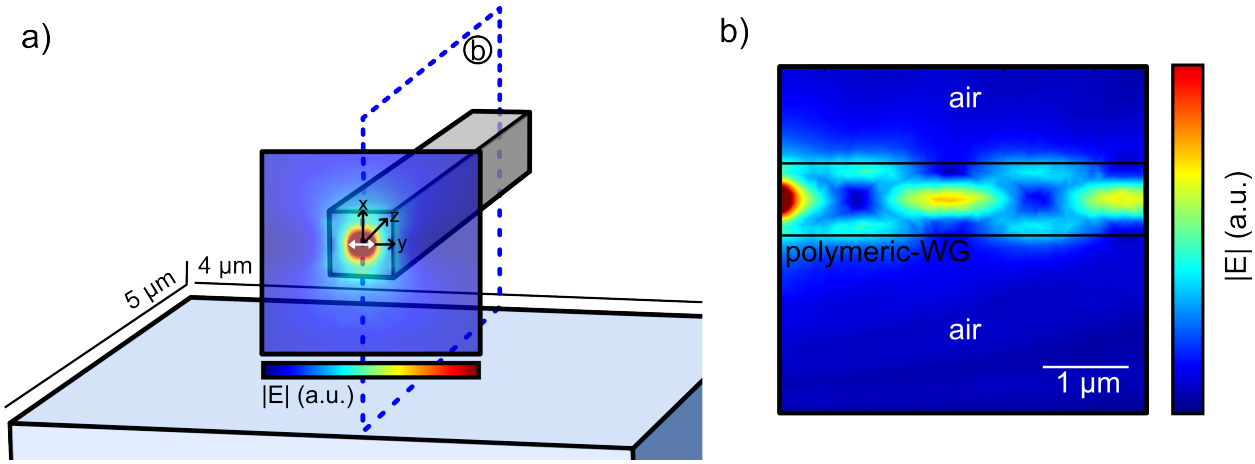

Figure 5.6 – **a)** Layout of the 3D numerical simulations displaying half of the waveguide total length (10 µm) and 2D color map plotting the electric field norm on the plane containing the dipolar emitter (white arrow), mimicking a single molecule and placed at the center of the polymeric waveguide. **b)** The electric field norm in the respective waveguide section showing interference among the guided modes supported by the polymeric structure.

than can be calculated by means of numerical simulations performed with Comsol. With a simulation set-up analogous to the one discussed in Chapter 3.2.3 (and shown for this specific case in **Figure 5.5a** and **b** for two different bent radii), we estimate bend losses of 6.4% for the lowest suspended waveguide of radius = 3µm (corresponding to the minimum measured thickness of the IP-G spin-coated layer), which reduce to values below 1% for couplers with radius > 10µm. Note that these vales represent an overestimation of the coupling efficiencies, since in our simulations only the fundamental guided mode is excited. Being more delocalized into the cladding, higher order modes will contribute to the radiation and transition losses, hence reducing the effective coupling efficiency.

Finally, we estimate the key figures of merit of the emitter-to-waveguide coupling, i.e. the coupling efficiency β-factor and emission enhancement α. This is done by computing with Comsol the electromagnetic field excited by a dipolar source located at the center of the waveguide, using a 3D model analogous to that described in Chapter 3.2.2 and illustrated in **Figure 5.6a**. As we can observe from **Figure 5.6b**, interference among the propagating modes occurs, yielding to $\beta = 52\%$. Coupling efficiencies up to 80% can be obtained upon optimization of the waveguide geometrical parameters [259].

The same simulation domain is then converted into a homogeneous medium, setting the refractive indices of all subdomains equal to that of air. The ratio between the total radiated power calculated in the presence of the waveguide and the power flow through the surface of a volume with equal size but in the homogeneous simulation domain, yields an enhancement factor $\alpha = 1.2\%$.

5.3 Experimental Results

The writing procedure can possibly damage the DBT-doped Ac NCs by e.g. heating and destabilizing the crystalline matrix, resulting in reduced performances of the single-photon emission. If a fast fabrication process is desirable in vision of a large-scale production, for our purpose it is actually necessary, as it would minimize the time in which the NC is exposed to a high intensity laser excitation.

In order to fabricate high quality structure in a compatibly short time, it is necessary to find a compromise between the laser power, the repetition rate, the writing speed, and the line-distance along the xy-plan and the z-axis. We tackle this issue starting with sorting out the voxel dimensions for the employed photoresists (Section 5.3.1), which defines the resolution of our 3D lithographic process. Structures fabricated at different height allows to characterize the stability of the suspended device and identify a range of optimal writing parameters, according to preliminary measurements on the transmission of the bare waveguides (Section 5.3.2). The first successfull hybrid device fabricated is finally presented in Section 5.3.3.

5.3.1 Writing parameters optimization

In order to establish the best suited parameters for DLW of IP-G/IP-Dip waveguide, we start considering the basic building block for the fabrication of 3D structures, that is the voxel. Owing to its ellipsoid shape, it is usually defined in terms of the aspect ratio between the major axis (r_z) over the minor one (r_{xy}). A rough estimation of the voxel dimensions can be given according to the empirical rule [272]:

$$r_{xy} = \frac{0.325\lambda}{\sqrt{2}\mathrm{NA}^{0.91}}; \quad r_z = \frac{0.532\lambda}{\sqrt{2}} \left(\frac{1}{n - \sqrt{n^2 - \mathrm{NA}^2}} \right) \tag{5.1}$$

where λ is the wavelength of the laser, n is the refractive index of the medium and NA is the numerical aperture of the objective. By inserting the specific parameters of our system, $\lambda = 780$nm, NA $= 1.4$, $n = 1.52$, we find the voxel diameters: $d_{xy} = 2r_{xy} \simeq 264$nm and $d_z = 2r_z \simeq 780$ nm.

Equations (5.1) highlight the importance of the objective NA in the achievement of minimum feature sizes, as it affects the resolution in a nonlinear manner. However, they don't account for other writing parameters, such as the laser power and the exposure time (i.e. the writing speed), that profoundly affect the shape and the size of the voxel. In particular, increasing the writing power (at fixed speed) or decreasing the writing speed (at fixed power)

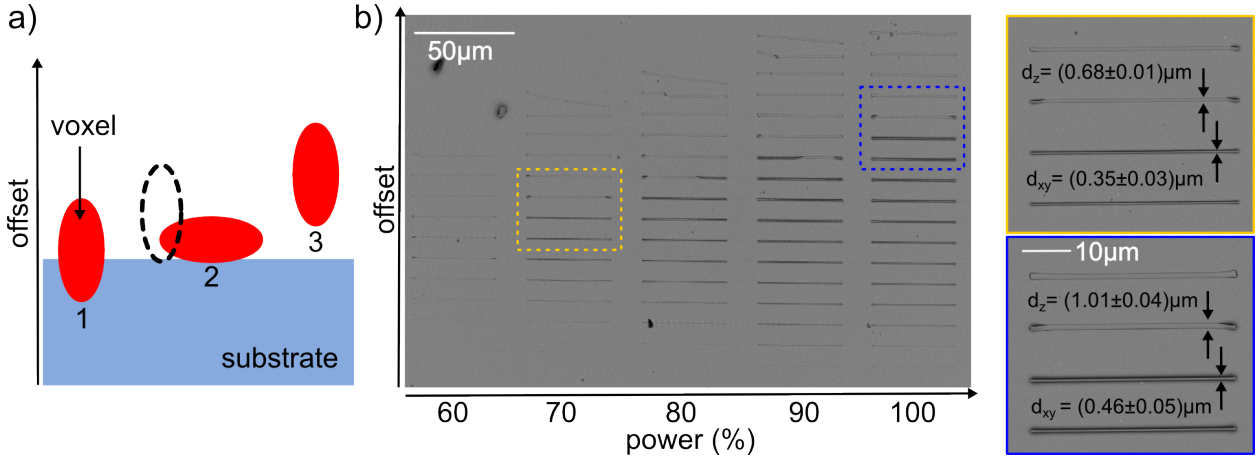

Figure 5.7 – **a)** Principle of the ascending scan exposure method: arrays of line sets are printed with incrementally increased offset from the substrate, with fixed laser power and scan speed. At small offsets, the lines properly attach to the substrate (1). Lines written at increasingly larger offsets start falling apart but still stick to the substrate and hence survive the washing step (2). When the offset is further increased, the lines cannot properly stick to the substrate and are washed away during the developing step (3). **b)** SEM image of 3D-DLW lines written at fixed writing speed, increasing the offset with 0.1 µm step from below the substrate surface at each subsequent line (from bottom to top). The same set of lines is fabricated for different writing power (increasing from left to right).

results in an increase of the aspect ratio. Indeed, the intensity distribution of a gaussian beam scales differently along xy and z and, correspondingly, the voxel lateral size saturates while its height keeps increasing. In addition, specific laser power and scan speed combinations can lead either to a low degree of polymerization or to micro-explosions resulting from a rapid temperature increase in the photoresist [273].

A standard approach to measure the voxel size is to employ an ascending scan exposure method [274], whose working principle is sketched in **Figure 5.7a**. According to this method, arrays of identical line sets (i.e. with fixed laser power and scan speed) are fabricated at different heights from the substrate surface. This is achieved incrementally increasing the offset, with a chosen step of 0.1 µm. At first, the lines are embedded in the substrate. Once the offset reaches the substrate interface, the written lines remains properly attached. For higher offset, the written lines tend to fall-off but stick to the substrate strong enough to survive the washing step. When the offset is further increased, the fallen-off lines do not properly stick to the substrate anymore and are hence washed away in the developing.

For this procedure, we set the writing speed at $100\,\mu m\,s^{-1}$, as it is expected to give an optimal voxel ratio of 2.7 for the IP- photoresists. Our set-up is calibrated to give 20 mW

laser power at the objective entrance for 100% setting[8]. Since the optimal power depends on the photosensitive resist material, we explore the effect of this parameter on the degree of polimerization of the written lines and on the voxel's size and shape, changing the power setting between 10% to 100%. The dimensions of the properly polymerized free-standing line is then evaluated with scanning electron microscopy (SEM, PHENOM-World), after sputtercoating of 10 nm gold layer.

Figure 5.7b show the SEM image of the obtained fabricated sample for power ranging from 60% to 100%, since for lower power we don't observe well-defined polymeric line at the glass-resist interface after the development process. The polimerization threshold occurs starting from 70% laser power which is hence chosen as the laser power parameter. We observe no micro-explosions, as expected for the range of power investigated [273]. The voxel width is measured with ImageJ [275], finding a minimum value of $d_{xy} = (0.35 \pm 0.03)$ µm for power setting 70% and a maximum value of $d_{xy} = (0.46 \pm 0.05)$ µm for 100%. Fallen-off lines provide a convenient way to estimate the voxel height, yielding $d_z = (0.68 \pm 0.01)$ µm for 70% and $d_z = (1.01 \pm 0.04)$ µm for 100%. The aspect ratio as a function of the employed laser power hence varies between 1.9 and 2.2. These results are comparable for both IP-Dip and IP-G photoresists, allowing to fabricate the guiding structure around the NC in a single writing step, minimizing the impact of the lithographic process on the NC.

According to the design of the guiding structure discussed in Section 5.2.4, our device is several voxel sizes large in all three dimensions and cannot be written using a single DLW trajectory. We hence decompose the volume of the 3D device to be written into a spiral pattern of lines, with relative distance less than a voxel size. In general, decreasing the number of lines correspond to a reduced fabrication time. However, a higher voxel overlap between adjacent lines can lead to a more homogeneous and stable structure, as discussed in the following section

5.3.2 Stability of the 3D waveguides and throughput analysis

In order to study the stability of the DLW devices, we fabricate structures written with three different set of lines on the xy-plane and suspended at increasing height h from the substrate, between the minimum (3 µm) and the maximum (20 µm) value of the IP-G layer thickness. For sake of simplicity, we employ the solely IP-Dip photoresist, drop-casted directly on the silica substrate. Owing to the similar voxel size and the identical parameters employed in the lithographic process, an identical behavior is expected.

[8]The laser power is measure with a power meter (PM100USB, Thorlabs) and is defined as percentage in Photonic Professional GT. The same convention will be followed through the rest of the chapter.

The layout of the entire guiding structure is designed to be completely imaged in our field of view of about 100 µm defined by the optics of the set-up, as described in Chapter 3.4.1.

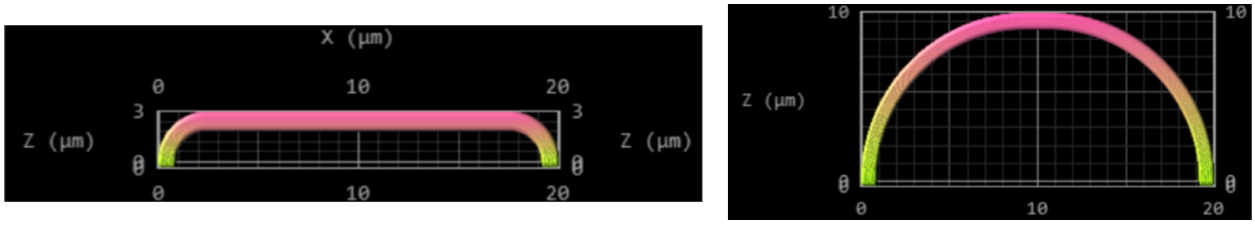

Figure 5.8 – Examples of rendering of the suspended waveguide according to the code for 3 µm and 10 µm IP-G thickness.

Choosing a total length on the xy-plane of 20 µm for the entire device, the final geometry of the waveguide is defined by the radius r of the quarter ring couplers, where $r = h$. Therefore, the shape of the device changes from straight waveguides connected to the substrate with two quarter ring couplers (for h <9 µm) to arcs, whose total size is defined by $2r$. The trajectory coordinates are generated with a Matlab code, once specified the number of lines on the xy-plane, according to the voxel dimensions evaluated in Section 5.3.1. A rendering of the obtained spiral pattern of lines is shown in **Figure 5.8** for two devices, respectively with h =3 µm and h =10 µm.

The trajectory coordinates are then implemented in the .gwl file to be read by the software NanoWrite. To ensure optimal adhesion of the written waveguides, the lithographic process starts slightly below the substrate (0.1 µm), writing the structures from the bottom layer to the top for maximal stability.

With this procedure, we fabricate sets of waveguides with height ranging from 3 µm to 20 µm (step 0.5 µm) for 7, 12, 20 number of lines on the xy-plane. We observe that the waveguides remain stable up to a height h = 13 µm. After this value they start deforming and falling on the substrate. A SEM image of the suspended waveguides is shown in **Figure 5.9a** and a zoom of one of them is displayed in **Figure 5.9b**. We observe only one case of damaged structure, showing a micro-explosion probably due to one-photon absorption from a local impurity (**Figure 5.9c**).

Two examples of fallen waveguides are shown in **Figure 5.9d** and **e** written with 20 and 7 lines, respectively. As expected, the uniformity of the written structure increases with increasing number of lines.

From SEM images we obviously cannot identify the best writing parameters in terms of guiding performance. We hence perform a preliminary study on the transmission of the suspended waveguides with the set-up described in Chapter 3.4.1. For this purpose, we

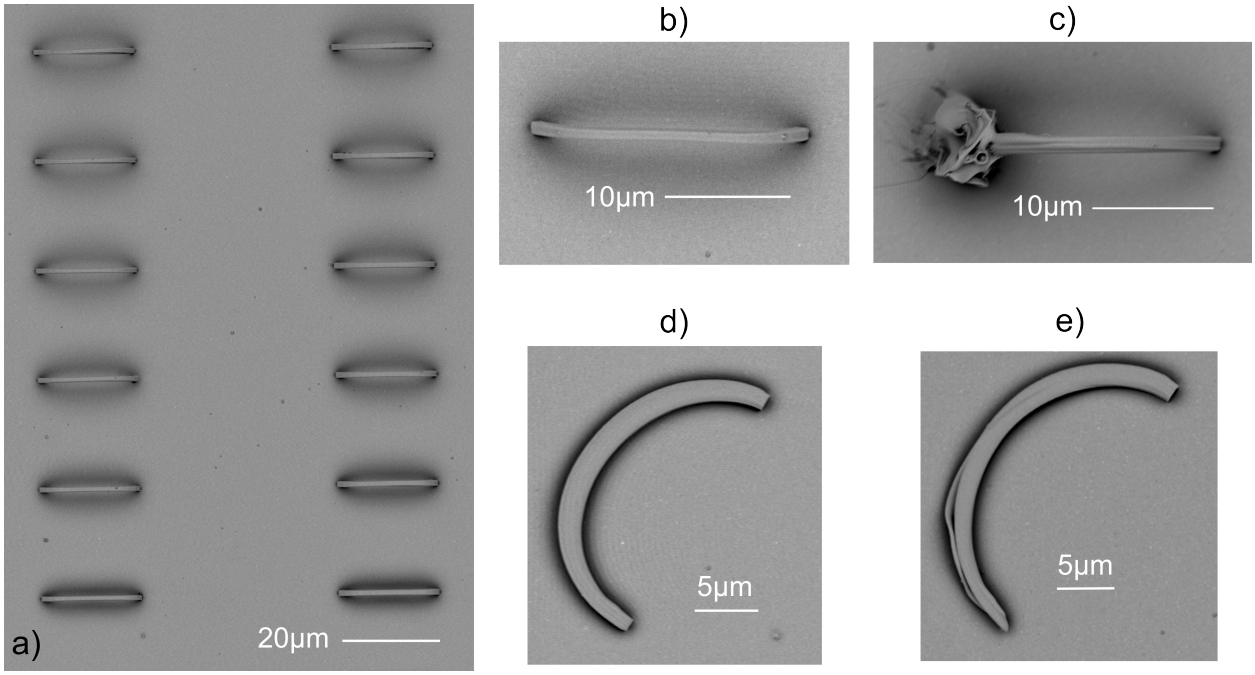

Figure 5.9 – SEM images of 3D polymeric waveguides. **a)** Two sets of correctly suspended waveguides. **b)** Zoom on a single suspended waveguide. **c)** The only damaged polymerized structure observed, where the micro-explosion is probably due to one-photon absorption from a local impurity. **d)** and **e)** are two examples of fallen waveguides written with 20 and 7 lines respectively, highlighting that an increased number of writing lines is needed to fabricate uniform structures.

fabricate three sets of three identical structures with height h=10 µm for 7, 12, 20 number of lines on the xy-plane.

Transmission measurements are performed on each waveguide, focusing the 767 nm-laser into one of the couplers and collecting the out-coupled light with the EM-CCD camera (without LP filter), upon optimization of the incident angle to match the waveguide mode direction in free space. Following the same protocol discussed in Chapter 3.4.2, counts collected from the out-coupler area (red square in **Figure 5.10**) are corrected for the background (BG), corresponding to the average counts collected from two areas with the same size but far from the out-coupler. The value of the BG-corrected guided counts is then normalized with those integrated in an area with the same size and containing the laser spot reflected from a silver mirror (BG-corrected in the same way). The square root of this value corresponds to the single coupler efficiency η_c, assuming a perfect mode-matching at the in-coupler.

The result of this analysis is reported in **Figure 5.11a**, plotting the coupling efficiencies for the triplet of waveguides as a function of the number of lines. As predictable, η_c and its reproducibility increases with increasing resolution. The highest throughput measured is 47%, which is well below the value estimated with simulations. This can be due to several

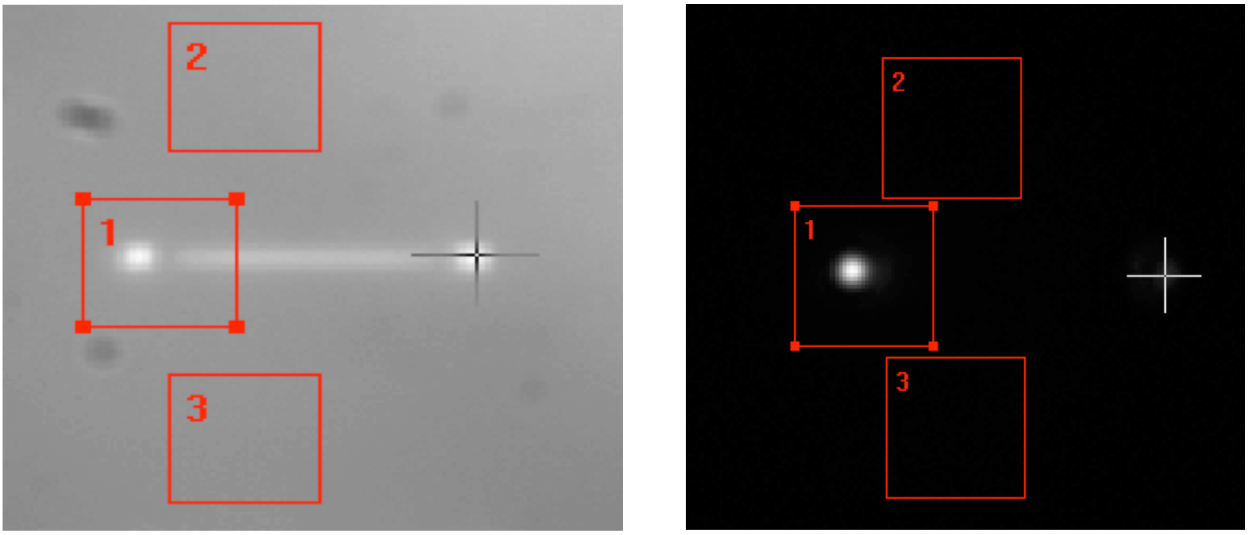

Figure 5.10 – Throughput measurement procedure: the structure is first identified with the white light (left). The integration areas (in red) are then defined around one of the coupler and far from the structure for background (BG) counts. The 767 nm laser is focused onto one of the coupler (white cross), and the counts corresponding to the guided light are integrated in the out-put coupler area. The single coupler efficiency is given by the normalization of the guided-BG corrected counts with those integrated in an area with the same size and containing the laser spot reflected from a silver mirror (BG-corrected in the same way).

concurrent effects. As anticipated in Section 5.2.4, propagation of various spatial modes is expected. Moreover, there can be losses due to a not perfect adhesion of the polymer to the substrate. In addition, it should be underlined here that throughput measurements account for all losses contributions related to bends, fabrication imperfections and absorption.

A more careful analysis of the losses is needed to decouple all these contributions. This can be done fabricating and characterizing different sets of waveguides. In particular, in order to estimate bend losses (both radiative and transition losses), transmission measurements should be done on waveguides with same total length and different bend radii. For the estimation of the propagation losses, transmission measurements should be done on waveguides with identical bend radii and different length.

To conclude our preliminary characterization on the suspended waveguides, we compare the out-coupler spot profile with the reflection of the laser beam on the silver mirror, as imaged in transmission measurements. Vertical and horizontal line-cuts from EM-CCD images are plot in **Figure 5.11b** and the numerical evaluation of the overlap integral in equation 3.1 between the two spots yields 0.87.

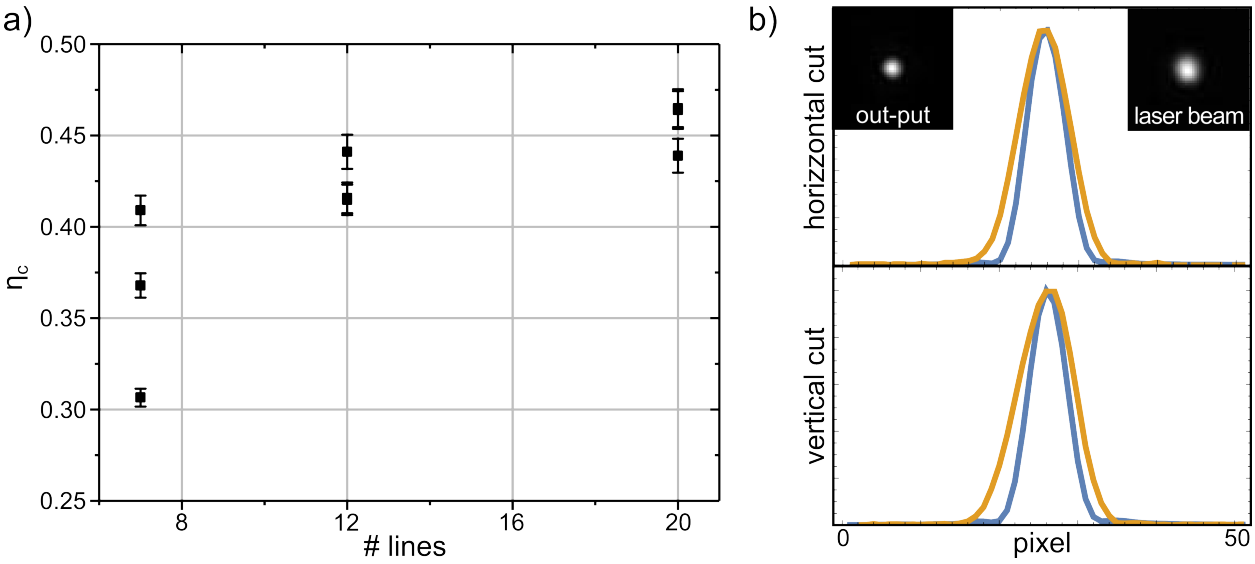

Figure 5.11 – **a)** Out-coupling efficiency measured from triplets of identical waveguides with height h=10 µm as a function of number of lines on the xy-plane. As predictable, η_c and its reproducibility increases with increasing resolution and the highest throughput measured is 47%. **b)** The spot profile at the out-put coupler is compared with the EM-CCD image of reflection of the laser beam on the silver mirror (both shown in the inset). Vertical and horizontal line-cuts from the two images suggests a good mode-matching, as confirmed by numerical evaluation of the overlap integral that yields a value of 0.87.

5.3.3 Integration of the organic nanocrystals

In order to verify that the organic NCs are not relevantly affected by the writing procedure, we start considering highly doped DBT:Ac NCs. We first expose the bare NCs desiccated on a glass substrate to the intensity of the pulsed laser, simulating a written squared area of 50 µm x 50 µm, with the optimal writing parameters previously discussed. We observe a reduction of the maximum detected counts with respect to the unexposed NCs, probably due to the local heating caused by the pulsed laser. However, the photoresists might increase the thermal stability of the embedded NCs, limiting their interaction with ambient oxygen.

To fabricate suspended waveguides hosting single NCs, we follow the protocol described in Section 5.2.3, desiccating Ac NCs on the spin-coated IP-G layer and then covering them with an IP-Dip drop. Due to the high viscosity of the bottom photoresist and the platelet-like shape of the NCs, the vast majority of the crystals don't dip into the resist. We also notice that IP-Dip drop-casting does not perturb this condition in a relevant way. Indeed, despite the low refractive index contrast between Ac and the IP-photoresists, NCs can be visualized within the photoresists' volume with the CCD camera of the DLW workstation as motionless light-grey points, displaced along the same focal plane. This is probably due to an acetone shell formed on the support-free NCs.

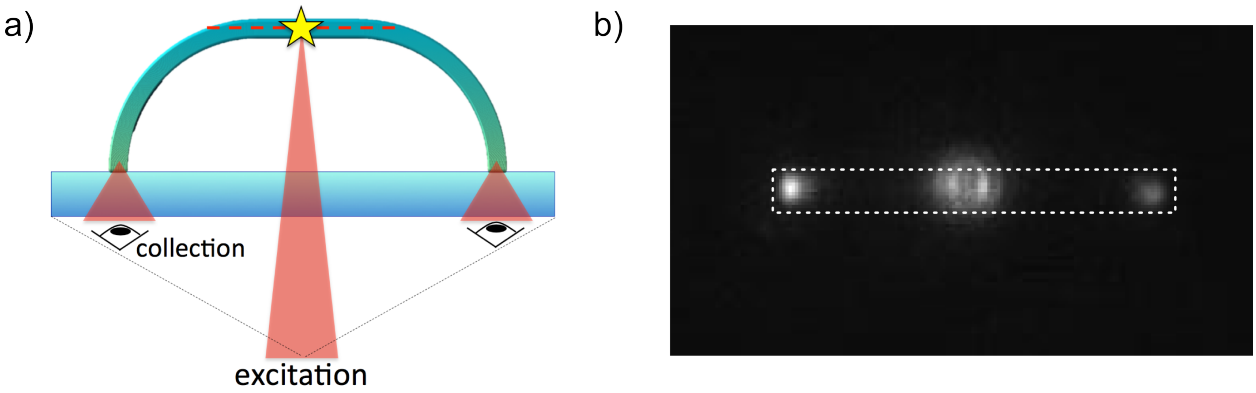

Figure 5.12 – **a)** Illustration of a fabricated single DBT:doped Ac NC wired up in a suspended WG. Once fluorescence from the NC is detected with the EM-CCD camera focusing the 767 nm-laser close to the center of the waveguide, the laser position is kept at the NC position and fluorescence is detected focusing on the plane of the couplers. **b)** Evidence of guided light coming out from the couplers of a fabricated hybrid device.

A well isolated NC is then selected to be wired up. The effective thickness of the IP-G bottom layer at the NC location is estimated by monitoring on the NanoWrite software the z-variation between the NC and the silica/IP-G interface. If this value belongs to the range of stability, the trajectory coordinates are generated with the Matlab code and implemented in the .gwl file, together with the optimal writing parameters. Real-time monitoring of the lithographic process allows to have a first indication on the success of this protocol, that however can only be confirmed upon development of the sample and detection of fluorescence by means of the confocal microscope set-up.

We hence verify the presence of a NC close to the waveguide's center focusing the 767 nm-laser and imaging its fluorescence with the EM-CCD camera of the confocal microscope. Keeping the laser position at the NC but now focusing on the plane of the couplers (**Figure 5.12a**), guided light coming out from the couplers can be observed (**Figure 5.12b**).

In conclusion, we demonstrate that organic NCs can be successfully integrated into photosensitive polymers. We identify the optimal writing parameters for IP-G and IP-Dip photoresists and our preliminary results show that the fluorescence emission of DBT molecules is not relevantly affected by the 3D lithographic process implemented with Nanoscribe and the subsequent developing step. This needs to be confirmed with measurements at cryogenic temperatures on the spectral properties of single molecules, specifically their emission linewidths and their spectral stability in time.

A more detailed characterization of the losses in our suspended waveguide is needed and the geometry of the guiding structure itself can be improved and optimized with dedicated

FEM simulations. However, DLW resolution is limited by the voxel size and fabrication of single-mode waveguides in the near-IR may require advanced 3D lithography techniques, as e.g. stimulated-emission-depletion [276].

Finally, the laser writing set-up can be implemented for in-situ excitation and detection of fluorescence from individual NCs, allowing for real-time monitoring of the emission property of the DBT molecules and for a more reliable writing process.

5.4 Organic NCs in PVA

Polyvinyl alcohol (PVA) is a widely used water-soluble synthetic polymer with good transparency, excellent chemical and thermal stability, good membrane-forming properties and stain resistance [277]. PVA is a linear molecule consisting of a vinyl alcohol C_2H_4O monomer and a pendant hydroxyl group (**Figure 5.13a**). Being a hydrophilic polymer, PVA can be readily used to form organic dye-PVA nanocomposite [278] and, more in general, it represents a natural host matrix for all hydrophobic materials, as their solubility in water is very low. It hence represents an interesting candidate as a host materials for our organic NCs.

With the same protocol presented in Chapter 4.2.1, we grow DBT-doped Ac NCs directly in a sonicating aqueous solution of PVA (Sigma Aldrich, 5% in milliQ water), obtaining an analogous milky suspension of formed NCs. Dynamic light scattering (DLS) measurements on this suspension show a monodisperse size distribution centered around 200 nm (as deduced from the autocorrelation curve in blue in **Figure 5.13b**). We observe no precipitated particles after several months, suggesting that PVA viscosity inhibits clusterization of the suspended NCs and hence stabilizes the suspension. This is confirmed by DLS measurements performed on the same suspension approximately one year after the first measurement. From the obtained autocorrelation curve (plotted in red in **Figure 5.13b**), a monodisperse size distribution centered around 300 nm is obtained.

Fluorescence from NCs grown in PVA is verified by drop-casting 50 µL of the NC-PVA composite on a bare coverglass placed in the rotating plate of the spin-coater and spun at 1500 rpm for 120 s. This procedure yields a uniform film with thickness of (305 ± 5) nm - according to profilometric measurements - in which the organic NCs are embedded. A typical fluorescence wide-field image detected with the EM-CCD camera is shown in **Figure 5.13c** for Ac NCs with high DBT-concentration, where the bright spots correspond to individual NCs, randomly oriented inside the polymeric matrix. Let us remark that, owing to the small refractive index contrast between Ac and PVA ($n_{\mathrm{PVA}} = 1.48$), DBT-doped Ac NCs cannot be distinguish within the polymeric matrix in white light illumination.

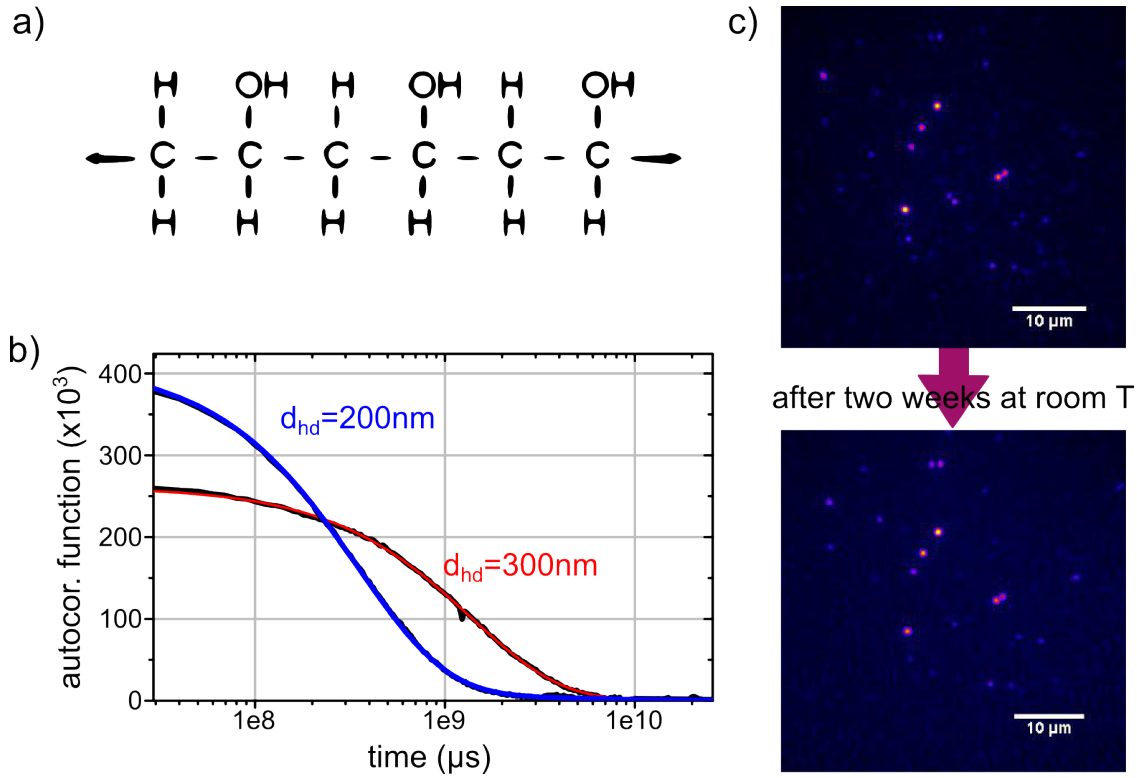

Figure 5.13 – **a)** Chemical structure of polyvinyl alcohol (PVA). **b)** Autocorrelation functions from DLS measurements on a suspension made of DBT:Ac NCs grown directly in an aqueous solution of PVA, performed right after reprecipitation (blue line) and after one year (red line). Both cases show a monodisperse size distribution with average particle diameter sizes of 200 nm and 300 nm, respectively. **c)** Comparison between wide-field fluorescence images of the same area of a spin-coated layer of PVA containing DBT:Ac NCs detected two weeks apart, keeping the sample at room temperature. The almost identical number of bright spots - corresponding to individual NCs - and their unchanged intensities demonstrate that PVA strongly reduces the sublimation of the organic NCs at room temperature.

As already mentioned in Chapter 4, the thermal stability of the PVA matrix strongly reduces the rate of sublimation of Ac at room temperature. This is inferred from **Figure 5.13d**, where we compare two wide-field fluorescence images of the same area of a spin-coated layer of PVA containing DBT:Ac NCs and acquired two weeks apart while keeping the sample at room temperature. The almost identical number of bright spots and their unchanged intensities demonstrate that PVA strongly reduces the sublimation of the NCs at room temperature.

The final properties of PVA depend on those of its parent polymer (polyvinyl acetate), its polymerization conditions and degree of hydrolysis. Interestingly, cross-linking of PVA improves its water-resistance, opening new domains of applications for this material [279]. For example, membrane of PVA presenting both hydrophilic and hydrophobic properties

can be achieved by selective cross-linking of PVA, which can be used in the separation of water/alcohol mixtures [280].

Cross-linking of PVA can be done by a chemical reaction (e.g. free-radical polymerization and chemical reaction of complementary groups) or by a physical reaction (e.g. heat treatments that induce crystallization of the polymeric chain or hydrogen bond between chains) [281]. Since the addition of chemical compounds to the suspension can in principle affect the

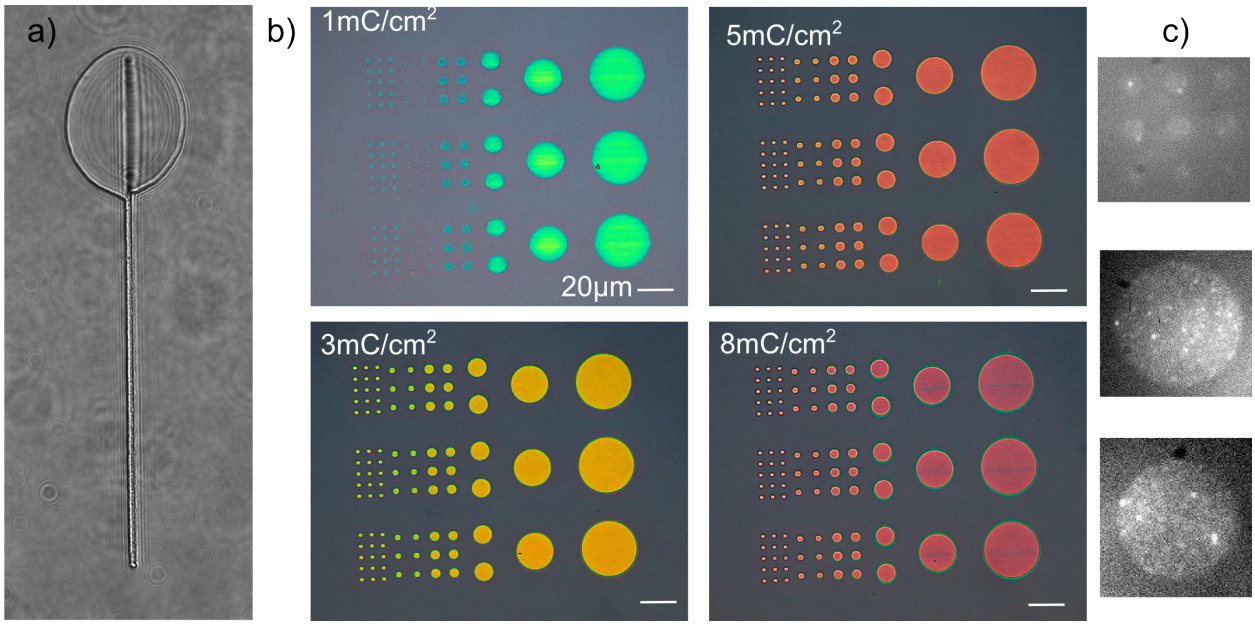

Figure 5.14 – **a)** Composite of PVA and NCs exposed to the high energy irradiation of the pulsed laser of the DLW workstation. The refractive index modification along the path followed by the scanning laser stems for cross-linking of PVA, which seems to start after formation of water bubbles. **b)** E-beam lithography on a thin film of NC-PVA spin-coated on a silicon chip for different exposure doses (detailed in the each micrograph). The high energy irradiations achieved with this method efficiently improve the PVA water-resistance, and the e-beam exposed areas survives after the development step. Different colors correspond to different thickness which ranges from approximately 60 nm and 175 nm, for the lowest and highest dose respectively. **c)** Wide-field images of e-beam patterned PVA embedding NCs showing fluorescence.

optical properties of the DBT-doped Ac NCs, we investigate the possibility to induce physical cross-linking of the NC-PVA composite by locally heating it with focused high energy irradiation.

As a first experiment, we expose the thin spin-coated NC-PVA film to the high intensity of the DLW workstation's pulsed laser. With the power set to the maximum vale (100%), we write line sets at the interface with the substrate for different writing speed in a range of reasonably slow values - between $1\,\mu m\,s^{-1}$ and $10\,\mu m\,s^{-1}$ - and monitoring the process in real-time with the CCD camera. Within this range, but in an almost unpredictable manner,

we observe a refractive index modification along the path followed by the scanning laser, signature of a structural change of the polymer. The process, however, is not reproducible within the available range of writing parameters but we observe that it occurs more likely together with water-bubbles formation (**Figure 5.14a**), evidence of the locally reached high temperature. However, none of the written lines can be localized on the substrate after the development step in milliQ water for 30 s (corresponding to the minimum time needed to dissolve a few hundreds nanometers PVA film). This result suggests that the intensity of the DLW workstation's pulsed laser induces a poor cross-linking degree.

Higher localized energies can be achieved exposing the sample to e-beam irradiation, which is know to efficiently pattern PVA upon addition of cross-linker agents [282]. In this case, H^+ ions released during the chemical reaction promoted by the e-beam exposure, induce PVA cross-linking with a corresponding increase of the polymer's molecular weight and of its solubility in water.

Relying on the electron-beam lithography (EBL) facility of the Institute of Photonic Sciences (ICFO) in Barcelona, we expose a thin film of NC-PVA spin-coated on a silicon chip to e-beam irradiation (spot size 5, 30 kV), observing that it is actually patternable even without addition of any cross-linker agent. **Figure 5.14b** shows microscope images of cylinders with basis of different size made of NC-PVA, obtained for different exposure doses (as detailed in the figure) and after developing the sample for 30 s in milliQ water. Different colors correspond to different thickness, which ranges from approximately 60 nm and 175 nm, for the lowest and highest dose respectively, according to AFM measurements. Wide-field fluorescence EM-CCD images from the e-beam written cylinders are shown in **Figure 5.14c**, showing fluorescence emission from DBT molecules after exposure to the e-beam irradiation.

As a final remark, let us note that identical results are obtained when exposing a bare PVA film to e-beam irradiation, hence excluding the contribution of the NCs to the cross-linking process.

5.4.1 NCs-PVA and 2D Materials hybrid platforms

In the last decade, the isolation of various 2D materials has created a new paradigm in materials science and has already been proposed for a number of electronic applications in the area of ultra thin and flexible devices, combining transparency and high conductivity. Moreover, because of the unusual properties associated with their 2D morphology, this new class of materials shows strong light-matter interaction and thus carries great potentials for major advancements also in nanophotonics [283].

The unique combination of tunable optical response and current experimental capability

for fabrication of different 2D materials make their nanoscale interaction with quantum emitters an ideal platform to study strong light-matter interaction [284]. Moreover, taking advantage from the technological maturity of nano-electromechanical system, active in-situ control of optical fields at the nanoscale has been recently demonstrated [285]. The coupling between individual emitters and 2D materials can have different physical origins, ranging from Stark shift [286] to dipolar-coupling induced modification of the emission intensity [287] or energy (*Casimir-Polder* shift) [288], thus offering interesting perspectives for fast electro-mechanical light modulation at the single photon level.

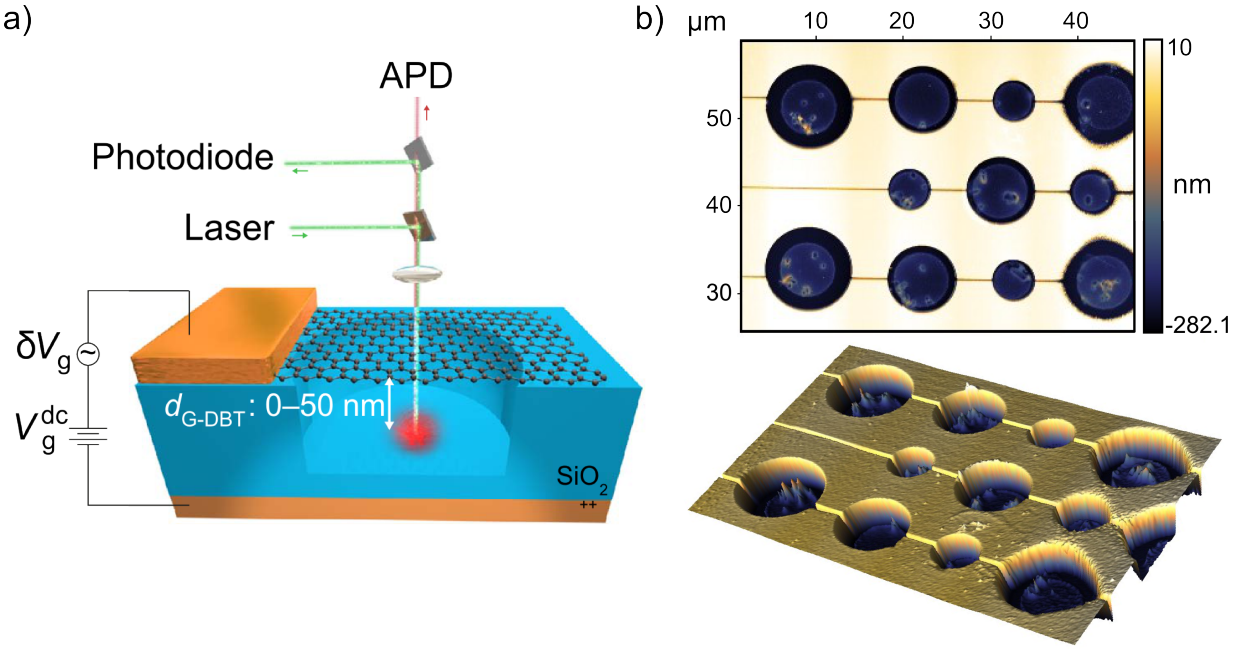

Figure 5.15 – **a)** Illustration of the optomechanical hybrid device (currently under implementation) to study the interaction between individual molecules and the electromechanical motion of a suspended 2D membrane. **b)** AFM image (2D and 3D) of the Si-SiO_2 chip fabricated in ICFO, where e-beam patterned PVA cylinders of approximately 30 nm thickness successfully embed organic NCs at the desired location and protect them from a developing step in acetone. The latter is necessary to ensure a sufficient residual-free area around the holes, enabling 2D membrane deposition.

In collaboration with the group of Frank Koppens, Institute of Photonic Sciences (ICFO) in Barcelona, we are currently working on developing 2D materials-DBT:Ac hybrid devices.

In a first project, we aim to fabricate a hybrid optomechanical device as sketched in **Figure 5.15a**, which consists of an on-chip graphene flake suspended a few tens of nanometers above a single DBT molecule, placed in a hole etched in a Si-SiO_2 chip. Ideally, at low temperature, this configuration would allow to study and accurately measure the distant-dependent emission frequency due to modified vacuum fluctuations. The interaction between individ-

ual molecules and the electromechanical motion of the 2D membrane is indeed predicted to yield a transition frequency shift of the single emitter, which can be read out detecting the field scattered by individual molecules [288]. As the frequency shift strongly depends on the relative distance between the emitter and the membrane, this system would represent a first practical scheme for position quantum sensing.

However, since the separation distance between graphene and emitter can range from approximately 5 nm to 50 nm, the main mechanism taking place is the induced emission intensity modification due to non-radiative energy transfer [143]. We hence choose a different 2D material with analogues mechanical properties of graphene that is molybdenum disulfide (MoS_2) [289]. Since MoS_2 has a direct band gap of about 1.8 eV, non-radiative energy transfer from DBT is avoided and thus the measurement of the emission frequency shift would not be affected by quenching of the fluorescence for small emitter-membrane separation distance.

As far as for the emitter, it is crucial to precisely position the DBT:Ac system inside few µm-diameter and few-tens-of nm deep holes, whose dimensions are determined by the mechanical property of the suspended 2D membrane. Moreover, the area around the holes should be sufficiently residual-free to allow successful transfer and suspension of the 2D membrane. Finally, since the 2D material transfer and suspension on a desired location on the chip is quite time-demanding, the DBT:Ac system should be protected against thermal instability.

This can be achieved by taking advantage of the combination of the sub-micrometric size of the DBT:Ac NCs with PVA, which simultaneously acts as a protective and patternable transparent layer. A possible strategy consists in drop-casting and desiccating DBT:Ac NCs on the silicon chip, until a reasonable number of holes result successfully filled. A thin PVA-film is then spin-coated on the entire device and e-beam patterned at the location of the holes. The chip is then rinsed in milliQ water (30 s) to remove the unexposed PVA and then in acetone (in which PVA is not soluble) for approximately 60 s, in order to dissolve the unprotected NCs displaced outside the holes.

Figure 5.15b shows an AFM image (2D and 3D rendering) of a hybrid device fabricated according to this protocol, where PVA cylinders of approximately 30 nm thickness successfully embed organic NCs at the desired location and protect them from the developing step in acetone which, on the other side, ensures a sufficient residual-free area around the holes.

A second experiment relies on the thin film flatness achievable by simply spin-coating PVA and its effectiveness as a protective layers for DBT:Ac NCs which allows, in principle, to transfer a 2D membrane directly on the polymeric layer. In this "sandwich" configuration

two different mechanisms can be studied: the coupling between single molecules and localized excitonic states induced in the 2D material by strain, and the Stark-tuning of molecules in PVA, using the 2D material as a transparent electrode.

The latter is particularly interesting for quantum optical experiments, as in principle individual 2D flakes can be transferred on individual cylinders of PVA, each containing a single DBT:Ac NC. This geometry would enable tuning of a molecular line to match that of the molecules embedded in all the other polymeric cylinders, providing a reliable platform of multiple sources generating indistinguishable single photons. Additionally, a careful choice of the thickness of the multilayered structure can determine an antenna-like design able to redirect the single photon emission into a narrow cone in free space toward the orthogonal direction (as e.g. shown in [160]), where the 2D flake provides emission frequency tunability.

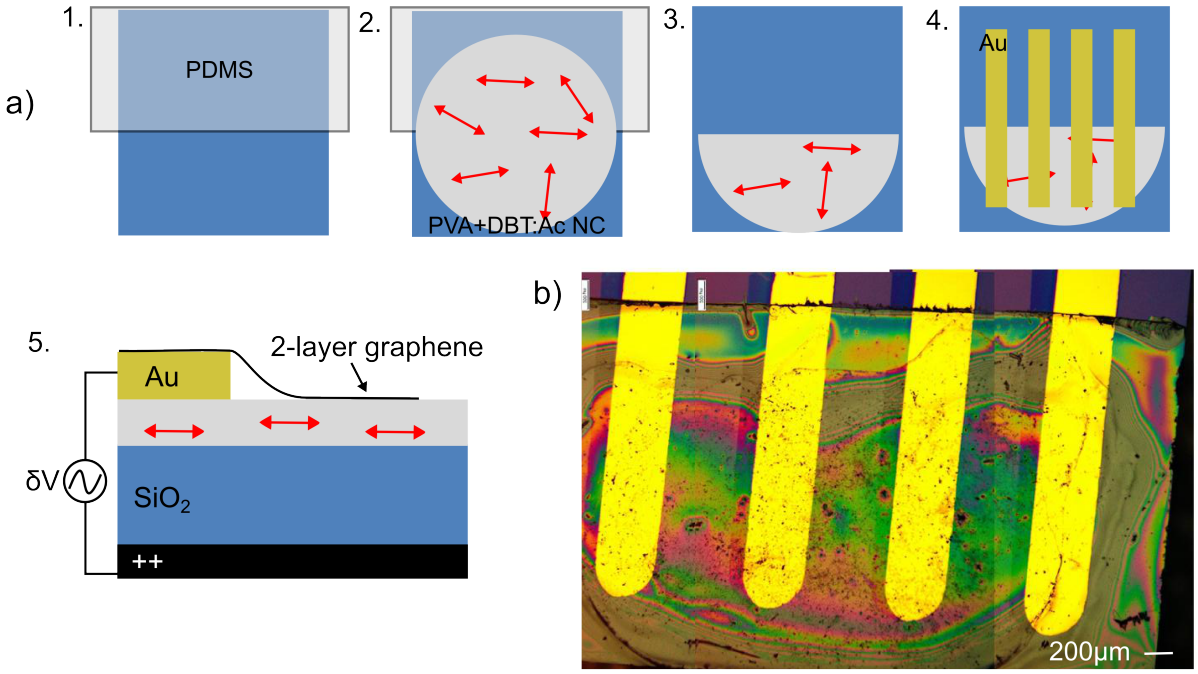

Figure 5.16 – **a)** Fabrication steps of the hybrid device proposed to study Stark tuning of single DBT molecules in Ac NCs in PVA using a 2D material as a transparent electrode. **b)** Microscope image of the fabricated device, where we can clearly distinguish dark spots corresponding to the NCs below the PVA layer, which hence successfully protect them from the high temperature and high vacuum conditions of the gold evaporation step.

Prompted by these interesting possibilities, we develop a first device made of PVA-covered DBT:Ac NCs desiccated on a silicon chip, half-covered by a thin tape of polydimethylsiloxane (PDMS), as illustrated in steps 1. and 2. of **Figure 5.16a**. The chip surface covered by

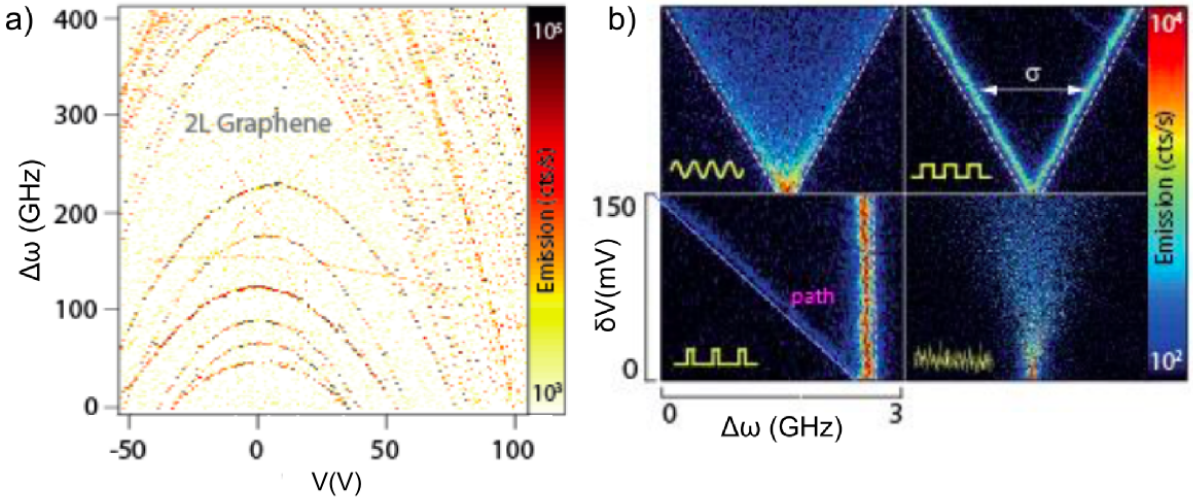

Figure 5.17 – **a)** 2D color map of the excitation spectrum as a function of applied DC gate voltage. A quadratic Stark-shift is mainly observed. **b)** Modulation of the emission spectrum of a single molecule realized for different Stark voltages.

the PDMS tape is preserved cleaned (step 3.) in order to efficiently deposit evaporated gold electrodes through a custom-built mask (step 4). **Figure 5.16b** shows a collage of microscope images of the fabricated device, where we can clearly distinguish dark spots corresponding to the NCs below the PVA layer, which successfully protect them from the high temperature and high vacuum conditions of the gold evaporation step.

The group of Prof. Koppens successfully transfer on this device a 2-layer graphene flakes (step 5 in **Figure 5.16a**). In **Figure 5.17a** we show that, with this device, the emission spectrum of a single molecule can be Stark-shifted by applying a DC external electric field **E**.

The energy level shift $W(E)$ can be written as [145]:

$$W(E) = W(0) - (\boldsymbol{\mu}_e - \boldsymbol{\mu}_g) \cdot \mathbf{E} - \frac{1}{2}((\alpha \mathbf{E}) \cdot \mathbf{E}) \tag{5.2}$$

with $(\boldsymbol{\mu}_e - \boldsymbol{\mu}_g)$ the difference between the dipole moments of the excited state and the ground state respectively, and α the polarizability induced by the field to the molecule.

In a host-matrix system in which the molecular symmetry is broken, the electric dipole moments of the molecule in the ground and excited states are different and the Stark effect is dominated by a linear response to the external electric field. When both the molecule and its insertion site in the matrix are centro-symmetric, both static dipole moments are zero, and the Stark effect, which then arises from the difference in polarizability between

the ground and excited states, is much weaker and purely quadratic. The more the system shows crystallinity, the more the effect becomes quadratical, since the external electric field introduces a polarization to the matrix [72].

In **Figure 5.17a** we plot as a 2D color map the excitation spectrum as a function of applied gate voltage. A quadratic Stark-shift is mainly observed.

The Stark shift of molecules is not limited to the case of an applied DC voltage and higher order effects induced by a modulation of the external electrical field can be observed [290]. In particular, applying weak AC, arbitrary periodic voltages with different waveforms (here at 1 kHz and amplitude δV) single molecule emission splits linearly into a double-peaked spectrum. With an asymmetric pulsed modulation with duty cycle $\neq 50\%$, we can control the relative fluorescence intensity given by the time spent at the modulation amplitude maxima, and artificial broadening is instead observed when applying a pink noise (bandwidth 100 kHz).

In conclusion, we demonstrate that DBT:Ac NCs can be successfully grown in an aqueous solution of PVA. Preliminary DLS measurements show that the obtained suspension, owing to its viscosity, is more stable in time than the original suspension of NCs in water discussed in Chapter 4.2.1, but a more accurate analysis on the stability in time of both suspensions is required. The excellent film-forming properties of PVA allows to obtain uniform few-hundreds-nm-thick films that act as protective layer for the embedded (or coated) organic NCs, improving their thermal stability and providing a uniform flat surface. Both features enable the implementation of a layered device in which the silicon chip substrate and the top-layer of graphene are used as electrodes to Stark-tune single molecule's linewidth at cryogenic temperatures.

First attempts of selective physical cross-linking of PVA induced by the high intensity of our DLW workstation's pulsed laser demonstrate that higher intensities or addition of cross-linker agents [291] should be considered in order to pattern PVA in 3D. Both methods can however relevantly affect the optical properties of the embedded NCs. As an alternative route, we are considering to grow DBT-doped Ac NCs in commercially available water-based photoresists, suitable for DLW [292, 293]. A suspended 3D sub-wavelength waveguide embedding a high density of DBT:Ac NCs would indeed represents an attractive platform for investigating polaritonic and quantum many-body phenomena [294].

On the other hand, e-beam irradiation is found to be an efficient method to pattern PVA, even without addition of any cross-linker agent, and fluorescence from exposed embedded NCs is observed. While the optimization of the lithographic parameters is still under inves-

tigation, this method can be readily employed for the realization of a hybrid optomechanical device to study the interaction between individual molecules and the electromechanical motion of a 2D suspended membrane.

Conclusions and Outlook

In this thesis we study possible platforms to integrate single-molecule based quantum emitters into dielectric waveguides, aiming at efficient emission, control and collection of single photons on-chip, an important step toward the implementation of photonic quantum technologies.

We first characterize dibenzoterrylene (DBT) molecules in bulk anthracene (Ac) crystals by means of a home-built scanning confocal microscope, equipped for single molecule microscopy and spectroscopy at cryogenic temperatures. We prove such quantum emitters are reliable sources of single photons, owing to their purity, brightness and photostability at room temperature, and their stable and Fourier-limited transition linewidth at 3 K.

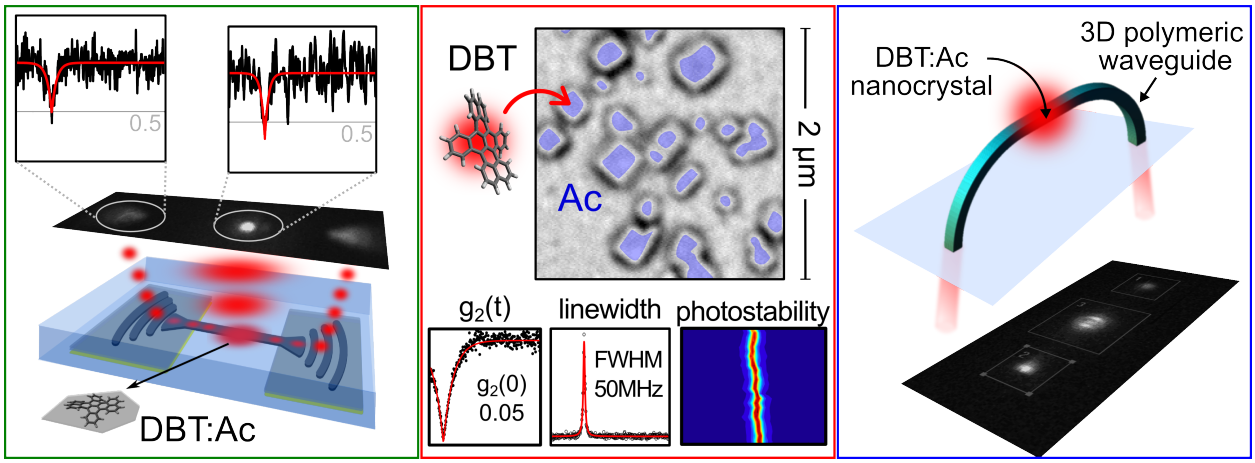

As a first scheme for integration, we grow few-tens-of-nanometer thin DBT:Ac crystals on top of a dielectric chip consisting of single-mode ridge waveguides and grating far-field couplers. On the resulting hybrid device we investigate the emission of single photons from DBT molecules into the waveguide mode at room temperature [42]. We observe that molecules in close proximity of the dielectric waveguides couple to the evanescent tail of the guided mode, with a measured coupling efficiency β up to (42±2)%, an on-chip purity $g^2_{\mathrm{on}}(0) = (0.01\pm0.10)$ and a photon-flux on chip at saturation $S^{\mathrm{on}}_{sat} = \frac{1}{2\tau}\mathrm{QY}\beta_{\mathrm{meas}} \simeq 48\,\mathrm{MHz}$. These results are competitive with state-of-the-art single-photon emission into ridge waveguide modes from other

solid state systems [32, 183, 187], while offering a platform with high versatility and advantages. Namely, with such a small foot-print, simple fabrication methods and scalability, our system holds promise for the assembly of integrated single-photon source arrays.

In order to improve control over DBT:Ac as a nanoscale single-photon source, we develop a simple and cost-effective reprecipitation method [215, 220] to fabricate Ac crystals with sub-micrometric size and tunable concentration of DBT molecules. X-ray diffraction confirms the crystallinity of the nanocrystals and atomic force microscopy shows an average thickness of 65 nm, which is particularly promising for the coupling to evanescent fields in the proximity of surfaces. Surprisingly, the optical properties of the bulk system at both room and cryogenic temperatures are preserved even in the nanocrystalline environment. In particular, DBT molecules in Ac nanocrystals do not suffer from spectral diffusion that has so far hindered the deployment of traditional inorganic nanocrystals for narrow-band applications and basic quantum optics operations with the emitted photons [81, 198, 203]. Owing to their reduced size we can instead envisage site-specific emitter engineering to deterministically implement complex hybrid nanostructures, such as photonic crystal cavities, waveguides or optical antennas. As a proof of principle, we demonstrate that, dispersed in water, DBT:Ac nanocrystals can be easily handled and manipulated at room temperature with a microinfiltration set-up. In principle, the average size of the nanocrystals grown via reprecipitation can be controlled and reduced by varying the fabrication conditions, such as water temperature, droplet size, injected solution concentration and addition of surfactants. These studies are subject of our current investigation.

The embedding of the DBT:Ac nanocrystals in polymeric photonic structures appears a natural and promising pathway for integrated quantum photonics, owing to the flexibility of the polymer synthesis process. The latter combines a broad tunability of the material electro-optical and mechanical properties with well-established 2D and 3D lithographic fabrication methods [241]. We report on preliminary results on the compatibility of the DBT:Ac nanocrystals with 3D-direct laser writing, using commercially available photoresists and the Nanoscribe workstation. We fabricate a suspended 3D polymeric waveguide embedding at its center a single nanocrystal and observe fluorescence guided light from the couplers. The design of the guiding structure is kept very simple since our first goal was to fabricate waveguides capable of integrating individual nanocrystals and to test whether the fluorescent system was compatible with the writing process. Finite element method simulations implemented with the software Comsol yield a coupling efficiency $\beta = 52\%$ for a dipolar source located at the center of such a waveguide and horizontally oriented. Coupling efficiencies up to 80% can be obtained upon optimization of the waveguide geometrical

parameters [259], representing a relevant improvement with respect to schemes based on evanescent coupling. As an alternative route, we are considering to grow DBT:Ac nanocrystals in commercially available water-based photoresists, suitable for DLW [292, 293]. A suspended 3D sub-wavelength waveguide embedding a high density of DBT:Ac nanocrystals would indeed represents an attractive platform for investigating polaritonic and quantum many-body phenomena [294].

We then demonstrate that DBT:Ac nanocrystals can be successfully grown also in an aqueous solution of polyvinyl alcohol (PVA). The excellent film-forming properties of PVA allows obtaining uniform few-hundreds-nm-thick films that act as protective layers for the embedded (or coated) organic nanocrystals, improving their thermal stability and providing a uniform flat surface. Both features enable the implementation of a layered device in which a silicon chip substrate and a top-layer of graphene are used as electrodes to Stark-tune single molecule's linewidth at cryogenic temperatures.

PVA patternability, i.e. selective cross-linking, is investigated by locally heating the material with focused high energy irradiation. Electron-beam irradiation is found to be an efficient method for PVA patterning, even without addition of cross-linker agents. Moreover, fluorescence from embedded nanocrystals is observed after exposure. While the optimization of the electron-beam lithography parameters is still under investigation, we already show promising results for the realization of a hybrid optomechanical device, enabling the study of the interaction between individual molecules and a 2D suspended membrane [288].

Finally, patterned PVA embedding DBT:Ac nanocrystals presents interesting perspectives for the realization of arrays of single-photon sources. Indeed, flakes of 2D materials can be transferred on isolated PVA island containing one nanocrystal and employed as transparent electrodes. This geometry would enable spatially selective Stark-tuning of the molecular lines to match that of other molecules. Additionally, a careful choice of the multilayer thickness would result in an antenna-like configuration (as e.g. [160]), redirecting emission into a narrow cone in free space, with the 2D flake providing also frequency tunability.

Acknowledgments

I am deeply grateful to my advisor, Dr. Costanza Toninelli, for her guidance, scientific support, patience and encouragement during this challenging but wonderful journey that was my PhD at the Department of Physics of the University of Florence. I especially thank Costanza for supporting me in good and harder times, for providing me opportunities and for granting me the freedom to embark on new projects.

I am particularly grateful to the members of the Quantum Nanophotonics group (LENS, Florence), with whom I shared the lab during the 3 years of my PhD. I want to thank Pietro Lombardi for his vast scientific knowledge and his support with the experimental set-up; Fabrizio Sgrignuoli - the number cruncher of the group - for introducing me to the world of computational physics; Maja Colautti for her dedication and her inexhaustible enthusiasm. Thank you for all those moments when more than two hands were needed in the lab!

I would also like to thank the past members of the group, Giacomo Mazzamuto - who I especially commend for the fruitful discussions (about science and beyond) - Andrea Tabani, Sahrish Rizvi and Simona Checcucci. It was an enriching opportunity to meet and share the lab with all of you.

I am grateful to Professor Francesco S. Cataliotti and his group - with whom we shared much more than the lab - for the invaluable support.

I would like to thank Daniele Martella for sharing his expertise in the chemistry lab and Sara Nocentini and Dmitry Nuzhdin for teaching me how to properly deal (and don't mess up!) with the Nanoscribe.

Several people deserve proper acknowledgement for having provided us access to their laboratories and equipments. In particular, I thank Bruno Tiribilli for the AFM facilities, Marianna Mamusa (CSGI, Florence) for dynamic light scattering experiments, Samuele Ciattini and Laura Chelazzi (CRIST, Florence) for XRD measurements, Professor Diederik Wiersma for access to clean room facilities, Professor Francesca Intonti for letting me use the micro-infiltration set-up, Marco Bellini and Chiara Corsi for Ti:sapphire operation.

I would like to thank also our collaborators around Europe. In particular, I am thankful to Professor Wolfram Pernice and his Responsive Nanosystem group (Münster University) and to Professor Frank Koppens and his group of Quantum Nano-Optolelectronics (ICFO,

Barcelona), and especially Kevin Schädler. I am also grateful to Professor Philippe Lalanne and his group of Light in Complex Nanostructures (Institut d'Optique, Bordeaux) and in particular to Rémi Faggiani.

I sincerely thank Professor Arno Rauschenbeutel and Professor Matteo Galli for kindly accepting to referee my PhD thesis. Their valuable comments, suggestions and questions helped me improve my research and gain a wider and deeper perspective.

I would like to thank my family, my friends and, in particular, a *dear french friend of mine* for their endless support, inspirations and love in my life. It is to you, I wish to dedicate this thesis.

Bibliography

[1] A. Imamoḡlu, H. Schmidt, G. Woods, and M. Deutsch, "Strongly interacting photons in a nonlinear cavity," *Physical Review Letters*, vol. 79, no. 8, p. 1467, 1997.

[2] C. Ciuti, G. Bastard, and I. Carusotto, "Quantum vacuum properties of the intersubband cavity polariton field," *Physical Review B*, vol. 72, no. 11, p. 115303, 2005.

[3] D. P. DiVincenzo, "The physical implementation of quantum computation," *arXiv preprint quant-ph/0002077*, 2000.

[4] C. H. Bennett and G. Brassard, "Quantum cryptography: Public key distribution and coin tossing," *Theoretical Computer Science*, vol. 560, pp. 7–11, 2014.

[5] J. L. O'Brien, A. Furusawa, and J. Vučković, "Photonic quantum technologies," *Nature Photonics*, vol. 3, no. 12, pp. 687–695, 2009.

[6] M. Ohtsu, "Nanophotonics and nanofabrication," *History*, vol. 1, pp. 1–2, 2009.

[7] H.-K. Lo, M. Curty, and K. Tamaki, "Secure quantum key distribution," *Nature Photonics*, vol. 8, no. 8, pp. 595–604, 2014.

[8] M. Wahl, M. Leifgen, M. Berlin, T. Röhlicke, H.-J. Rahn, and O. Benson, "An ultrafast quantum random number generator with provably bounded output bias based on photon arrival time measurements," *Applied Physics Letters*, vol. 98, no. 17, p. 171105, 2011.

[9] J. P. Dowling and K. P. Seshadreesan, "Quantum optical technologies for metrology, sensing, and imaging," *Journal of Lightwave Technology*, vol. 33, no. 12, pp. 2359–2370, 2015.

[10] J. Cheung, C. Chunnilall, E. Woolliams, N. Fox, J. Mountford, J. Wang, and P. Thomas, "The quantum candela: a re-definition of the standard units for optical radiation," *Journal of Modern Optics*, vol. 54, no. 2-3, pp. 373–396, 2007.

[11] T. D. Ladd, F. Jelezko, R. Laflamme, Y. Nakamura, C. Monroe, and J. L. O'Brien, "Quantum computers," *Nature*, vol. 464, no. 7285, pp. 45–53, 2010.

[12] H. J. Kimble, "The quantum internet," *Nature*, vol. 453, no. 7198, pp. 1023–1030, 2008.

[13] A. K. Ekert, "Quantum cryptography based on bell's theorem," *Physical Review Letters*, vol. 67, no. 6, p. 661, 1991.

[14] A. Beveratos, R. Brouri, T. Gacoin, A. Villing, J.-P. Poizat, and P. Grangier, "Single photon quantum cryptography," *Physical Review Letters*, vol. 89, no. 18, p. 187901, 2002.

[15] S. Ritter, C. Nölleke, C. Hahn, A. Reiserer, A. Neuzner, M. Uphoff, M. Mücke, E. Figueroa, J. Bochmann, and G. Rempe, "An elementary quantum network of single atoms in optical cavities," *Nature*, vol. 484, no. 7393, pp. 195–200, 2012.

[16] J. Volz, M. Scheucher, C. Junge, and A. Rauschenbeutel, "Nonlinear π phase shift for single fibre-guided photons interacting with a single resonator-enhanced atom," *Nature Photonics*, vol. 8, no. 12, pp. 965–970, 2014.

[17] B. Hacker, S. Welte, G. Rempe, and S. Ritter, "A photon-photon quantum gate based on a single atom in an optical resonator," *Nature*, vol. 536, no. 7615, pp. 193–196, 2016.

[18] M. Lukin and A. Imamoğlu, "Controlling photons using electromagnetically induced transparency," *Nature*, vol. 413, no. 6853, pp. 273–276, 2001.

[19] J. Hwang and E. Hinds, "Dye molecules as single-photon sources and large optical nonlinearities on a chip," *New Journal of Physics*, vol. 13, no. 8, p. 085009, 2011.

[20] S. M. Skoff, D. Papencordt, H. Schauffert, B. C. Bayer, and A. Rauschenbeutel, "An optical nanofiber-based interface for single molecules," *arXiv preprint arXiv:1604.04259*, 2016.

[21] E. Knill, R. Laflamme, and G. J. Milburn, "A scheme for efficient quantum computation with linear optics," *Nature*, vol. 409, no. 6816, pp. 46–52, 2001.

[22] S. Aaronson and A. Arkhipov, "The computational complexity of linear optics," in *Proceedings of the forty-third annual ACM symposium on Theory of computing*. ACM, 2011, pp. 333–342.

[23] C. Hong, Z.-Y. Ou, and L. Mandel, "Measurement of subpicosecond time intervals between two photons by interference," *Physical Review Letters*, vol. 59, no. 18, p. 2044, 1987.

[24] B. Lounis and M. Orrit, "Single-photon sources," *Reports on Progress in Physics*, vol. 68, no. 5, p. 1129, 2005.

[25] I. Aharonovich, D. Englund, and M. Toth, "Solid-state single-photon emitters," *Nature Photonics*, vol. 10, no. 10, pp. 631–641, 2016.

[26] B. Lounis and W. E. Moerner, "Single photons on demand from a single molecule at room temperature," *Nature*, vol. 407, no. 6803, pp. 491–493, 2000.

[27] J. C. Howell, R. S. Bennink, S. J. Bentley, and R. Boyd, "Realization of the einstein-podolsky-rosen paradox using momentum-and position-entangled photons from spontaneous parametric down conversion," *Physical Review Letters*, vol. 92, no. 21, p. 210403, 2004.

[28] M. W. Doherty, N. B. Manson, P. Delaney, F. Jelezko, J. Wrachtrup, and L. C. Hollenberg, "The nitrogen-vacancy colour centre in diamond," *Physics Reports*, vol. 528, no. 1, pp. 1–45, 2013.

[29] E. Neu, M. Agio, and C. Becher, "Photophysics of single silicon vacancy centers in diamond: implications for single photon emission," *Optics Express*, vol. 20, no. 18, pp. 19 956–19 971, 2012.

[30] S. Buckley, K. Rivoire, and J. Vučković, "Engineered quantum dot single-photon sources," *Reports on Progress in Physics*, vol. 75, no. 12, p. 126503, 2012.

[31] W. Moerner, "Single-photon sources based on single molecules in solids," *New Journal of Physics*, vol. 6, no. 1, p. 88, 2004.

[32] I. E. Zadeh, A. W. Elshaari, K. D. Jons, A. Fognini, D. Dalacu, P. J. Poole, M. E. Reimer, and V. Zwiller, "Deterministic integration of single photon sources in silicon based photonic circuits," *Nano letters*, vol. 16, no. 4, pp. 2289–2294, 2016.

[33] S. J. Kress, F. V. Antolinez, P. Richner, S. V. Jayanti, D. K. Kim, F. Prins, A. Riedinger, M. P. Fischer, S. Meyer, and K. M. McPeak, "Wedge waveguides and resonators for quantum plasmonics," *Nano letters*, vol. 15, no. 9, pp. 6267–6275, 2015.

[34] P. Lodahl, S. Mahmoodian, and S. Stobbe, "Interfacing single photons and single quantum dots with photonic nanostructures," *Reviews of Modern Physics*, vol. 87, no. 2, p. 347, 2015.

[35] M. Fujiwara, K. Yoshida, T. Noda, H. Takashima, A. W. Schell, N. Mizuochi, and S. Takeuchi, "Manipulation of single nanodiamonds to ultrathin fiber-taper nanofibers and control of nv-spin states toward fiber-integrated λ-systems," *Nanotechnology*, vol. 27, no. 45, p. 455202, 2016.

[36] A. W. Schell, J. Kaschke, J. Fischer, R. Henze, J. Wolters, M. Wegener, and O. Benson, "Three-dimensional quantum photonic elements based on single nitrogen vacancy-centres in laser-written microstructures," *Scientific Reports*, vol. 3, 2013.

[37] J.-T. Shen and S. Fan, "Strongly correlated two-photon transport in a one-dimensional waveguide coupled to a two-level system," *Physical Review Letters*, vol. 98, no. 15, p. 153003, 2007.

[38] L. Nakhimovsky, M. Lamotte, and J. Joussot-Dubien, *Handbook of low temperature electronic spectra of polycyclic aromatic hydrocarbons*. Elsevier, 1989.

[39] A. A. Nicolet, C. Hofmann, M. A. Kol'chenko, B. Kozankiewicz, and M. Orrit, "Single dibenzoterrylene molecules in an anthracene crystal: Spectroscopy and photophysics," *ChemPhysChem*, vol. 8, no. 8, pp. 1215–1220, 2007.

[40] C. Toninelli, K. Early, J. Bremi, A. Renn, and V. Sandoghdar, "Near-infrared single-photons from aligned molecules in ultrathin crystalline films at room temperature," *Optics Express*, vol. 18, no. 7, pp. 6577–6582, 2010.

[41] A. A. Nicolet, P. Bordat, C. Hofmann, M. A. Kol'chenko, B. Kozankiewicz, R. Brown, and M. Orrit, "Single dibenzoterrylene molecules in an anthracene crystal: main insertion sites," *ChemPhysChem*, vol. 8, no. 13, pp. 1929–1936, 2007.

[42] P. Lombardi, A. Ovvyan, S. Pazzagli, G. Mazzamuto, G. Kewes, O. Neitzke, N. Gruhler, O. Benson, W. Pernice, and F. Cataliotti, "Photostable molecules on chip: integrated single photon sources for quantum technologies," *ACS Photonics*, 2017. [Online]. Available: http://pubs.acs.org/doi/abs/10.1021/acsphotonics.7b00521

[43] L. Mandel and E. Wolf, *Optical coherence and quantum optics*. Cambridge University Press, 1995.

[44] R. Loudon, *The quantum theory of light*. Oxford University Press, 2000.

[45] M. Fox, *Quantum optics: an introduction*. Oxford University Press, 2006.

[46] C. Gerry and P. Knight, *Introductory quantum optics*. Cambridge University Press, 2005.

[47] X. Zou and L. Mandel, "Photon-antibunching and sub-poissonian photon statistics," *Physical Review A*, vol. 41, pp. 475–476, 1990.

[48] R. H. Brown and R. Twiss, "A test of a new type of stellar interferometer on sirius," *Nature*, vol. 178, no. 4541, pp. 1046–1048, 1956.

[49] H. Kimble, M. Dagenais, and L. Mandel, "Photon antibunching in resonance fluorescence," *Physical Review Letters*, vol. 39, no. 11, pp. 691–695, 1977.

[50] M. O. Scully and M. S. Zubairy, *Quantum optics*. Cambridge University Press, 1997.

[51] L. Novotny and B. Hecht, *Principles of nano-optics*. Cambridge University Press, 2012.

[52] E. Fermi, "Quantum theory of radiation," *Reviews of Modern Physics*, vol. 4, pp. 87–132, 1932.

[53] S. M. Barnett, B. Huttner, and R. Loudon, "Spontaneous emission in absorbing dielectric media," *Physical Review Letters*, vol. 68, no. 25, p. 3698, 1992.

[54] G. Björk, S. Machida, Y. Yamamoto, and K. Igeta, "Modification of spontaneous emission rate in planar dielectric microcavity structures," *Physical Review A*, vol. 44, no. 1, p. 669, 1991.

[55] E. M. Purcell, "Spontaneous emission probabilities at radio frequencies," *Physical Review*, vol. 69, p. 681, 1946.

[56] K. H. Drexhage, "Iv interaction of light with monomolecular dye layers," *Progress in Optics*, vol. 12, pp. 163–232, 1974.

[57] R. G. Hulet, E. S. Hilfer, and D. Kleppner, "Inhibited spontaneous emission by a rydberg atom," *Physical Review Letters*, vol. 55, pp. 2137–2140, 1985.

[58] P. Goy, J. Raimond, M. t. Gross, and S. Haroche, "Observation of cavity-enhanced single-atom spontaneous emission," *Physical Review Letters*, vol. 50, pp. 1903–1906, 1983.

[59] A. Kamli and M. Babiker, "Dielectric cavity qed between photonic crystals: An effective uniaxial medium approach," *Physical Review A*, vol. 62, no. 4, p. 043804, 2000.

[60] F. L. Kien, N. H. Quang, and K. Hakuta, "Spontaneous emission from an atom inside a dielectric sphere," *Optics Communications*, vol. 178, no. 1, pp. 151–164, 2000.

[61] Y. Yamamoto, S. Machida, K. Igeta, and Y. Horikoshi, "Enhanced and inhibited spontaneous emission of free excitons in gaas quantum wells in a micro-cavity," in *Coherence and Quantum Optics VI*. Springer, 1989, pp. 1249–1257.

[62] J. L. Jewell, Y. Lee, J. Harbison, A. Scherer, and L. Florez, "Vertical-cavity surface-emitting lasers-design, growth, fabrication, characterization," *IEEE Journal of Quantum Electronics*, vol. 27, pp. 1332–1346, 1991.

[63] M. Brune, P. Nussenzveig, F. Schmidt-Kaler, F. Bernardot, A. Maali, J. Raimond, and S. Haroche, "From lamb shift to light shifts: Vacuum and subphoton cavity fields measured by atomic phase sensitive detection," *Physical Review Letters*, vol. 72, no. 21, p. 3339, 1994.

[64] Q. A. Turchette, C. Hood, W. Lange, H. Mabuchi, and H. J. Kimble, "Measurement of conditional phase shifts for quantum logic," *Physical Review Letters*, vol. 75, no. 25, p. 4710, 1995.

[65] J. Gérard, B. Sermage, B. Gayral, B. Legrand, E. Costard, and V. Thierry-Mieg, "Enhanced spontaneous emission by quantum boxes in a monolithic optical microcavity," *Physical Review Letters*, vol. 81, no. 5, p. 1110, 1998.

[66] E. Hinds and V. Sandoghdar, "Cavity qed level shifts of simple atoms," *Physical Review A*, vol. 43, no. 1, p. 398, 1991.

[67] D. A. Steck, *Quantum and atom optics*, 2006. [Online]. Available: http://steck.us/teaching

[68] J. W. Goodman, *Statistical optics*. Wiley Online Library, 1985.

[69] A. Einstein, "Zur quantentheorie der strahlung," *Physikalische Zeitschrift*, vol. 18, pp. 121–128, 1917.

[70] C. Cohen-Tannoudji, J. Dupont-Roc, and G. Grynberg, *Atom-photon interactions: basic processes and applications*. Wiley Online Library, 1998.

[71] J. R. Lakowicz, *Principles of fluorescence spectroscopy*. Springer, 2007.

[72] C. Brunel, B. Lounis, P. Tamarat, and M. Orrit, "Triggered source of single photons based on controlled single molecule fluorescence," *Physical Review Letters*, vol. 83, no. 14, p. 2722, 1999.

[73] J.-B. Trebbia, H. Ruf, P. Tamarat, and B. Lounis, "Efficient generation of near infrared single photons from the zero-phonon line of a single molecule," *Optics Express*, vol. 17, no. 26, pp. 23 986–23 991, 2009.

[74] S. Scheel, "Single-photon sources–an introduction," *Journal of Modern Optics*, vol. 56, no. 2-3, pp. 141–160, 2009.

[75] S. Prawer and I. Aharonovich, *Quantum information processing with diamond: Principles and applications*. Elsevier, 2014.

[76] C. Zinoni, B. Alloing, L. Li, F. Marsili, A. Fiore, L. Lunghi, A. Gerardino, Y. B. Vakhtomin, K. Smirnov, and G. Gol'tsman, "Single-photon experiments at telecommunication wavelengths using nanowire superconducting detectors," *Applied physics letters*, vol. 91, no. 3, p. 031106, 2007.

[77] R. Brouri, A. Beveratos, J.-P. Poizat, and P. Grangier, "Photon antibunching in the fluorescence of individual color centers in diamond," *Optics Letters*, vol. 25, no. 17, pp. 1294–1296, 2000.

[78] C. Becher, A. Kiraz, P. Michler, A. Imamoğlu, W. Schoenfeld, P. Petroff, L. Zhang, and E. Hu, "Nonclassical radiation from a single self-assembled inas quantum dot," *Physical Review B*, vol. 63, no. 12, p. 121312, 2001.

[79] M. Oxborrow and A. G. Sinclair, "Single-photon sources," *Contemporary Physics*, vol. 46, no. 3, pp. 173–206, 2005.

[80] M. Nirmal, B. O. Dabbousi, M. G. Bawendi, J. Macklin, J. Trautman, T. Harris, and L. E. Brus, "Fluorescence intermittency in single cadmium selenide nanocrystals," *Nature*, vol. 383, no. 6603, pp. 802–804, 1996.

[81] U. Jantzen, A. B. Kurz, D. S. Rudnicki, C. Schäfermeier, K. D. Jahnke, U. L. Andersen, V. A. Davydov, V. N. Agafonov, A. Kubanek, and L. J. Rogers, "Nanodiamonds carrying silicon-vacancy quantum emitters with almost lifetime-limited linewidths," *New Journal of Physics*, vol. 18, no. 7, p. 073036, 2016.

[82] A. Diaspro, G. Chirico, C. Usai, P. Ramoino, and J. Dobrucki, "Photobleaching," in *Handbook of biological confocal microscopy*. Springer, 2006, pp. 690–702.

[83] W. Göhde, U. Fischer, H. Fuchs, J. Tittel, T. Basché, C. Bräuchle, A. Herrmann, and K. Müllen, "Fluorescence blinking and photobleaching of single terrylenediimide molecules studied with a confocal microscope," *The Journal of Physical Chemistry A*, vol. 102, no. 46, pp. 9109–9116, 1998.

[84] J. Bernard, L. Fleury, H. Talon, and M. Orrit, "Photon bunching in the fluorescence from single molecules: A probe for intersystem crossing," *The Journal of Chemical Physics*, vol. 98, no. 2, pp. 850–859, 1993.

[85] W. Moerner and D. P. Fromm, "Methods of single-molecule fluorescence spectroscopy and microscopy," *Review of Scientific Instruments*, vol. 74, no. 8, pp. 3597–3619, 2003.

[86] C. Santori, D. Fattal, J. Vučković, G. S. Solomon, and Y. Yamamoto, "Indistinguishable photons from a single-photon device," *Nature*, vol. 419, no. 6907, pp. 594–597, 2002.

[87] P. Grangier, "Quantum physics: Single photons stick together," *Nature*, vol. 419, no. 6907, pp. 577–577, 2002.

[88] H. Bernien, L. Childress, L. Robledo, M. Markham, D. Twitchen, and R. Hanson, "Two-photon quantum interference from separate nitrogen vacancy centers in diamond," *Physical Review Letters*, vol. 108, no. 4, p. 043604, 2012.

[89] A. Sipahigil, M. L. Goldman, E. Togan, Y. Chu, M. Markham, D. J. Twitchen, A. S. Zibrov, A. Kubanek, and M. D. Lukin, "Quantum interference of single photons from remote nitrogen-vacancy centers in diamond," *Physical Review Letters*, vol. 108, no. 14, p. 143601, 2012.

[90] V. Ahtee, R. Lettow, R. Pfab, A. Renn, E. Ikonen, S. Götzinger, and V. Sandoghdar, "Molecules as sources for indistinguishable single photons," *Journal of Modern Optics*, vol. 56, no. 2-3, pp. 161–166, 2009.

[91] J.-B. Trebbia, P. Tamarat, and B. Lounis, "Indistinguishable near-infrared single photons from an individual organic molecule," *Physical Review A*, vol. 82, no. 6, p. 063803, 2010.

[92] N. Somaschi, V. Giesz, L. De Santis, J. Loredo, M. P. Almeida, G. Hornecker, S. L. Portalupi, T. Grange, C. Antón, and J. Demory, "Near-optimal single-photon sources in the solid state," *Nature Photonics*, vol. 10, no. 5, pp. 340–345, 2016.

[93] J. Wolters, N. Sadzak, A. W. Schell, T. Schröder, and O. Benson, "Measurement of the ultrafast spectral diffusion of the optical transition of nitrogen vacancy centers in nano-size diamond using correlation interferometry," *Physical Review Letters*, vol. 110, no. 2, p. 027401, 2013.

[94] K. Heshami, D. G. England, P. C. Humphreys, P. J. Bustard, V. M. Acosta, J. Nunn, and B. J. Sussman, "Quantum memories: emerging applications and recent advances," *Journal of modern optics*, vol. 63, no. 20, pp. 2005–2028, 2016.

[95] S. Bozhevolnyi and F. García-Vidal, "Focus on plasmonics," *New Journal of Physics*, vol. 10, no. 10, p. 105001, 2008.

[96] F.-G. Deng and G. L. Long, "Bidirectional quantum key distribution protocol with practical faint laser pulses," *Physical Review A*, vol. 70, no. 1, p. 012311, 2004.

[97] A. Kuhn, M. Hennrich, and G. Rempe, "Deterministic single-photon source for distributed quantum networking," *Physical Review Letters*, vol. 89, no. 6, p. 067901, 2002.

[98] T. Monz, P. Schindler, J. T. Barreiro, M. Chwalla, D. Nigg, W. A. Coish, M. Harlander, W. Hänsel, M. Hennrich, and R. Blatt, "14-qubit entanglement: Creation and coherence," *Physical Review Letters*, vol. 106, no. 13, p. 130506, 2011.

[99] J. F. Clauser and A. Shimony, "Bell's theorem. experimental tests and implications," *Reports on Progress in Physics*, vol. 41, no. 12, p. 1881, 1978.

[100] A. Aspect, P. Grangier, and G. Roger, "Experimental tests of realistic local theories via bell's theorem," *Physical Review Letters*, vol. 47, no. 7, p. 460, 1981.

[101] Z. Yan, Y. Duan, L. Helt, M. Ams, M. J. Withford, and M. Steel, "Generation of heralded single photons beyond 1100 nm by spontaneous four-wave mixing in a side-stressed femtosecond laser-written waveguide," *Applied Physics Letters*, vol. 107, no. 23, p. 231106, 2015.

[102] A. L. Migdall, D. Branning, and S. Castelletto, "Tailoring single-photon and multiphoton probabilities of a single-photon on-demand source," *Physical Review A*, vol. 66, no. 5, p. 053805, 2002.

[103] M. J. Collins, C. Xiong, I. H. Rey, T. D. Vo, J. He, S. Shahnia, C. Reardon, T. F. Krauss, M. Steel, and A. S. Clark, "Integrated spatial multiplexing of heralded single-photon sources," *Nature communications*, vol. 4, 2013.

[104] F. Kaneda, B. G. Christensen, J. J. Wong, H. S. Park, K. T. McCusker, and P. G. Kwiat, "Time-multiplexed heralded single-photon source," *Optica*, vol. 2, no. 12, pp. 1010–1013, 2015.

[105] K. Beha, H. Fedder, M. Wolfer, M. C. Becker, P. Siyushev, M. Jamali, A. Batalov, C. Hinz, J. Hees, and L. Kirste, "Diamond nanophotonics," *Beilstein Journal of Nanotechnology*, vol. 3, p. 895, 2012.

[106] P. Tonndorf, R. Schmidt, R. Schneider, J. Kern, M. Buscema, G. A. Steele, A. Castellanos-Gomez, H. S. van der Zant, S. M. de Vasconcellos, and R. Bratschitsch, "Single-photon emission from localized excitons in an atomically thin semiconductor," *Optica*, vol. 2, no. 4, pp. 347–352, 2015.

[107] T. T. Tran, K. Bray, M. J. Ford, M. Toth, and I. Aharonovich, "Quantum emission from hexagonal boron nitride monolayers," *Nature Nanotechnology*, vol. 11, no. 1, pp. 37–41, 2016.

[108] M. Abbarchi, F. Troiani, C. Mastrandrea, G. Goldoni, T. Kuroda, T. Mano, K. Sakoda, N. Koguchi, S. Sanguinetti, and A. Vinattieri, "Spectral diffusion and line broadening in single self-assembled GaAs/ AlGaAs quantum dot photoluminescence," *Applied physics letters*, vol. 93, no. 16, p. 162101, 2008.

[109] M. Orrit and T. Basché, "Steady light from quantum dots, at last. But how?" *ChemPhysChem*, vol. 10, no. 14, pp. 2383–2385, 2009.

[110] M. J. Fernée, T. Plakhotnik, Y. Louyer, B. N. Littleton, C. Potzner, P. Tamarat, P. Mulvaney, and B. Lounis, "Spontaneous spectral diffusion in CdSe quantum dots," *The journal of physical chemistry letters*, vol. 3, no. 12, pp. 1716–1720, 2012.

[111] B. Lounis, H. Bechtel, D. Gerion, P. Alivisatos, and W. Moerner, "Photon antibunching in single CdSe/ZnS quantum dot fluorescence," *Chemical Physics Letters*, vol. 329, no. 5, pp. 399–404, 2000.

[112] P. Michler, A. Imamoğlu, M. Mason, P. Carson, G. Strouse, and S. Buratto, "Quantum correlation among photons from a single quantum dot at room temperature," *Nature*, vol. 406, no. 6799, pp. 968–970, 2000.

[113] H. Wang, Z.-C. Duan, Y.-H. Li, S. Chen, J.-P. Li, Y.-M. He, M.-C. Chen, Y. He, X. Ding, and C.-Z. Peng, "Near-transform-limited single photons from an efficient solid-state quantum emitter," *Physical Review Letters*, vol. 116, no. 21, p. 213601, 2016.

[114] A. Gruber, A. Dräbenstedt, C. Tietz, L. Fleury, J. Wrachtrup, and C. Von Borczyskowski, "Scanning confocal optical microscopy and magnetic resonance on single defect centers," *Science*, vol. 276, no. 5321, pp. 2012–2014, 1997.

[115] C. Kurtsiefer, S. Mayer, P. Zarda, and H. Weinfurter, "Stable solid-state source of single photons," *Physical Review Letters*, vol. 85, no. 2, p. 290, 2000.

[116] F. Jelezko, C. Tietz, A. Gruber, I. Popa, A. Nizovtsev, S. Kilin, and J. Wrachtrup, "Spectroscopy of single NV centers in diamond," *Single Molecules*, vol. 2, no. 4, pp. 255–260, 2001.

[117] A. Beveratos, R. Brouri, T. Gacoin, J.-P. Poizat, and P. Grangier, "Nonclassical radiation from diamond nanocrystals," *Physical Review A*, vol. 64, no. 6, p. 061802, 2001.

[118] J. Rabeau, A. Stacey, A. Rabeau, S. Prawer, F. Jelezko, I. Mirza, and J. Wrachtrup, "Single nitrogen vacancy centers in chemical vapor deposited diamond nanocrystals," *Nano letters*, vol. 7, no. 11, pp. 3433–3437, 2007.

[119] T. Gaebel, M. Domhan, I. Popa, C. Wittmann, P. Neumann, F. Jelezko, J. R. Rabeau, N. Stavrias, A. D. Greentree, and S. Prawer, "Room-temperature coherent coupling of single spins in diamond," *Nature Physics*, vol. 2, no. 6, pp. 408–413, 2006.

[120] E. Togan, Y. Chu, A. Trifonov, L. Jiang, J. Maze, L. Childress, M. G. Dutt, A. S. Sørensen, P. Hemmer, and A. S. Zibrov, "Quantum entanglement between an optical photon and a solid-state spin qubit," *Nature*, vol. 466, no. 7307, pp. 730–734, 2010.

[121] C. Wang, C. Kurtsiefer, H. Weinfurter, and B. Burchard, "Single photon emission from siv centres in diamond produced by ion implantation," *Journal of Physics B: Atomic, Molecular and Optical Physics*, vol. 39, no. 1, p. 37, 2005.

[122] E. Neu, D. Steinmetz, J. Riedrich-Möller, S. Gsell, M. Fischer, M. Schreck, and C. Becher, "Single photon emission from silicon-vacancy colour centres in chemical vapour deposition nano-diamonds on iridium," *New Journal of Physics*, vol. 13, no. 2, p. 025012, 2011.

[123] T. Iwasaki, F. Ishibashi, Y. Miyamoto, Y. Doi, S. Kobayashi, T. Miyazaki, K. Tahara, K. D. Jahnke, L. J. Rogers, and B. Naydenov, "Germanium-vacancy single color centers in diamond," *Scientific Reports*, vol. 5, 2015.

[124] X. S. Xie and J. K. Trautman, "Optical studies of single molecules at room temperature," *Annual review of physical chemistry*, vol. 49, no. 1, pp. 441–480, 1998.

[125] W. Moerner and M. Orrit, "Illuminating single molecules in condensed matter," *Science*, vol. 283, no. 5408, pp. 1670–1676, 1999.

[126] L. Fleury, B. Sick, G. Zumofen, B. Hecht, and U. P. Wild, "High photo-stability of single molecules in an organic crystal at room temperature observed by scanning confocal optical microscopy," *Molecular Physics*, vol. 95, no. 6, pp. 1333–1338, 1998.

[127] F. Kulzer, F. Koberling, T. Christ, A. Mews, and T. Basche, "Terrylene in p-terphenyl: single-molecule experiments at room temperature," *Chemical Physics*, vol. 247, no. 1, pp. 23–34, 1999.

[128] P. Tamarat, A. Maali, B. Lounis, and M. Orrit, "Ten years of single-molecule spectroscopy," *The Journal of Physical Chemistry A*, vol. 104, no. 1, pp. 1–16, 2000.

[129] T. Basché, W. Moerner, M. Orrit, and H. Talon, "Photon antibunching in the fluorescence of a single dye molecule trapped in a solid," *Physical Review Letters*, vol. 69, no. 10, p. 1516, 1992.

[130] W. Ambrose, T. Basché, and W. Moerner, "Detection and spectroscopy of single pentacene molecules in ap-terphenyl crystal by means of fluorescence excitation," *The Journal of Chemical Physics*, vol. 95, no. 10, pp. 7150–7163, 1991.

[131] A. W. Snyder and J. Love, *Optical waveguide theory*. Springer Science & Business Media, 2012.

[132] E. A. Marcatili, "Dielectric rectangular waveguide and directional coupler for integrated optics," *Bell Labs Technical Journal*, vol. 48, no. 7, pp. 2071–2102, 1969.

[133] R. G. Hunsperger and J. R. Meyer-Arendt, "Integrated optics: theory and technology," *Applied Optics*, vol. 31, p. 298, 1992.

[134] M. Davanço and K. Srinivasan, "Efficient spectroscopy of single embedded emitters using optical fiber taper waveguides," *Optics Express*, vol. 17, no. 13, pp. 10 542–10 563, 2009.

[135] V. Klimov and M. Ducloy, "Spontaneous emission rate of an excited atom placed near a nanofiber," *Physical Review A*, vol. 69, no. 1, p. 013812, 2004.

[136] A. V. Boriskin, S. V. Boriskina, A. Rolland, R. Sauleau, and A. I. Nosich, "Test of the fdtd accuracy in the analysis of the scattering resonances associated with high-q whispering-gallery modes of a circular cylinder," *JOSA A*, vol. 25, no. 5, pp. 1169–1173, 2008.

[137] J.-M. Jin, *The finite element method in electromagnetics*. John Wiley & Sons, 2015.

[138] "Comsol multiphysics reference manual, version 5.1," *COMSOL, Burlington, MA*. [Online]. Available: www.comsol.com

[139] C. Yeh and F. I. Shimabukuro, *The essence of dielectric waveguides*. Springer, 2008.

[140] J.-P. Berenger, "A perfectly matched layer for the absorption of electromagnetic waves," *Journal of computational physics*, vol. 114, no. 2, pp. 185–200, 1994.

[141] Y. Chen, T. R. Nielsen, N. Gregersen, P. Lodahl, and J. Mørk, "Finite-element modeling of spontaneous emission of a quantum emitter at nanoscale proximity to plasmonic waveguides," *Physical Review B*, vol. 81, no. 12, p. 125431, 2010.

[142] P. Siyushev, G. Stein, J. Wrachtrup, and I. Gerhardt, "Molecular photons interfaced with alkali atoms," *Nature*, vol. 509, no. 7498, pp. 66–70, 2014.

[143] G. Mazzamuto, A. Tabani, S. Pazzagli, S. Rizvi, A. Reserbat-Plantey, K. Schädler, G. Navickaite, L. Gaudreau, F. Cataliotti, and F. Koppens, "Single-molecule study for a graphene-based nano-position sensor," *New Journal of Physics*, vol. 16, no. 11, p. 113007, 2014.

[144] C. Eggeling, J. Widengren, R. Rigler, and C. Seidel, "Photobleaching of fluorescent dyes under conditions used for single-molecule detection: Evidence of two-step photolysis," *Analytical Chemistry*, vol. 70, no. 13, pp. 2651–2659, 1998.

[145] T. Basché, W. Moerner, M. Orrit, and U. Wild, *Single-molecule optical detection, imaging and spectroscopy*. VCH, Weinheim, 1997.

[146] K. K. Rebane and I. Rebane, "Peak value of the cross-section of zero-phonon line's absorption," *Journal of luminescence*, vol. 56, no. 1, pp. 39–45, 1993.

[147] W. Moerner, T. Plakhotnik, T. Irngartinger, M. Croci, V. Palm, and U. P. Wild, "Optical probing of single molecules of terrylene in a shpol'kii matrix: A two-state single-molecule switch," *The Journal of Physical Chemistry*, vol. 98, no. 30, pp. 7382–7389, 1994.

[148] N. Manson, J. Harrison, and M. Sellars, "Nitrogen-vacancy center in diamond: Model of the electronic structure and associated dynamics," *Physical Review B*, vol. 74, no. 10, p. 104303, 2006.

[149] E. Neu, C. Hepp, M. Hauschild, S. Gsell, M. Fischer, H. Sternschulte, D. Steinmüller-Nethl, M. Schreck, and C. Becher, "Low-temperature investigations of single silicon vacancy colour centres in diamond," *New Journal of Physics*, vol. 15, no. 4, p. 043005, 2013.

[150] L. Li, E. H. Chen, J. Zheng, S. L. Mouradian, F. Dolde, T. Schröder, S. Karaveli, M. L. Markham, D. J. Twitchen, and D. Englund, "Efficient photon collection from a nitrogen vacancy center in a circular bullseye grating," *Nano letters*, vol. 15, no. 3, pp. 1493–1497, 2015.

[151] J. Veerman, A. Otter, L. Kuipers, and N. Van Hulst, "High definition aperture probes for near-field optical microscopy fabricated by focused ion beam milling," *Applied Physics Letters*, vol. 72, no. 24, pp. 3115–3117, 1998.

[152] A. Kramer, J.-M. Segura, A. Hunkeler, A. Renn, and B. Hecht, "A cryogenic scanning near-field optical microscope with shear-force gapwidth control," *Review of Scientific Instruments*, vol. 73, no. 8, pp. 2937–2941, 2002.

[153] C. Hofmann, A. Nicolet, M. A. Kolachenko, and M. Orrit, "Towards nanoprobes for conduction in molecular crystals: Dibenzoterrylene in anthracene crystals," *Chemical Physics*, vol. 318, no. 1, pp. 1–6, 2005.

[154] K. D. Major, Y.-H. Lien, C. Polisseni, S. Grandi, K. W. Kho, A. S. Clark, J. Hwang, and E. Hinds, "Growth of optical-quality anthracene crystals doped with dibenzoterrylene for controlled single photon production," *Review of Scientific Instruments*, vol. 86, no. 8, p. 083106, 2015.

[155] N. Karl, "Crystals: Growth, properties and applications," *Berlin: Springer-Verlag*, vol. 1, no. 1, pp. 129–53, 1980.

[156] M. Orrit, *Single molecules optics*, 2011. [Online]. Available: http://www.molphys.leidenuniv.nl/monos/students/

[157] A. A. L. Nicolet, *Single-molecule probes in organic field-effect transistors*. LION/MoNOS, Faculty of Science, Leiden University, 2007.

[158] Y. Tian, P. Navarro, and M. Orrit, "Single molecule as a local acoustic detector for mechanical oscillators," *Physical Review Letters*, vol. 113, no. 13, p. 135505, 2014.

[159] M. Kol'chenko, A. Nicolet, M. Galouzis, C. Hofmann, B. Kozankiewicz, and M. Orrit, "Single molecules detect ultra-slow oscillators in a molecular crystal excited by ac voltages," *New Journal of Physics*, vol. 11, no. 2, p. 023037, 2009.

[160] S. Checcucci, P. Lombardi, S. Rizvi, F. Sgrignuoli, N. Gruhler, F. B. Dieleman, F. S. Cataliotti, W. H. Pernice, M. Agio, and C. Toninelli, "Beaming light from a quantum emitter with a planar optical antenna," *Light: Science & Applications*, vol. 6, no. 4, p. e16245, 2017.

[161] D. Wang, H. Kelkar, D. Martin-Cano, T. Utikal, S. Götzinger, and V. Sandoghdar, "Coherent coupling of a single molecule to a scanning fabry-perot microcavity," *Physical Review X*, vol. 7, no. 2, p. 021014, 2017.

[162] S. Faez, P. Türschmann, H. R. Haakh, S. Götzinger, and V. Sandoghdar, "Coherent interaction of light and single molecules in a dielectric nanoguide," *Physical Review Letters*, vol. 113, no. 21, p. 213601, 2014.

[163] T. Plakhotnik, E. A. Donley, and U. P. Wild, "Single-molecule spectroscopy," *Annual review of physical chemistry*, vol. 48, no. 1, pp. 181–212, 1997.

[164] W. Moerner and L. Kador, "Optical detection and spectroscopy of single molecules in a solid," *Physical Review Letters*, vol. 62, no. 21, p. 2535, 1989.

[165] M. Orrit and J. Bernard, "Single pentacene molecules detected by fluorescence excitation in a p-terphenyl crystal," *Physical Review Letters*, vol. 65, no. 21, p. 2716, 1990.

[166] E. Betzig and R. J. Chichester, "Single molecules observed by near-field scanning optical microscopy," *Science*, vol. 262, no. 5138, pp. 1422–1425, 1993.

[167] C. Brunel, B. Lounis, P. Tamarat, and M. Orrit, "Optical spectroscopy of single molecules: application to nonlinear and quantum optics," *Journal of Luminescence*, vol. 87–89, pp. 105 – 108, 2000.

[168] S. Weiss, "Fluorescence spectroscopy of single biomolecules," *Science*, vol. 283, no. 5408, pp. 1676–1683, 1999.

[169] E. Abbe, "Beiträge zur theorie des mikroskops und der mikroskopischen wahrnehmung," *Archiv für mikroskopische Anatomie*, vol. 9, no. 1, pp. 413–418, 1873.

[170] R. H. Webb, "Confocal optical microscopy," *Reports on Progress in Physics*, vol. 59, no. 3, p. 427, 1996.

[171] G. Mazzamuto, "Single organic molecules and light transport in thin films," Ph.D. dissertation, University of Florence, 2016.

[172] ——, "Sistema di acquisizione dati e controllo per misure su singole molecole con tecniche di microscopia di fluorescenza. national instruments case study." [Online]. Available: http://sine.ni.com/cs/app/doc/p/id/cs-15965

[173] W. Becker, "The bh tcspc handbook," *Becker & Hickl GmbH*, 2008.

[174] C. Eggeling, S. Berger, L. Brand, J. Fries, J. Schaffer, A. Volkmer, and C. Seidel, "Data registration and selective single-molecule analysis using multi-parameter fluorescence detection," *Journal of Biotechnology*, vol. 86, no. 3, pp. 163–180, 2001.

[175] H. Yang and X. S. Xie, "Probing single-molecule dynamics photon by photon," *The Journal of Chemical Physics*, vol. 117, no. 24, pp. 10 965–10 979, 2002.

[176] "Quantum-nanophotonics group. LENS." [Online]. Available: http://www.lens.unifi.it/quantum-nanophotonics

[177] Y. Tian, P. Navarro, B. Kozankiewicz, and M. Orrit, "Spectral diffusion of single dibenzoterrylene molecules in 2, 3-dimethylanthracene," *ChemPhysChem*, vol. 13, no. 15, pp. 3510–3515, 2012.

[178] W. H. Hesselink and D. A. Wiersma, "Optical dephasing and vibronic relaxation in molecular mixed crystals: A picosecond photon echo and optical study of pentacene in naphthalene and p-terphenyl," *The Journal of Chemical Physics*, vol. 73, no. 2, pp. 648–663, 1980.

[179] D. Walser, G. Zumofen, A. Renn, and T. Plakhotnik, "Line broadening and line shifts in one-and two-photon single-molecule spectra," *The Journal of Physical Chemistry A*, vol. 105, no. 13, pp. 3022–3028, 2001.

[180] E. Vetsch, D. Reitz, G. Sagué, R. Schmidt, S. Dawkins, and A. Rauschenbeutel, "Optical interface created by laser-cooled atoms trapped in the evanescent field surrounding an optical nanofiber," *Physical Review Letters*, vol. 104, no. 20, p. 203603, 2010.

[181] A. Politi, M. J. Cryan, J. G. Rarity, S. Yu, and J. L. O'brien, "Silica-on-silicon waveguide quantum circuits," *Science*, vol. 320, no. 5876, pp. 646–649, 2008.

[182] M. Arcari, I. Söllner, A. Javadi, S. L. Hansen, S. Mahmoodian, J. Liu, H. Thyrrestrup, E. H. Lee, J. D. Song, and S. Stobbe, "Near-unity coupling efficiency of a quantum emitter to a photonic crystal waveguide," *Physical Review Letters*, vol. 113, no. 9, p. 093603, 2014.

[183] R. S. Daveau, K. C. Balram, T. Pregnolato, J. Liu, E. H. Lee, J. D. Song, V. Verma, R. Mirin, S. W. Nam, and L. Midolo, "Efficient fiber-coupled single-photon source based on quantum dots in a photonic-crystal waveguide," *Optica*, vol. 4, no. 2, pp. 178–184, 2017.

[184] C. Polisseni, K. D. Major, S. Boissier, S. Grandi, A. S. Clark, and E. Hinds, "Stable, single-photon emitter in a thin organic crystal for application to quantum-photonic devices," *Optics Express*, vol. 24, no. 5, pp. 5615–5627, 2016.

[185] S. Romero-García, F. Merget, F. Zhong, H. Finkelstein, and J. Witzens, "Silicon nitride cmos-compatible platform for integrated photonics applications at visible wavelengths," *Optics Express*, vol. 21, no. 12, pp. 14 036–14 046, 2013.

[186] Y. Ding, C. Peucheret, H. Ou, and K. Yvind, "Fully etched apodized grating coupler on the soi platform with- 0.58 db coupling efficiency," *Optics Letters*, vol. 39, no. 18, pp. 5348–5350, 2014.

[187] M. Davanco, J. Liu, L. Sapienza, C.-Z. Zhang, J. V. D. M. Cardoso, V. Verma, R. Mirin, S. W. Nam, L. Liu, and K. Srinivasan, "A heterogeneous iii-v/silicon integration platform for on-chip quantum photonic circuits with single quantum dot devices," *arXiv preprint arXiv:1611.07654*, 2016.

[188] P. Türschmann, N. Rotenberg, J. Renger, I. Harder, O. Lohse, T. Utikal, S. Götzinger, and V. Sandoghdar, "On-chip linear and nonlinear control of single molecules coupled to a nanoguide," *arXiv preprint arXiv:1702.05923*, 2017.

[189] M. Faraday, "The bakerian lecture: experimental relations of gold (and other metals) to light," *Philosophical Transactions of the Royal Society of London*, vol. 147, pp. 145–181, 1857.

[190] R. Rossetti, S. Nakahara, and L. E. Brus, "Quantum size effects in the redox potentials, resonance raman spectra, and electronic spectra of cds crystallites in aqueous solution," *The Journal of Chemical Physics*, vol. 79, no. 2, pp. 1086–1088, 1983.

[191] A. Ekimov and A. Onushchenko, "Quantum size effect in three-dimensional microscopic semiconductor crystals," *ZhETF Pisma Redaktsiiu*, vol. 34, p. 363, 1981.

[192] V. I. Klimov, *Nanocrystal quantum dots*. CRC Press, 2010.

[193] M. Bruchez, M. Moronne, P. Gin, S. Weiss, and A. P. Alivisatos, "Semiconductor nanocrystals as fluorescent biological labels," *Science*, vol. 281, no. 5385, pp. 2013–2016, 1998.

[194] S. Nie and S. R. Emory, "Probing single molecules and single nanoparticles by surface-enhanced raman scattering," *Science*, vol. 275, no. 5303, pp. 1102–1106, 1997.

[195] M. V. Kovalenko, L. Manna, A. Cabot, Z. Hens, D. V. Talapin, C. R. Kagan, V. I. Klimov, A. L. Rogach, P. Reiss, and D. J. Milliron, "Prospects of nanoscience with nanocrystals," 2015.

[196] F. Pisanello, G. Leménager, L. Martiradonna, L. Carbone, S. Vezzoli, P. Desfonds, P. D. Cozzoli, J.-P. Hermier, E. Giacobino, and R. Cingolani, "Non-blinking single-photon generation with anisotropic colloidal nanocrystals: towards room-temperature, efficient, colloidal quantum sources," *Advanced Materials*, vol. 25, no. 14, pp. 1974–1980, 2013.

[197] S. A. Empedocles and M. G. Bawendi, "Quantum-confined stark effect in single cdse nanocrystallite quantum dots," *Science*, vol. 278, no. 5346, pp. 2114–2117, 1997.

[198] A. L. Efros and D. J. Nesbitt, "Origin and control of blinking in quantum dots," *Nature Nanotechnology*, vol. 11, no. 8, pp. 661–671, 2016.

[199] P. Chandrasekaran, M. Arivanandhan, T. Jayakumari, and P. Anandan, "The impact of sintering temperature on structural, morphological and thermoelectric properties of zinc titanate nanocrystals," *Materials Research Express*, vol. 4, no. 7, p. 075036, 2017.

[200] B.-W. Park, B. Philippe, X. Zhang, H. Rensmo, G. Boschloo, and E. M. Johansson, "Bismuth based hybrid perovskites a3bi2i9 (a: methylammonium or cesium) for solar cell application," *Advanced Materials*, vol. 27, no. 43, pp. 6806–6813, 2015.

[201] G. Raino, G. Nedelcu, L. Protesescu, M. I. Bodnarchuk, M. V. Kovalenko, R. F. Mahrt, and T. Stöferle, "Single cesium lead halide perovskite nanocrystals at low temperature: fast single-photon emission, reduced blinking, and exciton fine structure," *ACS Nano*, vol. 10, no. 2, pp. 2485–2490, 2016.

[202] A. Sipahigil, K. D. Jahnke, L. J. Rogers, T. Teraji, J. Isoya, A. S. Zibrov, F. Jelezko, and M. D. Lukin, "Indistinguishable photons from separated silicon-vacancy centers in diamond," *Physical Review Letters*, vol. 113, no. 11, p. 113602, 2014.

[203] T. T. Tran, M. Kianinia, K. Bray, S. Kim, Z.-Q. Xu, A. Gentle, B. Sontheimer, C. Bradac, and I. Aharanovich, "Nanodiamonds with photostable, sub-gigahertz linewidths quantum emitters," *arXiv preprint arXiv:1705.06810*, 2017.

[204] G. Kewes, M. Schoengen, G. Mazzamuto, O. Neitzke, R.-S. Schönfeld, A. W. Schell, J. Probst, J. Wolters, B. Löchel, and C. Toninelli, "Key components for nano-assembled plasmon-excited single molecule non-linear devices," *arXiv preprint arXiv:1501.04788*, 2015.

[205] J. Riedrich-Möller, C. Arend, C. Pauly, F. Mücklich, M. Fischer, S. Gsell, M. Schreck, and C. Becher, "Deterministic coupling of a single silicon-vacancy color center to a photonic crystal cavity in diamond," *Nano letters*, vol. 14, no. 9, pp. 5281–5287, 2014.

[206] S. L. Mouradian, T. Schröder, C. B. Poitras, L. Li, J. Goldstein, E. H. Chen, M. Walsh, J. Cardenas, M. L. Markham, and D. J. Twitchen, "Scalable integration of long-lived quantum memories into a photonic circuit," *Physical Review X*, vol. 5, no. 3, p. 031009, 2015.

[207] A. Javadi, I. Söllner, M. Arcari, S. L. Hansen, L. Midolo, S. Mahmoodian, G. Kiršanskė, T. Pregnolato, E. Lee, and J. Song, "Single-photon non-linear optics with a quantum dot in a waveguide," *Nature communications*, vol. 6, p. 8655, 2015.

[208] E. Bermúdez-Ureña, C. Gonzalez-Ballestero, M. Geiselmann, R. Marty, I. P. Radko, T. Holmgaard, Y. Alaverdyan, E. Moreno, F. J. García-Vidal, and S. I. Bozhevolnyi, "Coupling of individual quantum emitters to channel plasmons," *Nature communications*, vol. 6, p. 7883, 2015.

[209] A. W. Schell, G. Kewes, T. Schröder, J. Wolters, T. Aichele, and O. Benson, "A scanning probe-based pick-and-place procedure for assembly of integrated quantum optical hybrid devices," *Review of Scientific Instruments*, vol. 82, no. 7, p. 073709, 2011.

[210] L. Liebermeister, F. Petersen, A. v. Münchow, D. Burchardt, J. Hermelbracht, T. Tashima, A. W. Schell, O. Benson, T. Meinhardt, and A. Krueger, "Tapered fiber coupling of single photons emitted by a deterministically positioned single nitrogen vacancy center," *Applied Physics Letters*, vol. 104, no. 3, p. 031101, 2014.

[211] U. Mitschke and P. Bäuerle, "The electroluminescence of organic materials," *Journal of Materials Chemistry*, vol. 10, no. 7, pp. 1471–1507, 2000.

[212] G. De La Torre, P. Vazquez, F. Agullo-Lopez, and T. Torres, "Phthalocyanines and related compounds: organic targets for nonlinear optical applications," *Journal of Materials Chemistry*, vol. 8, no. 8, pp. 1671–1683, 1998.

[213] K. Baba, H. Kasai, K. Nishida, and H. Nakanishi, "Functional organic nanocrystals," in *Nanocrystal*. InTech, 2011.

[214] D. Horn and J. Rieger, "Organic nanoparticles in the aqueous phase-theory, experiment, and use," *Angewandte Chemie International Edition*, vol. 40, no. 23, pp. 4330–4361, 2001.

[215] H. Kasai, H. S. Nalwa, H. Oikawa, S. Okada, H. Matsuda, N. Minami, A. Kakuta, K. Ono, A. Mukoh, and H. Nakanishi, "A novel preparation method of organic microcrystals," *Japanese Journal of Applied Physics*, vol. 31, no. 8A, p. L1132, 1992.

[216] H. Kasai, H. Kamatani, S. Okada, H. Oikawa, H. Matsuda, and H. Nakanishi, "Size-dependent colors and luminescences of organic microcrystals," *Japanese Journal of Applied Physics*, vol. 35, no. 2B, p. L221, 1996.

[217] H. Katagi, H. Kasai, S. Okada, H. Oikawa, K. Komatsu, H. Matsuda, Z. Liu, and H. Nakanishi, "Size control of polydiacetylene microcrystals," *Japanese Journal of Applied Physics*, vol. 35, no. 10B, p. L1364, 1996.

[218] H.-B. Fu and J.-N. Yao, "Size effects on the optical properties of organic nanoparticles," *Journal of the American Chemical Society*, vol. 123, no. 7, pp. 1434–1439, 2001.

[219] H.-R. Chung, E. Kwon, H. Oikawa, H. Kasai, and H. Nakanishi, "Effect of solvent on organic nanocrystal growth using the reprecipitation method," *Journal of Crystal Growth*, vol. 294, no. 2, pp. 459–463, 2006.

[220] P. Kang, C. Chen, L. Hao, C. Zhu, Y. Hu, and Z. Chen, "A novel sonication route to prepare anthracene nanoparticles," *Materials Research Bulletin*, vol. 39, no. 4, pp. 545–551, 2004.

[221] T. Tachikawa, H.-R. Chung, A. Masuhara, H. Kasai, H. Oikawa, H. Nakanishi, M. Fujitsuka, and T. Majima, "In situ and ex situ observations of the growth dynamics of single perylene nanocrystals in water," *Journal of the American Chemical Society*, vol. 128, no. 50, pp. 15 944–15 945, 2006.

[222] E. V. Keuren, E. Georgieva, and M. Durst, "Kinetics of the growth of anthracene nanoparticles," *Journal of Dispersion Science and Technology*, vol. 24, no. 5, pp. 721–729, 2003.

[223] P. A. Hassan, S. Rana, and G. Verma, "Making sense of brownian motion: colloid characterization by dynamic light scattering," *Langmuir*, vol. 31, no. 1, pp. 3–12, 2014.

[224] B. J. Frisken, "Revisiting the method of cumulants for the analysis of dynamic light-scattering data," *Applied Optics*, vol. 40, no. 24, pp. 4087–4091, 2001.

[225] D. Necas and P. Klapetek, "Gwyddion: an open-source software for SPM data analysis," *Central European Journal of Physics*, vol. 10, pp. 181–188, 2012. [Online]. Available: http://gwyddion.net

[226] H. P. Klug and L. E. Alexander, "X-ray diffraction procedures: For polycrystalline and amorphous materials," *X-Ray Diffraction Procedures: For Polycrystalline and Amorphous Materials, 2nd Edition, by Harold P. Klug, Leroy E. Alexander, pp. 992. ISBN 0-471-49369-4. Wiley-VCH, May 1974.*, p. 992, 1974.

[227] S. Gražulis, A. Daškevič, A. Merkys, D. Chateigner, L. Lutterotti, M. Quiros, N. R. Serebryanaya, P. Moeck, R. T. Downs, and A. Le Bail, "Crystallography open database (cod): an open-access collection of crystal structures and platform for world-wide collaboration," *Nucleic acids research*, vol. 40, no. D1, pp. D420–D427, 2011.

[228] C. P. Brock and J. Dunitz, "Temperature dependence of thermal motion in crystalline anthracene," *Acta Crystallographica Section B: Structural Science*, vol. 46, no. 6, pp. 795–806, 1990.

[229] S. Jo, H. Yoshikawa, A. Fujii, and M. Takenaga, "Epitaxial growth of anthracene single crystals on graphite (0001) substrate with physical vapor growth technique," *Surface Science*, vol. 592, no. 1, pp. 37–41, 2005.

[230] R. Meltzer, W. Yen, H. Zheng, S. Feofilov, M. Dejneka, B. Tissue, and H. Yuan, "Evidence for long-range interactions between rare-earth impurity ions in nanocrystals embedded in amorphous matrices with the two-level systems of the matrix," *Physical Review B*, vol. 64, no. 10, p. 100201, 2001.

[231] J. D. Jackson, "Classical electrodynamics," 1999.

[232] M. A. Lieb, J. M. Zavislan, and L. Novotny, "Single-molecule orientations determined by direct emission pattern imaging," *JOSA B*, vol. 21, no. 6, pp. 1210–1215, 2004.

[233] H. F. Arnoldus and J. T. Foley, "Transmission of dipole radiation through interfaces and the phenomenon of anti-critical angles," *JOSA A*, vol. 21, no. 6, pp. 1109–1117, 2004.

[234] J. A. Schuller, S. Karaveli, T. Schiros, K. He, S. Yang, I. Kymissis, J. Shan, and R. Zia, "Orientation of luminescent excitons in layered nanomaterials," *Nature Nanotechnology*, vol. 8, no. 4, pp. 271–276, 2013.

[235] S. Checcucci, "Planar optical antenna to direct light emission," Master's thesis, University of Florence, 2015.

[236] B. Kozankiewicz, J. Bernard, and M. Orrit, "Single molecule lines and spectral hole burning of terrylene in different matrices," *The Journal of Chemical Physics*, vol. 101, no. 11, pp. 9377–9383, 1994.

[237] B. Gmeiner, A. Maser, T. Utikal, S. Götzinger, and V. Sandoghdar, "Spectroscopy and microscopy of single molecules in nanoscopic channels: spectral behavior vs. confinement depth," *Physical Chemistry Chemical Physics*, vol. 18, no. 29, pp. 19 588–19 594, 2016.

[238] A. Walser, G. Zumofen, A. Renn, S. Götzinger, and V. Sandoghdar, "Spectral dynamics and spatial localization of single molecules in a polymer," *Molecular Physics*, vol. 107, no. 18, pp. 1897–1909, 2009.

[239] A.-M. Boiron, P. Tamarat, B. Lounis, R. Brown, and M. Orrit, "Are the spectral trails of single molecules consistent with the standard two-level system model of glasses at low temperatures?" *Chemical Physics*, vol. 247, no. 1, pp. 119–132, 1999.

[240] F. Intonti, S. Vignolini, V. Türck, M. Colocci, P. Bettotti, L. Pavesi, S. L. Schweizer, R. Wehrspohn, and D. Wiersma, "Rewritable photonic circuits," *Applied physics letters*, vol. 89, no. 21, p. 211117, 2006.

[241] P. C. Painter and M. M. Coleman, *Fundamentals of polymer science: an introductory text*. Technomic, 1994.

[242] D. Cumming, S. Thoms, S. Beaumont, and J. Weaver, "Fabrication of 3 nm wires using 100 kev electron beam lithography and poly (methyl methacrylate) resist," *Applied physics letters*, vol. 68, no. 3, pp. 322–324, 1996.

[243] V. R. Manfrinato, L. Zhang, D. Su, H. Duan, R. G. Hobbs, E. A. Stach, and K. K. Berggren, "Resolution limits of electron-beam lithography toward the atomic scale," *Nano letters*, vol. 13, no. 4, pp. 1555–1558, 2013.

[244] W. Stoffels, E. Stoffels, and K. Tachibana, "Polymerization of fluorocarbons in reactive ion etching plasmas," *Journal of Vacuum Science & Technology A: Vacuum, Surfaces, and Films*, vol. 16, no. 1, pp. 87–95, 1998.

[245] N. Kooy, K. Mohamed, L. T. Pin, and O. S. Guan, "A review of roll-to-roll nanoimprint lithography," *Nanoscale research letters*, vol. 9, no. 1, p. 320, 2014.

[246] R. R. Krchnavek, G. R. Lalk, and D. H. Hartman, "Laser direct writing of channel waveguides using spin-on polymers," *Journal of Applied Physics*, vol. 66, no. 11, pp. 5156–5160, 1989.

[247] M. Schumann, T. Bückmann, N. Gruhler, M. Wegener, and W. Pernice, "Hybrid 2d-3d optical devices for integrated optics by direct laser writing," *Light: Science & Applications*, vol. 3, no. 6, p. e175, 2014.

[248] D. Di Camillo, V. Fasano, F. Ruggieri, S. Santucci, L. Lozzi, A. Camposeo, and D. Pisignano, "Near-field electrospinning of light-emitting conjugated polymer nanofibers," *Nanoscale*, vol. 5, no. 23, pp. 11 637–11 642, 2013.

[249] Z.-P. Liu, Y. Li, Y.-F. Xiao, B.-B. Li, X.-F. Jiang, Y. Qin, X.-B. Feng, H. Yang, and Q. Gong, "Direct laser writing of whispering gallery microcavities by two-photon polymerization," *Applied Physics Letters*, vol. 97, no. 21, p. 211105, 2010.

[250] C.-W. Lee, S. Pagliara, U. Keyser, and J. J. Baumberg, "Perpendicular coupling to in-plane photonics using arc waveguides fabricated via two-photon polymerization," *Applied Physics Letters*, vol. 100, no. 17, p. 171102, 2012.

[251] A. Landowski, D. Zepp, S. Wingerter, G. von Freymann, and A. Widera, "Direct laser written polymer waveguides with out of plane couplers for optical chips," *arXiv preprint arXiv:1703.08488*, 2017.

[252] C. Paquet and E. Kumacheva, "Nanostructured polymers for photonics," *Materials Today*, vol. 11, no. 4, pp. 48–56, 2008.

[253] N. Lindenmann, G. Balthasar, D. Hillerkuss, R. Schmogrow, M. Jordan, J. Leuthold, W. Freude, and C. Koos, "Photonic wire bonding: a novel concept for chip-scale interconnects," *Optics Express*, vol. 20, no. 16, pp. 17 667–17 677, 2012.

[254] H.-B. Sun, T. Tanaka, K. Takada, and S. Kawata, "Two-photon photopolymerization and diagnosis of three-dimensional microstructures containing fluorescent dyes," *Applied Physics Letters*, vol. 79, no. 10, pp. 1411–1413, 2001.

[255] J. Li, B. Jia, G. Zhou, and M. Gu, "Fabrication of three-dimensional woodpile photonic crystals in a pbse quantum dot composite material," *Optics Express*, vol. 14, no. 22, pp. 10 740–10 745, 2006.

[256] M. Gaio, M. Moffa, M. Castro-Lopez, D. Pisignano, A. Camposeo, and R. Sapienza, "Modal coupling of single photon emitters within nanofiber waveguides," *ACS Nano*, vol. 10, no. 6, pp. 6125–6130, 2016.

[257] G. A. Lindsay, P. R. Ashley, M. C. Davis, A. J. Guenthner, M. Sanghadasa, and M. E. Wright, "New photonic and electronic polymers," *Materials Science and Engineering: B*, vol. 132, no. 1, pp. 8–11, 2006.

[258] S. Shukla, X. Vidal, E. P. Furlani, M. T. Swihart, K.-T. Kim, Y.-K. Yoon, A. Urbas, and P. N. Prasad, "Subwavelength direct laser patterning of conductive gold nanostructures by simultaneous photopolymerization and photoreduction," *Acs Nano*, vol. 5, no. 3, pp. 1947–1957, 2011.

[259] Q. Shi, B. Sontheimer, N. Nikolay, A. Schell, J. Fischer, A. Naber, O. Benson, and M. Wegener, "Wiring up pre-characterized single-photon emitters by laser lithography," *Scientific Reports*, vol. 6, p. 31135, 2016.

[260] K. S. Novoselov, A. K. Geim, S. Morozov, D. Jiang, Y. Zhang, S. Dubonos, I. Grigorieva, and A. Firsov, "Electric field effect in atomically thin carbon films," *Science*, vol. 306, no. 5696, pp. 666–669, 2004.

[261] H. Kodama, "Automatic method for fabricating a three-dimensional plastic model with photo-hardening polymer," *Review of Scientific Instruments*, vol. 52, no. 11, pp. 1770–1773, 1981.

[262] T. Nakamoto, K. Yamaguchi, P. A. Abraha, and K. Mishima, "Manufacturing of three-dimensional micro-parts by uv laser induced polymerization," *Journal of Micromechanics and Microengineering*, vol. 6, no. 2, p. 240, 1996.

[263] S. Maruo, O. Nakamura, and S. Kawata, "Three-dimensional microfabrication with two-photon-absorbed photopolymerization," *Optics Letters*, vol. 22, no. 2, pp. 132–134, 1997.

[264] M. Farsari and B. N. Chichkov, "Materials processing: Two-photon fabrication," *Nature Photonics*, vol. 3, no. 8, pp. 450–452, 2009.

[265] S. Kawata, H.-B. Sun, T. Tanaka, and K. Takada, "Finer features for functional microdevices," *Nature*, vol. 412, no. 6848, pp. 697–698, 2001.

[266] D. Wu, Q.-D. Chen, L.-G. Niu, J.-N. Wang, J. Wang, R. Wang, H. Xia, and H.-B. Sun, "Femtosecond laser rapid prototyping of nanoshells and suspending components towards microfluidic devices," *Lab on a Chip*, vol. 9, no. 16, pp. 2391–2394, 2009.

[267] W. Zhang, P. Soman, K. Meggs, X. Qu, and S. Chen, "Tuning the poisson's ratio of biomaterials for investigating cellular response," *Advanced functional materials*, vol. 23, no. 25, pp. 3226–3232, 2013.

[268] Z.-B. Sun, X.-Z. Dong, W.-Q. Chen, S. Nakanishi, X.-M. Duan, and S. Kawata, "Multicolor polymer nanocomposites: in situ synthesis and fabrication of 3d microstructures," *Advanced Materials*, vol. 20, no. 5, pp. 914–919, 2008.

[269] J. Fischer, J. B. Mueller, J. Kaschke, T. J. Wolf, A.-N. Unterreiner, and M. Wegener, "Three-dimensional multi-photon direct laser writing with variable repetition rate," *Optics Express*, vol. 21, no. 22, pp. 26 244–26 260, 2013.

[270] "Ip-photoresis datasheet." [Online]. Available: http://www.nanoscribe.de/files/1814/0662/4393/IP-Resist_IP-Dip_web.pdf

[271] L. T. Fairhall, "Industrial toxicology." *Industrial Toxicology.*, pp. 172–173, 1949.

[272] M. H. Olsen, "Two-photon polymerization of immune cell scaffolds," Ph.D. dissertation, DTU Nanotech, Department of Micro- and Nanotechnology, Technical University of Denmark, 2013. [Online]. Available: http://orbit.dtu.dk/ws/files/82890420/prod11387460099286.Mark_Olsen_PhD_1.pdf

[273] M. Guney and G. Fedder, "Estimation of line dimensions in 3d direct laser writing lithography," *Journal of Micromechanics and Microengineering*, vol. 26, no. 10, p. 105011, 2016.

[274] H.-B. Sun, T. Tanaka, and S. Kawata, "Three-dimensional focal spots related to two-photon excitation," *Applied Physics Letters*, vol. 80, no. 20, pp. 3673–3675, 2002.

[275] C. A. Schneider, W. S. Rasband, and K. W. Eliceiri, "Nih image to imagej: 25 years of image analysis," *Nature methods*, vol. 9, no. 7, pp. 671–675, 2012.

[276] J. Fischer and M. Wegener, "Three-dimensional direct laser writing inspired by stimulated-emission-depletion microscopy," *Optical Materials Express*, vol. 1, no. 4, pp. 614–624, 2011.

[277] J. Wang and L. Ye, "Structure and properties of polyvinyl alcohol/polyurethane blends," *Composites Part B: Engineering*, vol. 69, pp. 389–396, 2015.

[278] S. Sreeja, S. Sreedhanya, N. Smijesh, R. Philip, and C. Muneera, "Organic dye impregnated poly (vinyl alcohol) nanocomposite as an efficient optical limiter: structure, morphology and photophysical properties," *Journal of Materials Chemistry C*, vol. 1, no. 24, pp. 3851–3861, 2013.

[279] C. Hassan and N. Peppas, "Structure and applications of poly (vinyl alcohol) hydrogels produced by conventional crosslinking or by freezing/thawing methods," *Biopolymers· PVA Hydrogels, Anionic Polymerisation Nanocomposites*, pp. 37–65, 2000.

[280] R. Guo, X. Ma, C. Hu, and Z. Jiang, "Novel pva–silica nanocomposite membrane for pervaporative dehydration of ethylene glycol aqueous solution," *Polymer*, vol. 48, no. 10, pp. 2939–2945, 2007.

[281] W. Hennink and C. Van Nostrum, "Novel crosslinking methods to design hydrogels," *Advanced drug delivery reviews*, vol. 64, pp. 223–236, 2012.

[282] J. Marqués-Hueso, R. Abargues, J. Canet-Ferrer, S. Agouram, J. L. Valdés, and J. P. Martinez-Pastor, "Au-pva nanocomposite negative resist for one-step three-dimensional e-beam lithography," *Langmuir*, vol. 26, no. 4, pp. 2825–2830, 2009.

[283] F. J. G. de Abajo, "Graphene nanophotonics," *Science*, vol. 339, no. 6122, pp. 917–918, 2013.

[284] F. H. L. Koppens, D. E. Chang, and F. J. García de Abajo, "Graphene plasmonics: A platform for strong light-matter interactions," *Nano Letters*, vol. 11, no. 8, pp. 3370–3377, 2011.

[285] A. Reserbat-Plantey, K. G. Schädler, L. Gaudreau, G. Navickaite, J. Güttinger, D. Chang, C. Toninelli, A. Bachtold, and F. H. Koppens, "Electromechanical control of nitrogen-vacancy defect emission using graphene nems," *Nature communications*, vol. 7, 2016.

[286] K. Tielrooij, L. Orona, A. Ferrier, M. Badioli, G. Navickaite, S. Coop, S. Nanot, B. Kalinic, T. Cesca, and L. Gaudreau, "Electrical control of optical emitter relaxation pathways enabled by graphene," *Nature Physics*, vol. 11, no. 3, pp. 281–287, 2015.

[287] L. Gaudreau, K. Tielrooij, G. Prawiroatmodjo, J. Osmond, F. G. de Abajo, and F. Koppens, "Universal distance-scaling of nonradiative energy transfer to graphene," *Nano Letters*, vol. 13, no. 5, pp. 2030–2035, 2013.

[288] C. A. Muschik, S. Moulieras, M. Lewenstein, F. Koppens, and D. Chang, "Harnessing vacuum forces for quantum sensing of graphene motion," *arXiv preprint arXiv:1304.8090*, 2013.

[289] K. F. Mak, C. Lee, J. Hone, J. Shan, and T. F. Heinz, "Atomically thin mos 2: a new direct-gap semiconductor," *Physical Review Letters*, vol. 105, no. 13, p. 136805, 2010.

[290] L. Kador, T. Latychevskaia, A. Renn, and U. P. Wild, "Radio-frequency stark effect modulation of single-molecule lines," *Journal of luminescence*, vol. 86, no. 3, pp. 189–194, 2000.

[291] N. Karimi, P. Kunwar, and J. Toivonen, "Direct laser writing of fluorescent silver nanoclusters in polyvinyl alcohol films," in *Frontiers in Optics*. Optical Society of America, 2015, pp. FTu5E–4.

[292] E. Käpylä, T. Sedlačík, D. B. Aydogan, J. Viitanen, F. Rypáček, and M. Kellomäki, "Direct laser writing of synthetic poly (amino acid) hydrogels and poly (ethylene glycol) diacrylates by two-photon polymerization," *Materials Science and Engineering: C*, vol. 43, pp. 280–289, 2014.

[293] E. M. Ahmed, "Hydrogel: Preparation, characterization, and applications: A review," *Journal of advanced research*, vol. 6, no. 2, pp. 105–121, 2015.

[294] I. Carusotto and C. Ciuti, "Quantum fluids of light," *Reviews of Modern Physics*, vol. 85, no. 1, p. 299, 2013.